Terra Tasmania Resources

2017 ANNUAL REPORT

Exploration License EL30/2011

Exploration Activity of
Terra Tasmania Resources Pty Ltd

Submitted pursuant to the
Mineral Resources Development Act 1995

12 December 2017

PREFACE

This Report has been prepared in accordance with the conditions outlined in Exploration Licence EL30/2011, subject to the Mineral Resources Development Act 1995 (As amended). To the best of Terra Tasmania Resources Pty Ltd ('TTR') knowledge, the report presented herein represents the intentions and work program undertaken leading up to and including the time of printing of the report.

During preparation of this report TTR has relied upon data, surveys, analysis, designs, plans and other information provided by past reports, third parties, and other individuals and organisations referenced herein. Except as otherwise stated in this report, TTR has not independently verified the accuracy or completeness of all nominated third party data, surveys, analysis, designs, plans and additional supporting information.

Terra Tasmania Resources Pty Ltd does not accept any responsibility for use of any part of this report by third parties.

Terra Tasmania Resources Pty. Ltd.

PO Box 103,

Scamander, Tasmania 7215

Australia

ACN: 141 081 889

ABN: 75 141 081 889

M: +61 419 599954 (Chairman, Dean Lisson)

+61 418 128838 (Director / General Manager, Phillip Simpson)

E: deanlisson@tassie.net.au

philsimpson@bigpond.com

Date of Issue: 12 December 2017

CONTENTS

Preface 2

1. Executive Summary and Recommendations 14

1.2 Methodology Used To Continue Work in 2017 14

2. STeP Analysis Progress Report 20

2.1 Geodynamic Analysis (GDA) results in 2017 20

2.1.1 Introduction – Method of GDA Assessment of Subsurface Oil and Gas Prospectivity 20

2.1.2 Geodynamic Analysis at 1:15,000,000 23

2.2 Thermal Mapping 28

Materials 28

Preprocessing 31

Methodology 33

Results 36

2.3 Mineral Indexes 41

Introduction - Hydrocarbon microseepage 41

Rremote Detection of Induced Surface Manifestations 43

Bleached red beds 43

Carbonate enrichment 44

Vegetation stress 45

Other Anomalies 45

Spectral indexes of various types of rocks 46

2.4 Relief Plasticity or Paleo-reconstruction Analisys (PRA) 75

Introduction 75

Continental-Scale PRA; Oil and Gas Fields of Australia 80

Identification and Analysis of Flow Structures of EL30/2011 at 1:500,000. Regional Analysis 88

2.5 Structuremetric Analysis (SMA) 102

2.6 Proprietary Spectrometric Analysis (PSA) 108

2.7 Existing 2D Seismic Evaluation 112

Post-processing 112

Interpretation of the Available 2D Post-Processed Seismic Data 113

2.8 Visualization of All Previous and New Prospects and Leads – Work in Progress 115

2.9 Morphometric Analysis (MMA) 122

Residual Relief Maps 122

Combined Analysis of Base Level & Residual Relief Maps 141

Differential Base Level Maps 149

2.10 Radar Differential Interferometry 159

General information 159

Area of Interest and Source Data 162

Processing 178

Radar Interferometry Process 179

Results 189

Conclusions 196

3. Appendixes 198

Appendix 1 – Source Satellite Data 198

Multispectral Data 198

DATA TYPE 199

PARAMETERS AND CHARACTERISTICS 199

OVERVIEW 199

Landsat-7 (ETM+) 199

Landsat-8 (OLI/TIRS) 200

TERRA (ASTER) 202

TERRA (ASTER) Day mode 203

TERRA (ASTER) Night mode 204

Radar Data 207

DATA TYPE 207

PARAMETERS AND CHARACTERISTICS 207

Alos Palsar Level 1.1 Single-look complex (SLC) 210

Alos Palsar Level 1.5 211

Topographical Data 212

DATA TYPE 212

PARAMETERS AND CHARACTERISTICS 212

SRTM (Shuttle Radar Topography Mission) 212

Australia National DEM based on SRTM 213

Aster GDEM v2 (Global Digital Elevation Model) 214

ASF radiometrically terrain corrected ALOS PALSAR 215

Appendix 2 - Existing Processed Seismic Post Processing and Interpretation 216

Figure 1: Fragment of the trans-planetary system of geodynamic control with nodes around the Australian continent. 20

Figure 2: Planetary tectonogens and nodes that influence Australian continent. 21

Figure 3: Pentagon-shaped area. 22

Figure 4: Geodynamic result of Bouguer gravity map of Australia analysis 24

Figure 5: Geodynamic result of Magnetic map of Australia analysis. 25

Figure 6: General Geodynamic observation of seismic activity of Australia. 26

Figure 7: Geodynamic pattern of tectonogens, nodes, and concentric systems over the map of natural resources of Australia. 27

Figure 8: Geodynamic pattern of tectonogens, nodes, and concentric system over the map of natural resources of Australia with HC-basins (shown via red ovals). 28

Figure 9: LandSat Scene LE70900892000097EDC00. 30

Figure 10: LE70900892001099ASA00. 31

Figure 11: Scheme of TM method; model of registration of thermal field. 35

Figure 12: The model of multitemporal registration of the thermal field. 35

Figure 13: Map of the thermal field (2000/04/06). 37

Figure 14: Map of the thermal field (2001/04/09). 38

Figure 15. Cloudiness mask. 39

Figure 16: Thermal field gradient of EL30/2011. 40

Figure 17: Surface alterations caused by migrating hydrocarbons (reproduced with permission from Duchscherer, 1982). 42

Figure 18. Spectra of minerals associated with hydrocarbon micro-seepage. 44

Figure 19: Hydrothermally altered rocks containing clay and alunite. 47

Figure 20. Rocks containing Fe2+ ion. 48

Figure 21. Rocks containing Fe^{3+} ion. 49

Figure 22. Iron-bearing minerals. 51

Figure 23: Hydrothermally altered rocks that have been subjected to oxidation of iron-bearing sulphides. 53

Figure 24. Carbonate rocks. 55

Figure 25: Rocks with metal iron. 56

Figure 26: Normalized difference vegetation index. 58

Figure 27: Mineral composite of AOI. 60

Figure 28: Hydrothermal composite. 62

Figure 29: Natural Color. Landsat 8 OLI, bands: 4,3,2. 63

Figure 30: Natural Color. Landsat 8 OLI, bands: 4,3,2. 64

Figure 31: Natural Color. Landsat 8 OLI, bands: 4,3,2. 65

Figure 32: Natural Color. Landsat 8 OLI, bands: 4,3,2. 66

Figure 33: Landsat 8 OLI, bands: 7,6,4. SWIR (Short Wave Infrared) Highlights rock formations. 67

Figure 34: Landsat 8 OLI, bands: 7,6,4. SWIR (Short Wave Infrared) Highlights rock formations. 68

Figure 35: Landsat 8 OLI, bands: 7,6,4. SWIR (Short Wave Infrared) Highlights rock formations. 69

Figure 36: Landsat 8 OLI, bands: 7,6,4. SWIR (Short Wave Infrared) Highlights rock formations. 70

Figure 37: Landsat 8 OLI, bands: 7,4,2. Geology Highlights geologic features. 71

Figure 38. Landsat 8 OLI, bands: 7,4,2. Geology Highlights geologic features. 72

Figure 39: Landsat 8 OLI, bands: 7,4,2. Geology Highlights geologic features. 73

Figure 40: Landsat 8 OLI, bands: 7,4,2. Geology Highlights geologic features. 74

Figure 41: Position of the island of Tasmania. 1:30,000,000. 77

Figure 42: Tectonic map of the southeastern Australia and Tasmania. 1:25,000,000. 78

Figure 43: Geological map of Tasmania. 1:500,000. 79

Figure 44: Select oil and gas fields on the tectonic map of southeastern Australia and Tasmania. Scale 1:25,000,000. 80

Figure 45: Litho-dynamic situation in southeastern Australia and Tasmania. 1:25,000,000. 81

Figure 46: Major oil and gas fields of southeastern Australia on the tectonic map of southeastern Australia and Tasmania relative to the large depressions (basins). 1:25,000,000. 83

Figure 47. Linear structures of the southeastern Australia and Tasmania. 1:25, 000,000. 84

Figure 48: Circular structures based on the map of litho-dynamic flows of southeastern Australia and Tasmania. 1:25,000.000. 85

Figure 49: Linear and circular structures of southeastern Australia and Tasmania. 1:25,000,000. 86

Figure 50: Zones of HC prospectivity, linear and circular structures of the southeastern Australia and Tasmania. 1:25,000,000. 87

Figure 51: Zones of HC prospectivity, linear and circular structures of the southern Australia and Tasmania. 1:25,000,000. 88

Figure 52. Topographic map of Tasmania. Scale 1:500000. 89

Figure 53. Relieve plasticity map of Tasmania. 1:500,000. 90

Figure 54: Litho-dynamic systems of Tasmania. 1:500,000. 92

Figure 55: Paleo-deltaic structures and depressions. 1:500,000. 94

Figure 56: Litho-dynamic circular structures of Tasmania. 1:500, 000. 95

Figure 57: Litho-dynamic circular structures of EL30/2011. Scale 1:500, 000. 96

Figure 58: Linear zones of tension of the earth's crust within Tasmania. Scale 1:500, 000. 97

Figure 59: Linear zones of tension of the earth's crust within Tasmania. Scale 1:500, 000. 98

Figure 60: Integration of all predictive criteria of HC potential (paleo-delta, contact zones of flow subsystems, depressions, circular and linear structures). 1:500,000. 99

Figure 61: Areas of convergence of predictive criteria on the map of litho-dynamic flows. 1:500,000. 100

Figure 62: Areas of convergence of predictive criteria on the map of litho-dynamic flows. 1:500,000. 101

Figure 63: HC-prospective areas on previously identified prognostic areas of EL30/2011. 1:500,000. 102

Figure 64: Superposition of Structuremetric analysis and geodynamic analysis. 1:100,000. 103

Figure 65: Local mapping of stress fields. 1:25,000. 104

Figure 66: HC leads based on SMA analysis of local stress fields. 1:25,000. 105

Figure 67: SMA QC areas at 1:5,000 within the HC trend delineated at 1:100,000. 106

Figure 68: SMA QC areas at 1:5,000 within the HC leads delineated at 1:25,000. 107

Figure 69: HC-bearing anomalies derived using PSA. 1:25,000. 108

Figure 70: Prospective resources of oil (in MMBO) for each PSA anomaly. 110

Figure 71 Prospective resources of gas (in BCF) for each PSA anomaly. 111

Figure 72: Prospective resources of oil and gas (in MMBO and BCF) for each PSA anomaly. 112

Figure 73: Noise cancellation work flow. 113

Figure 74: Original vs. noise-cancelled data. 113

Figure 75: The base map of the Bracknell Dome area and positions of cross sections. 115

Figure 76: Cross Section 1 (using STeP) and seismic section TB-01 PM through the Bracknell Dome area. 116

Figure 77: Cross Section 2 (using STeP), seismic section TB-01 PM through the Bracknell Dome area, and horizons picked on the STeP cross section as they correlate with the seismic section TB-01 SA. 117

Figure 78: Zoomed in Cross Section 2 (using STeP) and horizons picked on the STeP cross section as they correlate with the seismic section TB-01 SA. 118

Figure 79: 3D visualization of the Bracknell Dome area. 1:100,000. 118

Figure 80: 3D visualization of the Bracknell Dome area. 1:50,000. 119

Figure 81: 3D visualization of the Bracknell Dome area and picked horizons. 1:25,000. 119

Figure 82: 3D visualization of the Bracknell Dome area and picked structure and horizons. 1:25,000. 120

Figure 83: 3D visualization of the Bracknell Dome area and picked faults and horizons. 1:25,000. 120

Figure 84: 3D visualization zoom into proposed drilling location at Bracknell Dome and picked structure. 1:25,000. 121

Figure 85: 3D visualization zoom into proposed drilling location at Bracknell Dome and picked structure. 1:25,000. 121

Figure 86: Cumulative Residual Relief map corresponding to Base Level 2. 123

Figure 87: Cumulative Residual Relief map corresponding to Base Level 3. 124

Figure 88: Cumulative Residual Relief map corresponding to Base Level 4. 125

Figure 89: Cumulative Residual Relief map corresponding to Base Level 5. 126

Figure 90: Cumulative Residual Relief map corresponding to Base Level 6. 127

Figure 91: Cumulative Residual Relief map corresponding to Base Level 7. 128

Figure 92: Regional (Trend) Residual Relief map corresponding to Base Level 2. 129

Figure 93: Regional (Trend) Residual Relief map corresponding to Base Level 3. 130

Figure 94: Regional (Trend) Residual Relief map corresponding to Base Level 4. 131

Figure 95: Regional (Trend) Residual Relief map corresponding to Base Level 5. 132

Figure 96: Regional (Trend) Residual Relief map corresponding to Base Level 6. 133

Figure 97: Regional (Trend) Residual Relief map corresponding to Base Level 7. 134

Figure 98: Local Residual Relief map corresponding to Base Level 2. 135

Figure 99: Local Residual Relief map corresponding to Base Level 3. 136

Figure 100: Local Residual Relief map corresponding to Base Level 4. 137

Figure 101: Local residual relief map corresponding to Base Level 5. 138

Figure 102: Local residual relief map corresponding to Base Level 6. 139

Figure 103: Local residual relief map corresponding to Base Level 7. 140

Figure 104: Example of direct relief 141

Figure 105: Example of inverse relief 141

Figure 106: Example of revealing local tectonic structures. 142

Figure 107: Local Residual Relief and Base Level maps 2nd order. 143

Figure 108: Local Residual Relief and Base Level maps 3rd order. 144

Figure 109: Local Residual Relief and Base Level maps 4th order. 145

Figure 110: Local Residual Relief and Base Level maps 5th order. 146

Figure 111: Local Residual Relief and Base Level maps 6th order. 147

Figure 112: Local Residual Relief and Base Level maps 7th order. 148

Figure 113: Difference of Base Levels 6 and 7. 150

Figure 114: Difference of Base Levels 5 and 6. 151

Figure 115: Difference of Base Levels 4 and 5. 152

Figure 116: Difference of Base Levels 3 and 4. 153

Figure 117: Difference of Base Levels 2 and 3. 154

Figure 118: Difference between adjacent levels for Base Levels 2 through 7. 155

Figure 119: Potentially HC-prospective areas related to the intensive uplifting forming the inverse relief (relevant to the corresponding tectonic activation period). 156

Figure 120: Difference between adjacent levels for Base Levels 2 through 7. 157

Figure 121: Potentially HC-prospective areas related to paleo-valleys. 158

Figure 122: Schematic representation of the principle of scanning by a satellite radar system (Rosen, 2009) 159

Figure 123: The geometric principle of obtaining radar interferometric pairs. 161

Figure 124: AOI EL30/2011 163

Figure 125: Time-Position plot, which provides the normal distance between the Super Master (y axis) and the input acquisition dates (x axis). 178

Figure 126: Time-Baseline plot - provides the normal baseline (y axis) and the input acquisition dates (x axis). 179

Figure 127: Geodetic Control Points. 188

Figure 128: Displacement surface for the period 2017/06/25 – 2017/06/13. 190

Figure 129: Displacement surface for the period 2017/07/07 – 2017/06/13. 191

Figure 130: Displacement surface for the period 2017/07/19 – 2017/06/13. 192

Figure 131: Displacement surface for the period 2017/08/12 – 2017/06/13. 193

Figure 132: Displacement surface for the period 2017/09/05 – 2017/06/13. 194

Figure 133: Time profiles of the surface displacements measured in specific location along line A. 195

Figure 134: Contours (red) of potential anticlinal structural traps. 197

TTR during 2017 was restricted in the implementation of its previously stated work program due to the postponement in receiving the 2-year Extension of Term of EL30/2011. Concerns in Tasmania regarding the controversial drilling technology known as 'fracking' kept tenement administration decisions for Category 4 Minerals tenements in suspense until legal consideration to the wording of all future licence documents was completed and approved by the Minister. TTR's funding partner, Argentine oil and gas exploration and production company, Petroquimica Comodoro Rivadavia SA (PCR) delayed full funding of the EL30/2011 Work Program, due to the concerns with conditions precedent involved in the EL30/2011 Extension of Term process plus an additional TTR Category 4 Minerals application, that all formed part of the consolidated financing agreement executed by PCR and TTR.

Despite all procedural challenges, TTR has proceeded expediently with ongoing satellite analysis through its technical team at Terra Insight Services (TIS) in New York.

TIS, a service arm of TERT, continued its remote sensing satellite technology application to further identify prospects and leads on EL30/2011 that were identified in the past and outlined in TTR's report for year 2016.

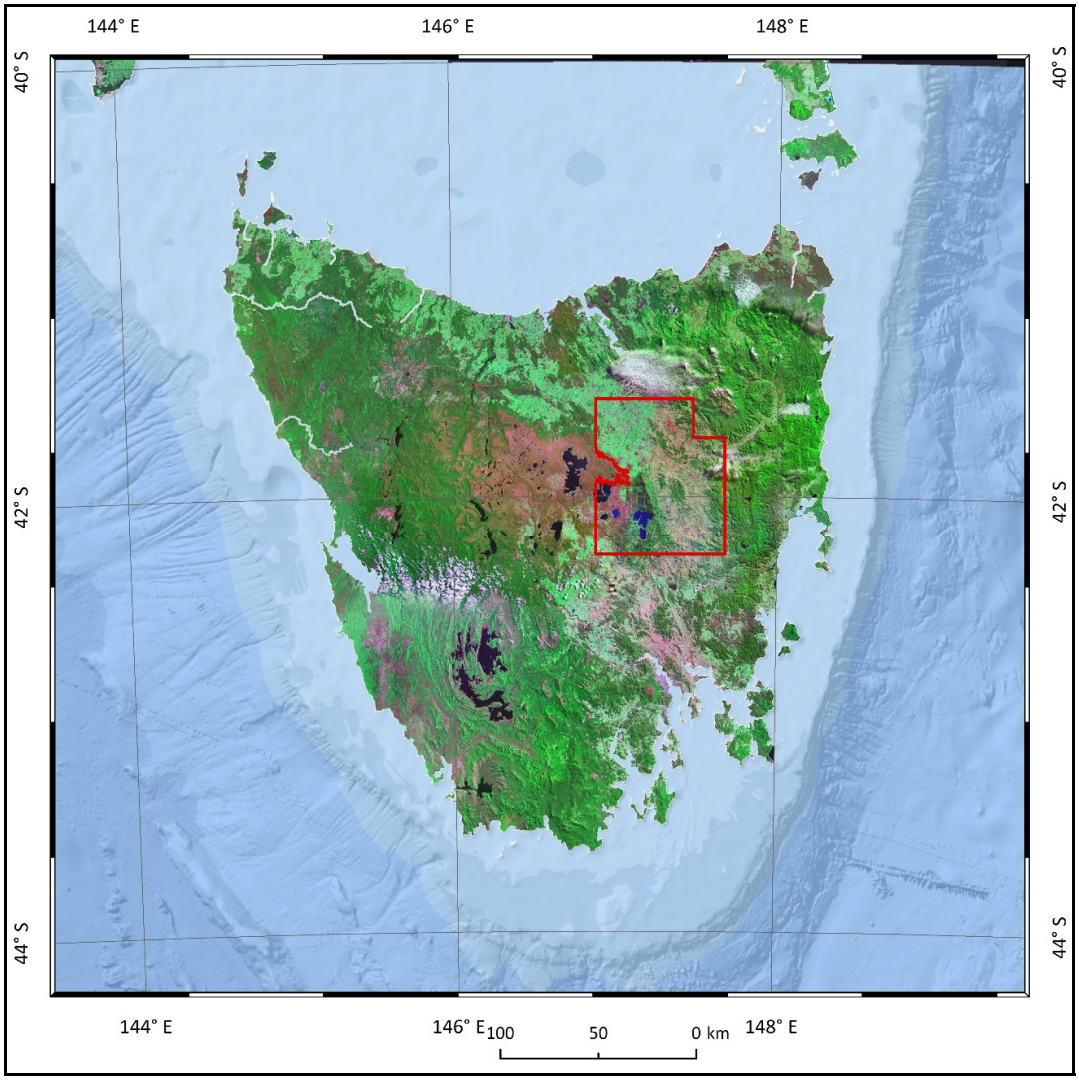
TTR planned to combine the STeP analysis of EL30/2011 and an adjacent tenement (*under ELA status*) on a regional basis in order to bring efficiencies into its overall budget, but proceeded with the STeP satellite survey solely on EL30/2011 due to (a) time constraints and (b) to complete the body of work that maintained TTR's alignment with its stated EL30/2011 Work Program.

Terra Insight Services Inc, of New York (TIS) carried out additional satellite analyses, both at regional and local scales (*that was initially unplanned*), for the ongoing advancement of TTR and its Work Program. In short, while the STeP analysis is not complete, it has progressed significantly and been expanded with several additional remote sensing data sets, including Radar Interferometry, Morphometric Analysis (*based on two sets of digital elevation data*) and Reservoir / Structural Visualization.

In continuation of the Play Based findings of Dr. Andre Coffa and Petrogeos Consulting in Melbourne (VIC) as per Dr. Coffa's recommendations in the 2015 Annual Report, TTR elected to use the subterranean remote sensing (STeP) satellite technology to supplement the work already done over EL30/2011 and solidify the hydrocarbon plays and prospects. While in 2016, certain trends and anomalies advanced Dr. Coffa's play-based analysis, the STeP program of 2017 has rendered several anomalies and features that assert the potential presence of HC's in large quantities (*please refer to the **Table 4** of geological resources of oil and gas within EL30/2011*).

TTR has additionally post-processed one of the two data volumes of regional 2D seismic that was furnished to TTR by MRT in digital processed format. The second data volume is not accessible from MRT in digital processed format.

TTR looks forward with anticipation to completing the STeP program in 2018 and continuing with the sequential steps of the Work Program.



TERRA TASMANIA RESOURCES (EL30/2011)

Terra Insight Services, Inc.

Date Submitted: 11/27/2017

1. EXECUTIVE SUMMARY AND RECOMMENDATIONS

1.2 METHODOLOGY USED TO CONTINUE WORK IN 2017

Based on the work carried out in 2016 and its recommendations, work with several STeP® methods was carried further to "zoom" into the leads and prospects identified previously and to obtain additional structural and spectral data on the tenement to move closer to the geophysical field work and exploratory drilling.

Dating back to 2011, the original TTR work program entailed STeP® survey conducted by Terra Insight Services, Inc. (www.terrainsight.com) and was accepted by MRT. TTR has reverted to the STeP survey as a part of the play-based approach in order to elevate the value of all of the geological research and use STeP as an additional input and a part of the approach and in order to better high-grade the Area of Interest (AOI or EL30/2011) into zones of prospectivity.

In order to better understand the work carried out in 2017, in furtherance of the work started in 2016 or as from the beginning, the methodologies and action items described below are highlighted Yellow (to show that the work in 2017 furthered that of 2016) or Green (to show that the work was started in 2017 only). Purple highlight indicates work under the appropriate heading is complete.

STeP is a multi-stage approach that consists of the application of the following methodologies:

- Geodynamic Analysis (GDA);
- Morphometric Analysis (MMA);
- Paleo-reconstruction (PRA);
- Structuremetric Analysis (SMA);
- Spectrometric Analysis (PSP-RSS); Complete.
- Conventional Remote sensing; Complete.
- Integration of all methods with traditional datasets;
- Other mathematical and geological methods such as artificial neural networks or radar interfometry. Radar Interferometry is Complete.

A full STeP description is available to better understand the methods carried out as a part of this play-based approach. The brief description is as follows:

- GDA is based on divisibility of the lithosphere, where most mineragenic systems are confined to specific locations that are calculable and inherited. Thus, GDA uses these principles to located zones of prospectivity;
- MMA is based on the principle of erosion basis being connected with tectonics, and it quantifies the erosion network in order to located vertical movements or uplifts irrespective of their lithology;
- PRA represents the interior using the model of flows, which examines the Earth from the perspective of dynamics, or movements within the geomedium, and, among other things, locates depocenters, deltaic features, zones of accumulation that are most favorable for accumulation of HCs, as well as interprets such flow patterns in connection with directions of HC migration;

- SMA uses stress patterns in order to identify paleo-stress and zones of unique paleo-stress that are acoustically different in terms of being HC-saturated;
- PSP-RSS uses spectral manifestations of presence of HCs in the subsurface;
- Other methods are conventional and well-understood;
- Integration of STeP results with conventional datasets, including magnetic, gravity and seismic is a part of the STeP analysis.

STeP is typically carried out in two major phases: Phase 1 as a regional survey with exploration leads defined based on the scale ranging from 1:300,000 to 1:100,000, and Phase 2 as a local survey with exploration leads defined based on the scale ranging from 1:50,000 to 1:10,000. The activities/services and deliverables of the survey are defined as follows:

1. During Phase 1, which shall last for 8 calendar month from the date of execution of this contract, of STeP analysis, Contractor shall perform the following Services:
   - 1.1. Collect from Client and via other available public domain means and sources and analyze the geological, geophysical, geochemical, remote sensing, natural resources exploration records, and such other relevant data in connection with the SERVICE AREA;
   - 1.2. Conduct assessment of the geological situation of the SERVICE AREA based on the collected data;
   - 1.3. Acquire and select general and specific, digital satellite data/images, and then prepare and process these satellite data/images;
   - 1.4. Conduct Geodynamic analysis at the scales ranging between 1:2,500,000 and 1:300,000, as applicable;
   - 1.5. Conduct Morphometric analysis at the scales ranging between 1:300,000 and 1:100,000, as applicable;
   - 1.6. Conduct Paleo-reconstruction at scales ranging between 1:2,500,000 and 1:100,000, as applicable;
   - 1.7. Conduct Proprietary Spectrometric analysis at the scales ranging between 1:300,000 and 1:100,000, as applicable;
   - 1.8. Conduct Structuremetric analysis at the scale 1:100,000, as applicable;
   - 1.9. Conduct Photogeological studies; the scale and size of features and tectonic movements described in the study will correspond to their surface expression;
   - 1.10. Conduct traditional remote sensing studies onshore, such as thermal, lineament density, and spectral indexes mapping (and/or similar); the selection of such methods and their working scale are subject to the location and geology of the SERVICE AREA;
   - 1.11. Integrate all of the datasets collected via the activities described in items “1.1” through “1.10”, assess HC- prospectivity of the SERVICE AREA, and delineate exploration targets/structures, as applicable;
   - 1.12. Produce a report;
   - 1.13. Produce all cartographic materials.
   - 2.1. Acquire and select additional digital satellite data/images, as needed, prepare and process these satellite data/images;
   - 2.2. Conduct Morphometric analysis at the scales ranging between 1:100,000 and 1:50,000, as applicable;

2.3. Conduct Paleo-reconstruction at the scales ranging between 1:100,000 and 1:50,000, as applicable;

2.4. Conduct Proprietary Spectrometric analysis at the scales ranging between 1:50,000 and 1:10,000, as applicable;

2.5. Conduct Structuremetric analysis at the scale 1:10,000 or better, as applicable;

2.6. Integrate all of the datasets collected via the activities described in items "3.1" through "3.5", assess HC- prospectivity of the SERVICE AREA, delineate structures contours and determine potential drilling locations within each structure;

2.7. Produce a report;

2.8. Produce all cartographic materials.

3.1. Map(s) showing results of Geodynamic analysis at scale from 1:2,500,000 to 1:300,000, as applicable (from continental/regional scale to local); the results typically consist of a report and maps depicting various geodynamic elements, their analysis, and areas/contours of hydrocarbon prospectivity;

3.2. Map(s) showing results of morphometric analysis at the scale ranging between 1:300,000 and 1:100,000, as applicable; the results typically consist of an analytical report and maps containing varying morphometric constructs, base levels, areas of subsurface uplifts, anticlines, and/or closures;

3.3. Map(s) depicting results of paleo-reconstruction analysis at the scale ranging between 1:2,500,000 and 1:100,000, as applicable (from continental/regional scale to local); the results typically consist of an analytical report and maps containing paleo-reconstructions of the surface at different scales as well as of the base levels that are relevant to the investigations; paleo-reconstructive features and criteria are superimposed to produce a map of prospectivity for different scales and/or paleo-geographic levels;

3.4. Map(s) depicting results of Proprietary Spectrometric analysis at the scales ranging between 1:300,000 and 1:100,000, as applicable; the results typically consist of a short analytical report and map(s) containing spectral anomalies that are indicative of the presence of hydrocarbons;

3.5. Map(s) depicting results of Structuremetric analysis at the scale of 1:100,000 (also other map(s) may be provided at regional scales, as applicable); the results typically consist of an analytical report and maps containing stress fields and contours of targets, but may also include reconstructions of the phases of development of the sedimentary environment and other relevant information and maps as determined applicable in the course of the Services;

3.6. Map(s) depicting results of a traditional remote sensing nature, such as thermal maps, lineament density, spectral indexes, and/or similar with scale ranging from approximately 1:300,000 to 1:100,000, as applicable; the results typically consist of appropriate maps such as minerals indexes, thermal gradients, etc.;

3.7. Map(s) depicting the results of photogeological analysis at scale equivalent to the size and scale of relevant surface features being analyzed; the results

typically consist of an analytical report and appropriate maps of showing tectonic structures, directions of tectonic movements, natural phenomena at the surface indicative of certain subsurface events, etc.;

3.8. Map(s) showing the process of superposition and integration of all of the datasets and a resulting map of all exploration leads/structures/anomalies, as applicable, at the scales commensurate with the scale of each type of analysis;

3.9. Map(s) of all of the Deliverables described herein in a cartographic format, such as SHP (shape) or MPK, for ease of Client's integration of STeP findings with the Client's internal G&G systems;

3.10. The report will be delivered in soft copy and is anticipated to include, to the extent determined to be relevant, recommendations on the Service Area's prospectivity with written justifications and geological conclusions drawn from the STeP® findings:

3.10.1. General assessment of prospectivity for HCs;

3.10.2. Indication (mapping) of the contours of HCs prospectivity with scale 1:300,000 to 1:100,000, as applicable to the various parts of the analysis;

3.10.3. Selection of areas of prospectivity as leads or prospects in cartographic format and recommendations on their further exploration priority;

3.10.4. Interpretation of the analysis results and correlation with existing well control and other G&G data, if available.

In summary: the report will contain a myriad of maps, models, calculations and their interpretations leading to the conclusions and maps of contours of potential HC deposits within the Service Area. Such contours are considered high value exploration targets for further exploration. These anomalies will be high-graded in relation to their exploration priority.

4.1. Map(s) showing results of morphometric analysis at the scale ranging between 1:100,000 and 1:50,000, as applicable; the results typically consist of a short report and maps containing varying morphometric constructs, base levels, areas of subsurface uplifts, anticlines, and/or closures;

4.2. Map(s) depicting results of paleo-reconstruction analysis at the scale ranging between 1:1,000,000 and 1:50,000, as applicable; the results typically consist of a short report and maps containing paleo-reconstructions that are relevant to the investigation; paleo-reconstructive features and criteria are superimposed to produce a map of prospectivity for different scales and/or paleo-geographic levels;

4.3. Map(s) depicting results of Proprietary Spectrometric analysis at the scales ranging between 1:100,000 and 1:50,000, as applicable; the results typically consist of a short report and map(s) containing spectral anomalies that are indicative of the presence of hydrocarbons;

4.4. Map(s) depicting results of Structuremetric analysis at the scale of 1:10,000 (or better, as applicable); the results typically consist of a short report and

maps containing stress fields, structure contours, drilling locations for each analyzed structure, and target depths;

4.5. Map(s) showing the process of superposition and integration of all of the datasets and a resulting map of all exploration leads/structures/anomalies, as applicable, at the scales commensurate with the scale of each type of analysis;

4.6. Map(s) of all of the Deliverables described herein in a cartographic format, such as SHP (shape) or MPK, for ease of Client's integration of STeP findings with the Client's internal G&G systems;

4.7. The report will be delivered in soft copy and is anticipated to include:

4.7.1. Assessment of prospectivity for HCs of the local-scale targets analyzed in Phase 2;

4.7.2. Mapping of structure contours of HCs of the local-scale targets analyzed in Phase 2;

4.7.3. Table listing coordinates of proposed drilling locations and approximate target depths of potential reservoirs.

In summary: the report will contain a myriad of maps, models, calculations and their interpretations leading to the conclusions and maps of contours of potential HC structures at a local scale. Such contours are considered high value exploration targets for further exploration. These structures will be high-graded in relation to their exploration priority. Recommendations of the next steps are expected to be: limited 3D seismic surveys, geochemical surveys, STeP survey at a more detailed scale such as 1:10,000 or better. If 2D or 3D seismic is recommended, such seismic datasets are expected to validate the STeP structures and help solidify the drilling locations.

Each type of the analysis listed above is being carried out independently and in parallel with its other counterparts. Most of the analysis described herein are typically carried out based on several scales – from regional or even continental to local scales. Upon completion of all the separate types of processing listed above, they are all integrated in GIS and interpreted in connection with the local geology and geophysical information.

In 2016, the regional phase of STeP was being carried out, and a certain trend and zones of HC prospectivity have already been identified (**Figure 64**).

The following methodologies have been carried out in 2017 and presented in the following sections of this Report:

1. Collection of source data. Subject to further work, additional data may be colleted.
2. Geodynamic Analysis – furthered from GDA performed in 2016. Additional work is ongoing.
3. Mineral Indexes – furthered from the work performed in 2017. Work is complete.
4. Relief plasticity and Paleo-reconstruction. Additional work is ongoing.
5. Structuremetric Analysis. Additional work is ongoing.
6. Proprietary Spectrometry. Work is complete.
7. Morphometric Analysis. Work is ongoing and additional work was elected to be performed for the benefit of higher accuracy of results.
8. Radar interferometry. Work is complete.
9. Seismic postprocessing. Work is complete. Please note: only one tranche of the two tranches available were furnished to TTR in the processed format. That data was post-processed. The second tranche of data has not been furnished to TTR by MRT in a processed format (processing of that data will be challenging).

2. STEP ANALYSIS PROGRESS REPORT

2.1 GEODYNAMIC ANALYSIS (GDA) RESULTS IN 2017

2.1.1 INTRODUCTION – METHOD OF GDA ASSESSMENT OF SUBSURFACE OIL AND GAS PROSPECTIVITY

The general geological development of the area of interest (AOI) is attributed to the icosahedron-dodecahedron skeletal tectonogen framework of the Earth's interior. GDA distinguishes several major nodes that influence the Australian continent (**Figure 1**) including AOI.

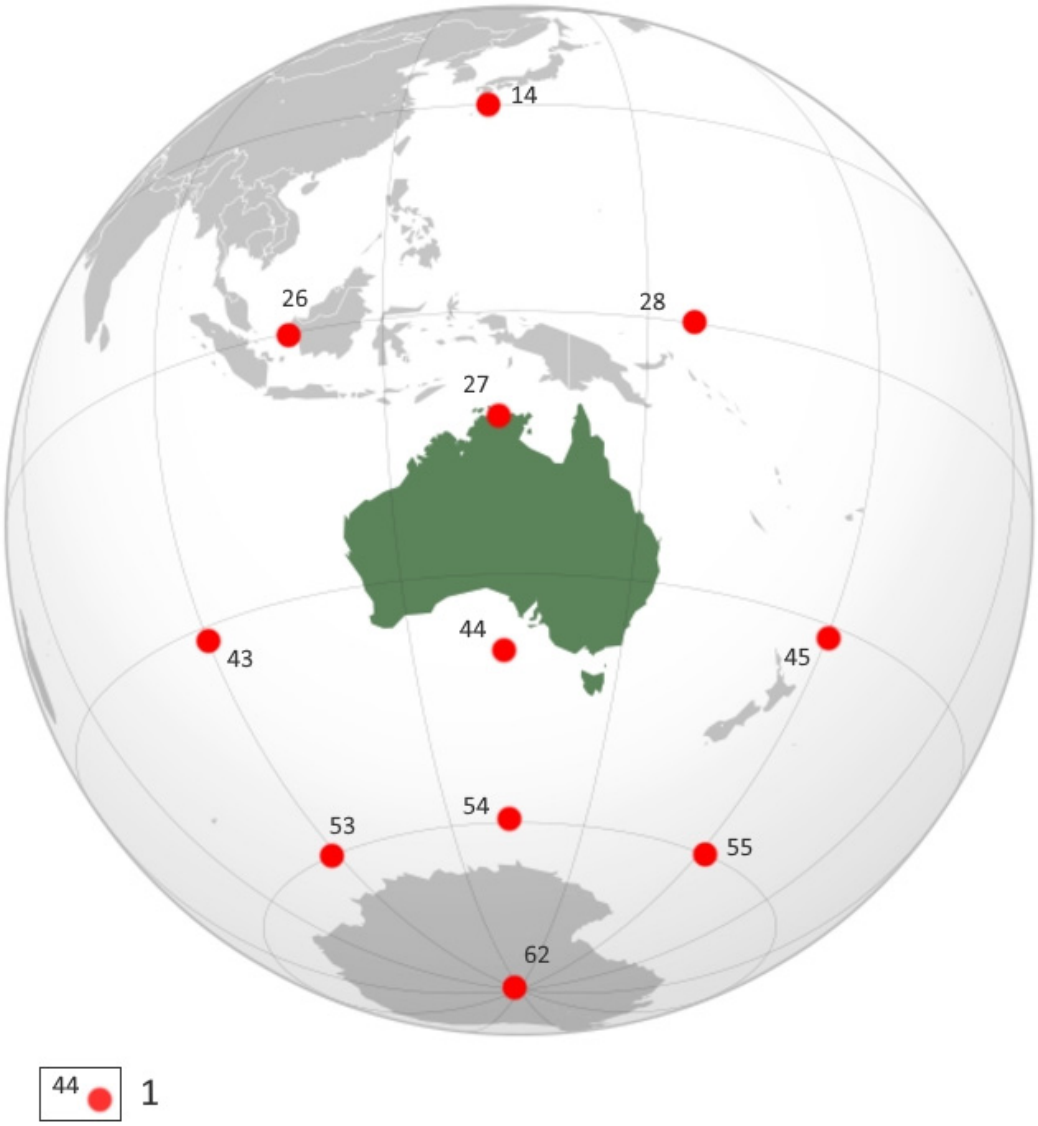


Figure 1: Fragment of the trans-planetary system of geodynamic control with nodes around the Australian continent.
1 – Main planetary nodes with numbers

The connection between these nodes comprises the system of planetary tectonogen framework (**Figure 2**).

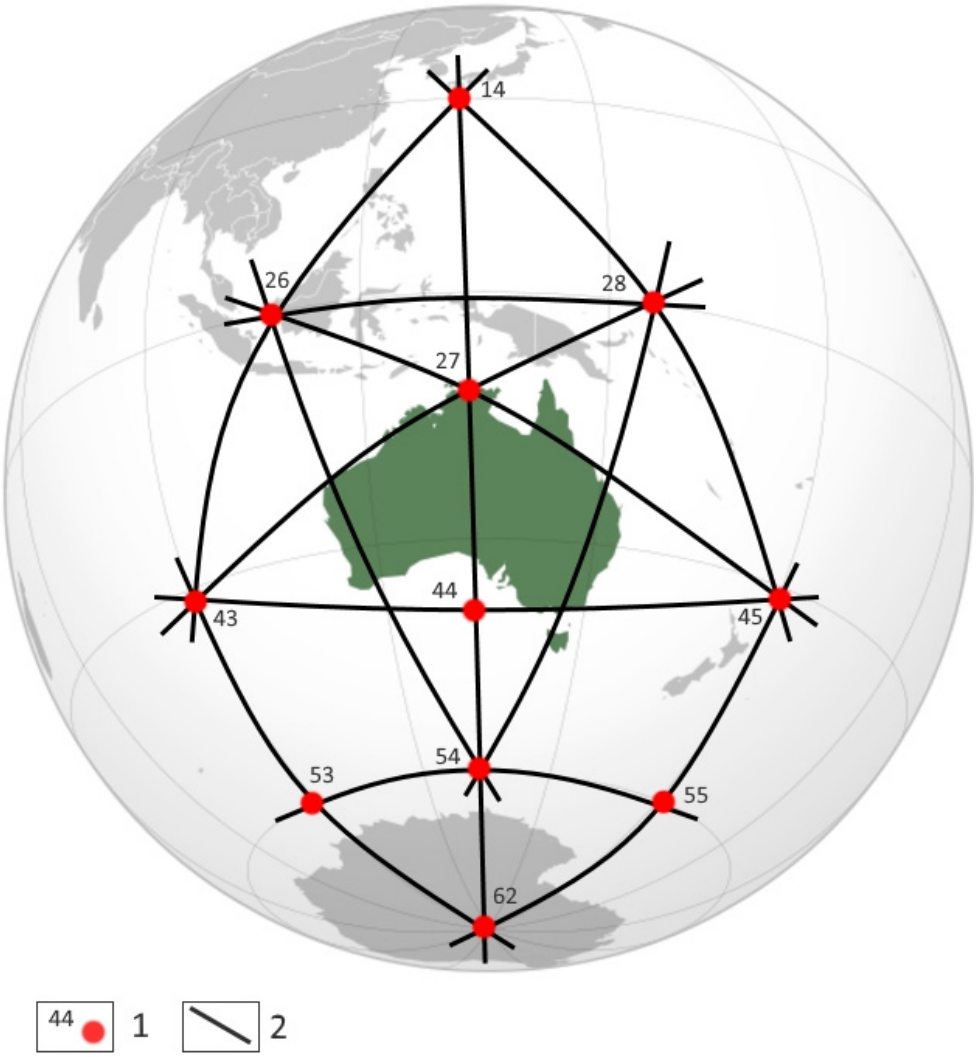


Figure 2: Planetary tectonogens and nodes that influence Australian continent.

1 –Planetary nodes with numbers; 2 –Tectonogens

This tectonogen framework system distinguishes the pentagon-shaped area that borders the Australian continent (**Figure 3**). This further solidifies the postulate that most geodynamic situations follow the icosahedral-dodecahedral system of symmetry (each side of a dodecahedron is a pentagon).

This confirms our conclusions that the basic geodynamic conditions obey the icosadro-dodecahedral symmetry system (since in a dodecahedron each of the faces has a pentagon shape).

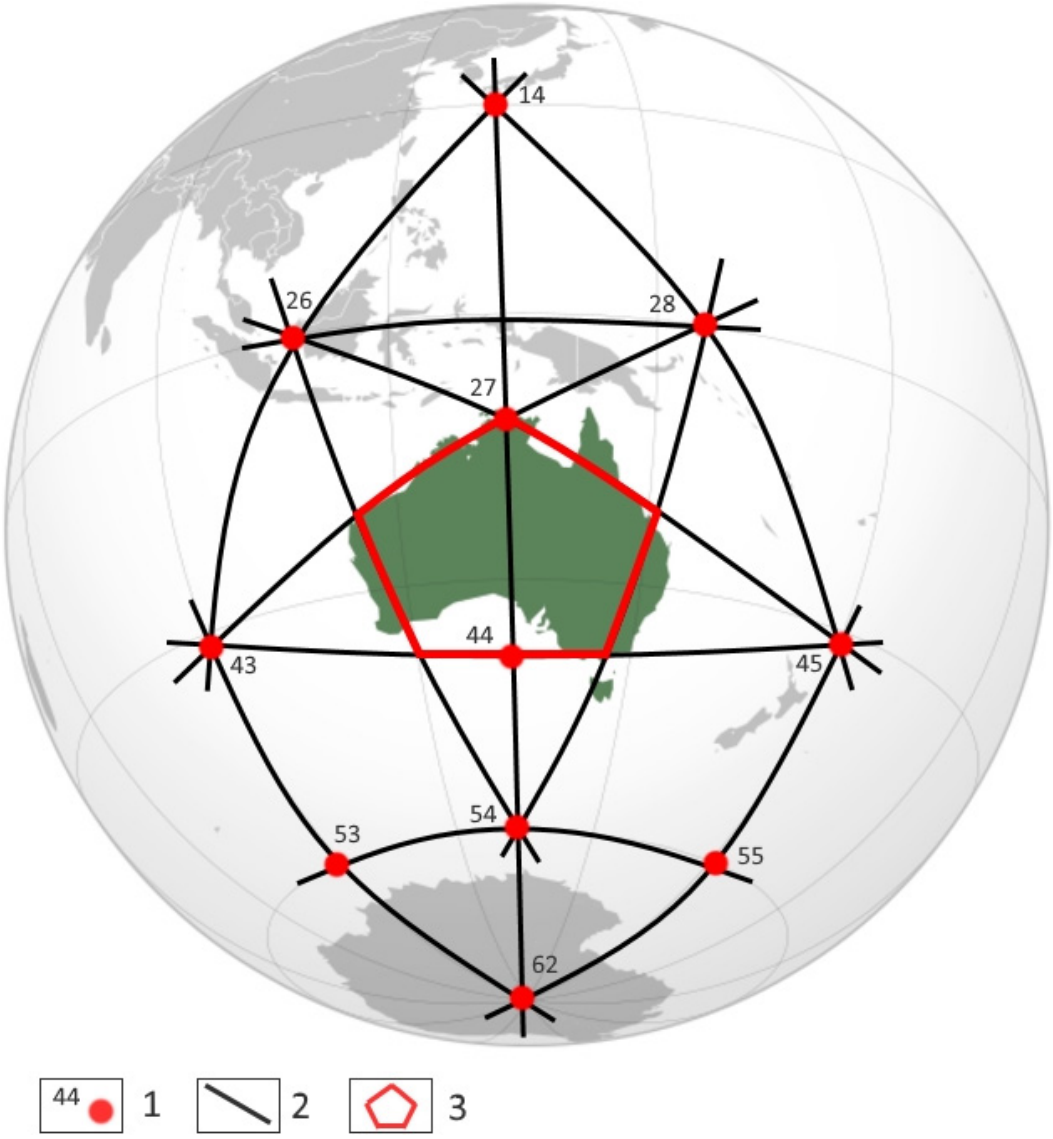


Figure 3: Pentagon-shaped area.

1 –Planetary nodes; 2 –Tectonogens; 3 - Pentagon-shaped area

The cube-octahedral tectonogen system of the continent is weakly expressed in the morpho-dynamic space and can be traced using its certain local manifestations. It is normal, as the cube-octahedral system of symmetry developed much earlier than the icosahedral-dodecahedral one, and, at the present time, it is practically fully concealed.

This state of affairs is found all over the planet, because the cube-octahedral symmetry system developed long before the icosahedral-dodecahedral system, and at the moment it turned out to be almost completely covered and reworked almost everywhere on Earth. Therefore, the lack of sufficient attributes for any geodynamic analysis of this system of symmetry, we are compelled not to take it into account.

2.1.2 GEODYNAMIC ANALYSIS AT 1:15,000,000

This first phase of GDA was performed at the scale of 1:15,000,000. Satellite, digital elevation, geological, and geophysical maps are typically evaluated to identify the main geodynamic criteria of the systemic organization of Tasmania.

The work revealed a number of patterns that make up the structure of the geological environment:

1. A discrete hierarchical framework of different-scale tectonogens that are global channels of de-fluidization.
2. Focal discharge in the upper horizons of the geosphere through the multi-rank nodes of tectonogen intersections and their zones of dynamic influence (ZDI).
3. The presence of discrete concentric systems of tectonic disturbances of varying rank, defining the concentrated nature of “unloading” of the mantle anomalies that area related to energy and fluid discharge.

This regional stage of GDA is best demonstrated if integrated and superimposed with varying geophysical maps such as the Bouguer gravity map of Australia (**Figure 4**) and the Magnetic map of Australia (**Figure 5**).

The pentagonal symmetry tectonogen framework (the five vertices of which are the nodes of continental rank, denoted in **Figure 4** and further in this report as A1, A2, A3, A4, 27 and 44) can be clearly traced using the gravimetric data as the base map (**Figure 4**).

The lowest-altitude region (the area of deflection) of the continent is attributed to the center of the pentagonal area. In its center is the Node A5 – a noted of the continental rank. The radius connecting all five nodes located at the pentagon’s vertices (A1, A2, A3, A4, 27) is equal to 1,780 km. Its outer perimeter is confined to "linear" mountain chains, confidently traced and controlled by the outer edges of the pentagonal system. The exception to this geometric confinement is located at the southern edge of the polyhedron, hidden by the ocean.

The Australian continent "widens" at the eastern flank of the pentagonal system reaching the radius of 2,100 km at its external concenter. The island of Tasmania is located within the zone of dynamic influence of this concenter. On the northern side of the Tasmania island, the external 2,100 km concenter intersects with one of the elements of the pentagonal frame – with tectonogen that develops between nodes 27 and A4, confidently traced from the northern tip of this pentagon to Tasmania.

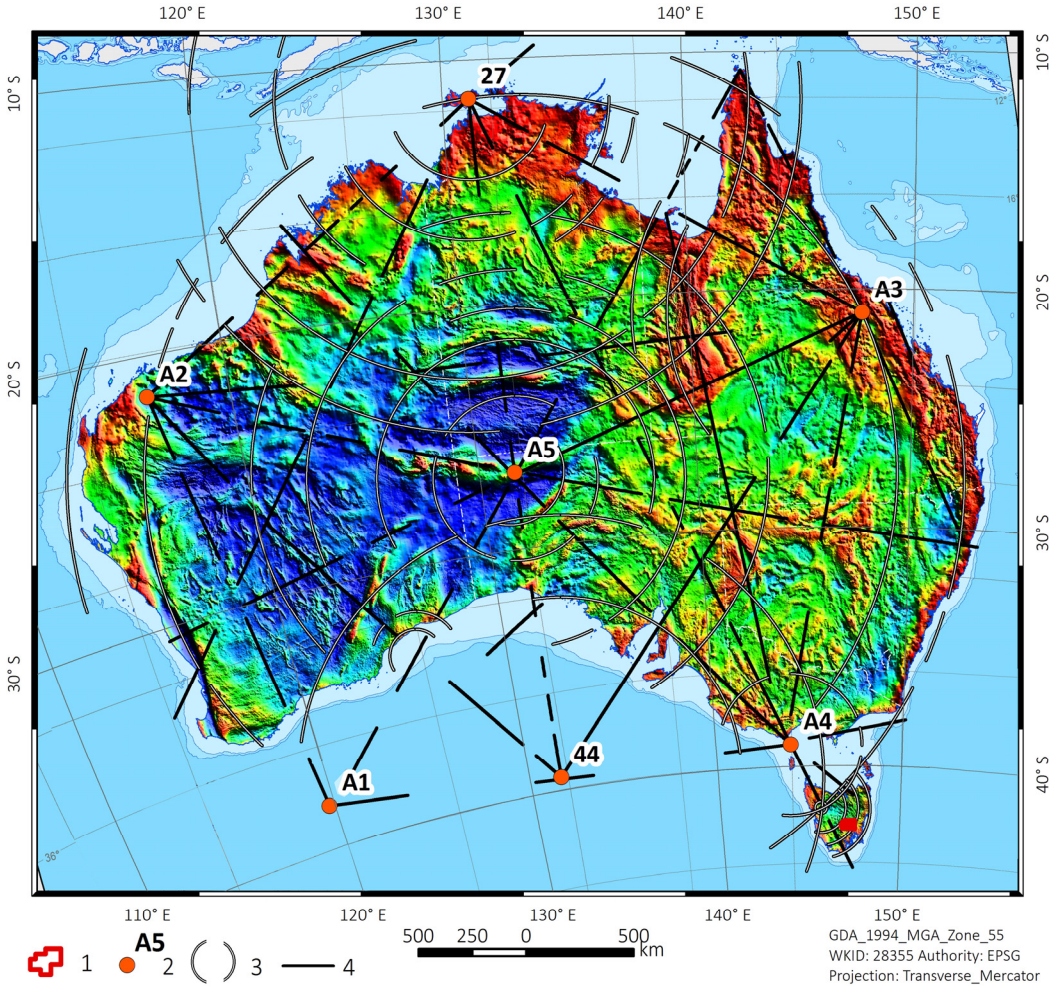


Figure 4: Geodynamic result of Bouguer gravity map of Australia analysis

1 –AOI EL30/2011; 2 –Nodes; 3 – Concentric systems; 4 - Tectonogens

The pentagonal framework of the Australian defined above can also be reliably identified usubg the magnetometric data as the base map (**Figure 5**). Both the linear and concentric systems can be traced along with the spatial confinement of the structural elements.

The level of the magnetic field of the Australian continent is predominantly high – greater than 15 nanotesla (red-blue color) over most of the territory. Low values (green-yellow) of magnetization characterize the vast northern and eastern flanks of the continent. The latter is apparently defined by the development of a large sedimentary basin within the territory.

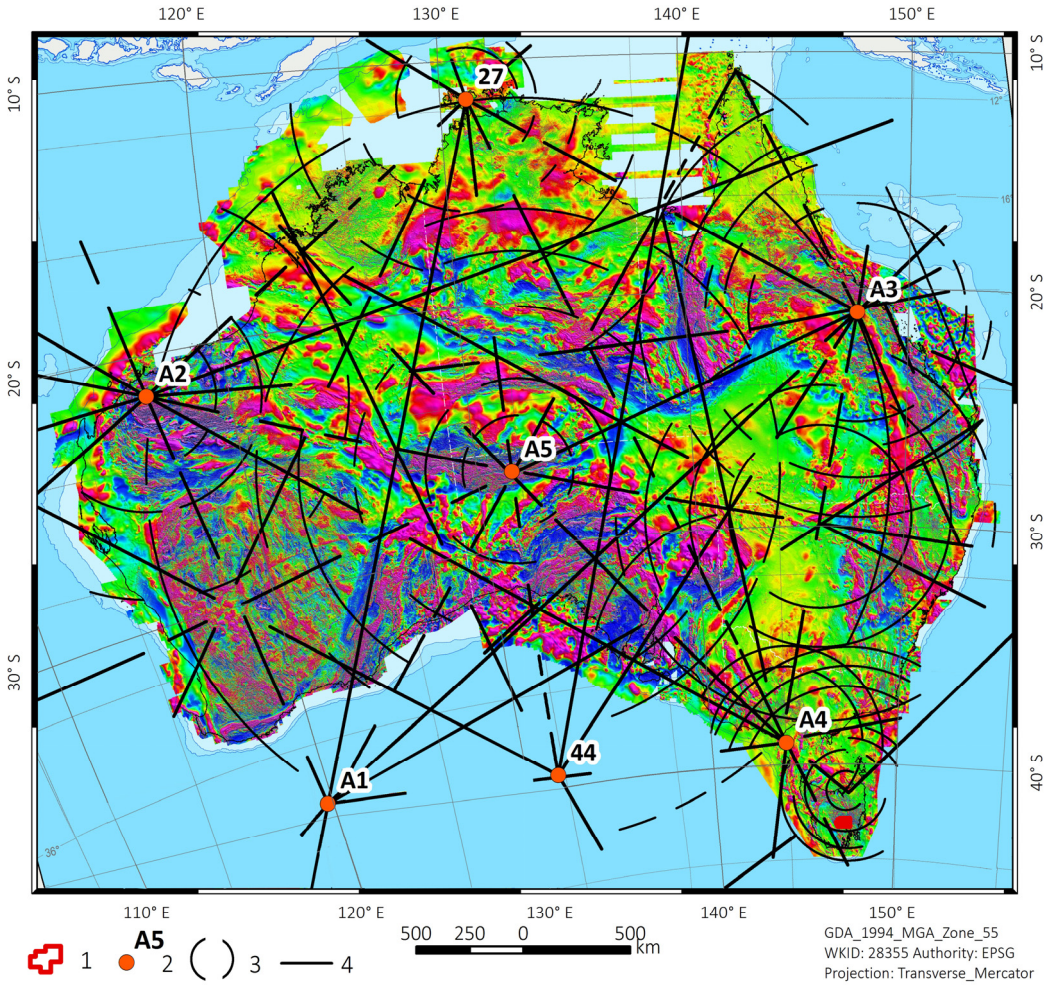


Figure 5: Geodynamic result of Magnetic map of Australia analysis.
1 –AOI EL30/2011; 2 –Nodes; 3 – Concentric systems; 4 - Tectonogens

Figure 6 and **Figure 7** show the analysis of the continental framework that defines the geodynamic morphology using the map of seismic activity and the map of mineral deposits.

The manifestation of seismic activity (**Figure 6**) as a consequence of tectonic activation processes; the manifestations of mineral deposits are tightly controlled by the geodynamic structural factors based on the pentagonal model of the global structure of the Australian continent.

These structural factors consist of the external concenters along the edge of the continent with the radii of 1,780 and 2,100 km. Their zones of dynamic influence are anomalously seismically active. High seismicity is also characteristic of the tectonogen skeletal framework of the continent as shown in **Figure 4** and **Figure 5** using the system of large structural, circular elements of the pentagonal framework of the continent.

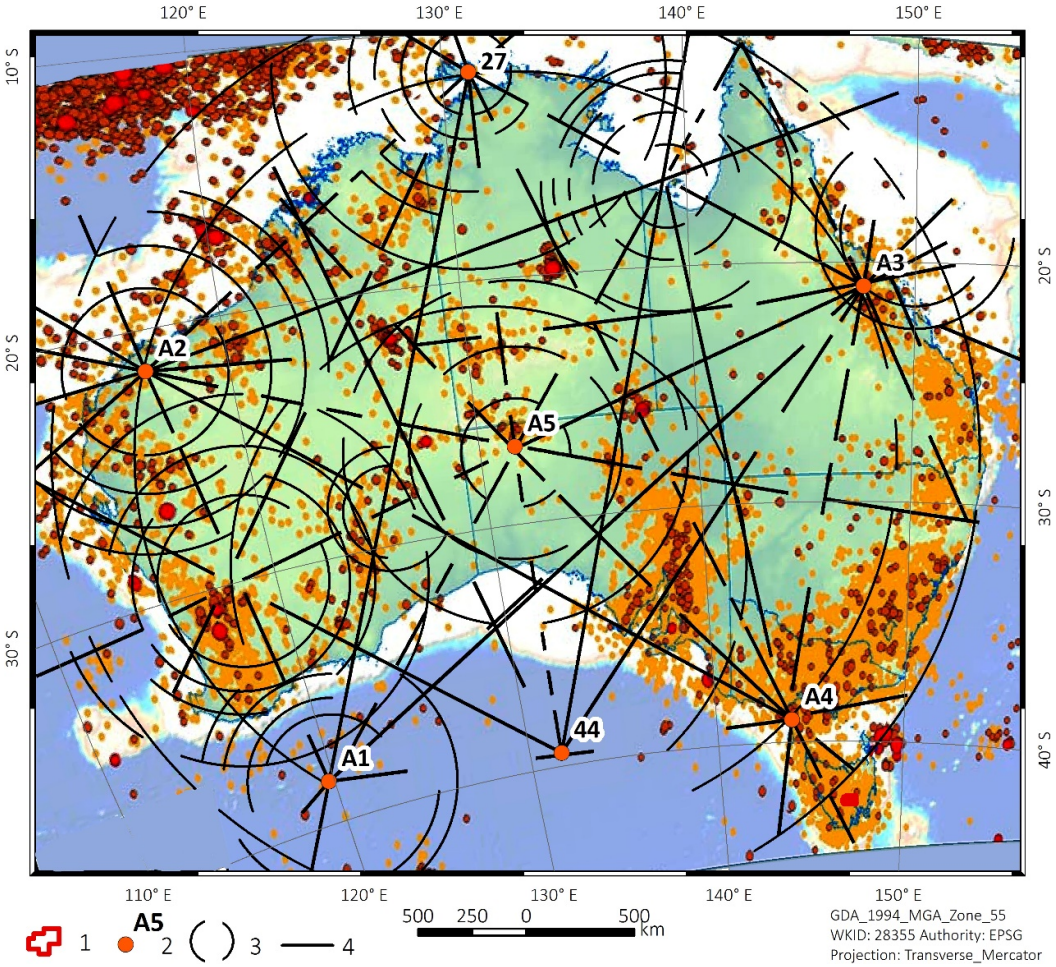


Figure 6: General Geodynamic observation of seismic activity of Australia.

1 –AOI EL30/2011; 2 – Nodes; 3 – Concentric systems; 4 - Tectonogens

Superposition of the GDA constructs with the mineral map (**Figure 7**) confirmed the presence of a pentagonal framework structure of the Australian continent and all the nodes previously allocated. It also shows that the main hydrocarbon basins are located within the concentric systems (**Figure 8**).

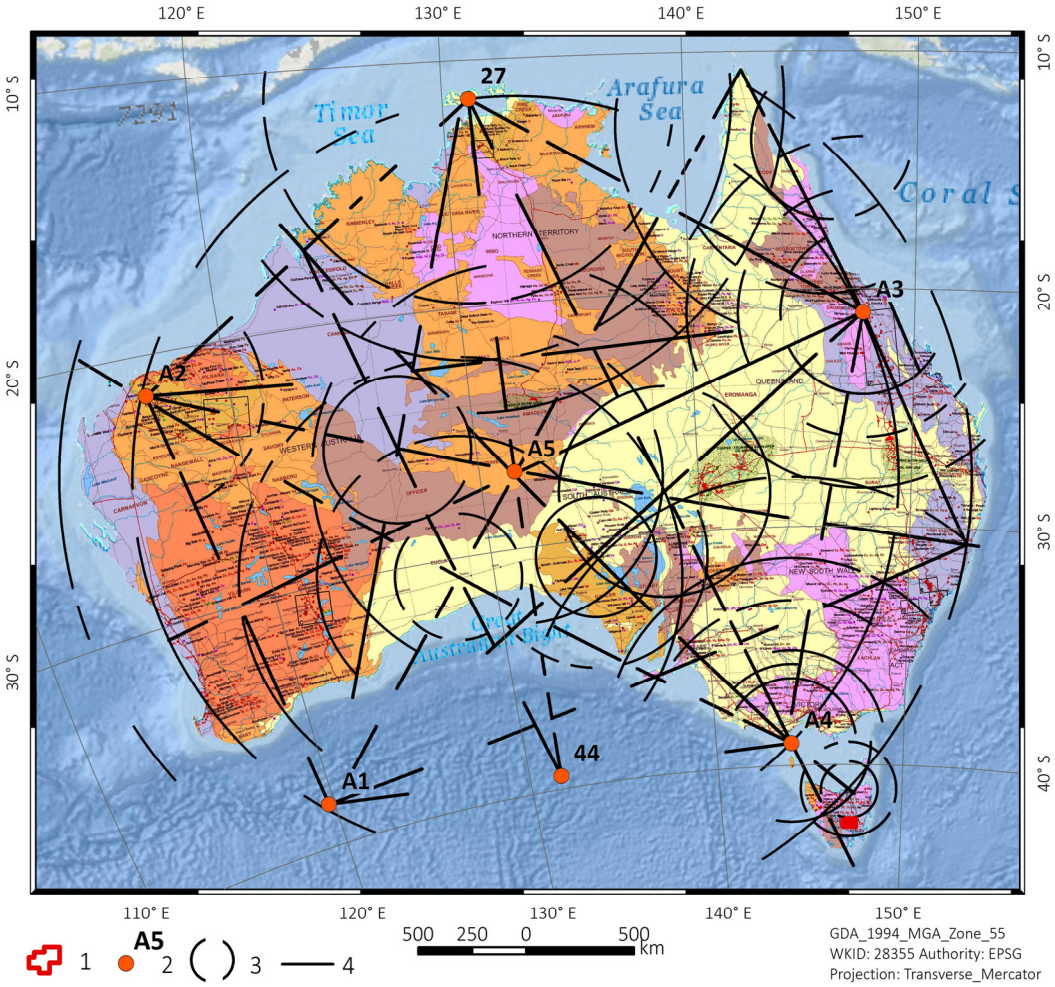


Figure 7: Geodynamic pattern of tectonogens, nodes, and concentric systems over the map of natural resources of Australia.

1 –AOI EL30/2011; 2 –Nodes; 3 – Concentric systems; 4 - Tectonogens

For example, even at this scale, it is apparent that the Cooper basin (marked with large a red ellipse in the central part of Australia, south of Eromanga) is bound:

- in the south, by one of the concenters of node A4;
- in the north-west, by the tectonogen passing from node A1 to A3; and
- in the north-east, by another concenter of node A3.

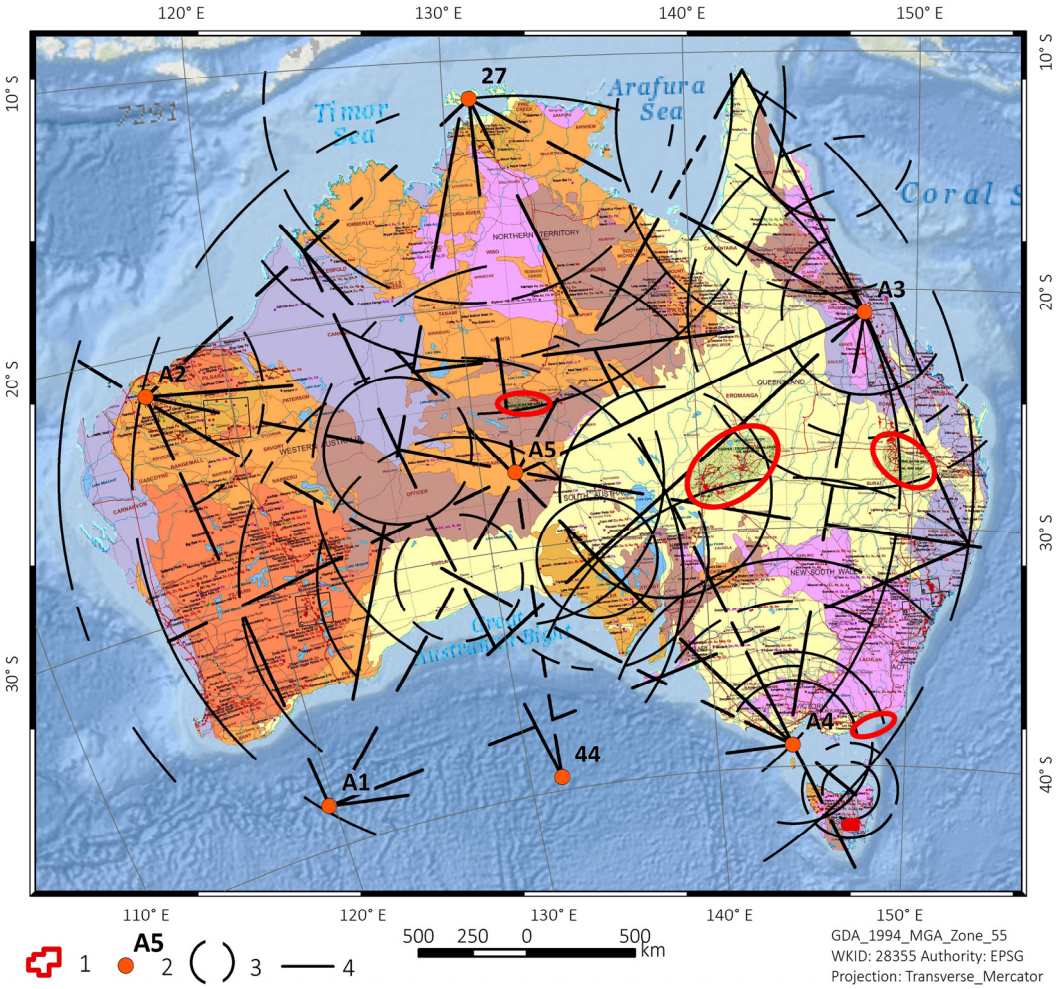


Figure 8: Geodynamic pattern of tectonogens, nodes, and concentric system over the map of natural resources of Australia with HC-basins (shown via red ovals).
1 –AOI EL30/2011; 2 –Nodes; 3 – Concentric systems; 4 – Tectonogens

Sub-regional and local-scale GDA are in progress and will be presented in the next report.

2.2 THERMAL MAPPING

Any body with the temperature differing from absolute zero emits heat energy - electromagnetic waves of a specific length and amplitude. Thermal infrared radiation refers to electromagnetic waves with the wavelength ranging between 3.5 and 20 micrometers. Most remote sensing applications use the wavelength ranging from 8 to 13 micrometers.

MATERIALS

The data used in this analysis is obtained with a spectral radiometer ETM+ from Landsat-7 (**Table 1**). It, among other data, registers thermal infrared (TIR - thermal infrared) radiation in the wavelength range of 10.4-12.5 microns. It is of note, because most natural terrestrial objects radiate heat within this range. In addition, within the same range, there exists a so-

called atmospheric "transparency window", the lowest loss of electromagnetic energy on absorption and scattering by molecules of atmospheric gases.

Table 1: Data used by TM

Data Product	Date	Level Processing	Spectral Range
LE70900892000097EDC00	2000-04-06	Landsat scenes are processed with the Standard Terrain Correction (Level 1T) **Standard Terrain Correction (Level 1T)** - provides systematic radiometric and geometric accuracy by incorporating ground control points while employing a Digital Elevation Model (DEM) for topographic accuracy.	Band 61 TIR low gain (10.4-12.5 µm) Band 62 TIR high gain (10.4-12.5 µm)
LE70900892001099ASA00	2001-04-09		

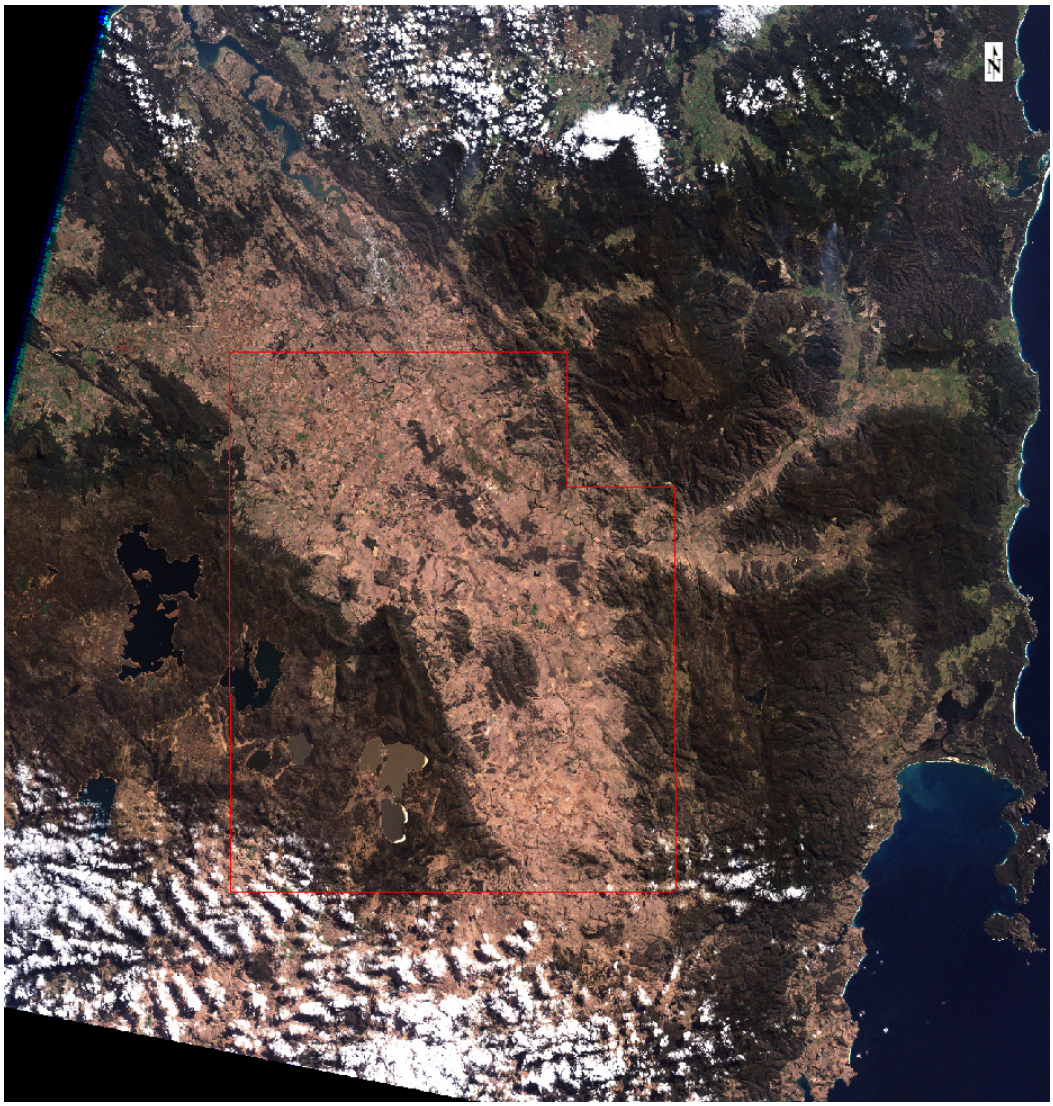


Figure 9: LandSat Scene LE70900892000097EDC00.



Figure 10: LE70900892001099ASA00.

PREPROCESSING

Georeference, convert TIR image data to radiance, thermal atmospheric correction, convert the dataset from radiance to emissivity and temperature.

Standard Terrain Correction (Level 1T) - provides systematic radiometric and geometric accuracy by incorporating ground control points while employing a Digital Elevation Model (DEM) for topographic accuracy. Some do not have ground-control or elevation data necessary for L1T correction, and in these cases, reference images to geographic coordinates and/or correct them to match base image geometry.

ENVI's image registration and geometric correction utilities allow you to reference pixel-based images to geographic coordinates and/or correct them to match base image geometry. Ground control points (GCPs) are selected using the Image and Zoom windows for both image-to-image and image-to-map registration. Coordinates are displayed for both base and uncorrected image GCPs, along with error terms for specific warping algorithms. Next GCP point prediction allows simplified selection of GCPs.

Warping is performed using resampling, scaling and translation (RST), polynomial functions (of order 1 through n), or Delaunay triangulation. Resampling methods supported include nearest-neighbor, bilinear interpolation, and cubic convolution. Comparison of the base and warped images using ENVI's multiple dynamic overlay capabilities allows quick assessment of registration accuracy.

Radiance is a measure of the amount of electromagnetic radiation leaving a point on the surface. More precisely, it is the rate at which light energy is emitted in a particular direction per unit of projected surface area. The standard unit is $\mathrm{W}/(\mathrm{m}^2)$. Most remote sensing devices directly measure radiance. **Convert TIR image data** digital numbers (DN) to radiance using published post-launch gain and offset values.

$$\text{Radiance} = \text{DN} \cdot \text{Gain} + \text{Bias}$$

which is also expressed as:

$$L_\lambda = LMIN_\lambda + \frac{LMAX_\lambda - LMIN_\lambda}{QCALMAX - QCALMIN} \cdot (DN - QCALMIN)$$

where:

- L_λ is the spectral radiance at the sensor's aperture in $\mathrm{W}/(\mathrm{m}^2 \cdot \mathrm{sr} \cdot \mu\mathrm{m})$;
- "Gain" is the Rescaled gain (the data product "gain" contained in the Level 1 product header or ancillary data record) in $\mathrm{W}/(\mathrm{m}^2 \cdot \mathrm{sr} \cdot \mu\mathrm{m})$;
- "Bias" is the Rescaled bias (the data product "offset" contained in the Level 1 product header or ancillary data record) in $\mathrm{W}/(\mathrm{m}^2 \cdot \mathrm{sr} \cdot \mu\mathrm{m})$;
- DN is the quantized calibrated pixel value in digital numbers;
- LMIN_λ is the spectral radiance that is scaled to QCALMIN in $\mathrm{W}/(\mathrm{m}^2 \cdot \mathrm{sr} \cdot \mu\mathrm{m})$;
- LMAX_λ is the spectral radiance that is scaled to QCALMAX in $\mathrm{W}/(\mathrm{m}^2 \cdot \mathrm{sr} \cdot \mu\mathrm{m})$;
- $\mathrm{QCALMIN}$ is the minimum quantized calibrated pixel value (corresponding to LMIN_λ) in DN;
- $\mathrm{QCALMAX}$ is the maximum quantized calibrated pixel value (corresponding to LMAX_λ) in DN.

In the context of remote sensing: A correction value added to or subtracted from every pixel in an image, typically by using image arithmetic.

Thermal Atmospheric Correction to approximate and remove the atmospheric contributions from thermal infrared radiance data. Thermal image data must be converted to radiance before performing the atmospheric correction.

The atmospheric correction algorithm used in ENVI is similar to the In-Scene Atmospheric Compensation algorithm (ISAC). This algorithm assumes that the atmosphere is uniform over the data scene and that a near-blackbody surface exists within the scene. The location of the

blackbody surface is not required for this correction. A single layer approximation of the atmosphere is used. No reflected downwelling radiance is also assumed.

The algorithm first determines the wavelength that most often exhibits the maximum brightness temperature. This wavelength is then used as the reference wavelength. Only spectra that have their brightest temperature at this wavelength are used to calculate the atmospheric compensation. At this point, for each wavelength, the reference blackbody radiance values are plotted against the measured radiances. A line is fitted to the highest points in these plotted data and the fit is weighted to assign more weight to regions with denser sampling. The compensation for this band is then applied as the slope and offset derived from the linear regression of these data with their computed blackbody radiances at the reference wavelength.

Upwelling atmospheric radiance and atmospheric transmission are approximated using the following method. First, the surface temperature of every pixel is estimated from the data and used to approximate the brightness temperature using the Planck function and assuming an emissivity of 1. Next, a line is fitted (using one of two methods) to a scatter plot of radiance vs. brightness temperature. The atmospheric upwelling and transmission are then derived from the slope and offset of this line.

Converting to Emissivity and Temperature. The radiation emitted from a surface in the thermal infrared wavelengths is a function of both the surface temperature and emissivity. The emissivity relates to the composition of the surface and is often used for surface constituent mapping. Reference Channel Emissivity to calculate emissivity and temperature values from thermal infrared radiance data. The reference channel emissivity technique assumes that all the pixels in one channel (band) of the thermal infrared data have a constant emissivity. Using this constant emissivity, a temperature image is calculated and those temperatures are used to calculate the emissivity values in all the other bands using the Planck function.

METHODOLOGY

The analysis of the thermal field entails construction of a series of multitemporal temperature and thermal emissivity maps, and identification of patterns hidden in them. The analysis is based on an additive model of the registered by satellite sensor of the thermal field, which results from mixing of the solar heat reflected by the surface and the internal heat flow from the Earth's core. The first component (reradiation of the acquired from outside thermal energy) depends on many factors (time of year and day, humidity, the amount of green biomass, soil type, lithological composition of rocks, etc.) and can vary substantially within a small area. The second component (geothermal energy) is determined solely by the geothermal gradient in the area as well as the heat capacity and thermal conductivity of rocks; its lateral changes are small, except for zones of anomalous heat flow (active faults, hotspots, fractured zones, etc.). Thus, in a total amount of heat radiated from the surface, the proportion of reradiated thermal energy significantly (by orders of magnitude) exceeds the amount geothermal heat in typically stable platform environments, although the reradiated component has a higher spatial and temporal variability as compared to the, more slowly

varying in space and constant in time[1], geothermal field. The aforementioned factors provide the basis (with certain strong restrictions and simplifications) for the separation of the reradiated component using a collection of the thermal information over the same study area carried out at different times.

The registration of the thermal field for differing dates helps filter high-frequency variations of heat caused by the heterogeneous heating of the surface and observe the changes in its low-frequency geothermal component. The model assumes relatively similar seasonal values of heat reaching the surface from the sun and possible changes in time of the endogenous thermal flux. The maximum values of such changes may be attributed to the zones of changes in subsurface rocks heterogeneity, fracturing, tectonically active zones, as well as thermo-physical qualities of the rocks. Stable areas devoid displacement can be characterized by constant or low-intensity flux of the geothermal energy. The difference of low-frequency components of the thermal field taken during similar dates for different years helps visualize the time gradient of the geothermal energy.

The processing algorithm consists of the following operations:

1. Construction of temperature brightness maps based on the special processing of the Earth's native thermal emission using the infrared sub-range of electromagnetic wavelengths (TIR – thermal infrared). Analysis of thermal field maps in relation to the presence of the anomalously cold zones attributed to cloud cover. Separation and exclusion from use of maps that contain such zones.

2. Selection of a pair of thermal maps obtained for similar dates in differing years.

3. Separation of the regional component of the thermal flux that is based on the morphological processing of digital satellite images (provided that similar parameters of the thermal map filtration algorithm are used for differing dates).

4. Calculation of the time gradient of the geothermal field. Location of zones with anomalous thermal flux.

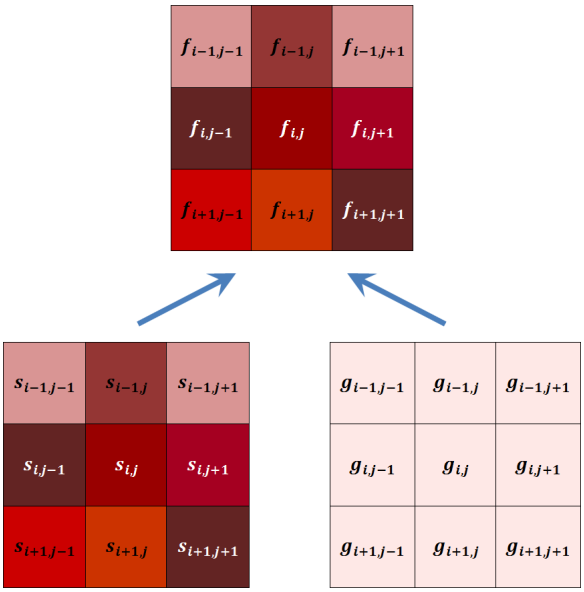


Figure 11: Scheme of TM method; model of registration of thermal field.
f - registered temperatures at the Earth's surface; s - temperatures caused by solar heating (obtained from an external source and re-scattered by the surface); g - temperatures caused by endogenous heat.

The given fragment is a raster with the central pixel's coordinates (*i, j*) and eight of its nearest neighbors. As can be seen from the diagram (the first basic idea of the technique), $f = s + g$, where $s \gg g$. Color displays the second basic idea of the analysis technique: high variability of *s* within a small area, and virtually no variation in *g*, i.e. $g = const$ within a small area. The third basic idea of the methodology is shown in **Figure 12**.

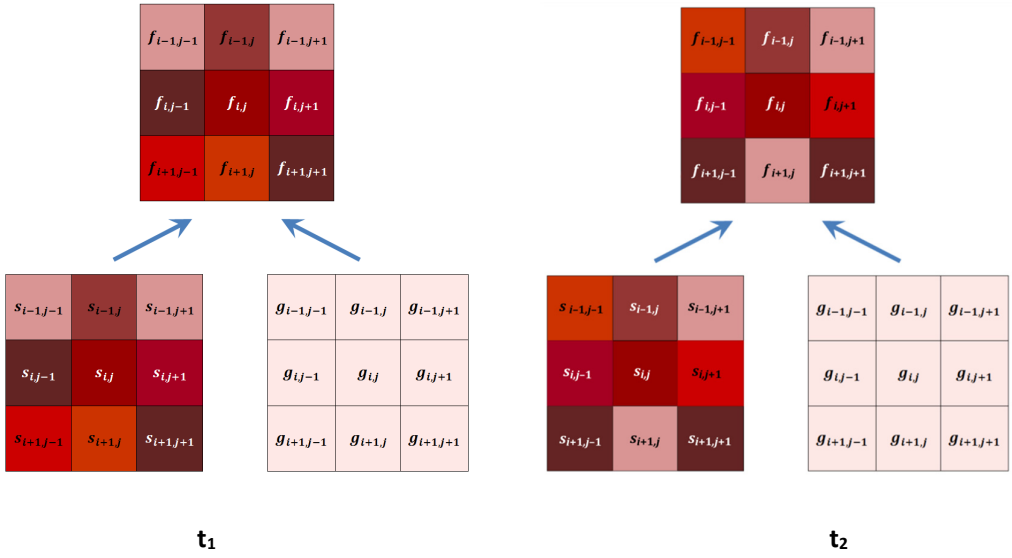


Figure 12: The model of multitemporal registration of the thermal field.

i.e. over time, *s* (and, therefore, *f*) significantly changes (due to the effects of external factors changing in time); however, the low-amplitude value of *g* also changes in time, although due to internal causes.

Thus, for a small area/vicinity:

$$f(t_1, x, y) = s(t_1, x, y) + g(t_1), \quad f(t_2, x, y) = s(t_2, x, y) + g(t_2).$$

The fourth idea entails separation of the local (s) and regional (g) components of the thermal field via the low-frequency filtration of the source surface temperatures. Such an operation is based on the operations of the morphological processing of digital images and is an effective way of determination of regional thermal field components.

$$g_1 = g(t_1, x, y), \quad g_2 = g(t_2, x, y).$$

Such regional thermal components are significant by themselves, and their difference is even more informative as not only reflecting the changes in the geothermal flux for a period of time, but also locating zones of intensification and weakening of the flux.

$$\Delta g = g_2 - g_1$$

Such thermal flux gradient zones can be associated with anomalous zones of energy and mass transfer caused by a structure-tectonic organization of the AOI and thermo-physical characteristics of its rocks.

RESULTS

For all satellite images suitable for the study of the thermal field within the given area, the specialized processing carried out and surface-temperature distribution maps were constructed. They all are made in the same style and are provided below.

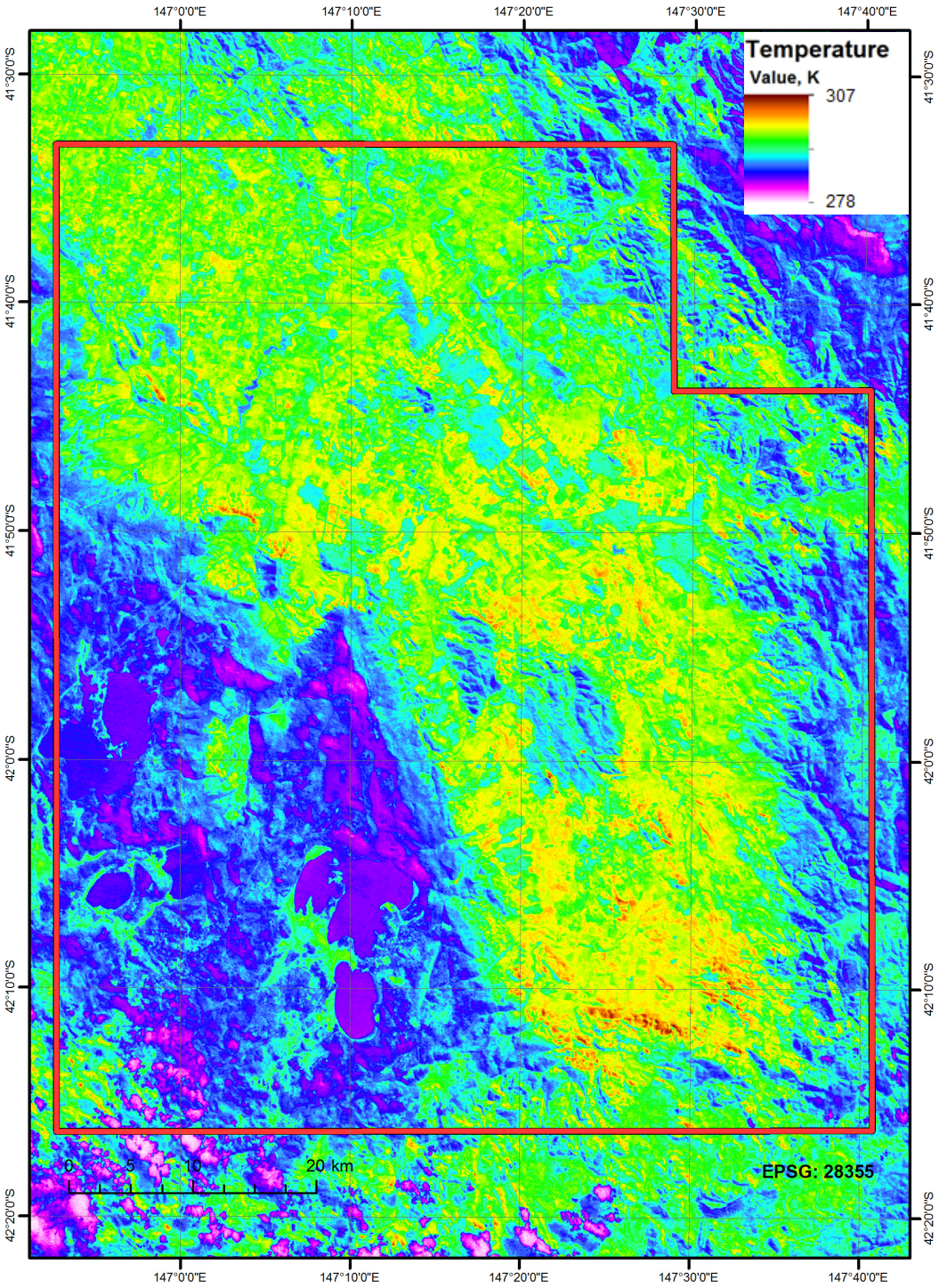


Figure 13: Map of the thermal field (2000/04/06).

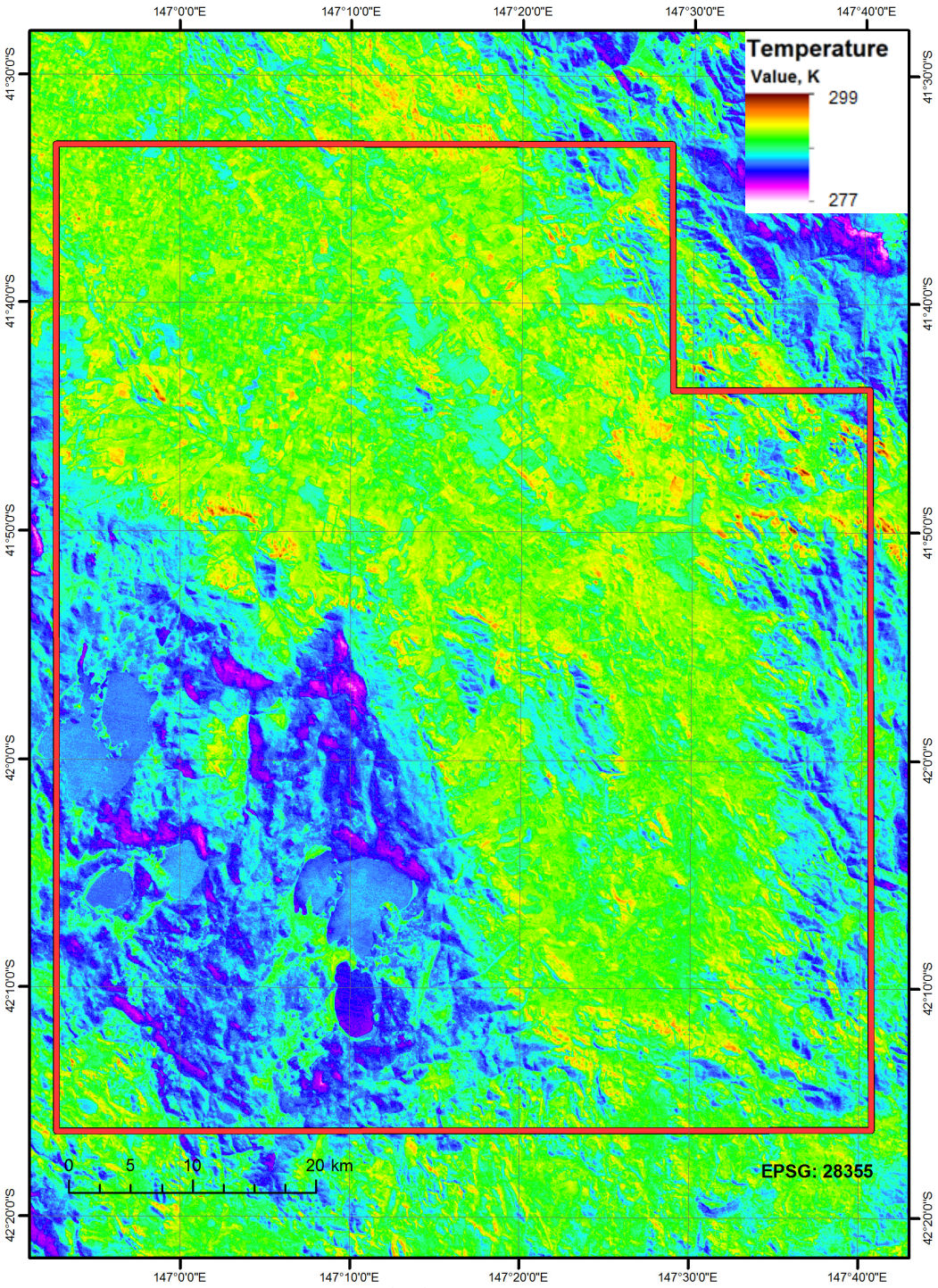


Figure 14: Map of the thermal field (2001/04/09).

The cloudiness mask was compiled and applied to the thermal images (**Figure 15**). All further operations were carried out with masked thermal fields.

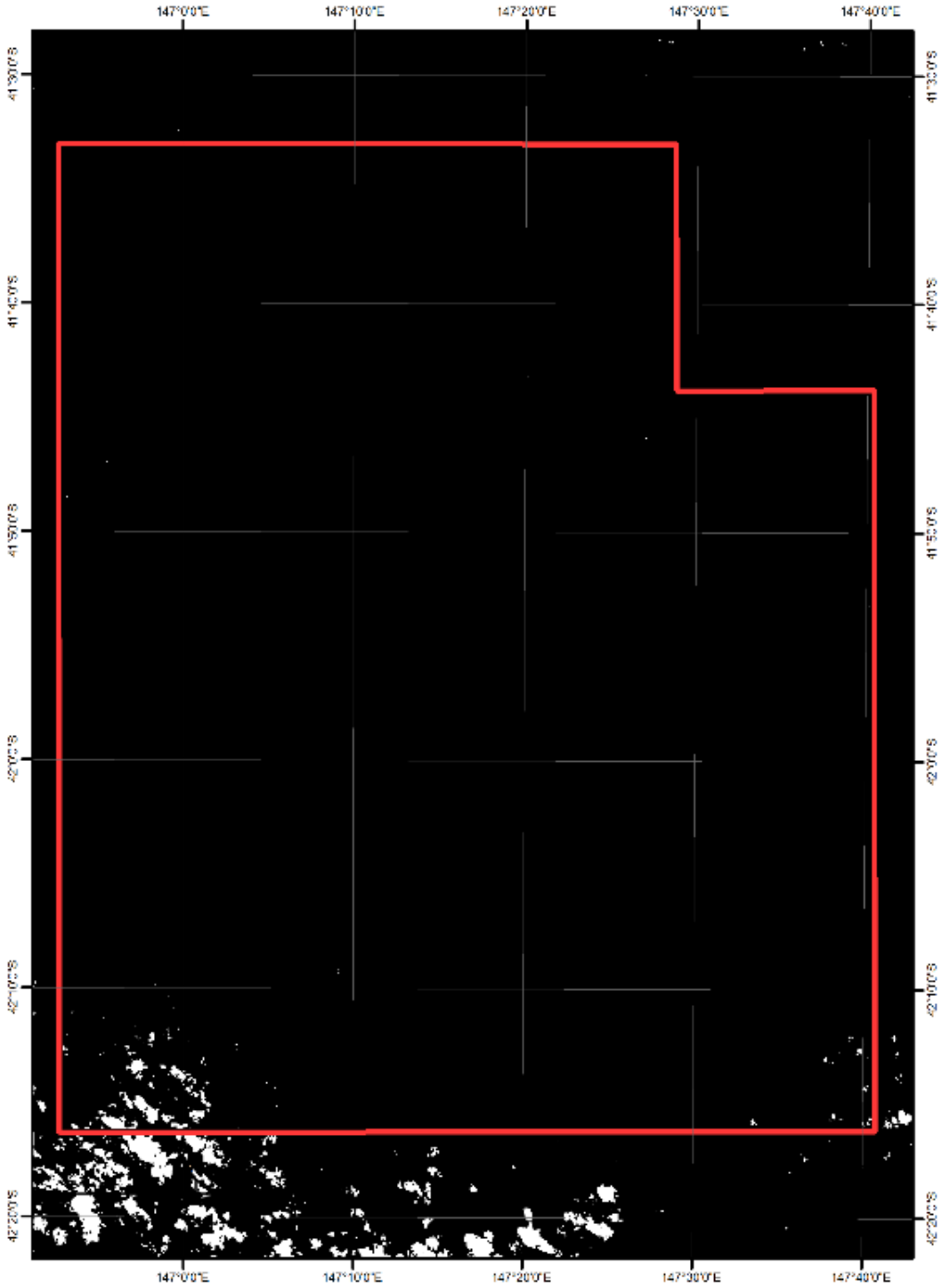


Figure 15. Cloudiness mask.

The software implementation of the methodology uses MatLab. Pre-processing of the thermal maps boiled down to the nonlinear median filtering. The generalization of the result was achieved using the low-frequency Gauss filter.

The gradient of the thermal flux described herein is shown in **Figure 16**.

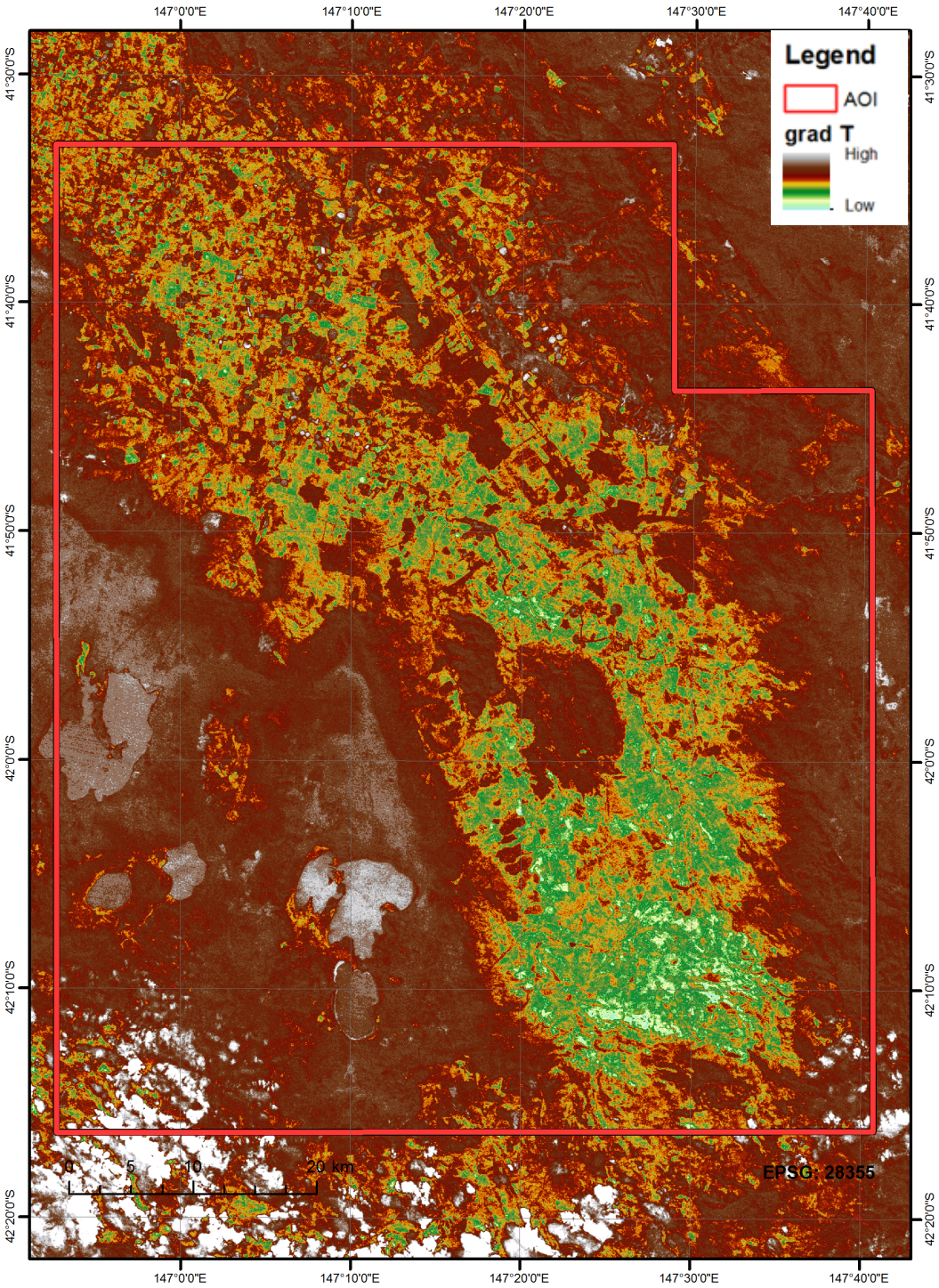


Figure 16: Thermal field gradient of EL30/2011.

Thermal mapping values do not possess the information that can directly lead to a qualitative geological interpretation (it is mostly caused by a myriad of factors whose influence is challenging to assess). However, the TM results will be utilized as input data for the automatic classification of AOI.

INTRODUCTION - HYDROCARBON MICROSEEPAGE

The occurrence at surface of hydrocarbon seeps suggests that an oil or gas reservoir leaks even though it acts as a trap for hydrocarbons. Macroseepage is the visible presence of oil and gas seeping to the surface. Macroseeps have been documented in various parts of the world (Davidson, 1963; Sittig, 1980; Hunt, 1981; Davis, 1967; Tedosco, 1995). Microseeps are invisible trace quantities of hydrocarbons seeping to the surface. The most persuasive evidence for microseepage is the measurement, sometimes over many years, of statistically-significant anomalous amounts of light hydrocarbons in soil gases and soils directly over oil and gas reservoirs (Price, 1986). In these cases, the hydrocarbons in the soil gas or soil have very similar carbon isotope ratios to those in the underlying reservoirs, whereas the hydrocarbons of near-surface biogenic origin have different carbon isotope ratios. There is also good compositional correlation between the hydrocarbons of a microseepage and those in the underlying reservoir (Saunders et al., 1991).

The occurrence of hydrocarbon microseepage directly above reservoirs points to vertical migration of hydrocarbons, despite the fact that groundwater movement might be expected to militate against this. Indeed, the cross-sectional shape of the hydrocarbon leakage pattern has been termed a "chimney", and most chimneys are nearly vertical (Tedosco, 1995). Vertical migration through the strata has been attributed to at least four mechanisms: effusion; diffusion; solution; and gas bubbles.

Effusion as free hydrocarbon gases is thought to be the principal mechanism leading to macroseepage. It arises as a result of the very large pressure differential that exists across a petroleum reservoir. Diffusion of hydrocarbon gases that are usually dissolved in groundwater has been observed through seemingly impermeable barriers (Rosaire et al., 1940). This form of migration is thought to contribute to microseeps. Also dissolved low molecular weight hydrocarbons in groundwater migrate through capping shales as a result of hydrodynamic or chemical potential drive (Duchscherer, 1980). Vertical ascent of ultra-small (colloidal size) gas bubbles through a network of inter-connected, groundwater-filled microfractures is advocated by Price (1986). Buoyant colloidal gas bubbles are readily displaced upward at rates of up to several millimetres per second. This fast ascent explains the rapid development of light hydrocarbon anomalies in soil gas over newly-filled gas storage reservoirs, and their rapid disappearance after a reservoir is depleted.

Although microseeps (and macroseeps) represent leakage from a temporarily stationary source of petroleum, they do not necessarily indicate the presence of economically-recoverable hydrocarbons at depth. The economic viability of the underlying reservoir can only be established by further exploration.

INDUCED SURFACE MANIFESTATIONS OF MICROSEEPAGE

The surface manifestation of hydrocarbon microseepage in not necessarily confined to the presence of trace quantities of hydrocarbons. Schumacher (1996) made a thorough review of the major hydrocarbon-induced changes affecting soils and sediments and their implications for surface exploration.

Schumacher (1996) contended that long-term leakage of hydrocarbons can establish locally-anomalous redox zones that favour the development of a diverse array of chemical and mineralogical changes. The bacterial oxidation of light hydrocarbons can directly or indirectly bring about significant changes in the pH and Eh of the surrounding environment, thereby influencing mineral stability and chemical reactivity. Such oxidation in the chimney above a leaking petroleum accumulation leads to dissolution or precipitation of minerals and the mobilisation or immobilisation of certain elements in the chimney, which thereby becomes mineralogically and chemically different from laterally-equivalent rocks (Pirson, 1969; Oehler and Stemberg, 1984; Price, 1986). The resulting alteration includes: the formation of calcite, pyrite, uraninite, elemental sulphur, and certain magnetic iron oxides and iron sulphides; bleaching of red beds; clay mineral alteration; electrochemical changes; radiation anomalies; and biogeochemical and geobotanical anomalies (**Figure 17**).

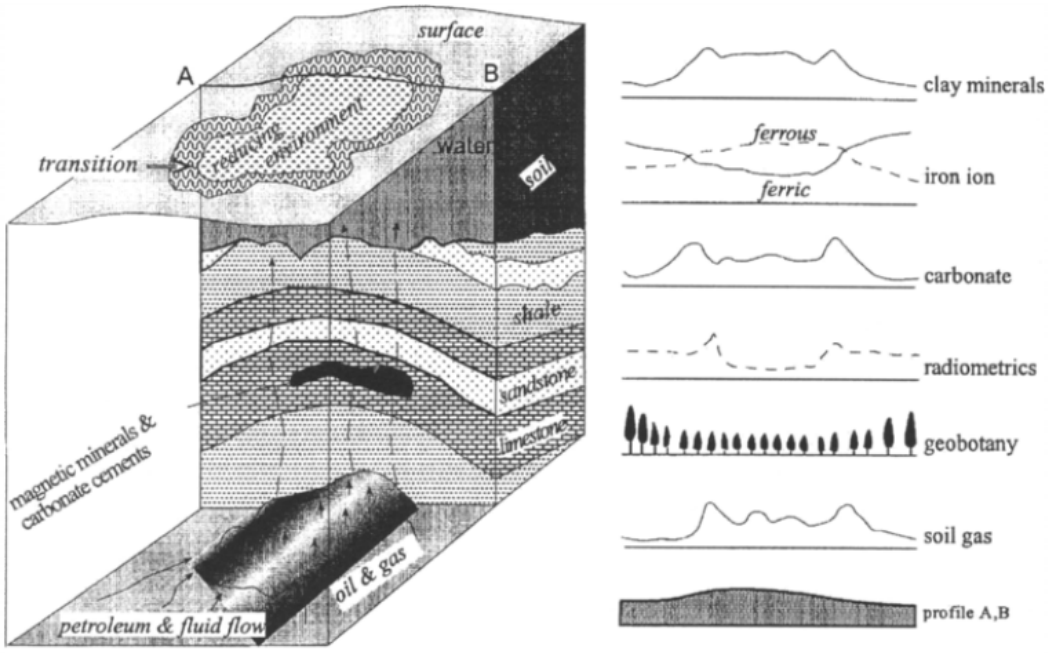


Figure 17: Surface alterations caused by migrating hydrocarbons (reproduced with permission from Duchscherer, 1982).

Where such changes can be measured and mapped at surface, they provide the basis for a number of surface exploration methods for petroleum. Some of these changes are in principle amenable to measurement and mapping by remote sensing techniques.

RREMOTE DETECTION OF INDUCED SURFACE MANIFESTATIONS

Remote sensing has the potential to detect hydrocarbon-induced alteration in rocks, soils and vegetation. Extensive studies have been performed on the reduction of ferric iron (red-bed bleaching), the conversion of feldspars and mixed-layer clays to kaolinite, the increase of carbonate content and the anomalous spectral reflectance of vegetation.

The attraction of remote sensing is that it offers a rapid and cost-effective means of conducting reconnaissance for hydrocarbon-induced alteration.

BLEACHED RED BEDS

The presence at surface of bleached and discolored red sandstones above petroleum accumulation has been widely noted, but detailed studies are few. Bleaching occurs whenever acidic, reducing fluids dissolve the ferric oxide (hematite) that gives the red bed its characteristic color. Reducing conditions also favor the formation of pyrite and siderite from the iron that is released during the dissolution of hematite. Leakage from petroleum accumulations of reducing agents such as hydrocarbons, H2S and CO2 could be responsible for bleaching overlying red beds (Schumacher, 1996).

The reflectance characteristics of various ferric and ferrous iron minerals, clay minerals and calcite are shown in **Figure 18**. Ferric iron (in hematite) exhibits its strongest reflectance at wavelengths greater than 1.0 µm; at progressively shorter wavelengths there is first a distinct absorption feature at 0.9 µm, then an increase in reflectance at 0.8 µm and finally, at still shorter wavelengths, reflectance falls off sharply (Hunt et al., 1973). On the other hand, the ferrous iron in non-transparent minerals such as pyrite and magnetite show a near-uniform low total reflectance, although transparent minerals such as siderite have broad shallow reflectance at 1.0-1.1 µm (Hunt, 1970). These characteristics can be used in remote sensing data-processing to separate bleached red beds from their unbleached equivalents.

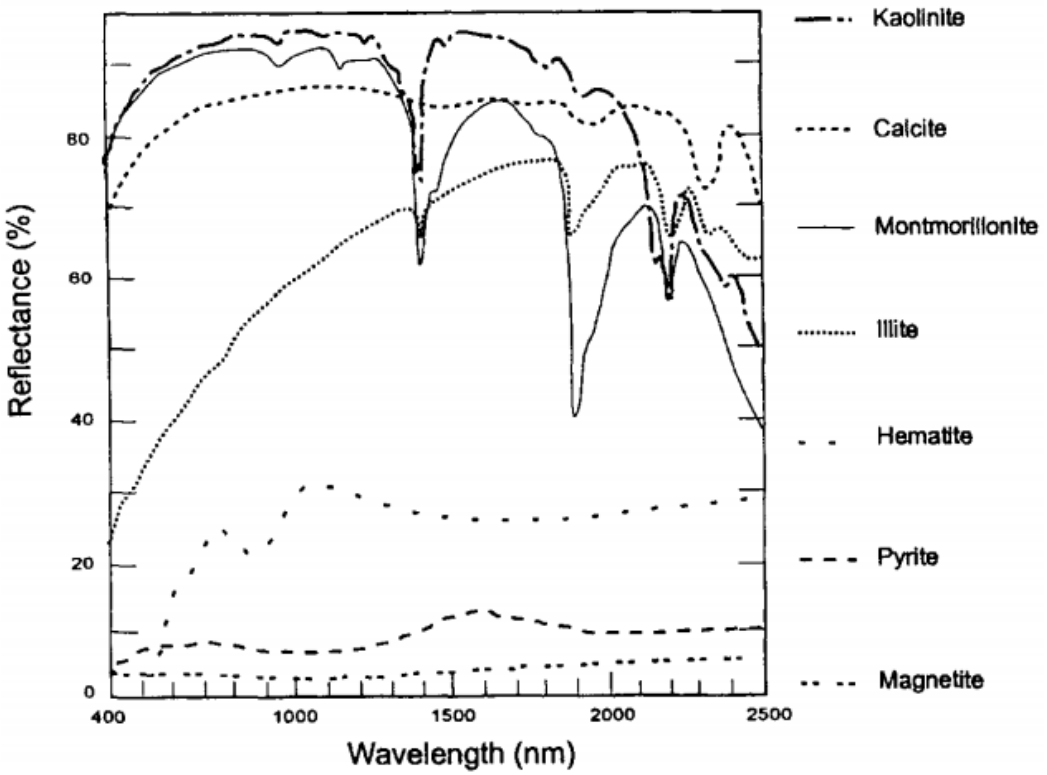


Figure 18. Spectra of minerals associated with hydrocarbon micro-seepage.

CARBONATE ENRICHMENT

The formation of diagenetic carbonates and carbonate cements, especially pore-filling and replacement calcite, are amongst the most common alteration features induced by hydrocarbon microseepage. These carbonates are a product of the oxidation of hydrocarbons such a methane to carbon dioxide, which in groundwater hydrolyses to bicarbonate anions. Dissolved calcium (and magnesium) in groundwater reacts with this bicarbonate to precipitate as carbonate minerals or carbonate cement. One of two reaction pathways applies, depending in the redox conditions, viz.,

aerobic $$CH_4 + 2O_2 + Ca^{2+} = CaCO_3 + H_2O + 2H^+$$

anaerobic $$CH_4 + SO_4^{2-} + Ca^{2+} = CaCO_3 + H_2O + H_2S$$

The resulting accumulation of carbonate at or near surface can be exploited as an indicator of a hydrocarbon reservoir at depth (Patton and Manwaring, 1984; Duchscherer, 1982; McDermott, 1940; MacElvain, 1963).

The carbon in this carbonate carries the isotopic signature of its parent hydrocarbon(s). The carbon of most carbonate minerals is derived from the atmosphere, freshwater or the marine environment and has a 13C isotopic value of about -10 to +5 per mil relative to the PDB standard (Fairbridge, 1972; Anderson and Arthur, 1983). The 13C content of most crude oil ranges from about -20 to -32 per mil, and that of methane ranges from -30 to -90 per mil. Thus, carbonate formed from hydrocarbon oxidation incorporates carbon that typically has a 13C

content more negative than -20 per mil. Depending on the proportion of carbon derived from hydrocarbon oxidation, the 13C content of the resultant carbonate can range from -10 to-60 per mil (Schumacher, 1996).

Remote sensing cannot detect the isotopic signature of carbonates, but it can detect the increase in carbonate formation and carbonate cement that hydrocarbon oxidation induces. Ground truth investigations can subsequently establish if this carbonate is indeed isotopically anomalous.

VEGETATION STRESS

Hydrocarbon microseepage creates a reducing environment in the soil and overburden at depths shallower than would be expected in the absence of microseepage. The presence of hydrocarbons stimulates the activity of hydrocarbon-oxidizing bacteria, which decreases oxygen content of the soil whilst increasing its contents of carbon dioxide and organic acids. These changes affect pH and Eh of soil, which in turn affect the solubility of elements that are plant nutrients and consequently their availability to vegetation (Schumacher, 1996). This may affect the root structure of vegetation and ultimately influence its vigor and hence its spectral reflectance (Feder, 1985).

Remote sensing of anomalous (or stressed) vegetation takes two forms. One is the mapping of the distribution of different species of vegetation and the differences in vigor and morphology within each species (Brooks, 1972; Siegel, 1974). Vegetation that is typically prolific is often stunted or absent in areas of unusual soil environments. On the other hand, some species thrive in environments that are toxic to most other species and are recognized as geobotanical indicators. The second approach is to determine differences in spectral characteristics between healthy and stressed vegetation. The spectral signatures of vegetation associated with hydrocarbon microseepage have been extensively studied. The main targets of attention are the green peak (at 0.56 µm), the red trough (at 0.67 µm), the shift of position of red edge and the height of the infrared shoulder.

In both cases, normal or background variability in the distribution and vigor of various species presents complications that need to be taken into account. Factors such as bedrock geology, soil type, slope, soil moisture and climate can have a more pronounced effect than that due to the presence of hydrocarbons (Rock, 1984; Klusman et al., 1992). Nevertheless, numerous accounts have been published of the detection of hydrocarbon-induced vegetation anomalies by remote sensing.

OTHER ANOMALIES

Everett and Petzel (1973) reported that some oil and gas fields in the Anadarko Basin of the Texas Panhandle and western Oklahoma are manifested on imagery data as unique features, appearing to be smudged or erased, which they term "hazy anomalies". Moore and Anderson (1985) found a circular tonal anomaly on a Landsat TM image of the Herg oil field of the western Hardeman Basin, north Texas, which did not correlate with any single soil type or

groups of soils, and suggest that it is possibly related to vertical migration of hydrocarbons causing chemically-altered soils or anomalous vegetation growth. Carter and Koger (1988) processed MSS and Landsat TM data from an area with hydrocarbon prospects. They suggest that, in the near-surface and surface rocks, soil and vegetation, structure and alteration (possibly due to hydrocarbon microseepage) can be detected by tonal and spectral anomalies in various filtered, contrast-stretched and edge-enhanced formats, in ratios of various bands in both color and black-and-white, and in false color composites.

We calculated a number of spectral indexes, incl. the clay minerals discussed in this report, the content of ferrous and ferric iron, carbonate content, vegetation and a number of others.

SPECTRAL INDEXES OF VARIOUS TYPES OF ROCKS

CLAY MINERALS RATIO

This band ratio highlights hydrothermally altered rocks containing clay and alunite.

$$Clay\ Minerals\ Ratio = \frac{SWIR1}{SWIR2}$$

Where:

Shortwave-infrared (SWIR) 1: 1.55-1.75 µm

SWIR2: 2.08-2.35 µm

For Landsat TM and ETM+, this corresponds to bands 5 (SWIR1) and 7 (SWIR2). This index works with any multispectral sensor with bands that fall within the listed ranges.

Reference: Drury, S. Image Interpretation in Geology. London: Allen and Unwin (1987), 243 pp.

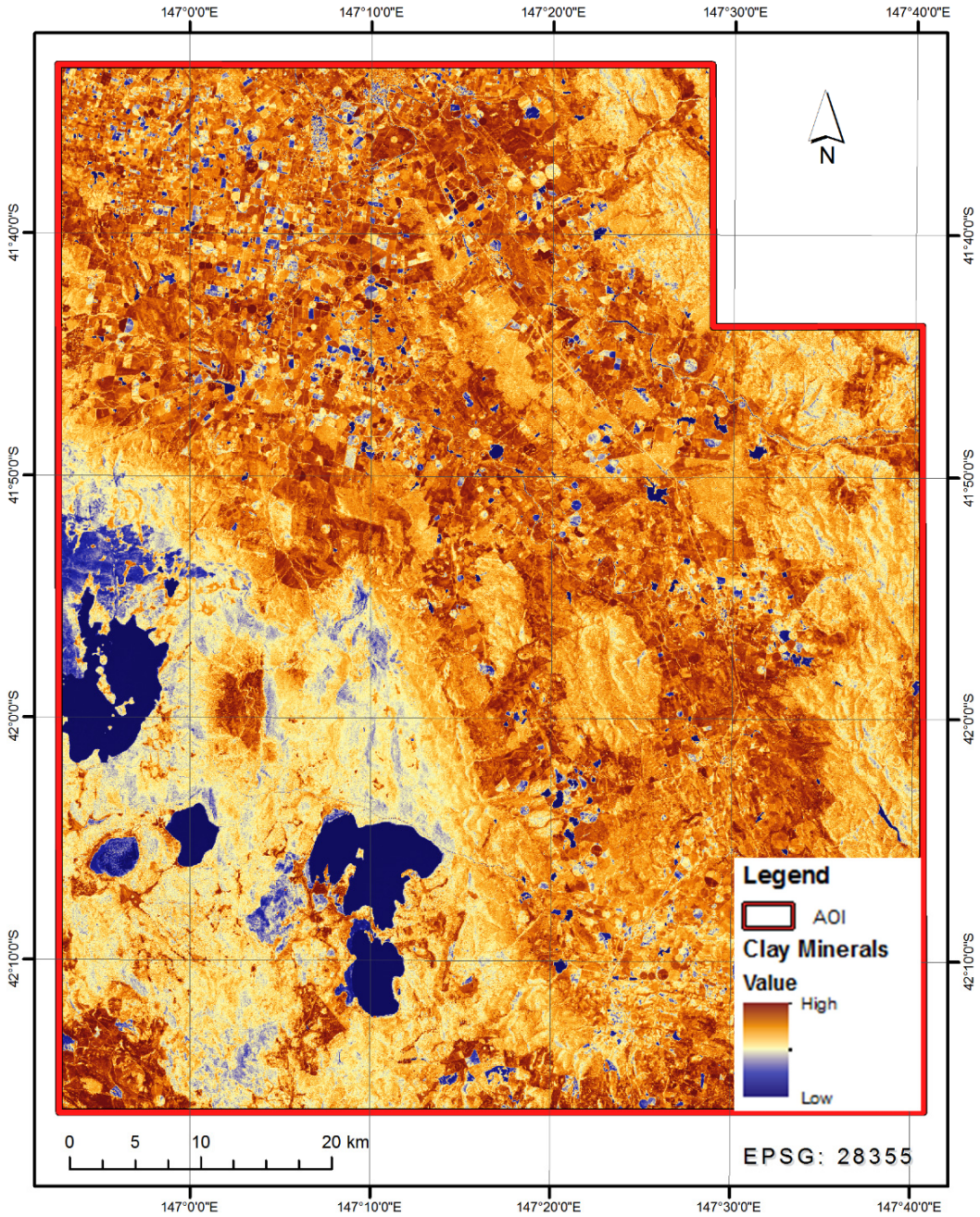


Figure 19: Hydrothermally altered rocks containing clay and alunite.

FERROUS IRON (FE2+)

This band ratio highlights rocks containing Fe2+ ion.

$$Ferrous\ Iron\ = \frac{SWIR2}{NIR} + \frac{Green}{Red}$$

Where (for Landsat 8):

NIR: 0.851-0.879 µm, SWIR2: 2.107-2.294 µm, Green: 0.533-0.59 µm Red: 0.646-0.673 µm

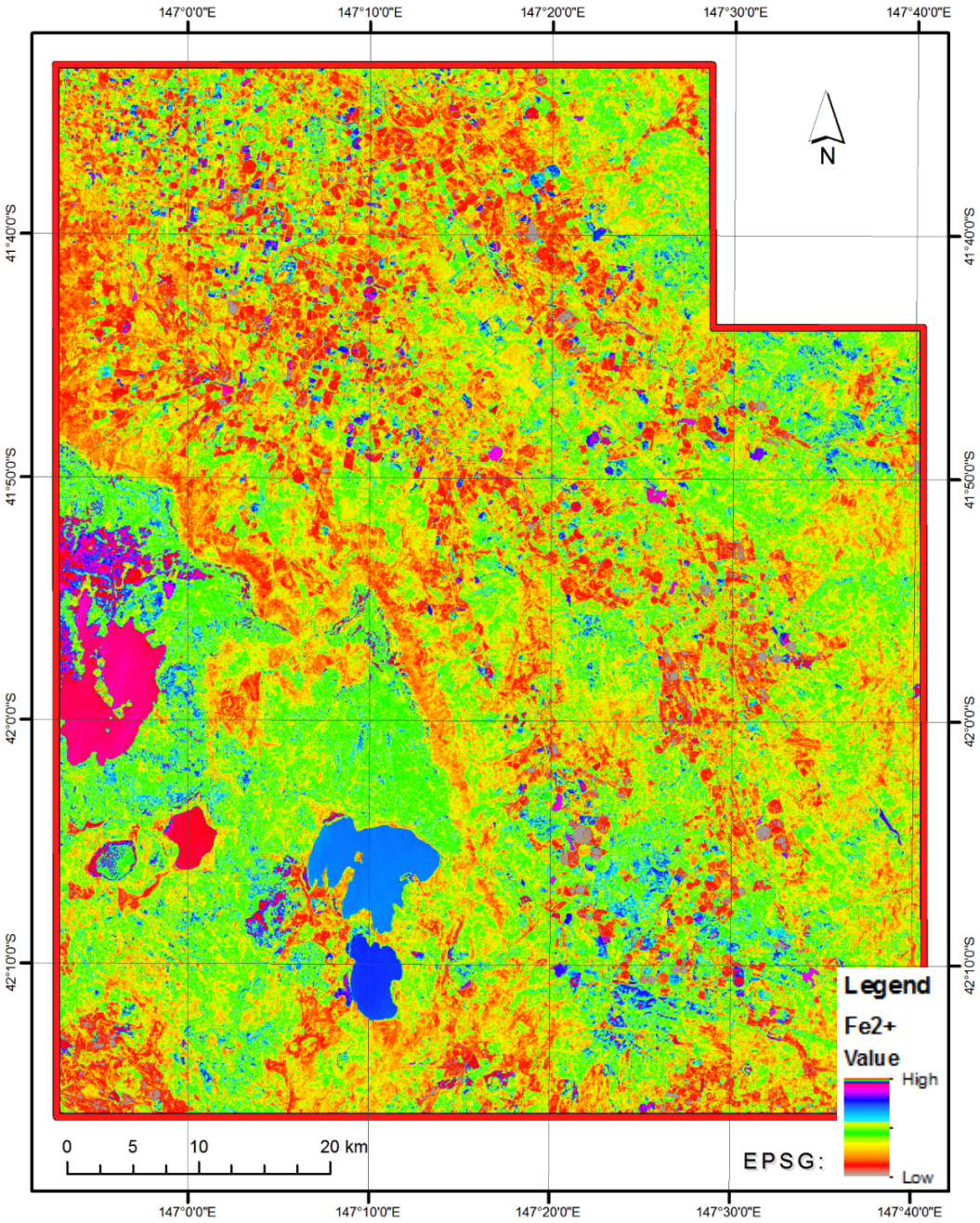


Figure 20. Rocks containing Fe2+ ion.

For Landsat 8 OLI this corresponds to bands 5 (NIR), 7 (SWIR2), 4 (Red) and 3 (Green). This index works with any multispectral sensor with bands that fall within the listed ranges.

Reference: Rowan, L.C.; Mars, J.C. Lithologic mapping in the Mountain Pass, California area using Advanced Spaceborne Thermal Emission and Reflection Radiometer (ASTER) data. Remote Sensing of Environment, 2003, 84, 350-366 pp.

FERRIC IRON (FE^{3+})

This band ratio highlights rocks containing Fe3+ ion.

$$Ferric\ Iron\ = \frac{Red}{Green}$$

Where (for Landsat 8):

Green: 0.533-0.59 µm

Red: 0.646-0.673 µm

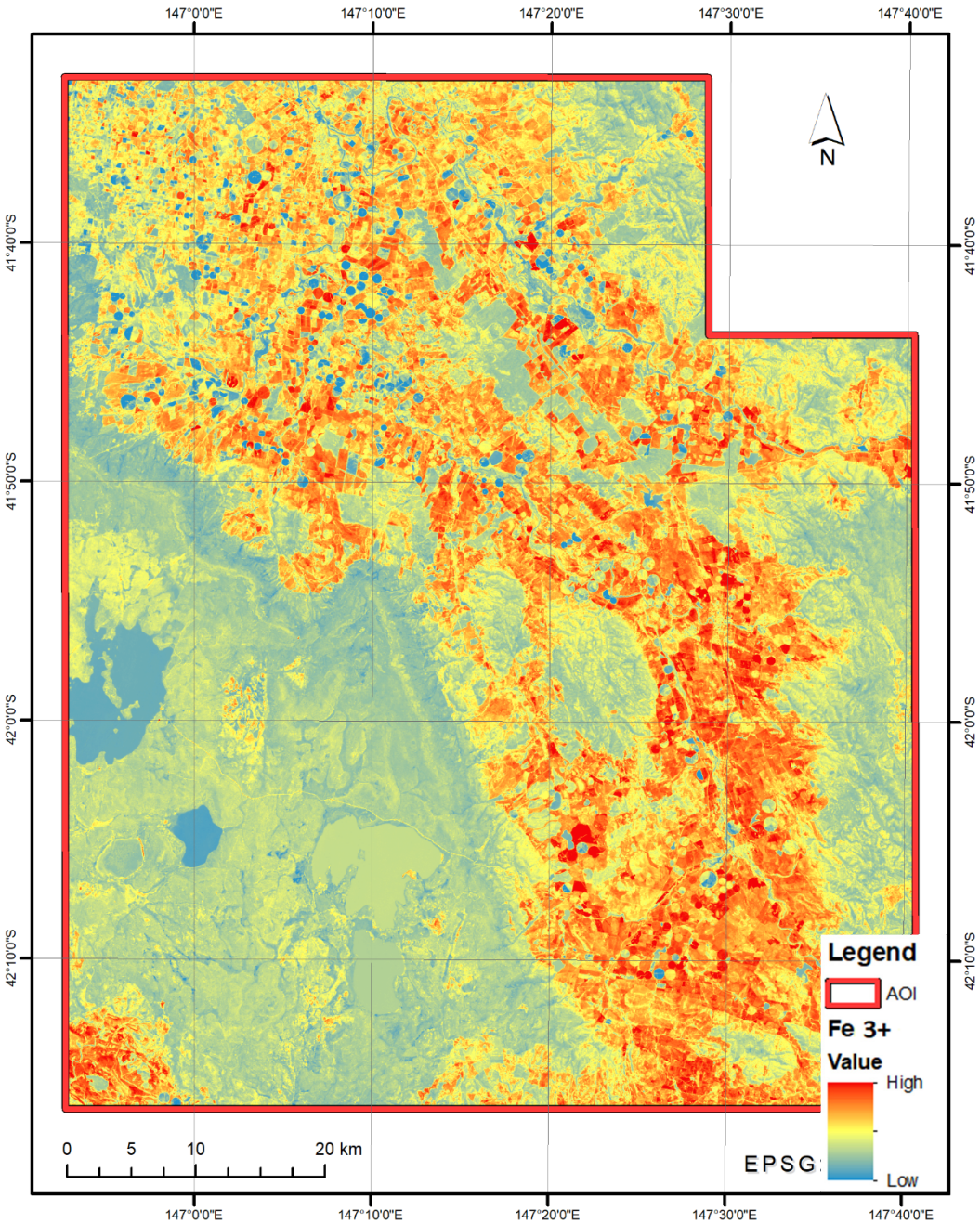


Figure 21. Rocks containing Fe^{3+} ion.

For Landsat 8 OLI this corresponds to bands 4 (Red) and 3 (Green). This index works with any multispectral sensor with bands that fall within the listed ranges.

Reference: Rowan, L.C.; Mars, J.C. Lithologic mapping in the Mountain Pass, California area using Advanced Spaceborne Thermal Emission and Reflection Radiometer (ASTER) data. Remote Sensing of Environment, 2003, 84, 350-366 pp.

FERROUS MINERALS RATIO

This band ratio highlights iron-bearing minerals.

$$Ferrous\ Minerals\ Ratio = \frac{SWIR}{NIR}$$

Where:

SWIR: 1.55-1.75 µm

NIR: 0.76-0.9 µm

For Landsat TM and ETM+, this corresponds to bands 5 (SWIR) and 4 (NIR). This index works with any multispectral sensor with bands that fall within the listed ranges.

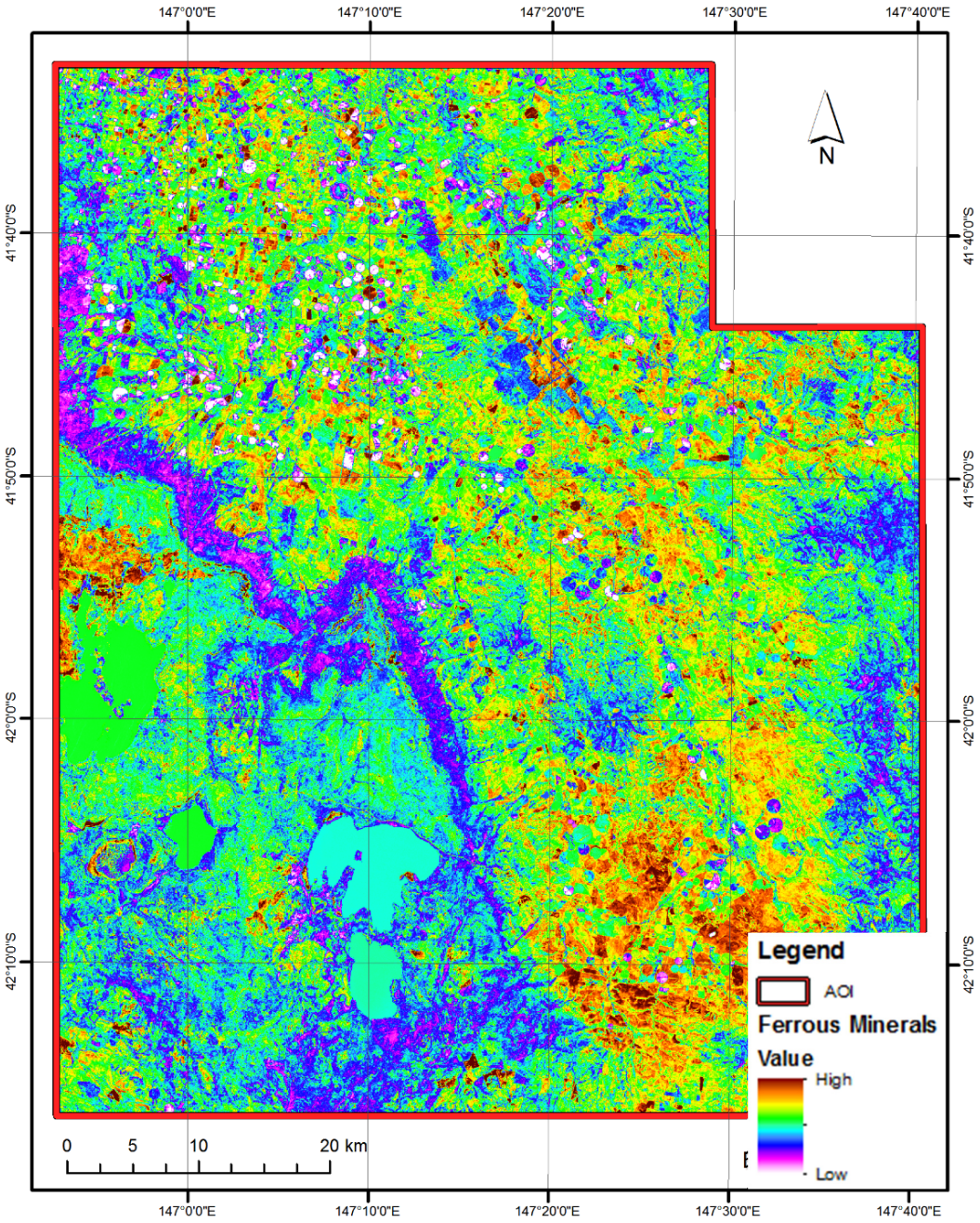


Figure 22. Iron-bearing minerals.

References:

Segal, D. "Theoretical Basis for Differentiation of Ferric-Iron Bearing Minerals, Using Landsat MSS Data." Proceedings of Symposium for Remote Sensing of Environment, 2nd Thematic Conference on Remote Sensing for Exploratory Geology, Fort Worth, TX (1982): 949-951.

Drury, S. Image Interpretation in Geology. London: Allen and Unwin (1987), 243 pp.

IRON OXIDE RATIO

This band ratio highlights hydrothermally altered rocks that have been subjected to oxidation of iron-bearing sulphides.

$$Iron\ Oxide\ Ratio = \frac{Red}{Blue}$$

Where:

Red: 0.63-0.69 µm

Blue: 0.45-0.52 µm

For Landsat TM and ETM+, this corresponds to bands 3 (Red) and 1 (Blue). This index works with any multispectral sensor with bands that fall within the listed ranges.

References:

Segal, D. "Theoretical Basis for Differentiation of Ferric-Iron Bearing Minerals, Using Landsat MSS Data." Proceedings of Symposium for Remote Sensing of Environment, 2nd Thematic Conference on Remote Sensing for Exploratory Geology, Fort Worth, TX (1982): pp. 949-951.

Drury, S. Image Interpretation in Geology. London: Allen and Unwin (1987), 243 pp.

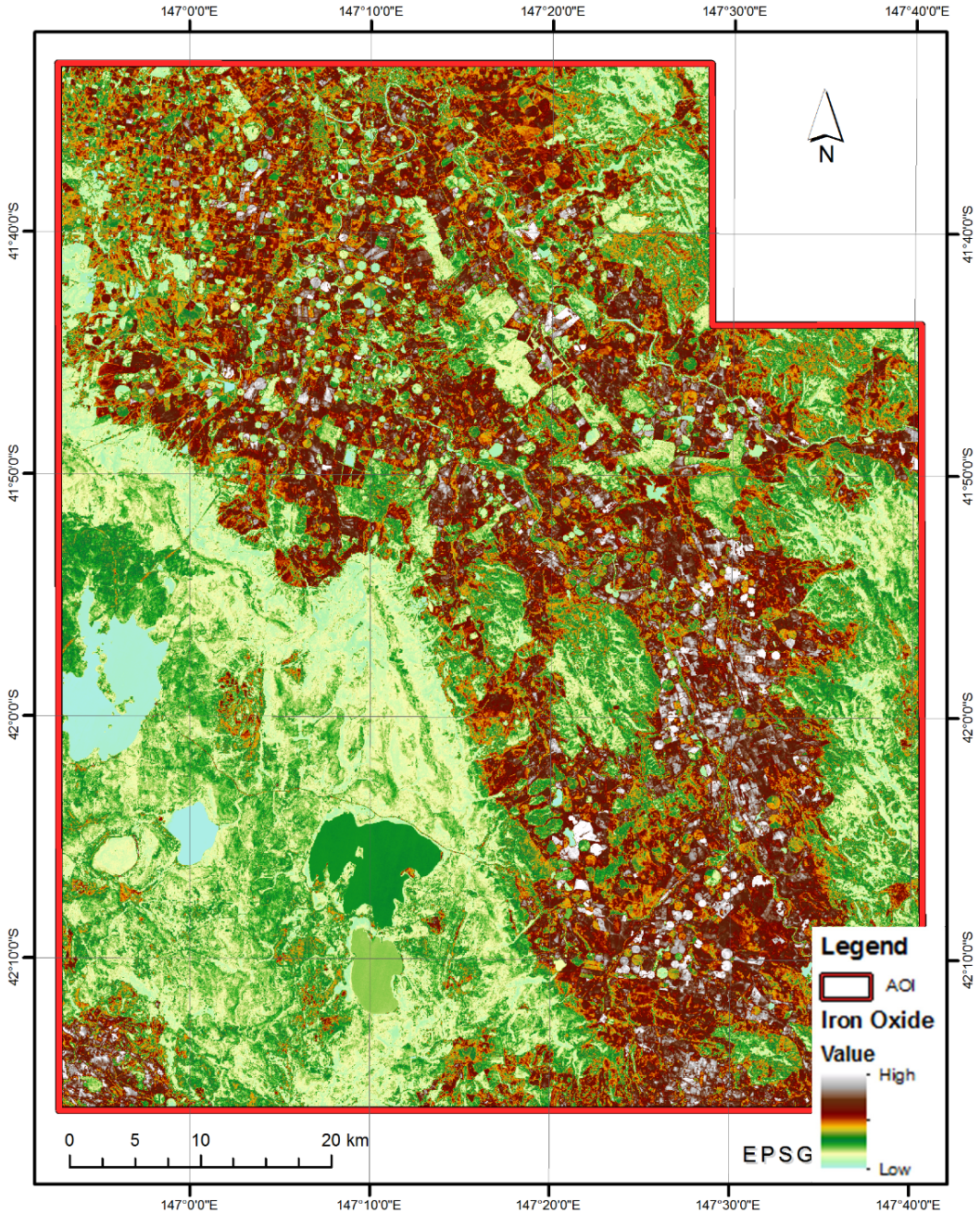


Figure 23: Hydrothermally altered rocks that have been subjected to oxidation of iron-bearing sulphides.

CARBONTE ROCKS

This band ratio highlights carbonate rocks.

$$Carbonate = \frac{TIRS1}{TIRS2}$$

Where:

TIRS1: 10.6-11.19 µm

TIRS2: 11.5-12.51 µm

For Landsat 8 TIRS this corresponds to bands 10 (TIRS1) and 11 (TIRS2). This index works with any thermal sensor with bands that fall within the listed ranges.

References:

Kalinowski, A.; Oliver, S. ASTER Mineral Index Processing Manual. Remote Sensing Applications, 2004.

Ninomiya, Y. Mapping quartz, carbonate minerals, and mafi cultramafic rocks using remotely sensed multispectral thermal infrared ASTER data. Proceedings of SPIE — The International Society for Optical Engineering, 2002, 4710, 191-202 pp.

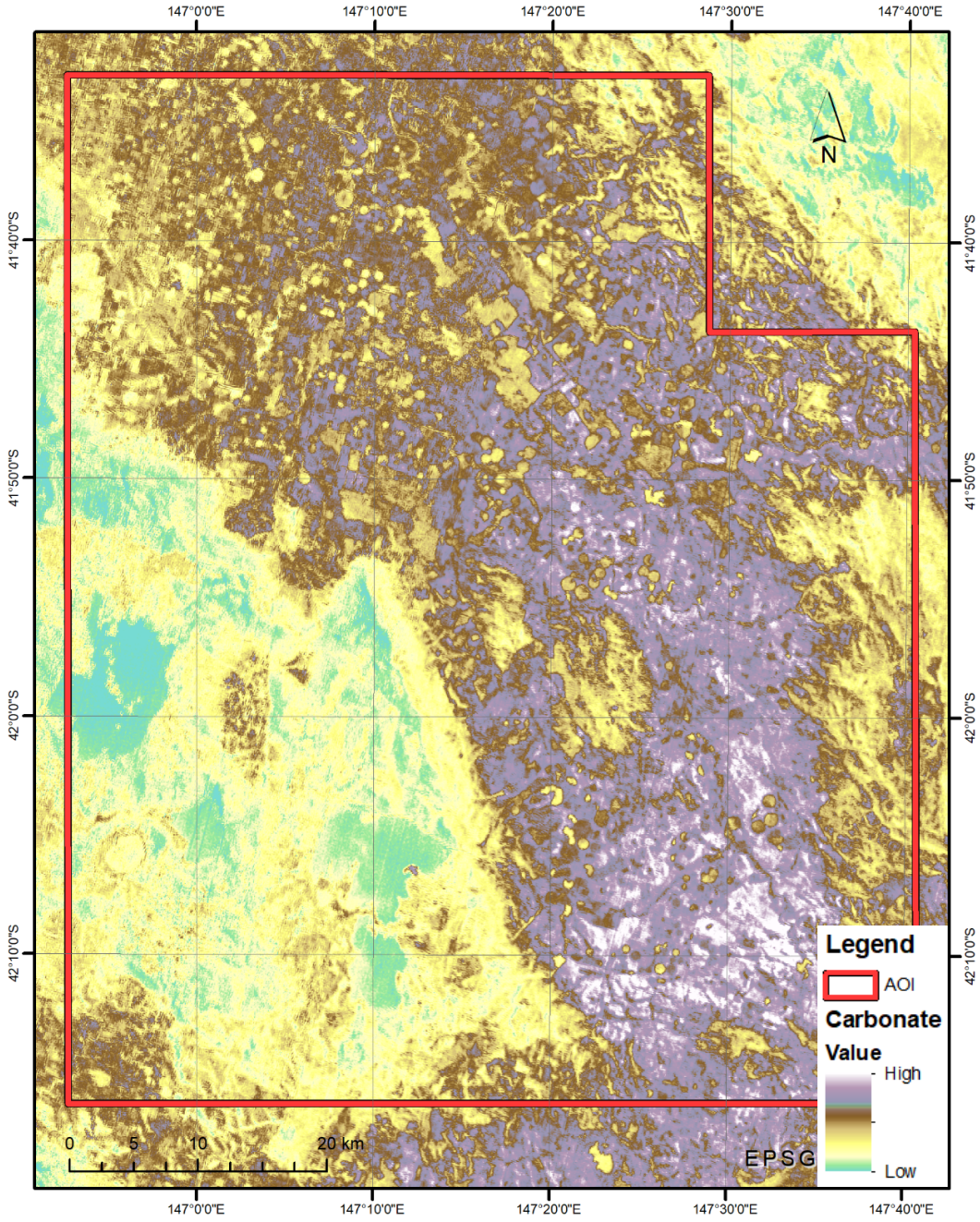


Figure 24. Carbonate rocks.

GOSSAN

This band ratio highlights rocks with metal iron.

$$Gossan = \frac{SWIR1}{Red}$$

Where:

SWIR1: 1.556-1.651 µm

Red: 0.646-0.673 µm

For Landsat 8 OLI this corresponds to bands 6 (SWIR1) and 4 (Red). This index works with any multispectral sensor with bands that fall within the listed ranges.

References: Volesky, J.C.; Stern, R.J.; Johnson, P.R. Geological control of massive sulfide mineralization in the Neoproterozoic Wadi Bidah shear zone, southwestern Saudi Arabia, inferences from orbital remote sensing and field studies. Precambrian Research , 2003, 123, 2-4, 235-247 pp.

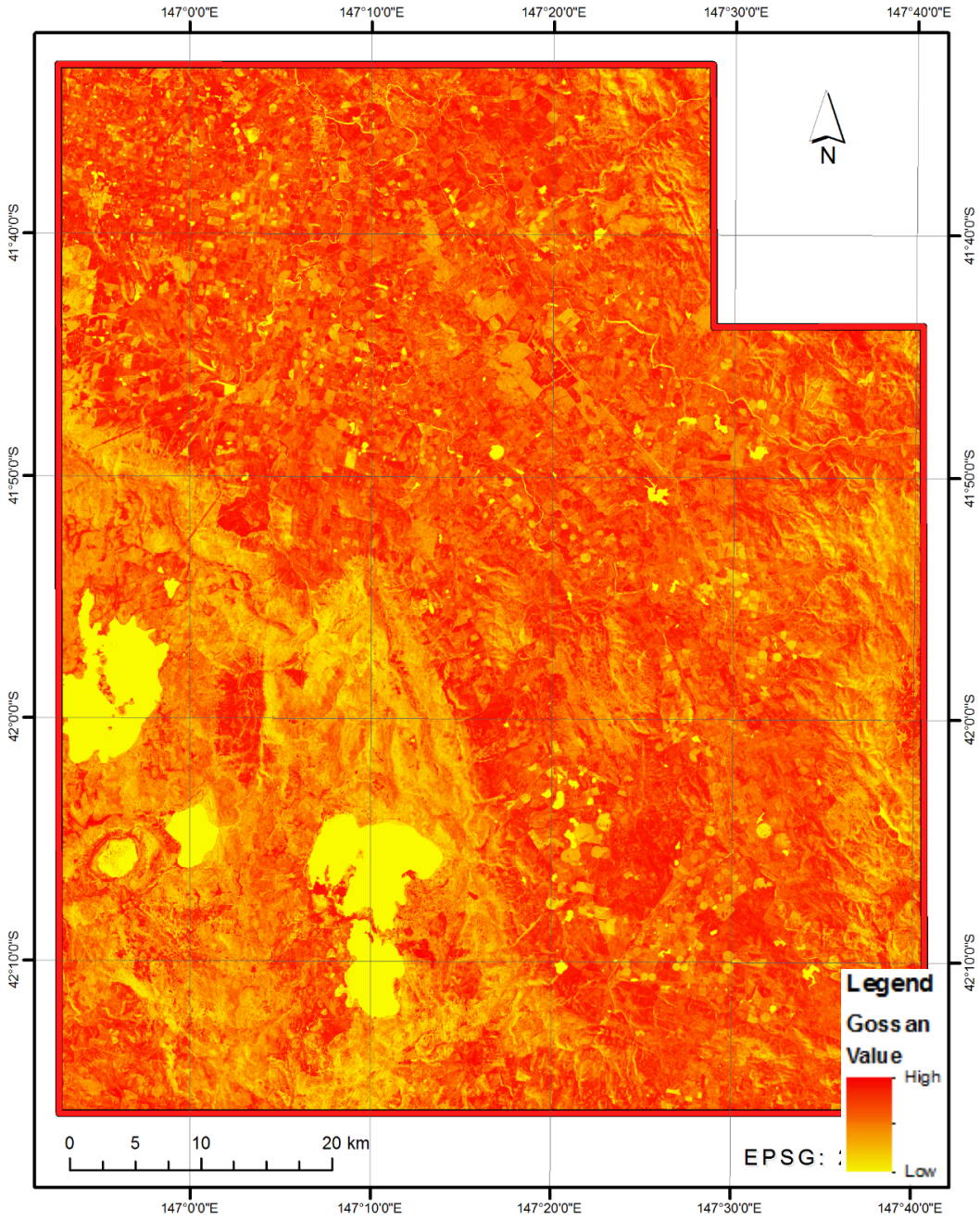


Figure 25: Rocks with metal iron.

NDVI

Normalized difference vegetation index.

$$NDVI = \frac{NIR - Red}{NIR + Red}$$

Where:

NIR: 0.851-0.879 µm

Red: 0.646-0.673 µm

For Landsat 8 OLI this corresponds to bands 5 (NIR) and 4 (Red). This index works with any multispectral sensor with bands that fall within the listed ranges.

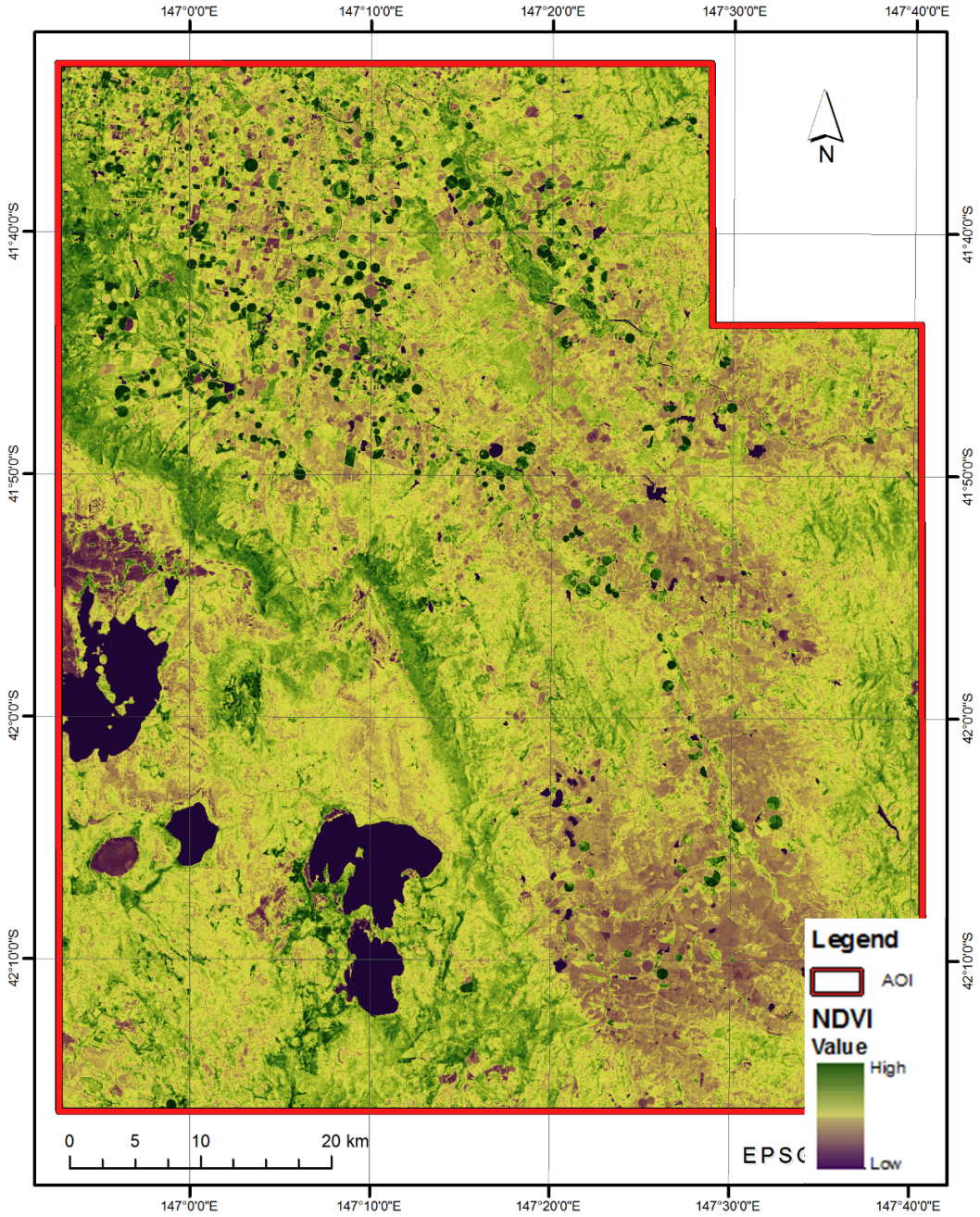


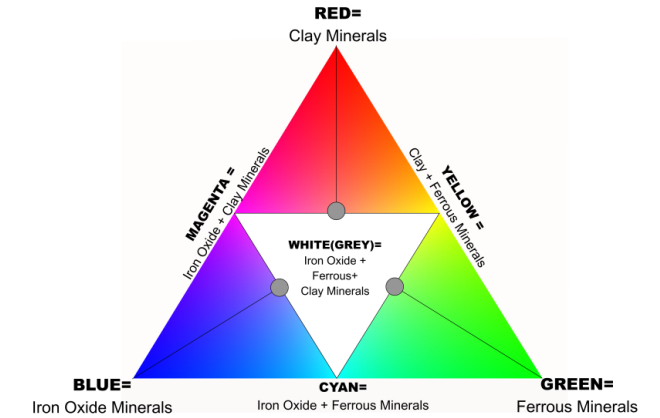
Figure 26: Normalized difference vegetation index.

As the next step, the overlay analysis technique (weighted summation) of a set of indices aims at identifying and localizing the conditions presented in **Figure 26**. The areas with open water, buildings, and other technogenic alterations must be masked on all the used spectral indices prior to the subsequent work.

Among the other thematic layers within the overlay analysis, the mineral and hydrothermal RGB-composites may also be useful (the indexes described above were combined into these composites).

MINERAL COMPOSITES

Table 2. Mineral composite in RGB-view

RGB display of respective band Ratios	Red	Green	Blue	Extra
	correspondent to			
Mineral Composite	Clay minerals	Ferrous mineral	Iron oxide minerals	

Mineral composite in RGB-view (Clay minerals as Red, Ferrous mineral as Green, Iron oxide minerals as Blue)

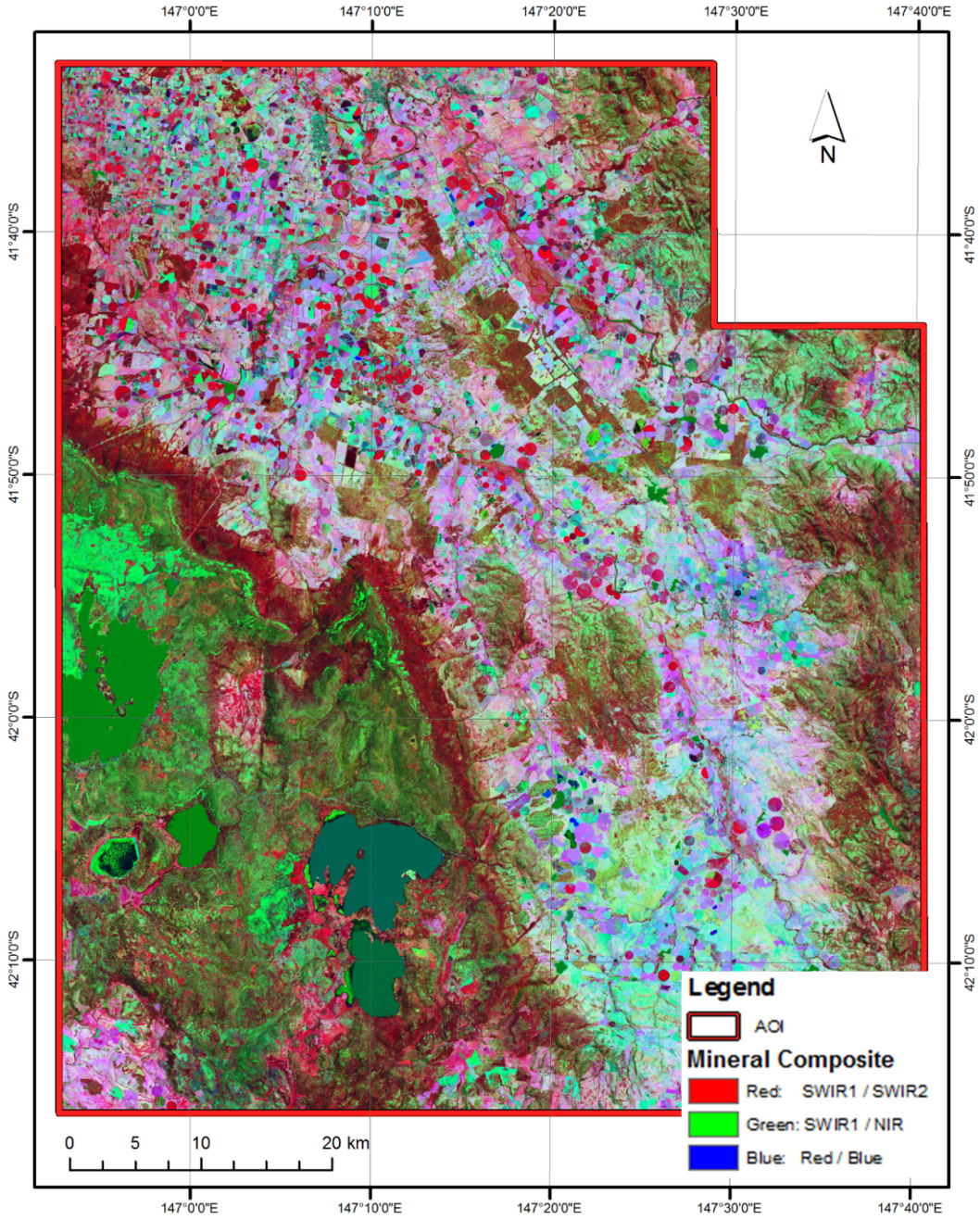
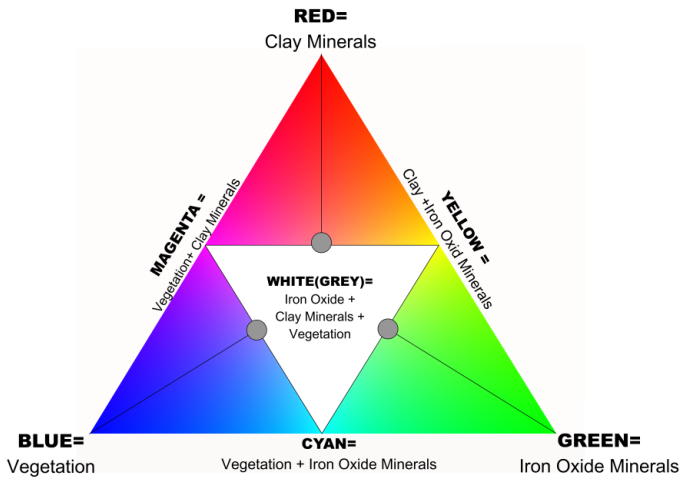


Figure 27: Mineral composite of AOI.

HYDROTHERMAL COMPOSITE

Table 3. Hydrothermal composite in RGB-view

RGB display of respective band Ratios	Red	Green	Blue	Extra
	correspondent to			
Hydrothermal composite	Clay minerals	Iron oxide minerals	Vegetated zones	

Hydrothermal composite in RGB-view (Clay minerals as Red, Iron oxide minerals as Green, Vegetated zones as Blue)

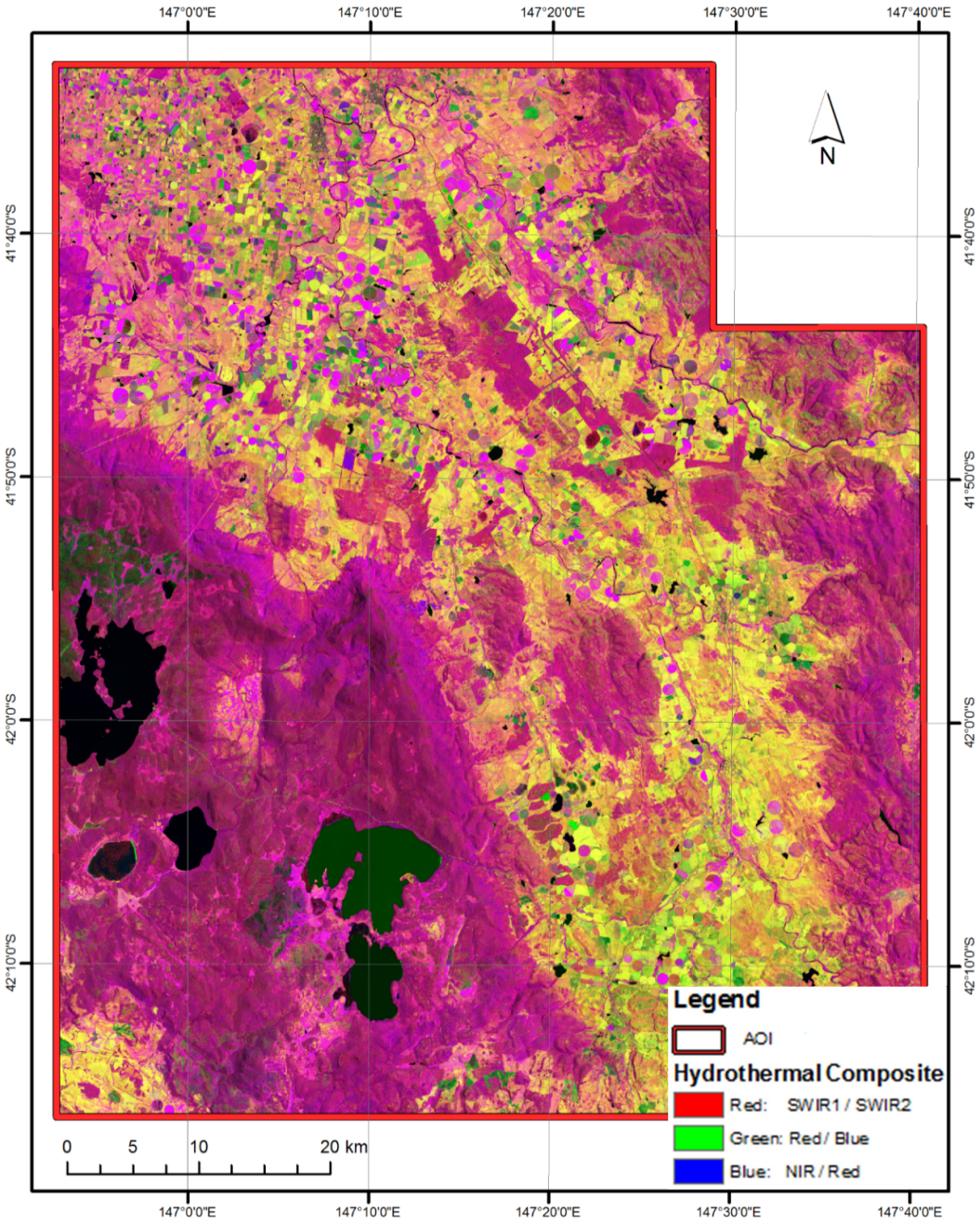


Figure 28: Hydrothermal composite.

The multitemporal sets of color composites in natural (TCC - true color composite) and artificial (FCC - false color composite) colors are often useful for the purposes of visual analysis.

TRUE COLOR COMPOSITES

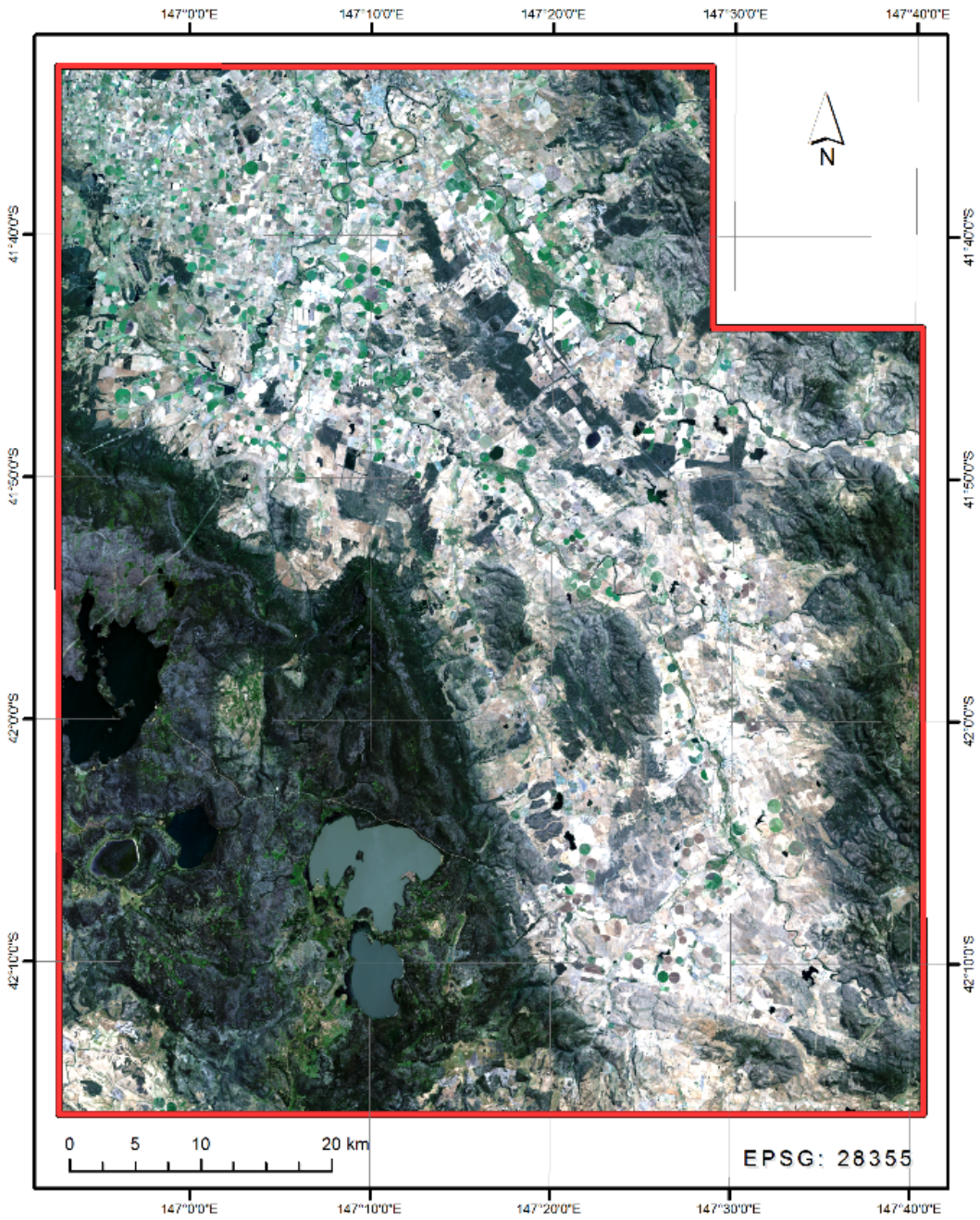


Figure 29: Natural Color. Landsat 8 OLI, bands: 4,3,2.

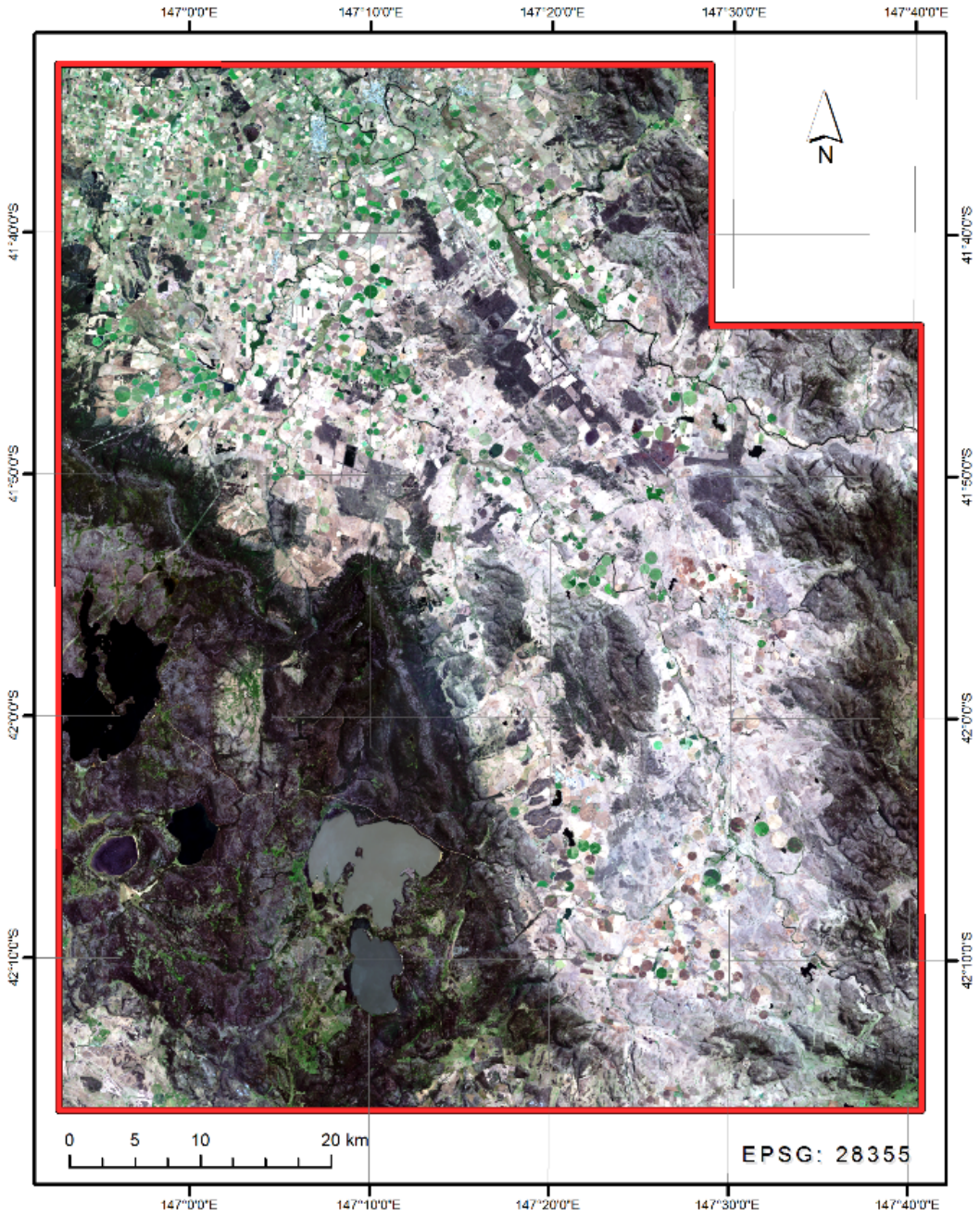


Figure 30: Natural Color. Landsat 8 OLI, bands: 4,3,2.



Figure 31: Natural Color. Landsat 8 OLI, bands: 4,3,2.

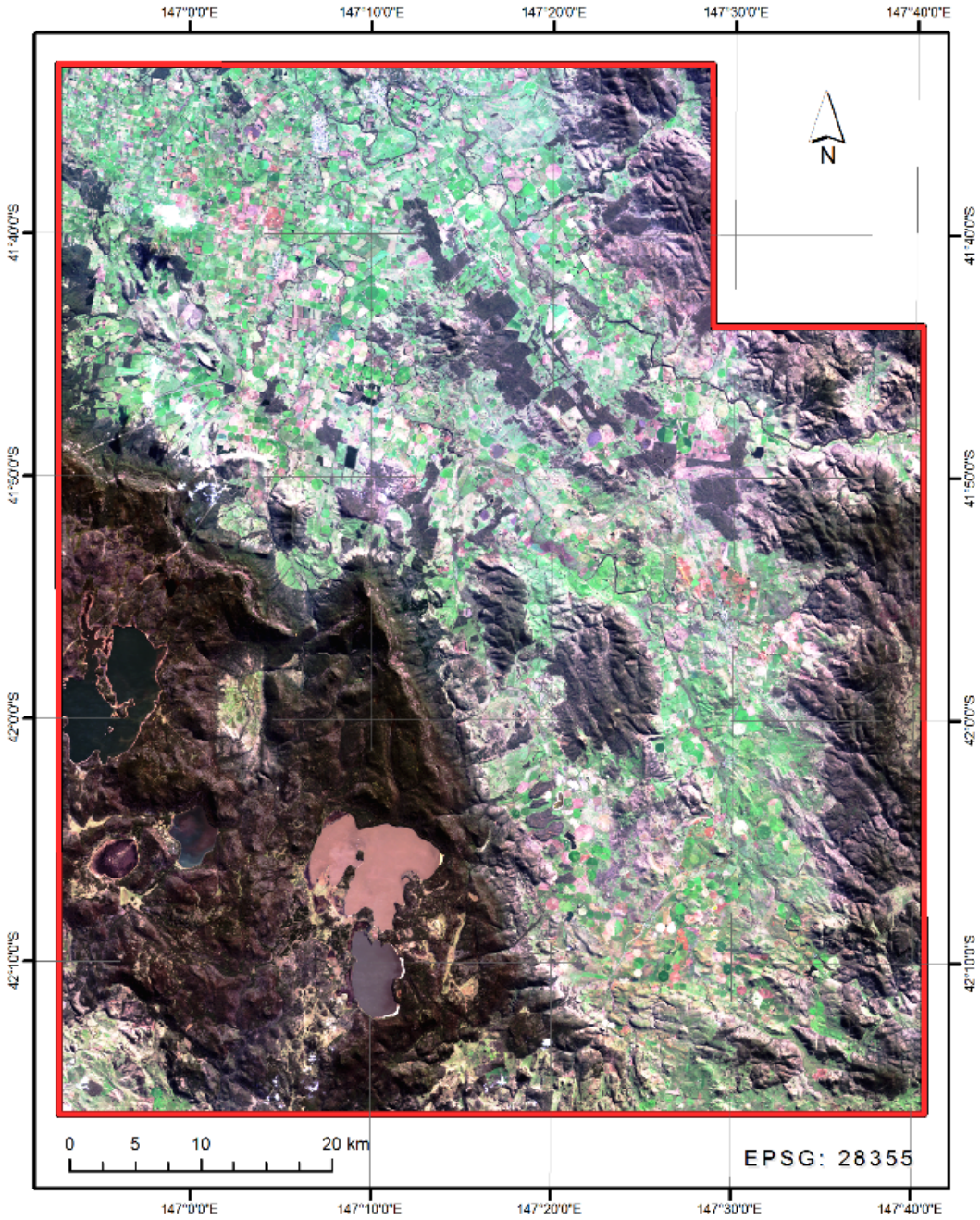


Figure 32: Natural Color. Landsat 8 OLI, bands: 4,3,2.

FALSE COLOR COMPOSITES

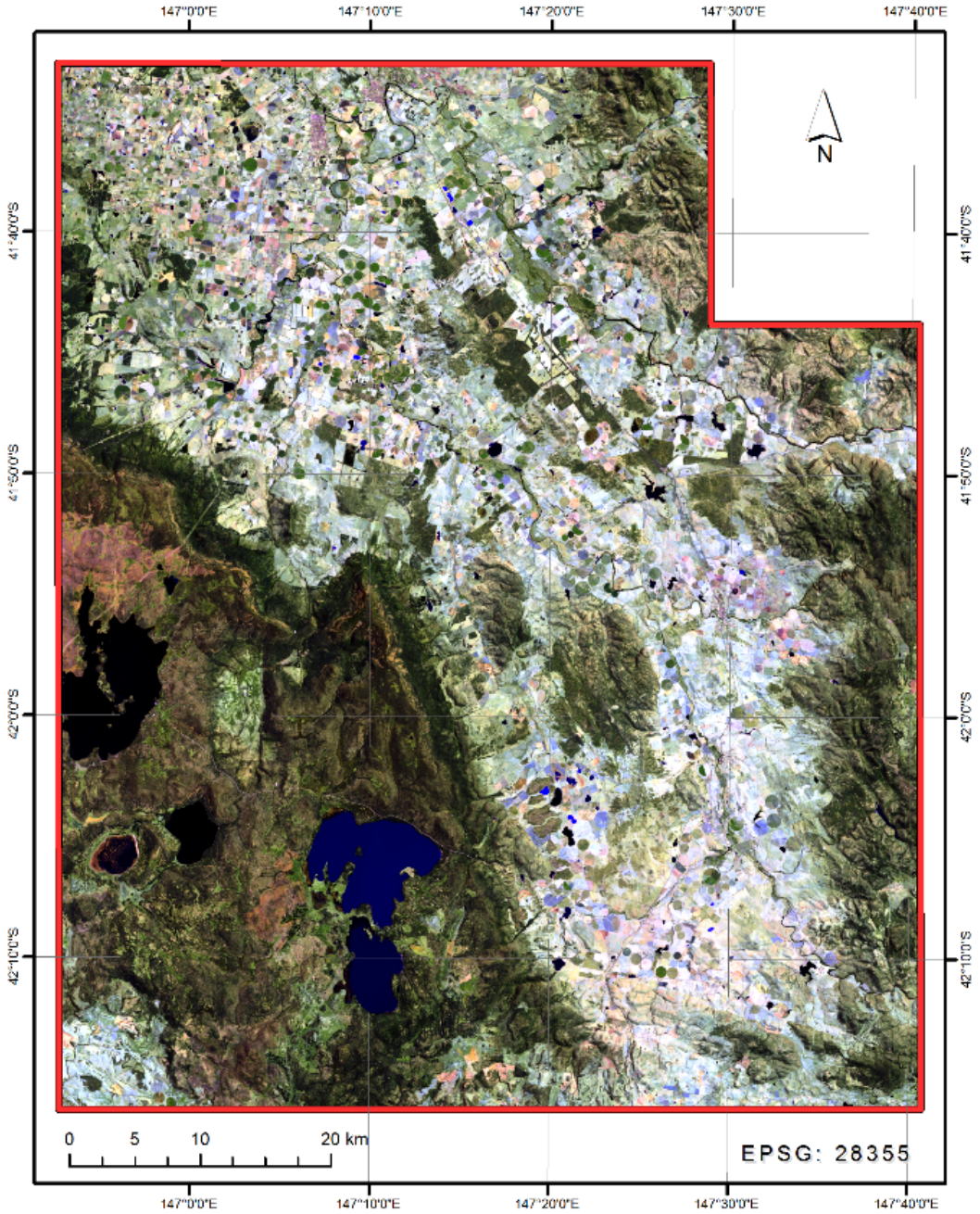


Figure 33: Landsat 8 OLI, bands: 7,6,4. SWIR (Short Wave Infrared) Highlights rock formations.

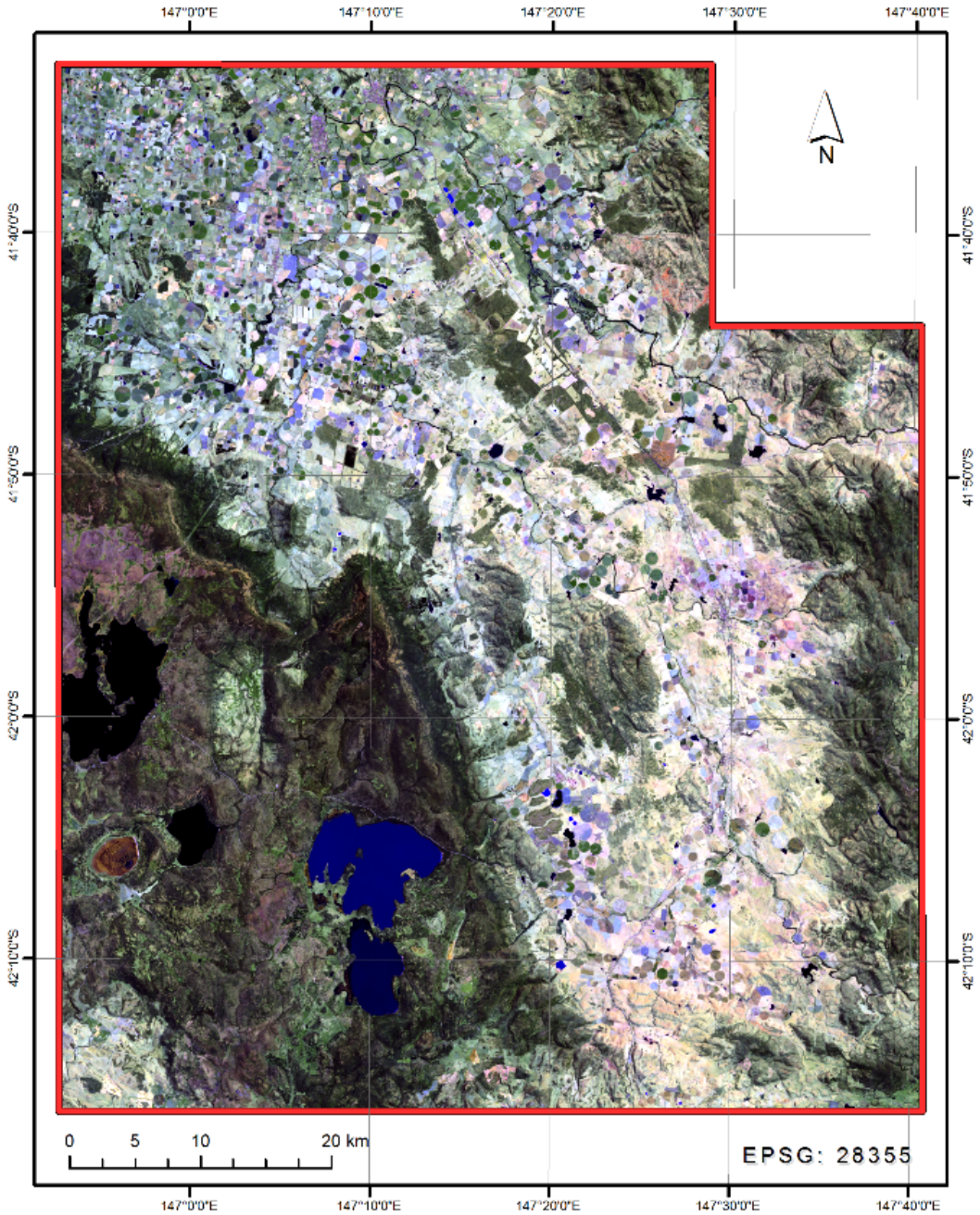


Figure 34: Landsat 8 OLI, bands: 7,6,4. SWIR (Short Wave Infrared) Highlights rock formations.

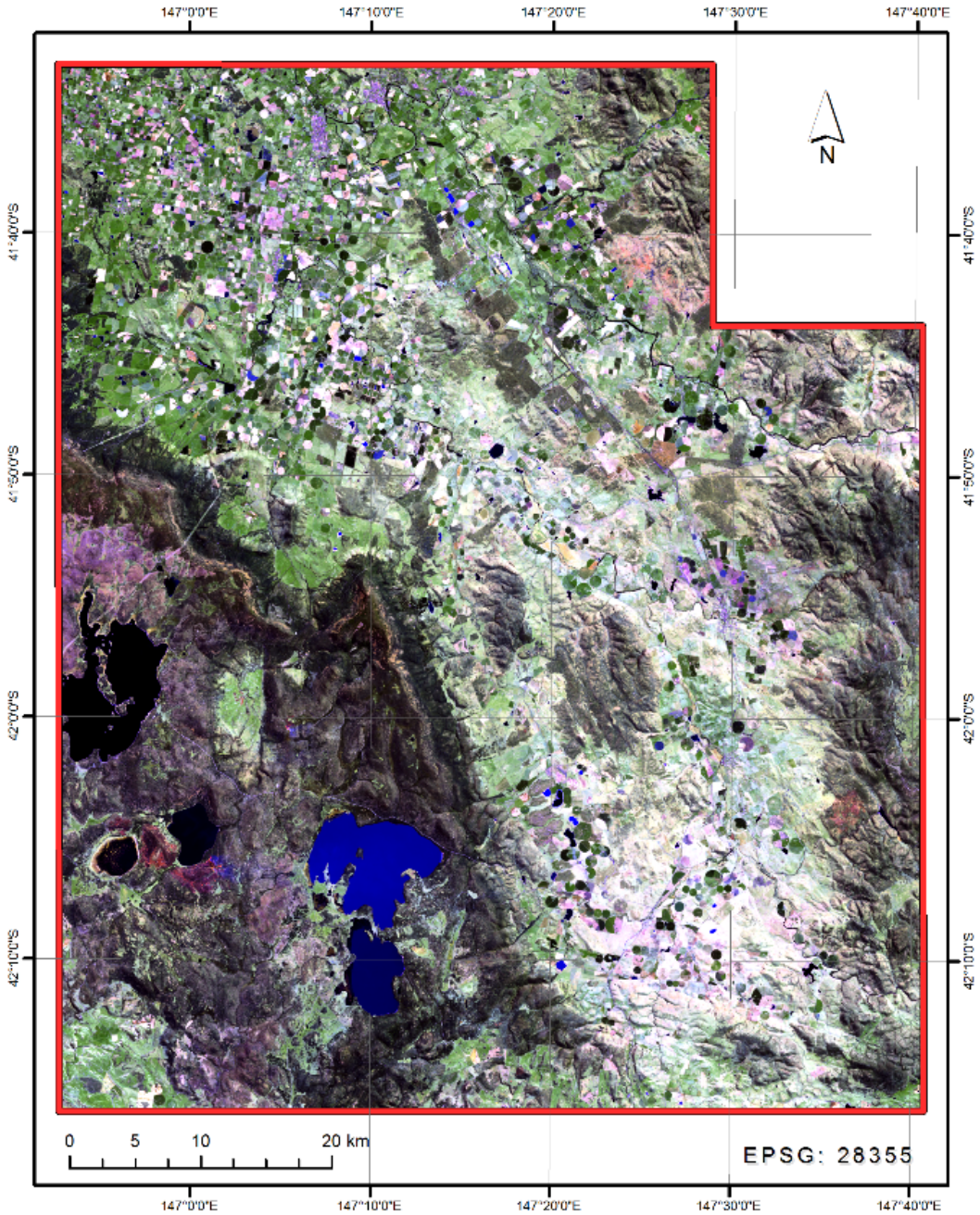


Figure 35: Landsat 8 OLI, bands: 7,6,4. SWIR (Short Wave Infrared) Highlights rock formations.

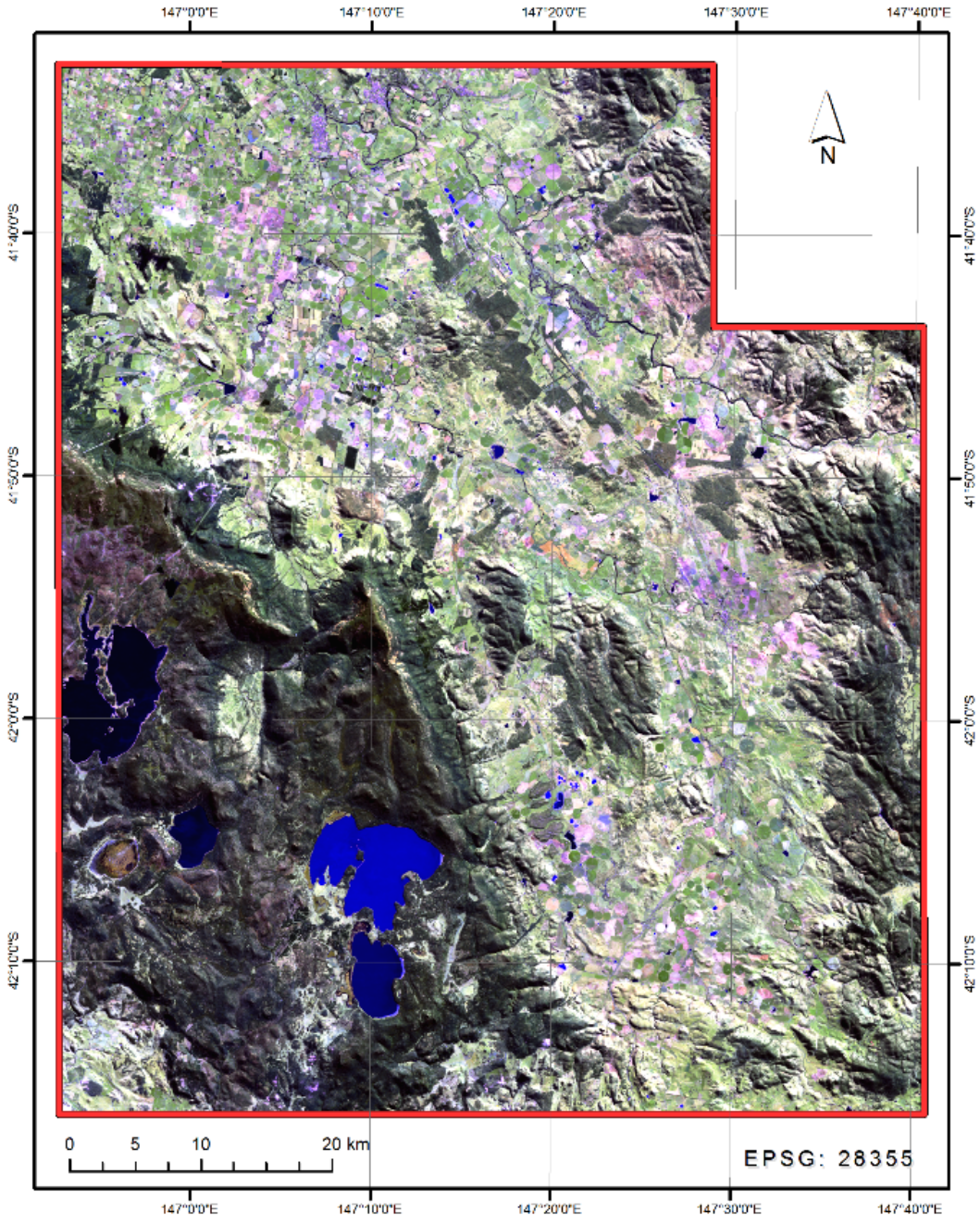


Figure 36: Landsat 8 OLI, bands: 7,6,4. SWIR (Short Wave Infrared) Highlights rock formations.

FALSE COLOR COMPOSITES

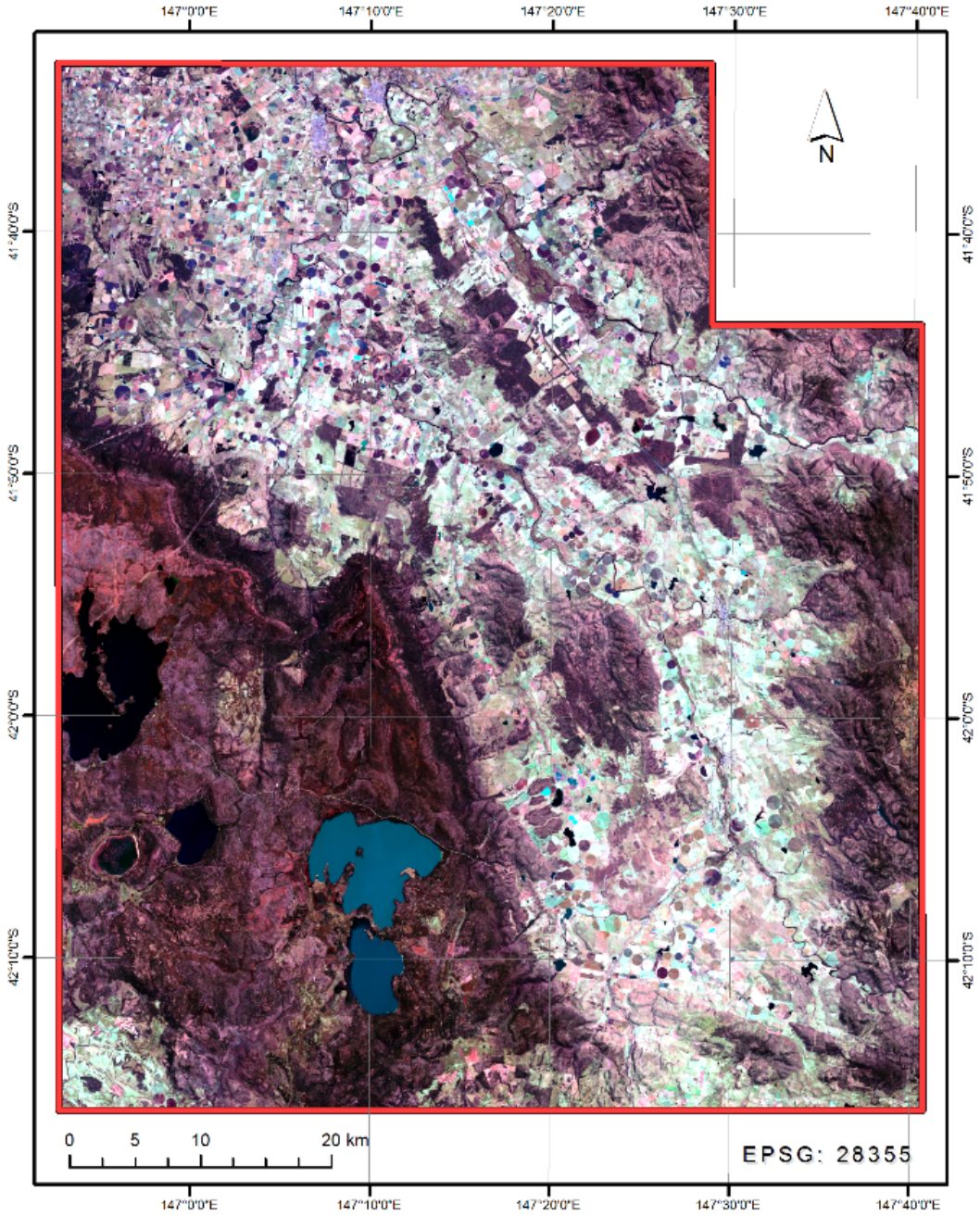


Figure 37: Landsat 8 OLI, bands: 7,4,2. Geology Highlights geologic features.

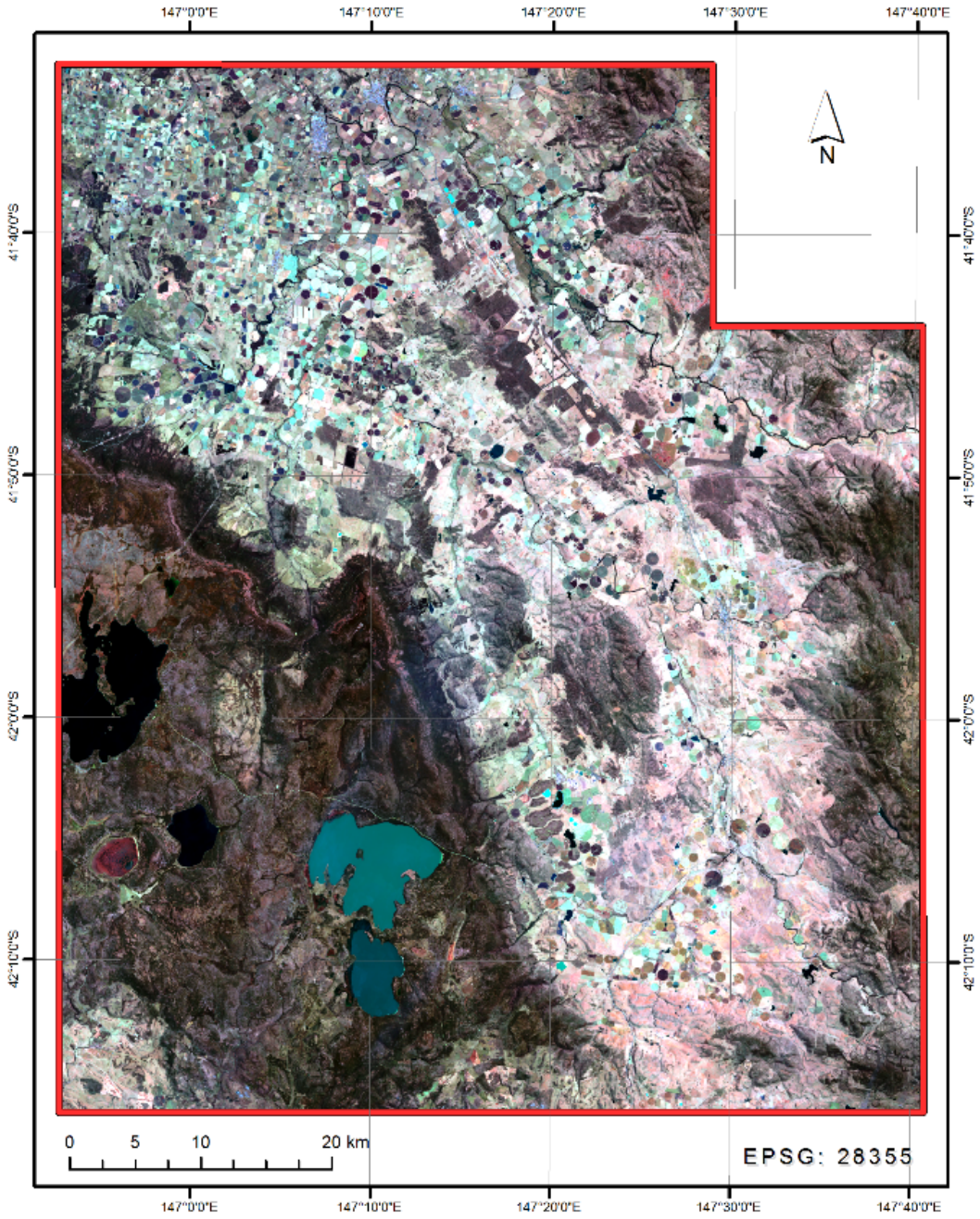


Figure 38. Landsat 8 OLI, bands: 7,4,2. Geology Highlights geologic features.

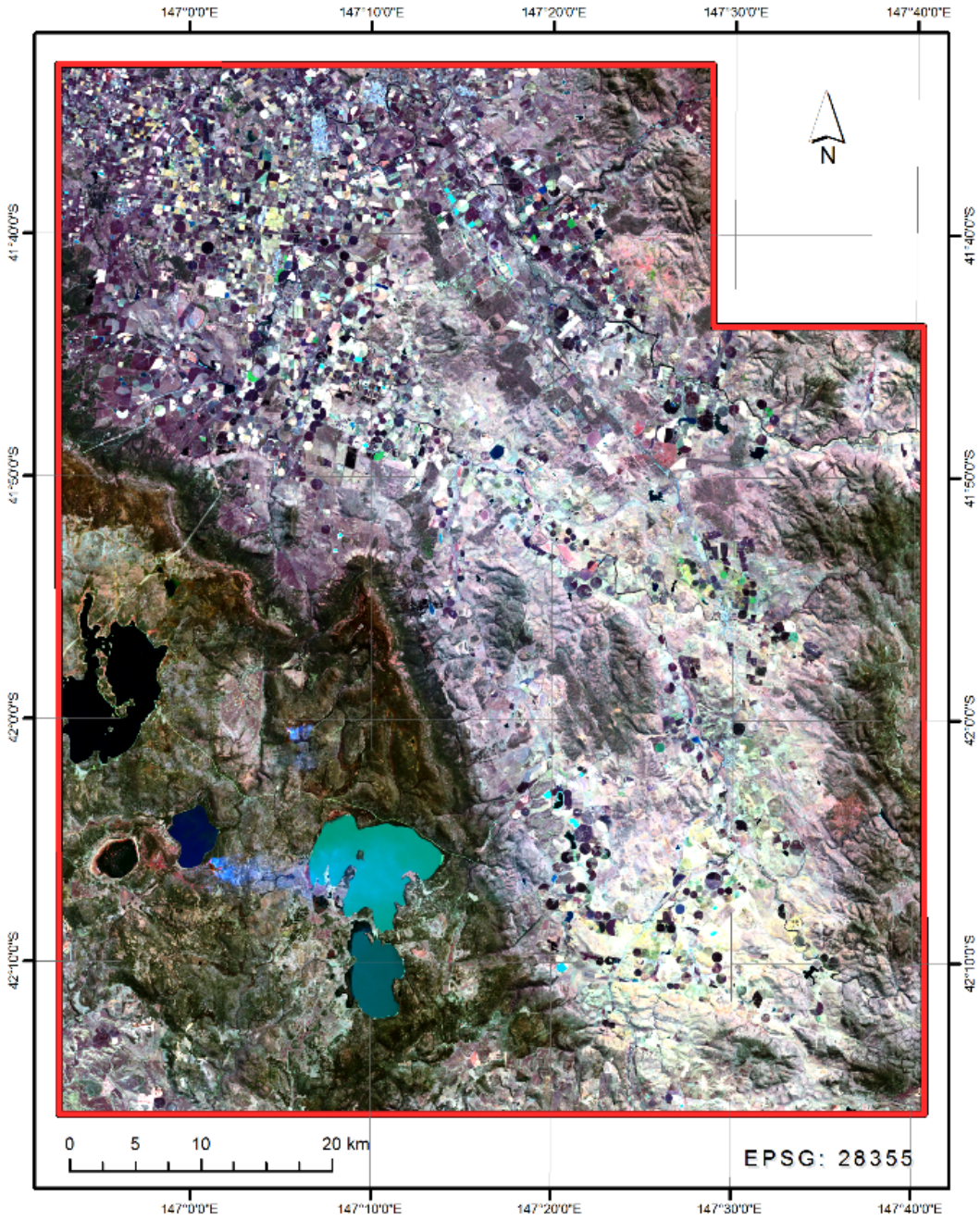


Figure 39: Landsat 8 OLI, bands: 7,4,2. Geology Highlights geologic features.

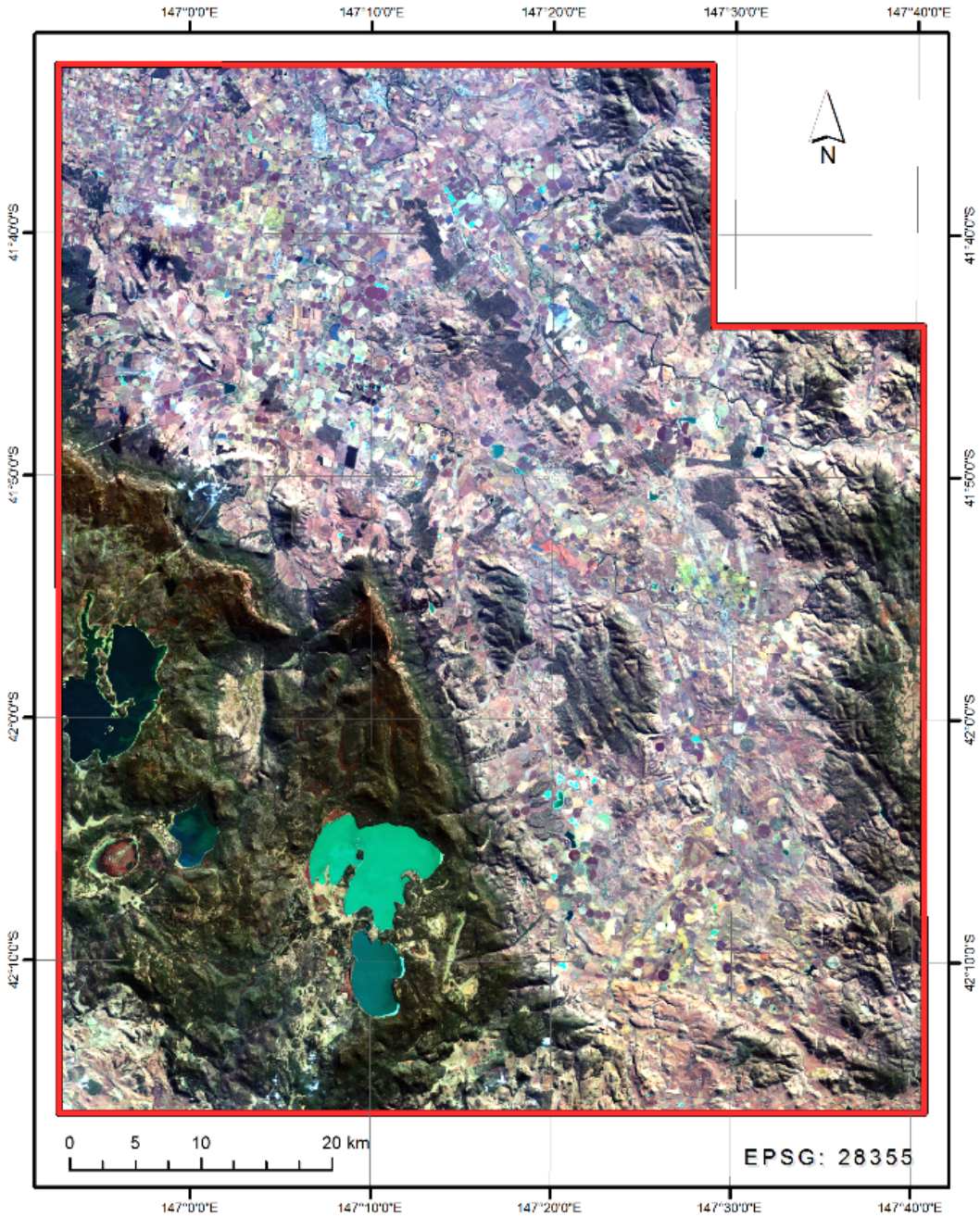


Figure 40: Landsat 8 OLI, bands: 7,4,2. Geology Highlights geologic features.

2.4 RELIEF PLASTICITY OR PALEO-RECONSTRUCTION ANALISYS (PRA)

INTRODUCTION

The method of paleo-reconstruction (PRA) allows performing certain paleo reconstructions of the litho-dynamic situation within AOI. The HC-prospectivity prognosis is being made based on the identified flow structures and the distribution of geological material according to the method's criteria. PRA analyzes the maps of flows of geological matter (or simply "flows") according to the following HC-prospectivity criteria:

1. Linear and circular faults/features;
2. Paleo-deltas;
3. Areas of the lithological mass distribution that manifest themselves in the gravitational field of the Earth;
4. Contact zones of independent flow systems;
5. Zones of attraction, such as depocenters and depressions;
6. Genetic dependency between HC systems within same flow systems;
7. Layer-by-layer overlay, as a positive superposition, of HC prospectivity the aforementioned HC-prospectivity criteria;
8. Positive superposition of HC-prospectivity areas derived via PRA at different scales.

GENERAL INFORMATION

The PRA method uses the physical and mathematical foundations of "relief plasticity". The AOI is being analyzed using topographic maps and digital elevation data at the scales of 1:500,000 and 1:200,000. The identified litho-dynamic flows form structures and systems, some of which originate from the depositions of paleo-rivers forming deltaic structures. The method also reveals areas of elevated stress in the crust that manifests via linear structures (LS), litho-dynamic circular structures (LCS), and zones of contact between litho-dynamic flow structures and their systems. The aforementioned criteria were used to evaluate the oil and gas prospectivity of EL30/2011. Their outputs' superposition allowed to identify the areas with conditions favorable for the accumulation of hydrocarbon deposits.

PRA of the litho-dynamic structures of the Earth's surface and/or the morphometric Base Levels in order to distinguish the present-day and paleo-areas of accumulation of the geological and geochemical material. These zones are manifested in the relief plasticity maps via deltaic flow structures, contact zones of multidirectional flows and their systems, deep circular and domal structures, areas of increased fracturing, and hydrocarbon generation (depocenters).

The first phase of PRA examines:

- the geographical location of the island;
- its position relative to the continent from the PRA perspective;

- commonality and/or diversity of litho-dynamic systems of the region;
- general geology of the region in connection with the location of oil and gas fields of Southern Australia and the shelf;
- location of prospective areas in Tasmania;
- the commonality or differences in the origin of hydrocarbons in Southern Australia and particularly of EL30/2011;
- paleotectonic structures, their interrelation/dependencies;
- schematic representation of the tectonically intense linear and circular structures (if any);

The second phase of PRA will consider the HC prospects of EL30/2011. The litho-dynamic maps of Tasmania and the AOI will be created using the scale of 1:500 000. The maps will show the favorable or unfavorable factors for the formation of hydrocarbon deposits.

In the third phase of PRA, EL30/2011 will be analyzed in further detail using the litho-dynamic maps with the scale 1:100,000. All of the aforementioned PRA factors will be integrated for the final prediction of the areas of HC prospectivity.

THE ISLAND OF TASMANIA

Although prior to the last ice age about 10,000 years ago, Tasmania was part of mainland Australia and the island is currently separated from the main continent by Bass Strait; Tasmania is included in the common continental shelf **Figure 41**.

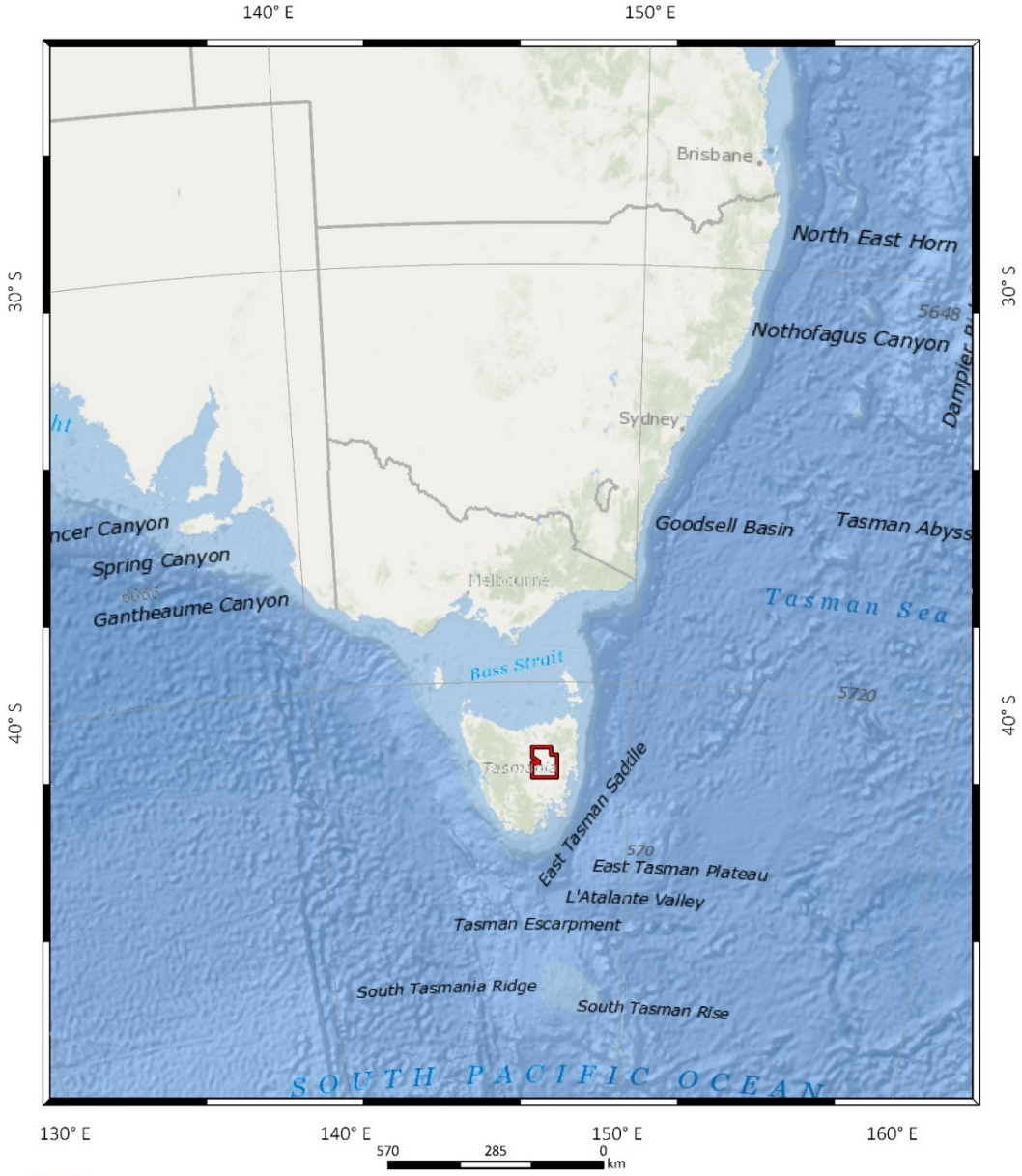


Figure 41: Position of the island of Tasmania. 1:30,000,000.

1 - Location of EL30/2011

The contiguity of the island with the mainland is confirmed using the tectonic map in **Figure 42**. The Australian continent is an ancient platform "encased" from the east by the Hercynian

geosyncline folding region (Tasmanian geosyncline or the Tasmanian zone of Paleozoic folding).

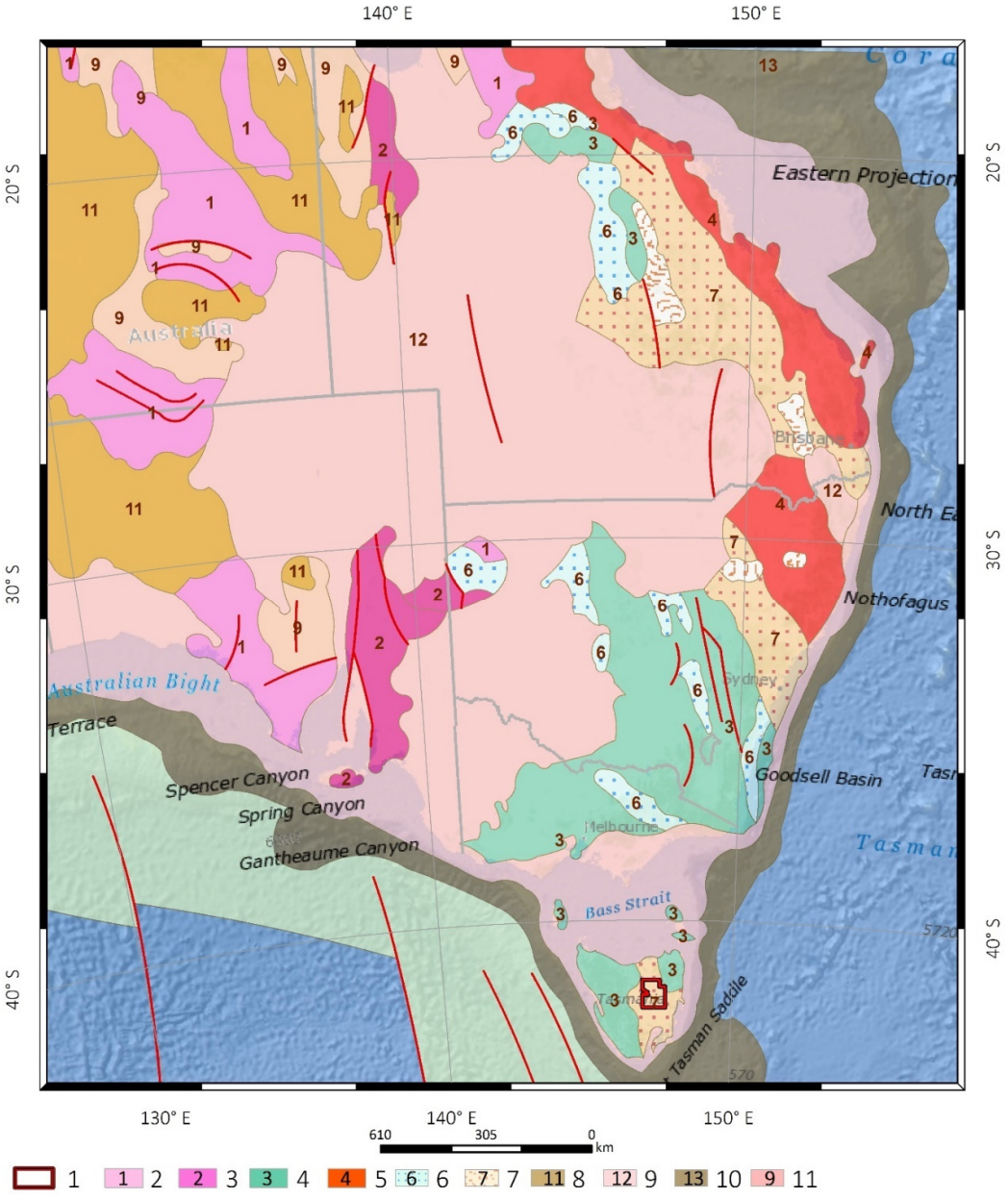


Figure 42: Tectonic map of the southeastern Australia and Tasmania. 1:25,000,000.

1 – Location of EL30/2011; 2 - outcrops of the early Precambrian crystalline basement; 3 – 5 – folding complexes: 3 – late Proterozoic - early Paleozoic; 4 – middle Paleozoic; 5 – late Paleozoic; 6 – 7 – intermountain depressions: 6 – middle Paleozoic; 7 – late Paleozoic - early Mesozoic; 8 – 9 – platform covers: 8 – Paleozoic; 9 – Mesozoic-Cenozoic; 10 – continental slope (including marginal plateau); 11 – late Proterozoic.

Most of the island consists of intrusions of Jurassic diabase into other rocks, sometimes forming extensive columnar structures (**Figure 43**). Tasmania is the world's largest area of distribution of diabase. The central plateau and the southeastern part of the island are generally composed of it. In the southern part, approximately at the level of the administrative center of Hobart, diabase passes through the layers of sandstone and other sedimentary rocks. In the southwestern part of the island, the Precambrian quartzite of the very old marine

sediments form sharp ridges and mountains. In the northeast and east, the occurrences of continental granites are similar to coastal granites of mainland Australia. The northwestern and western parts are characterized by mineral-rich volcanic rock. Limestone with karst caves can be found in the south and Northwest are also found. Zones of quartzite and dolerite in the higher mountains bear traces of glaciation, particularly in the central plateau and in the southwest of the island.

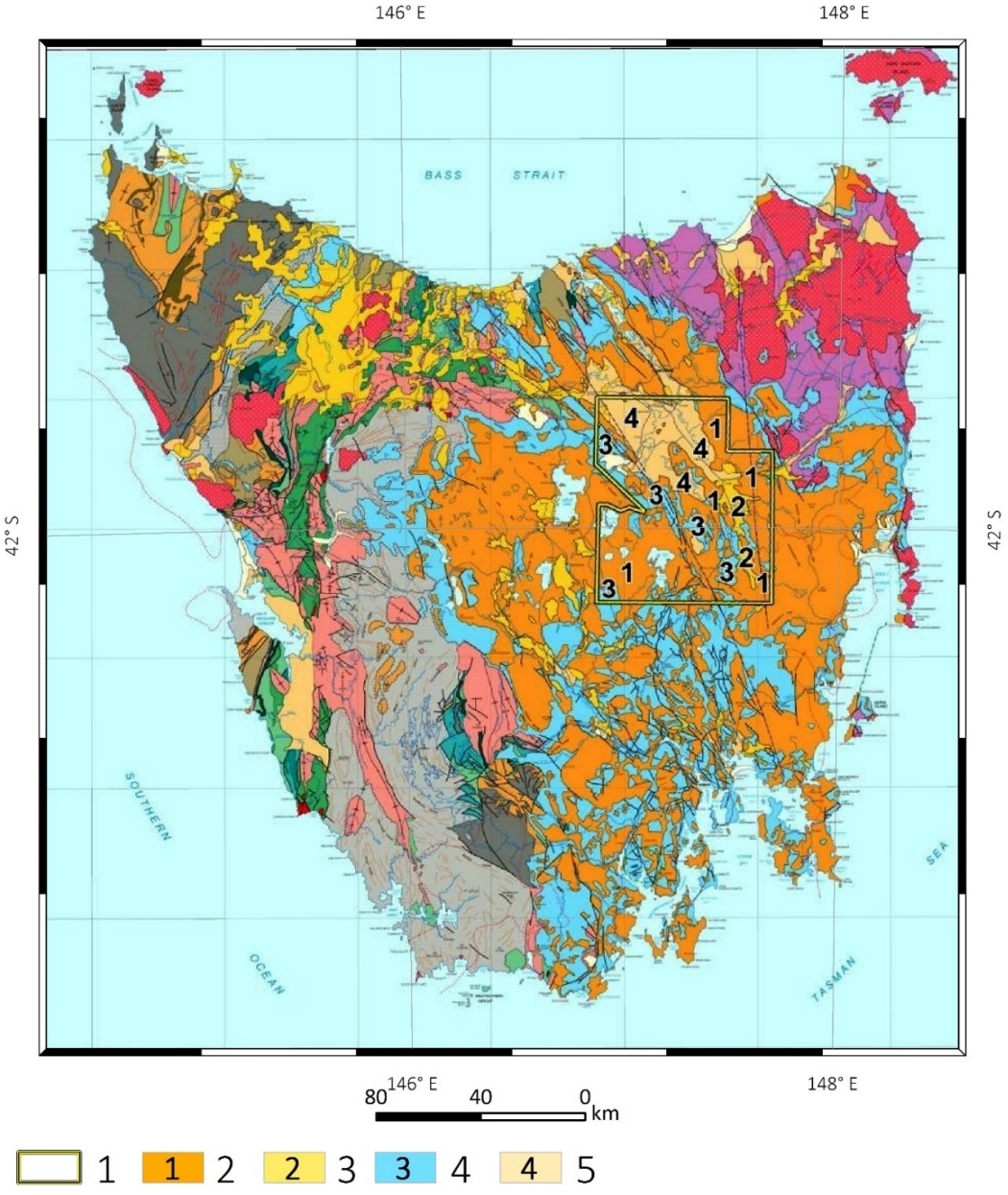


Figure 43: Geological map of Tasmania. 1:500,000.

1 – Location of EL30/2011; 2 - Jurassic dolerite intrusions; 3 – sediments of Cenozoic (tertiary) basalts; 4 – region of alternation of marine and terrigenous sediments Carboniferous-Triassic; 5 – marine, clastic, and carbonate shelf sequence of sediments of Cambrian-Devonian.

CONTINENTAL-SCALE PRA; OIL AND GAS FIELDS OF AUSTRALIA

The largest part of the commercial oil and gas reserves of Australia is concentrated in two pericontinental sedimentary basins. One of them is Gippsland located in Bass Strait with its Barracouta, Snapper, Marlin, Kingfish, and Halibut fields. Most of the resources of oil are in the Mesozoic deposits, and the resources of gas are in the Paleozoic, with 80% of the resources of hydrocarbons located in the depth interval of 1 to 3 km. The outlines of some of the deposits of southern Australia and Bass Strait are shown in **Figure 44**.

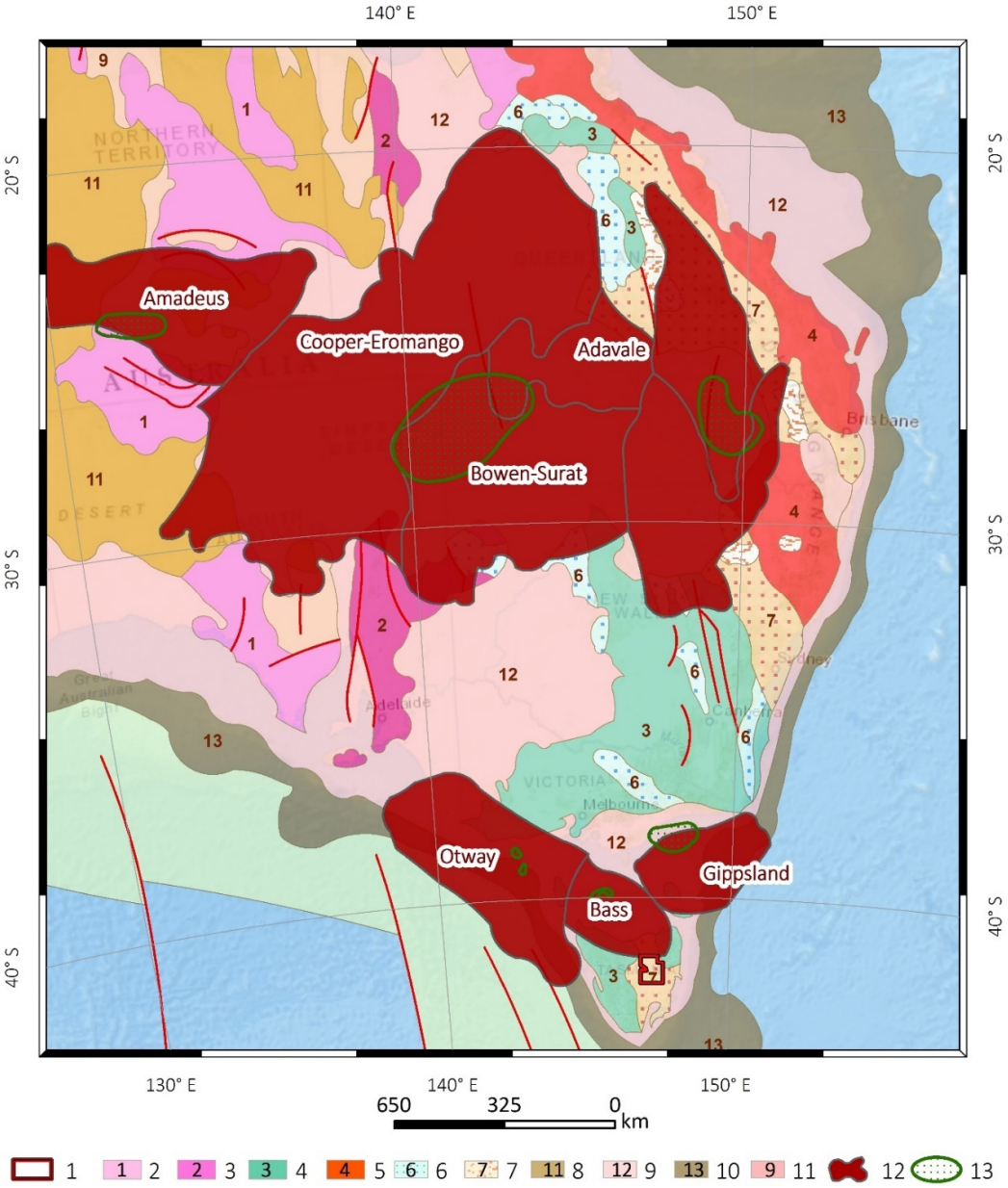


Figure 44: Select oil and gas fields on the tectonic map of southeastern Australia and Tasmania. Scale 1:25,000,000.

1 – Location of EL30/2011; 2 - outcrops of the early Precambrian crystalline basement; 3 – 5 – folding complexes: 3 – late Proterozoic-early Paleozoic; 4 – middle Paleozoic; 5 – late Paleozoic; 6 – 7 – intermountain depressions: 6 – middle Paleozoic; 7 – late Paleozoic-early Mesozoic; 8 – 9 – platform covers: 8 – Paleozoic;

9 – Mesozoic-Cenozoic; 10 – the continental slope (including marginal plateau); 11 – late Proterozoic; 12 - basins; 13 – known HC deposits.

PRA result in **Figure 45** shows the paleo-flows of the south Australian platform's basement. The identified flows-convexities are the elements of the global litho-dynamic system of the basement's skeletal structure, where varying tectonic structures of the platform cover have been forming over the period of 600 million years. The largest deflections play the role of attractors (accumulation depressions or depocenters) of the sedimentary material. One of such basins is shown as the Gippsland in Bass Strait.

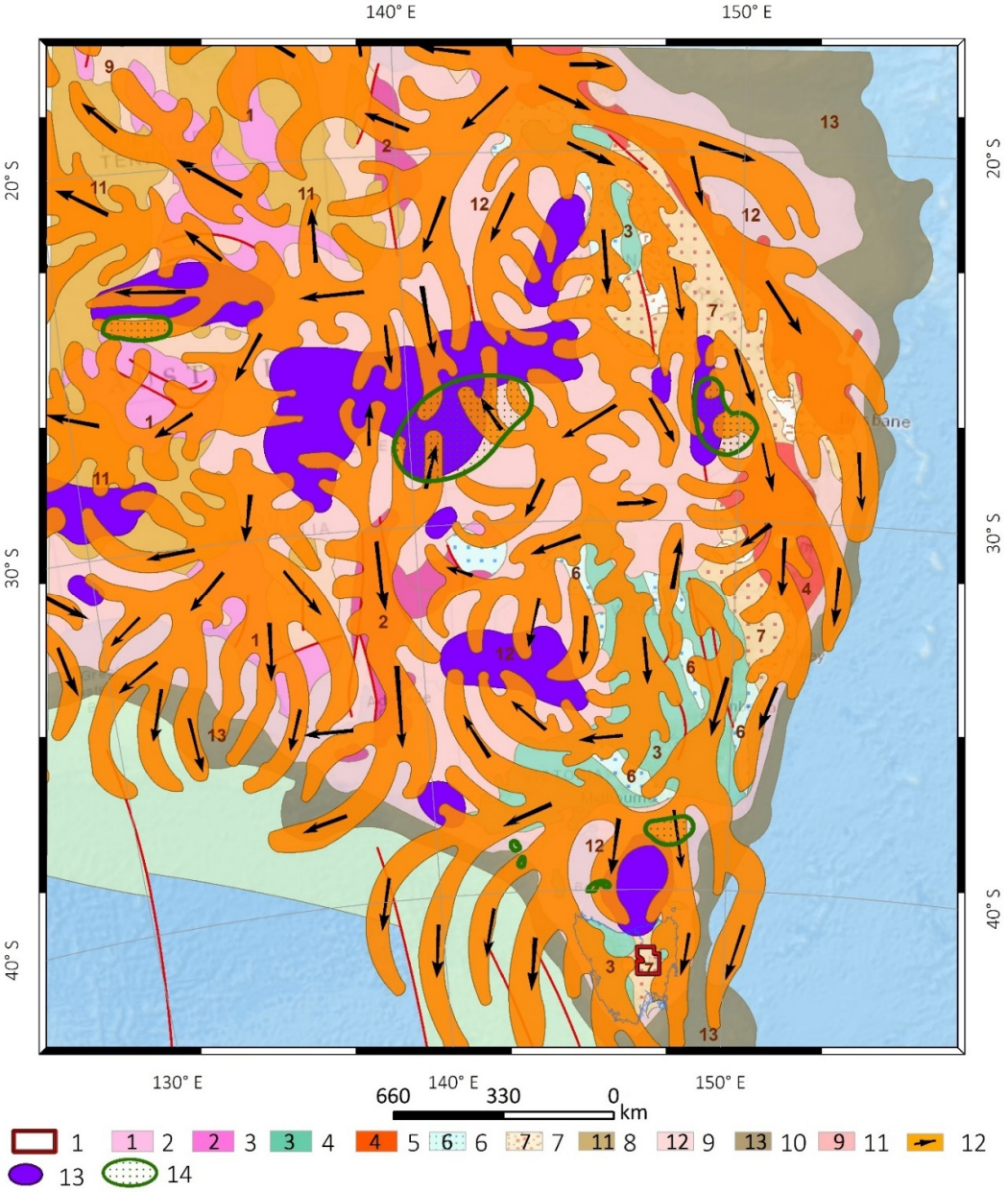


Figure 45: Litho-dynamic situation in southeastern Australia and Tasmania. 1:25,000,000.
1 – Location of EL30/2011; 2 - outcrops of the early Precambrian crystalline basement; 3 – 5 – fold complexes: 3 – late Proterozoic-early Paleozoic; 4 – middle Paleozoic; 5 – late Paleozoic; 6 – 7 – intermountain depressions: 6 – middle Paleozoic; 7 – late Paleozoic-early Mesozoic; 8 – 9 – platform covers: 8 – Paleozoic; 9 – Mesozoic-Cenozoic; 10 – continental slope (including

marginal plateau); 11 – late Proterozoic; 12 – litho-dynamic flows-convexities and vectors of their orientation in the gravity field; 13 – tectonic depression; 14 – known HC deposits.

Figure 45 shows that the litho-dynamic flows of Tasmania are a part of a single flow skeleton extended from mainland Australia. The common litho-dynamic system covers the large eastern (Great Dividing Range), central (the area of the Great Artesian Basin), and the southern (including Tasmania) territories of the continent. The litho-dynamic flow structure shown in **Figure 45** demonstrates the united genesis (a connection) of the mainland and the island.

The tectonic depressions and the locations of the relevant hydrocarbon deposits are shown in **Figure 46**. The correlation between the locations of these depocenters and the major HC deposits, including the Gippsland basin, is apparent. The flows help understand the direction of transport of material into these depressions. The main flow system between Australia and Tasmania is shown in green in **Figure 46**. Large HC fields such as Otway, Gippsland and Bass are located within the zones of its influence.

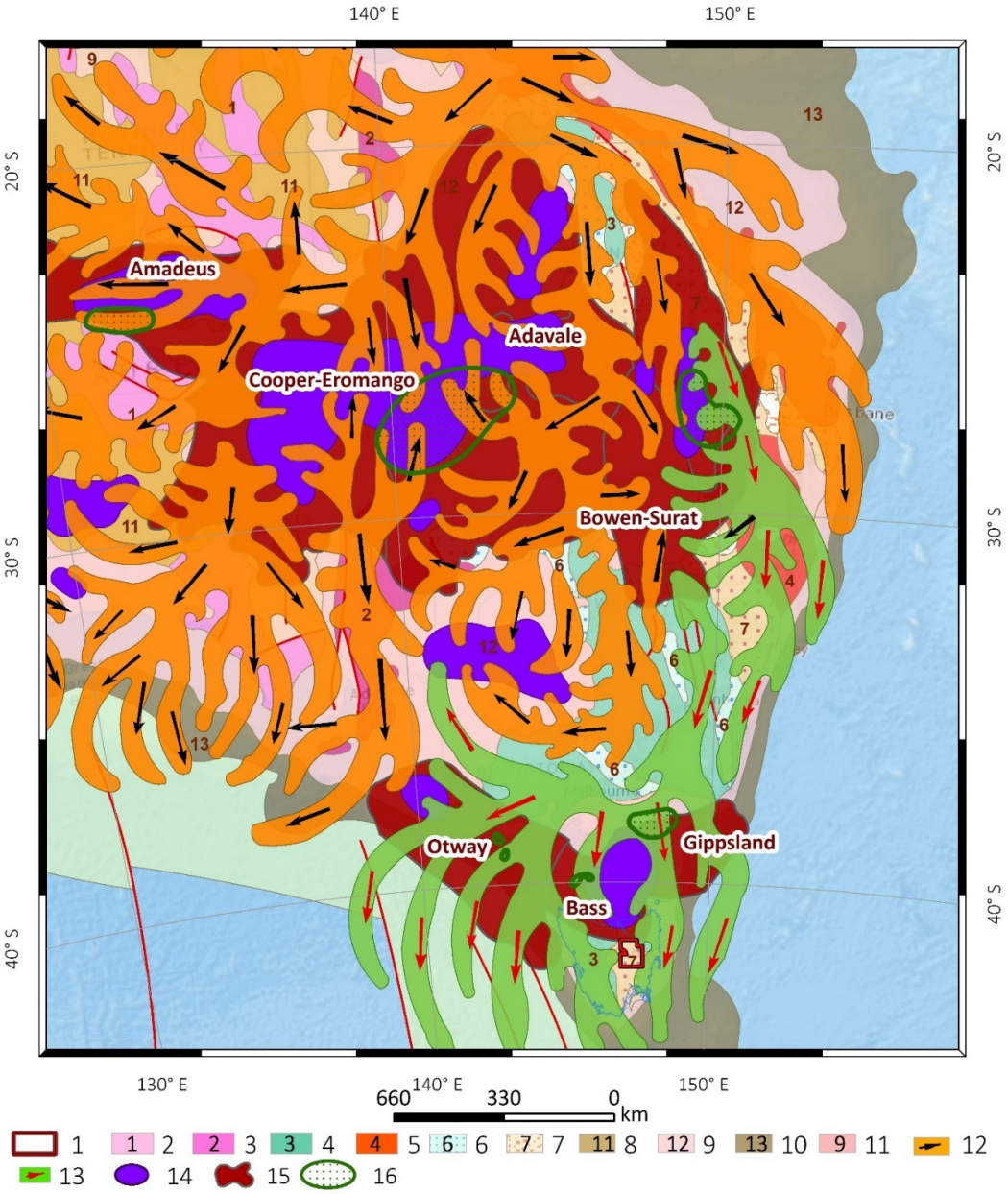


Figure 46: Major oil and gas fields of southeastern Australia on the tectonic map of southeastern Australia and Tasmania relative to the large depressions (basins). 1:25,000,000.

1 – Location of EL30/2011; 2 - outcrops of the early Precambrian crystalline basement; 3 – 5 – fold complexes: 3 – late Proterozoic-early Paleozoic; 4 – middle Paleozoic; 5 – late Paleozoic; 6 – 7 – intermountain depressions: 6 – middle Paleozoic; 7 – late Paleozoic - early Mesozoic; 8 – 9 – platform covers: 8 – Paleozoic; 9 – Mesozoic-Cenozoic; 10 – continental slope (including marginal plateau); 11 – late Proterozoic; 12 – litho-dynamic flows increase and the vector of their orientation in the field of gravity; 13 - main flow system connecting Australia and Tasmania; 14 – tectonic depression according to litho-dynamic territory; 15 – basins; 16 – known HC deposits.

In order to assess the oil and gas prospectivity of EL30/2011 from the regional perspective shown in **Figure 45**, linear and circular structures have been identified. The linear structures shown in **Figure 47** can be divided into three categories: 1) linear structures-convexities (highs); 2) linear concavities as extended depressions (lows); 3) combined linear structures

identified along the general direction of highs and lows. Nodes forming at the intersections of such linear structures are characterized as areas of increased stress in the earth's crust.

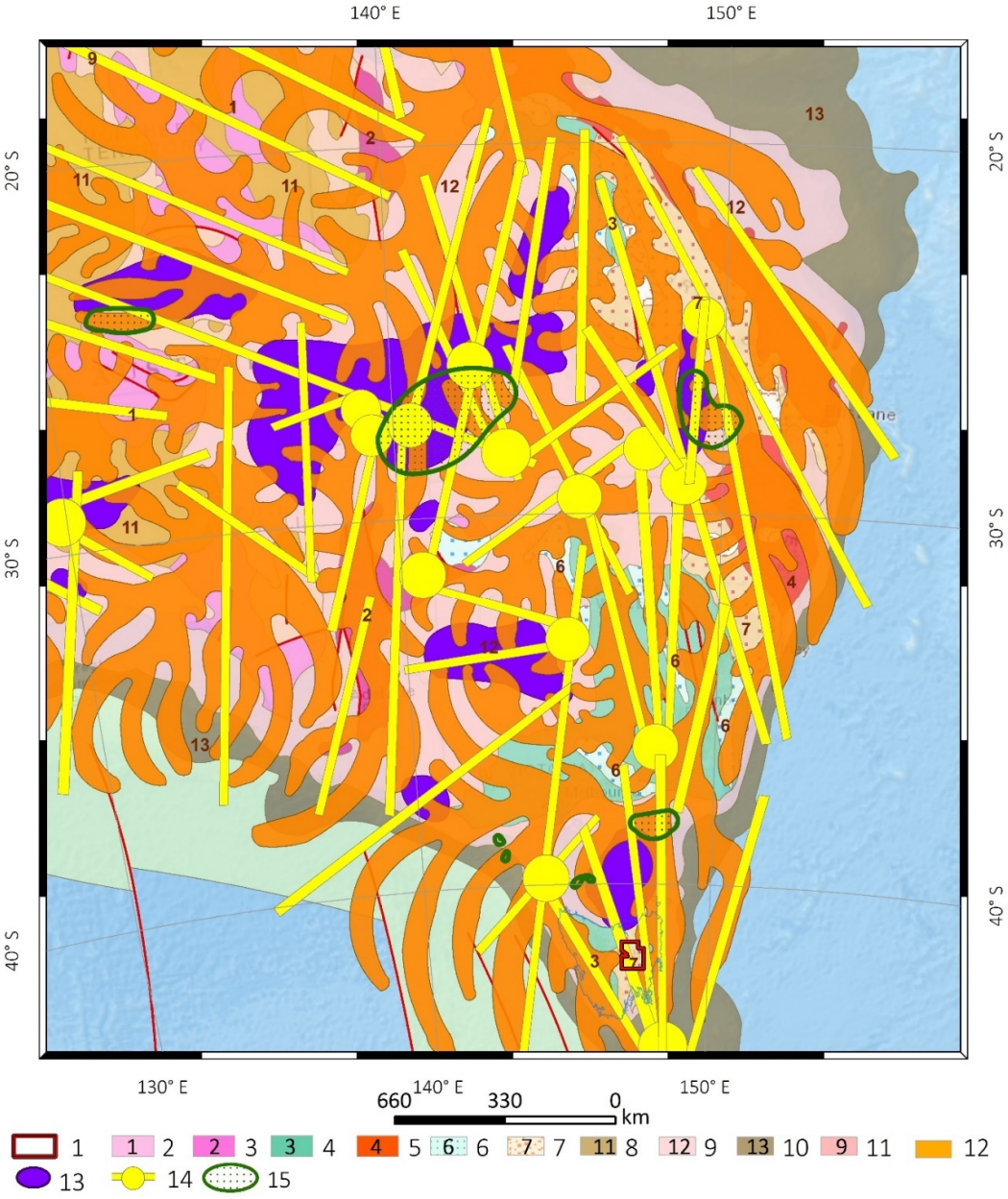


Figure 47. Linear structures of the southeastern Australia and Tasmania. 1:25, 000,000.

1 – Location of EL30/2011; 2 - outcrops of the early Precambrian crystalline basement; 3 – 5 – folding complexes: 3 – late Proterozoic-early Paleozoic; 4 – middle Paleozoic; 5 – late Paleozoic; 6 – 7 – intermountain depressions: 6 – middle Paleozoic; 7 – late Paleozoic-early Mesozoic; 8 – 9 – platform covers: 8 – Paleozoic; 9 – Mesozoic-Cenozoic; 10 – continental slope (including marginal plateau); 11 – late Proterozoic; 12 – litho-dynamic flows increase and the vector of their orientation in the field of gravity; 13 – tectonic depression according to lithodynamic territory; 14 – anomalous linear structures and their components; 15 - known HC deposits.

Circular structures detected using PRA are shown in **Figure 48**. These areas are typically clearly identifiable as the areas of curving of litho-dynamic flows around a certain center.

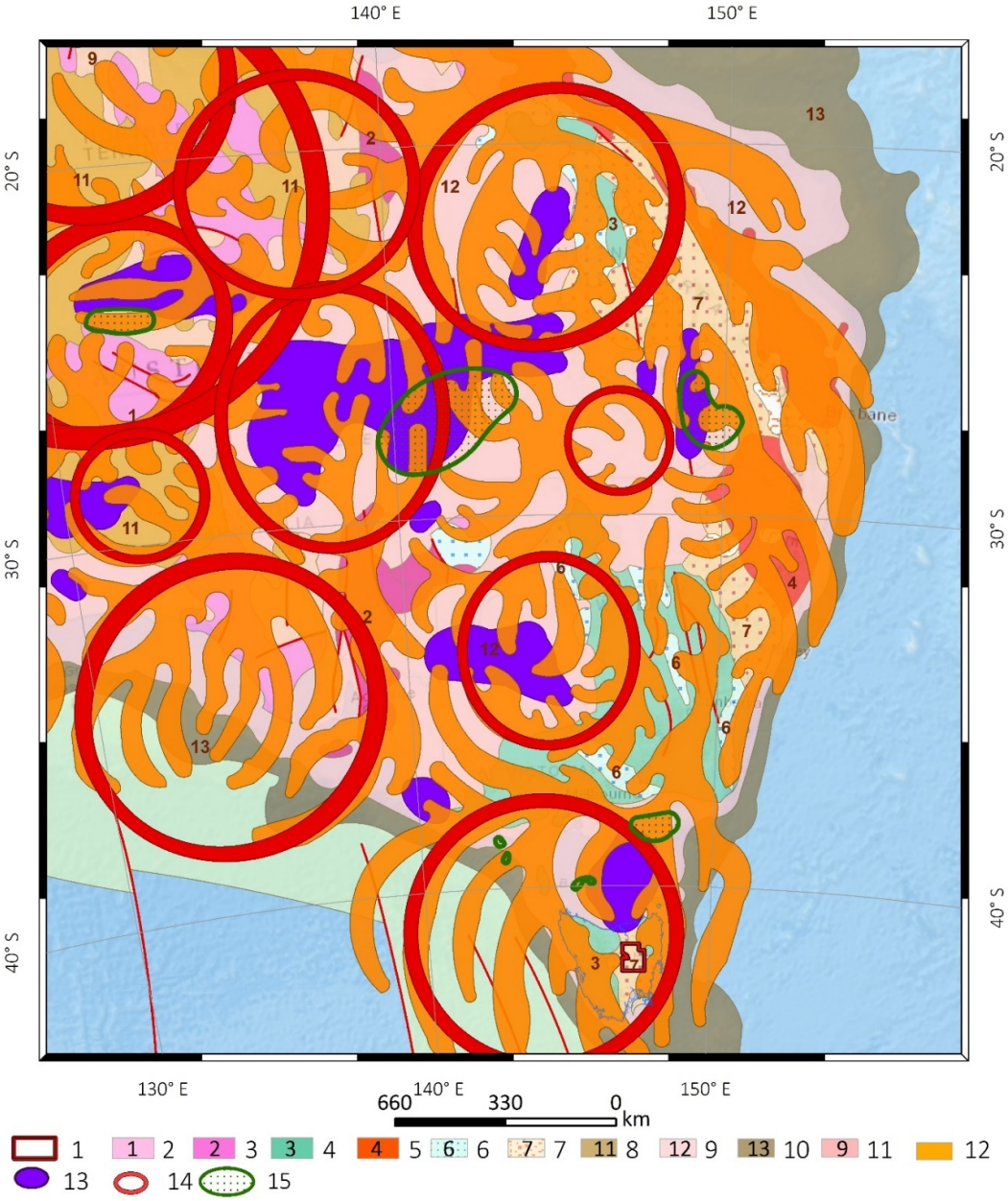


Figure 48: Circular structures based on the map of litho-dynamic flows of southeastern Australia and Tasmania. 1:25,000.000.

1 – Location of EL30/2011; 2 - outcrops of the early Precambrian crystalline basement; 3 – 5 – fold complexes: 3 – late Proterozoic-early Paleozoic; 4 – middle Paleozoic; 5 – late Paleozoic; 6 – 7 – intermountain depressions: 6 – middle Paleozoic; 7 – late Paleozoic-early Mesozoic; 8 – 9 – platform covers: 8 – Paleozoic; 9 – Mesozoic-Cenozoic; 10 – continental slope (including marginal plateau); 11 - late Proterozoic; 12 – litho-dynamic flows increase and the vector of their orientation in the field of gravity; 13 – tectonic depression according to lithodynamic territory; 14 – circle-shaped abnormal structures; 15 – known HC deposits.

Tectonic and impact forces may have caused the formation of linear and circular structures could, in turn causing great stress in the Earth's layers. The circular-shaped structures are expected to have the highest porosity around the peripheral areas of the circles. **Figure 49** shows the combined map of circular and linear structures.

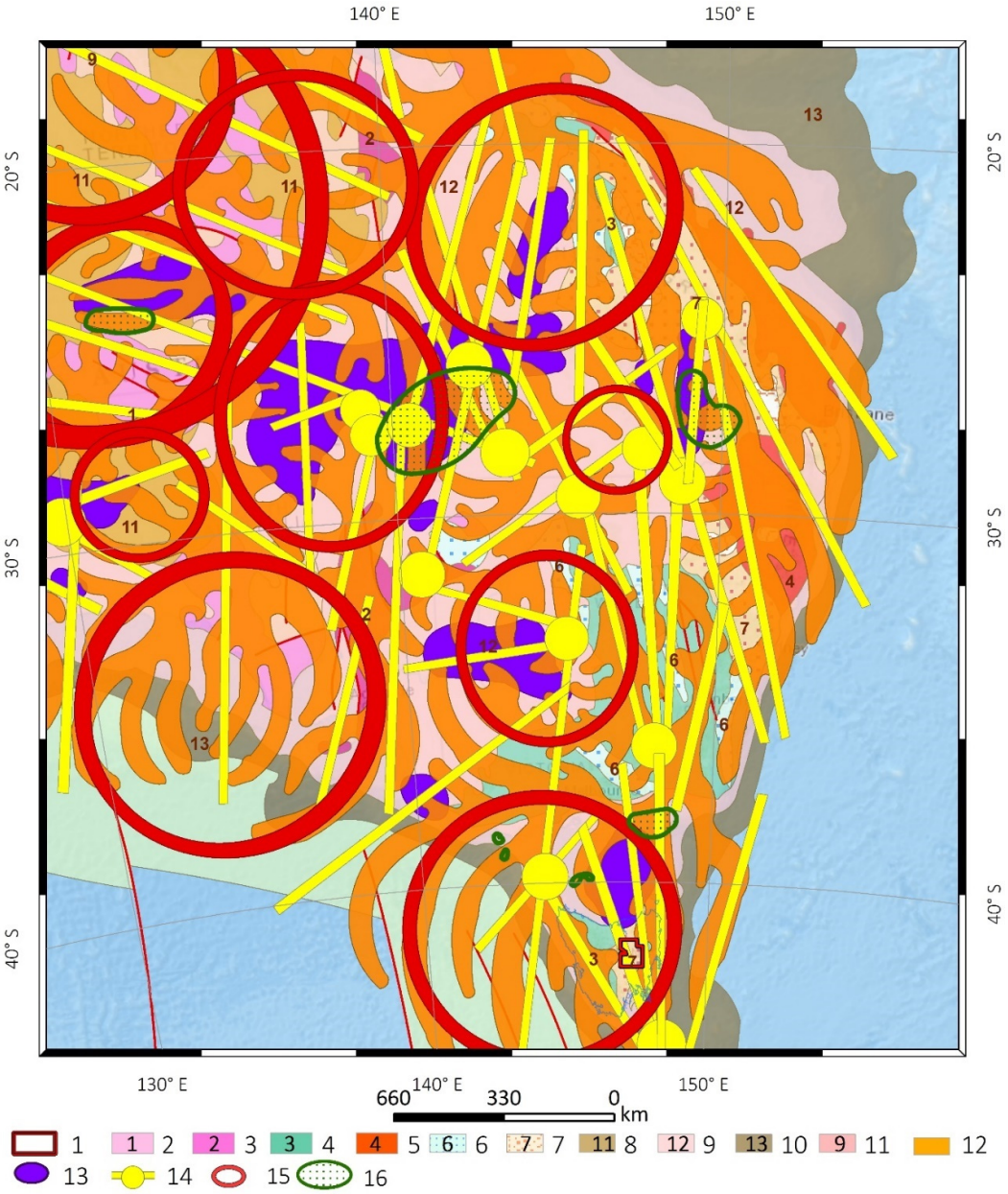


Figure 49: Linear and circular structures of southeastern Australia and Tasmania. 1:25,000,000.
1 – Location of EL30/2011; 2 - outcrops of the early Precambrian crystalline basement; 3 – 5 – fold complexes: 3 – late Proterozoic-early Paleozoic; 4 – mid Paleozoic; 5 – late Paleozoic; 6 – 7 – intermountain depressions: 6 – mid Paleozoic; 7 – late Paleozoic-early Mesozoic; 8 – 9 – platform covers: 8 – Paleozoic; 9 – Mesozoic-Cenozoic; 10 – continental slope (including marginal plateau); 11 - late Proterozoic; 12 – lithodynamic flows increase and the vector of their orientation in the field of gravity; 13 – tectonic depression according to litho-dynamic territory; 14 – linear anomalous structures and their components; 15 – anomalous circular-shaped structure; 15 – known HC deposits.

Two linear NS-orientation structures are also complicated by the large circular structure near the AOI. PRA considers the area of intersection of linear and circular structures to have the greatest HC potential (**Figure 50**).

According to the long-term experience of using the paleo-structural analysis of lithodynamics of the earth's crust layers, it was established that the areas of intersection of linear and annular

structures have the greatest prospects of formation of oil and gas reservoirs and reservoirs - **Figure 50**.

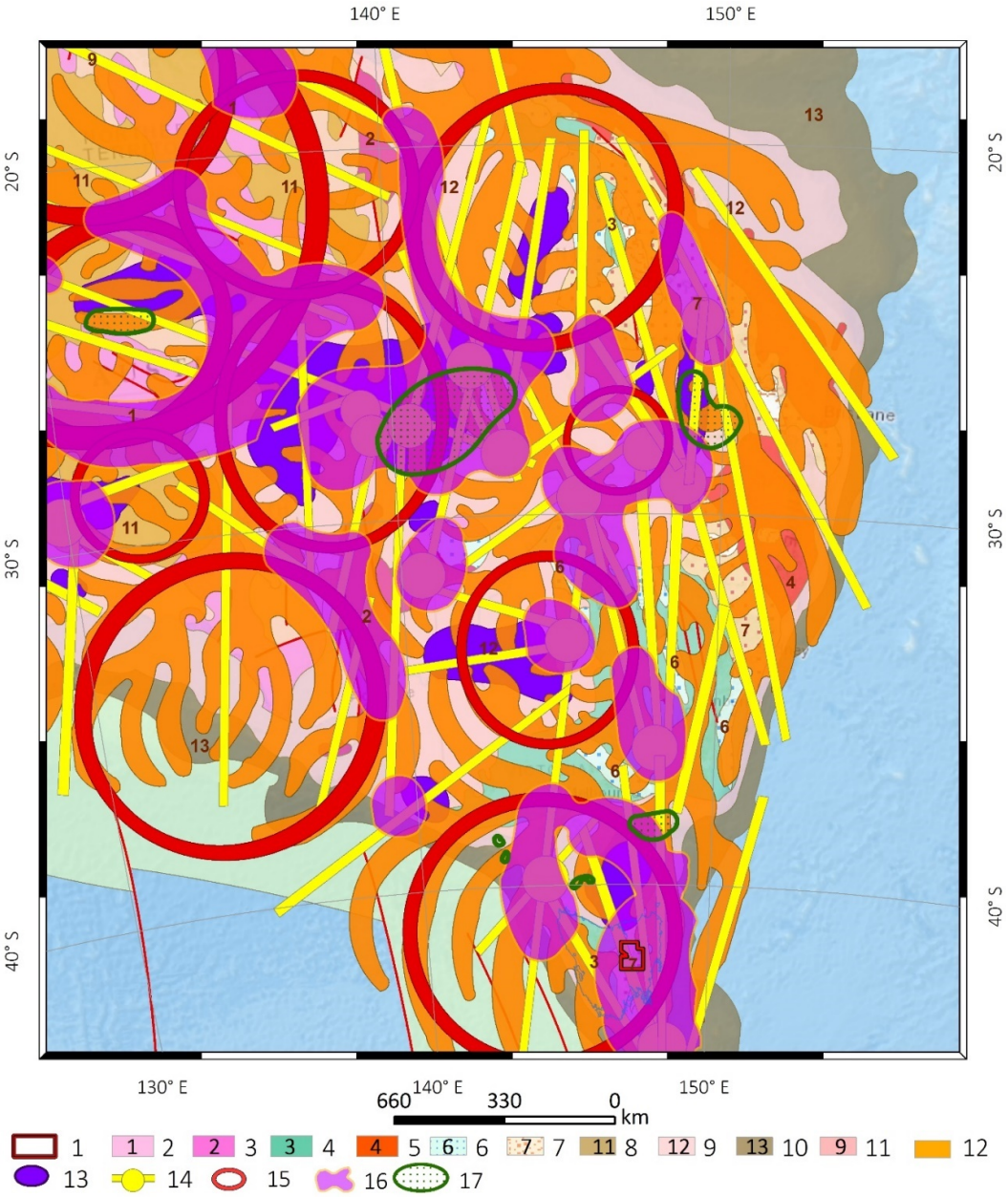


Figure 50: Zones of HC prospectivity, linear and circular structures of the southeastern Australia and Tasmania. 1:25,000,000.

1 – location of EL30/2011; 2 - early Precambrian crystalline basement; 3 – 5 – folding complexes: 3 – late Proterozoic-early Paleozoic; 4 – middle Paleozoic; 5 – late Paleozoic; 6 – 7 – intermountain depressions: 6 – middle Paleozoic; 7 – late Paleozoic-early Mesozoic; 8 – 9 – platform covers: 8 – Paleozoic; 9 – Mesozoic-Cenozoic; 10 – the continental slope (including marginal plateau); 11 - late Proterozoic; 12 – lithodynamic flows increase and the vector of their orientation in the field of gravity; 13 – tectonic depression according to lithodynamic territory; 14 – linear structure and its components; 15 –circular structure; 16 –area of hydrocarbon potential; 17 – known HC deposits.

According to the regional PRA, Tasmania is prospective for HCs, and the areas of the highest potential are in the northeastern and the western (including EL30/2011) parts of the island, as see in **Figure 51**.

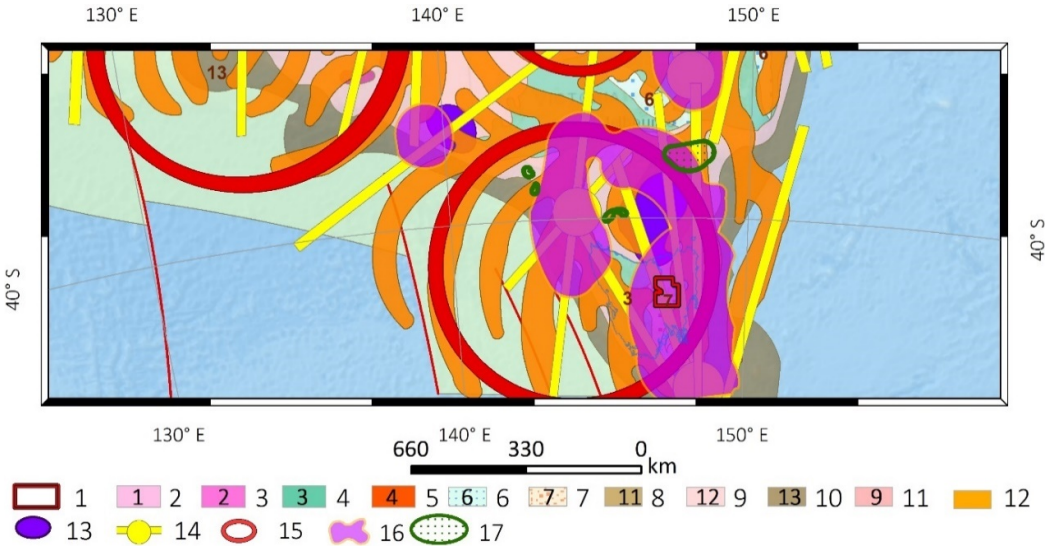


Figure 51: Zones of HC prospectivity, linear and circular structures of the southern Australia and Tasmania. 1:25,000,000.

1 – location of EL30/2011; 2 - early Precambrian crystalline basement; 3 – 5 – fold complexes: 3 – late Proterozoic-early Paleozoic; 4 – middle Paleozoic; 5 – late Paleozoic; 6 – 7 – intermountain depressions: 6 – middle Paleozoic; 7 – late Paleozoic-early Mesozoic; 8 – 9 – platform covers: 8 – Paleozoic; 9 – Mesozoic-Cenozoic; 10 – the continental slope (including marginal plateau); 11 - late Proterozoic; 12 – litho-dynamic flows increase and the vector of their orientation in the field of gravity; 13 – tectonic depression according to litho-dynamic territory; 14 – linear structure and its components; 15 –circular structure; 16 – predicted areas of the highest hydrocarbon potential; 17 – known HC deposits.

IDENTIFICATION AND ANALYSIS OF FLOW STRUCTURES OF EL30/2011 AT 1:500,000. REGIONAL ANALYSIS.

PRA of the AOI and its adjacent areas conducted at 1:500,000 (**Figure 52**) provides a general idea of the litho-dynamic situation of EL30/2011.

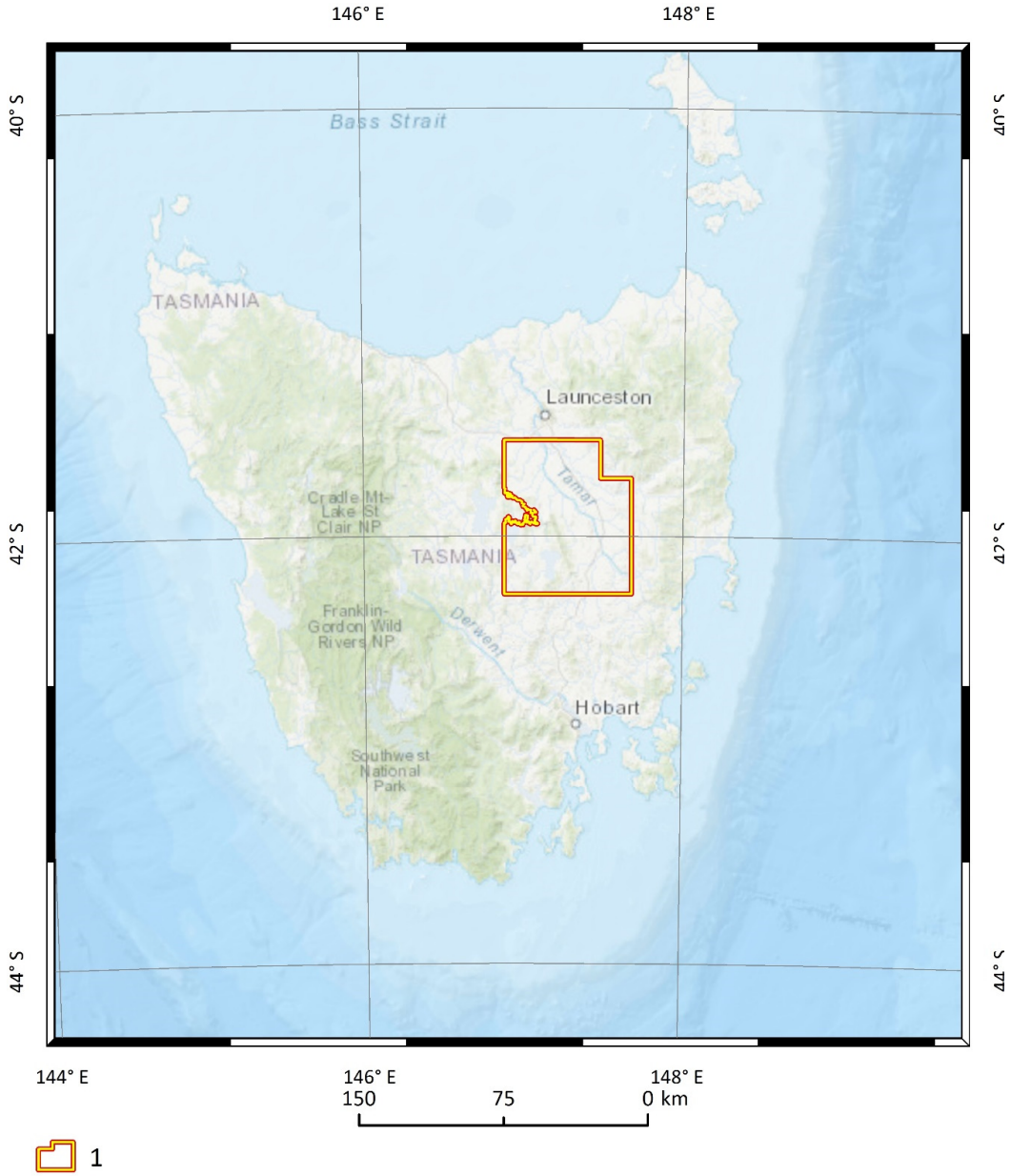


Figure 52. Topographic map of Tasmania. Scale 1:500000.

1 – Location of EL30/2011.

PALEO-RECONSTRUCTION

The objective is to transform the horizontals/isolines of the topographic map into a flows format to differentiate the area of EL30/2011 into positive (convexities) and negative (concavities) litho-dynamic flows and interpret their behavior.

A topographic, like a structural or a geological map, is a mathematical model of the surface relief with the elements of the modern drainage network. But the terrain on these maps is not static and cannot be differentiated. PRA is used to extract the dynamic information component from the topo/isobase maps and clearly separate each convexity and concavity, the method of PRA or relief plasticity. The relief is then presented in a form of extended

elements of convexities and concavities, although these flows are mostly not separated. They are interrelated, as each flow develops between its origin and end points. Elevation changes cause the body of each flow to take a certain share during the course of geological history, as the geological matter transports under the forces of gravity down the slope and affected by erosion processes causing the flows to bifurcate into smaller flows-appendages or thicken due to diluvial accumulations. PRA's objective includes the visualization of these flows. **Figure 53** shows a clear continuity of these flows from highlands to lowlands. At this scale, the flows are more differentiated and have a complex pattern due to the activity of exogenous processes.

Thus, PRA not only identifies the locations of the actual flows, but also helps represent the geological environment in its dynamic form allowing to characterize geological certain processes.

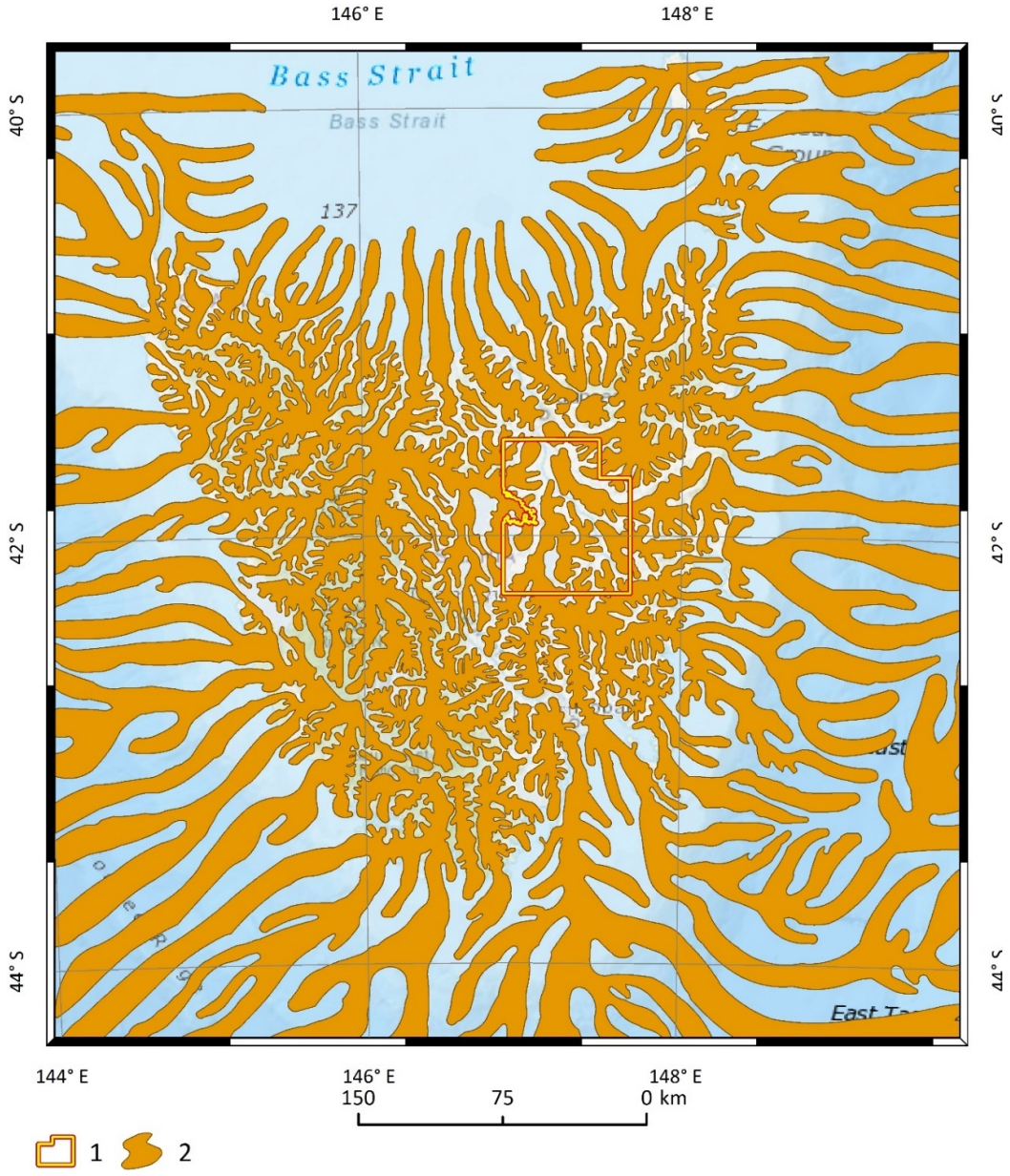


Figure 53. Relieve plasticity map of Tasmania. 1:500,000.

1 - location of EL30/2011; 2 - litho-dynamic flows.

LITHO-DYNAMIC FLOW STRUCTURES AND ZONES OF THEIR CONTACT

The objective of this action is to simplify/generalize the flows and their systems depicted to identify the litho-dynamic framework (structure of the flows) and determine the boundaries of these flow systems.

The combination of several flows that originate from a single source (an elevated point within the relief) is a complex body with distinguishable borders. Such a formation is called “litho-dynamic structure”. A combination of separate litho-dynamic structures similarly directed over hundreds or even thousands of miles is called “flow system”.

Visualization of flows-convexities allows to establish that the island of Tasmania is the area of contact between two litho-dynamic subsystems, conventionally called Western and Eastern as seen in **Figure 54**; they were identified earlier using the continental-scale PRA (**Figure 45**). These subsystems are parts of a larger East Australian litho-dynamic system, which in turn is a part of the Great Dividing Range. They source on the Australian mainland, bifurcate in the South of the Australian continent and eventually form the landmass of modern Tasmania. During the subsequent geological time, the Bass deflection formed within this system. Two major systems of the AOI (Eastern and Western) border each other. The largest part of EL30/2011 covers the Eastern subsystem (Eastern and Central part of the EL30/2011); the small part in the west of EL30/2011 covers the Western subsystem. The contact zone of the Western and Eastern subsystems extends across the entire EL30/2011 from North to South, occupying most of the Western sector of EL30/2011. Due to stress associated with the zones of contact, such areas are expected to have increased porosity in the rocks. In summary: from the PRA perspective, a deep and fundamental genetic connection between the hydrocarbon deposits of southern Australia and Bass Strait is entirely possible.

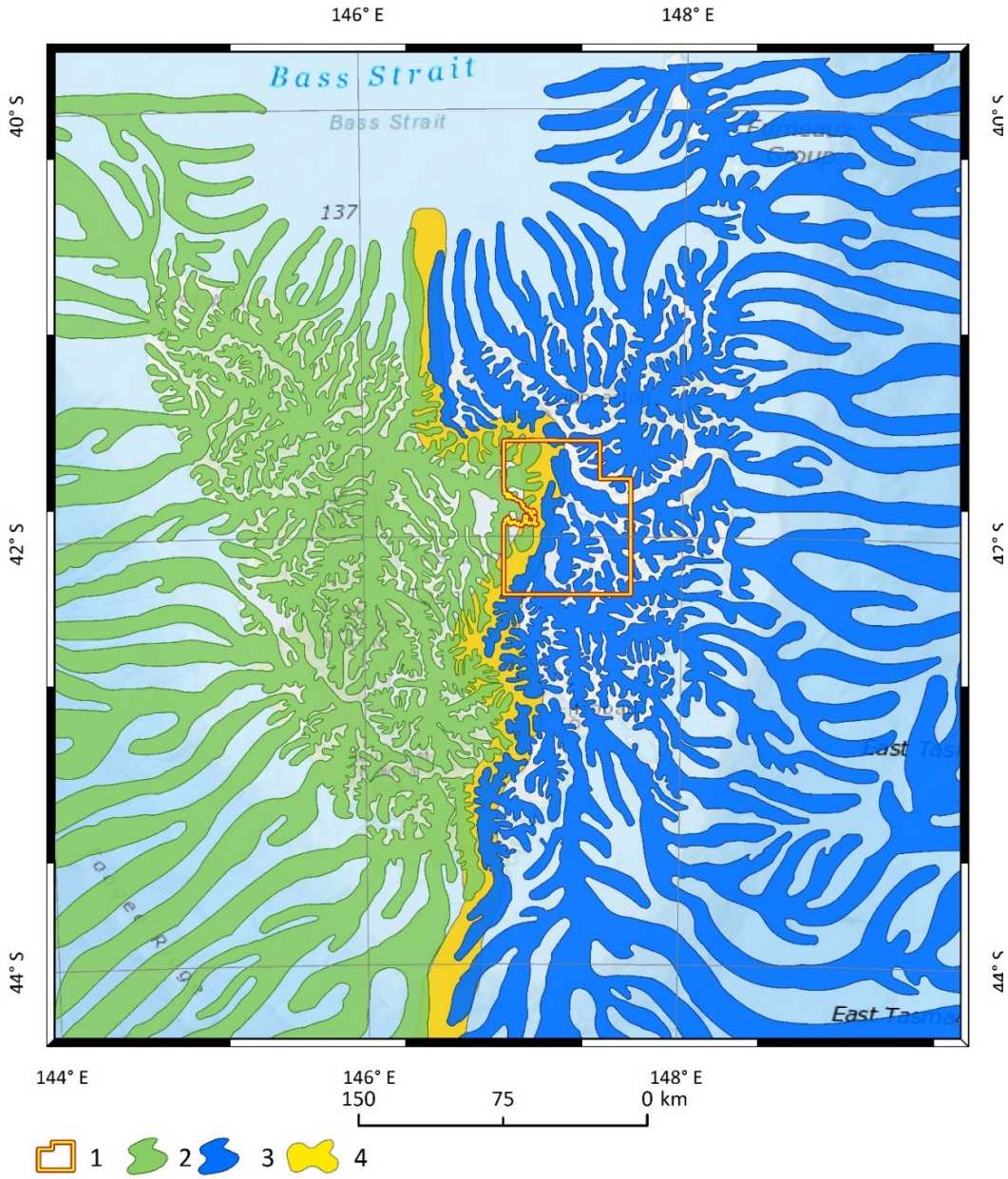


Figure 54: Litho-dynamic systems of Tasmania. 1:500,000.
1 – location of EL30/2011; 2 - flows of Western litho-dynamic subsystem; 3 –flows of Eastern litho-dynamic subsystem; 4 – contact zone of Western and Eastern litho-dynamic subsystems.

PALEO-DELTAIC STRUCTURES AND LARGE CLOSED DEPRESSIONS

The objective of this action is the delineation of paleo-deltas as areas associated with favorable reservoir qualities.

Given that the territory of Tasmania had larger water flows during its geological past, its current relief carries the inherited imprints of paleo-rivers and paleo-deltas. These forms are of geological and HC-exploration interest due to their lithological sand and clay makeup. Sandy sediments are often excellent HC accumulation reservoirs. HC prospectivity of deltaic

sediments were confirmed in the Caspian Sea, the Gulf of Mexico, Western Siberia, several areas in central US, etc., to mention a few examples. The cartographic analysis of deltaic litho-dynamic structures reveals a certain leaf-like or a fan shape. Four paleo-deltas were identified on the island of Tasmania, as seen in **Figure 55**.

The paleo-delta No. 1 is of interest from the PRA perspective. It is located in the center of the island and within the Western litho-dynamic subsystem. Its eastern part borders with EL30/2011. The mouth parts of the Delta are in contact with the Eastern litho-dynamic subsystem. Such an abnormal location of a paleo-delta is because it was formed by a major river system during the geological era, when the shoreline passed through the center of the island. The area of this paleo-delta has high HC potential.

Paleo-delta No. 2 is located on the eastern coast of Tasmania and has an almost identical orientation compared to delta No. 1. This structure may have been formed within the same river system as delta No. 1 during its expansion at a later time.

All four paleo-deltaic structures are presumed to be of a common genesis forming from a large paleo-river system originating in Australia. Over geological time, the positions of the deltas changed as the land uplifted and the sea level lowered.

Lithodynamic flows of most paleo-deltas are oriented toward large depressions that often serve as areas of accumulation of geological or organic material. Three are three such concavities within the island and around it. One of them is the Bass depression, and the second one is located to the East of the island. The third potential depocenter is located in the center of the island at the zone of convergence of two litho-dynamic subsystems. Two more potential depressions may be delineated in the south of Tasmania, although they are less relevant to this study.

A potential depocenter is located to the southwest of EL30/2011. Its potential is high, as the lithological and organic matter fed by a large delta No. 1 had transported into it for a long time.

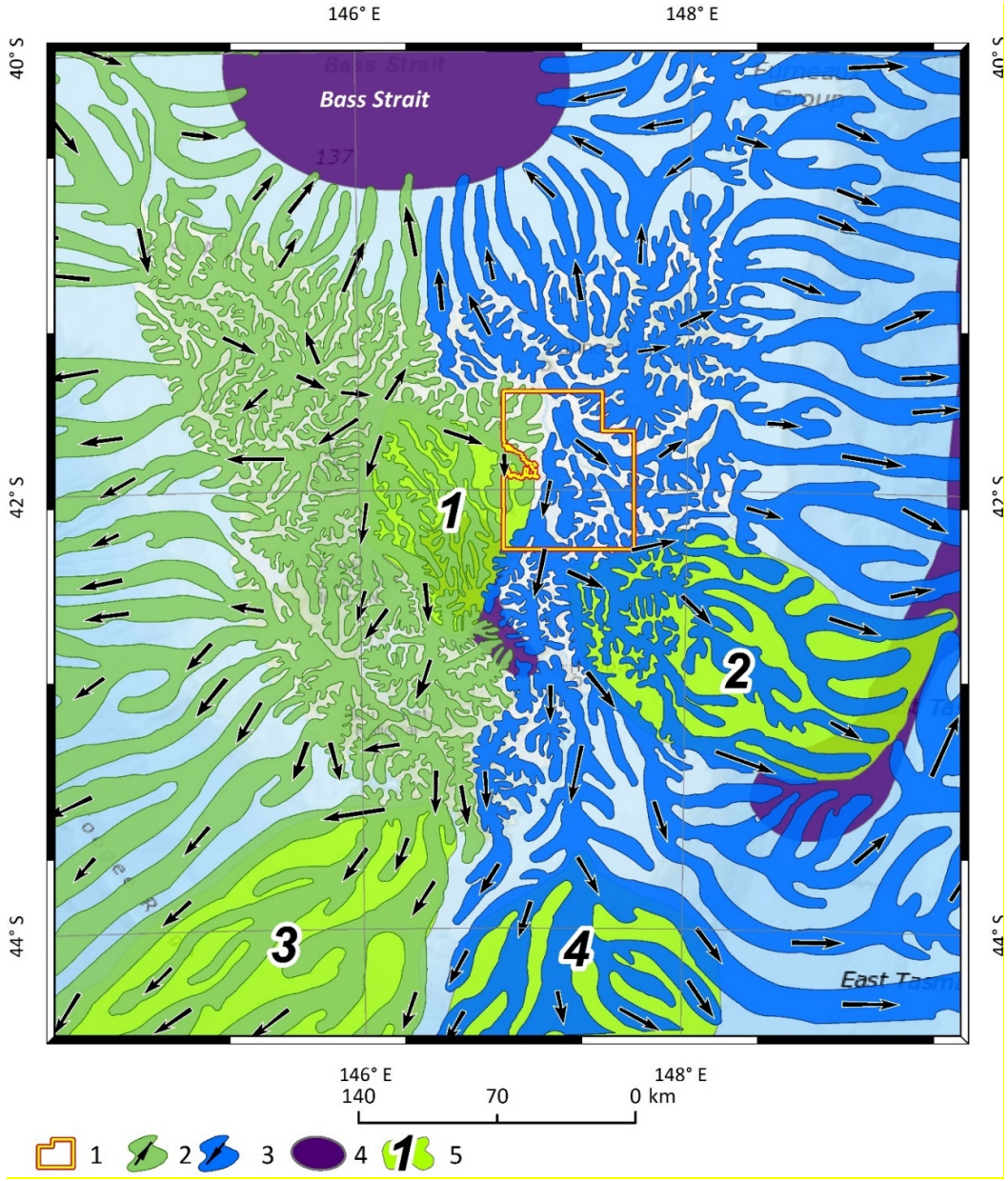


Figure 55: Paleo-deltaic structures and depressions. 1:500,000.
1 – location of EL30/2011; 2 - flows of Western litho-dynamic subsystems and the vector of their orientation; 3 – litho-dynamic flows of the Eastern subsystem, and the vector of their orientation; 4 - depression; 5 – paleo-delta.

CIRCULAR LITHO-DYNAMIC STRUCTURES AND LINEAR ZONES OF THE CRUST

The objective of this action is to identify circular and linear structures as areas of tectonic stress and increased fracturing.

All these formations are the result of tectonic activity at different times of the island's development. Now, it is a relatively stable area; however, traces of former activity (tectonic and even, perhaps, volcanoes manifesting as circular structures) are preserved in the forms of litho-dynamic structures (**Figure 56**). PRA allows identifying these structures and determining their location with high probability.

Three circular structures are identified within EL30/2011 – structures 1, 3, and 4. Circular structure 2 is located in close proximity to the block, but plays a minor role in improving the HC prospectivity of AOI.

Located in the northeastern part of AOI, Circular structure No. 1 (CS # 1) is one of the most important geological formations of the island. It had a great impact on the formation of hydrocarbon deposits of the EL30/2011. CS #4 almost contacts CS #1, favorably affecting the capacity of the AOI.

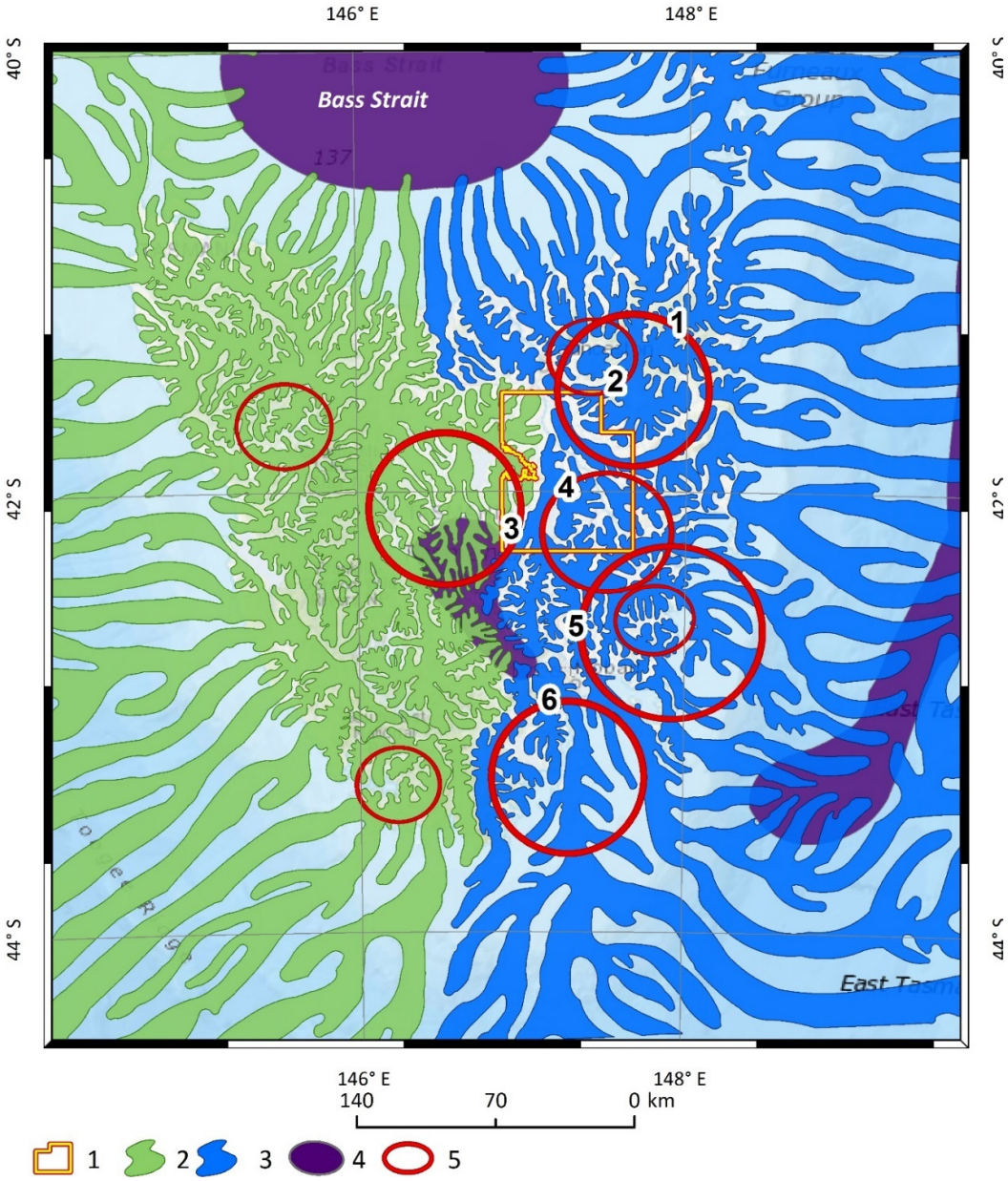


Figure 56: Litho-dynamic circular structures of Tasmania. 1:500, 000.
1 – location of EL30/2011; 2 - flows of Western litho-dynamic subsystem; 3 –flows of East litho-dynamic subsystem; 4 - depressions; 5 – circular structures and their numbers.

The detailed location of the circular structures within EL30/2011 is shown in **Figure 57**.

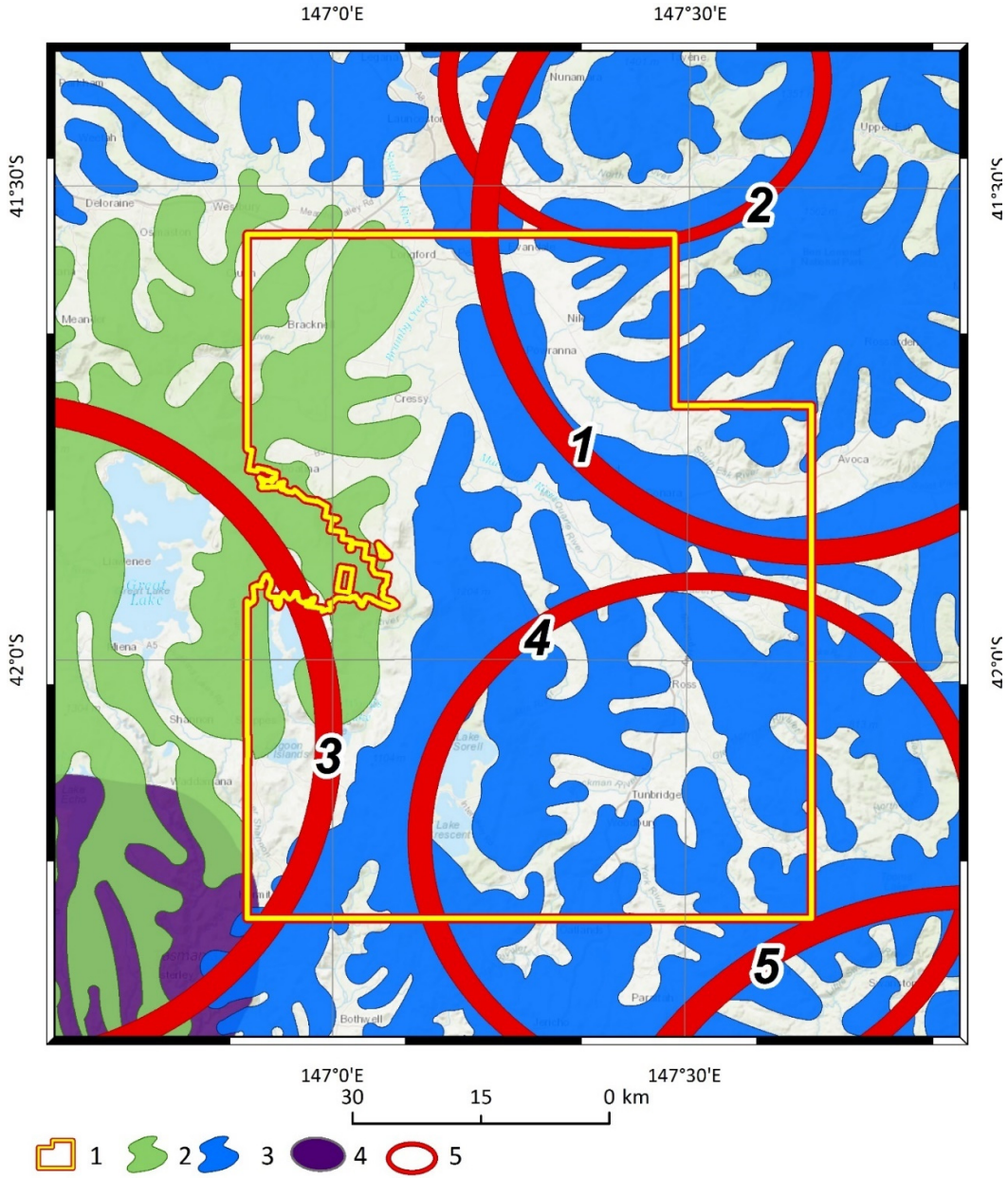


Figure 57: Litho-dynamic circular structures of EL30/2011. Scale 1:500, 000.
1 – location of EL30/2011; 2 - flows of Western litho-dynamic subsystem; 3 –flows of East litho-dynamic subsystem; 4 - depressions; 5 – circular structures and their numbers.

The linear features are of note as well – **Figure 58**.

1. Linear, elongated, and extended in length shape of lithodynamic flows-convexities and depressions between them. This behavior is especially characteristic of contact zones of adjacent flow structures.
2. Areas of anomalous change of direction of lithodynamic flows.
3. Linear zones of steep slopes (benches).
4. Combination of the first three criteria, such as, for instance, an extended linear flow-convexity continues in a nearby flow structure and changes its orientation within the zones of their contact.

Nodes of intersections of three or more linear structures and other areas of intersection of linear and circular structures (especially within areas of contact of several circular structures) are of note from the PRA perspective.

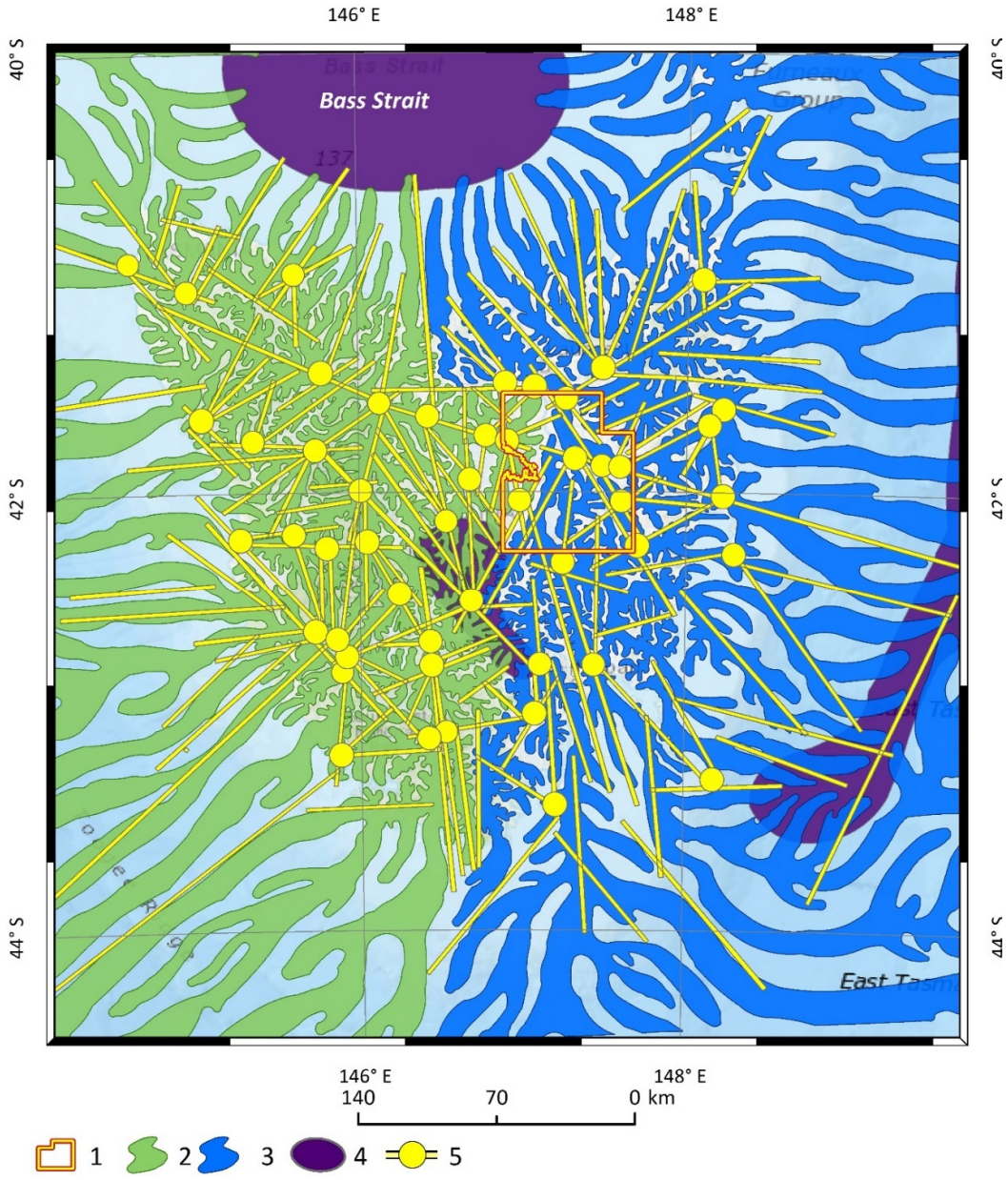


Figure 58: Linear zones of tension of the earth's crust within Tasmania. Scale 1:500, 000.
1 – location of EL30/2011; 2 - flows of Western litho-dynamic subsystem; 3 – flows of East litho-dynamic subsystem; 4 - depressions; 5 – linear structure of tension and nodes of their intersection.

A detailed map of the linear zones of stress within EL30/2011 is presented in **Figure 59**.

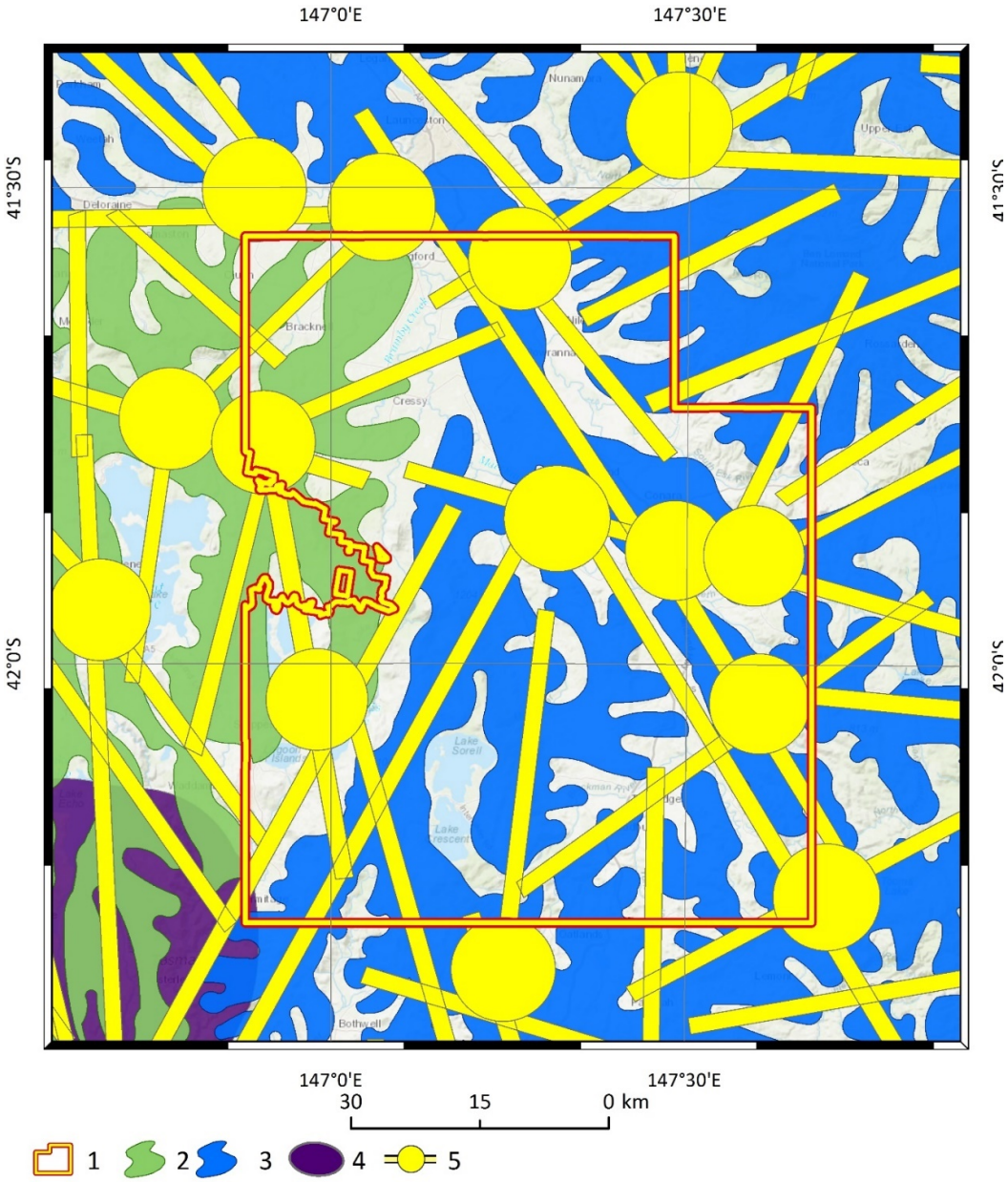


Figure 59: Linear zones of tension of the earth's crust within Tasmania. Scale 1:500, 000.
1 – location of EL30/2011; 2 - flows of Western litho-dynamic subsystem; 3 – flows of East litho-dynamic subsystem; 4 - depressions; 5 – linear structure of tension and nodes of their intersection.

RESULT – ZONES OF PROSPECTIVITY

The objective of this action is to integrate the previously identified criteria and delineate areas of oil and gas prospectivity at the given scale.

The results of all identified HC prospectivity criteria (contact zones, paleo-deltas, LCS, LS and the nodes of intersection of LS) were integrated as shown in resulting map – **Figure 60**.

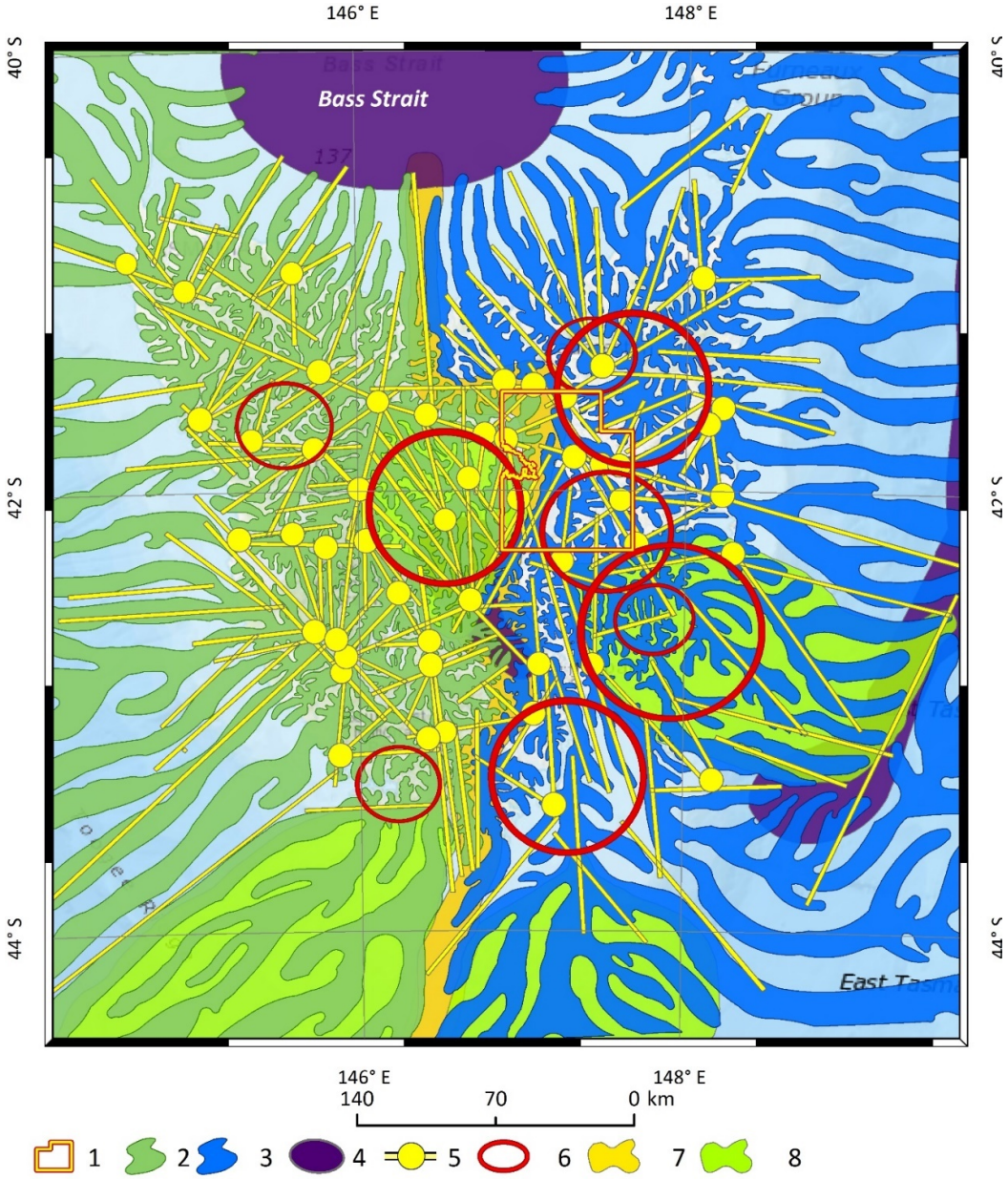


Figure 60: Integration of all predictive criteria of HC potential (paleo-delta, contact zones of flow subsystems, depressions, circular and linear structures). 1:500,000.

1 – location of EL30/2011; 2 - flows of Western litho-dynamic subsystem; 3 – flows of East litho-dynamic subsystem; 4 - depressions; 5 – linear structure of tension and nodes of their intersection; 6 – circular structures and their numbers; 7 –contact zone of Eastern and Western litho-dynamic subsystems; 8 – paleo-delta.

Areas of convergence of the PRA predictive factors are shown in **Figure 61**.

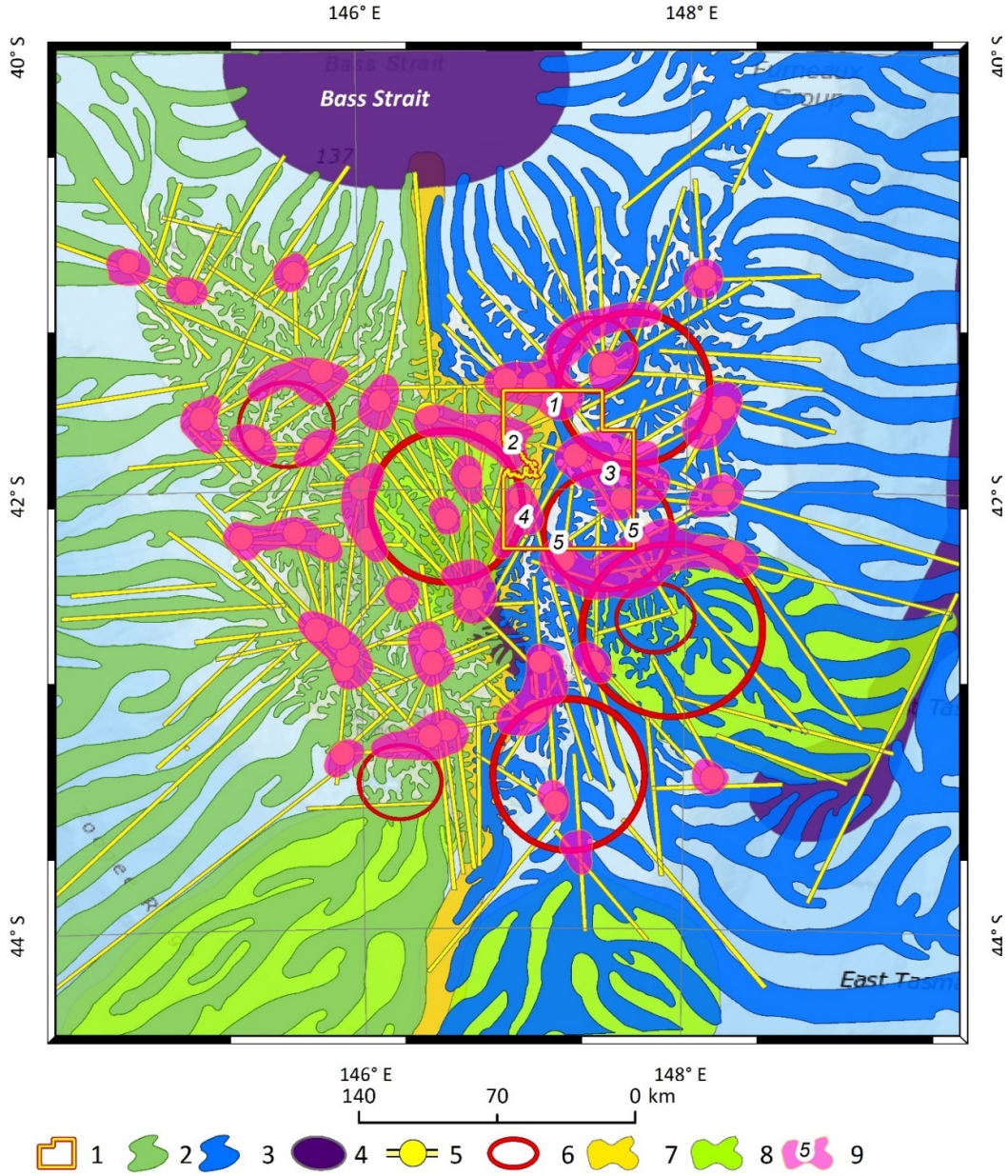


Figure 61: Areas of convergence of predictive criteria on the map of litho-dynamic flows. 1:500,000.
1 – location of EL30/2011; 2 - flows of Western lithodynamic subsystem; 3 – flows of East lithodynamic subsystem; 4 - depressions; 5 – linear structure of tension and nodes of their intersection; 6 – circular structures and their numbers; 7 –contact zone of Eastern and Western lithodynamic subsystems; 8 – paleo-delta; 9 – prognostic areas.

In greater detail, the PRA prospective areas are shown in **Figure 62**. All the prognostic areas are numbered for their detailed review and further evaluation at the scale of 1:100,000.

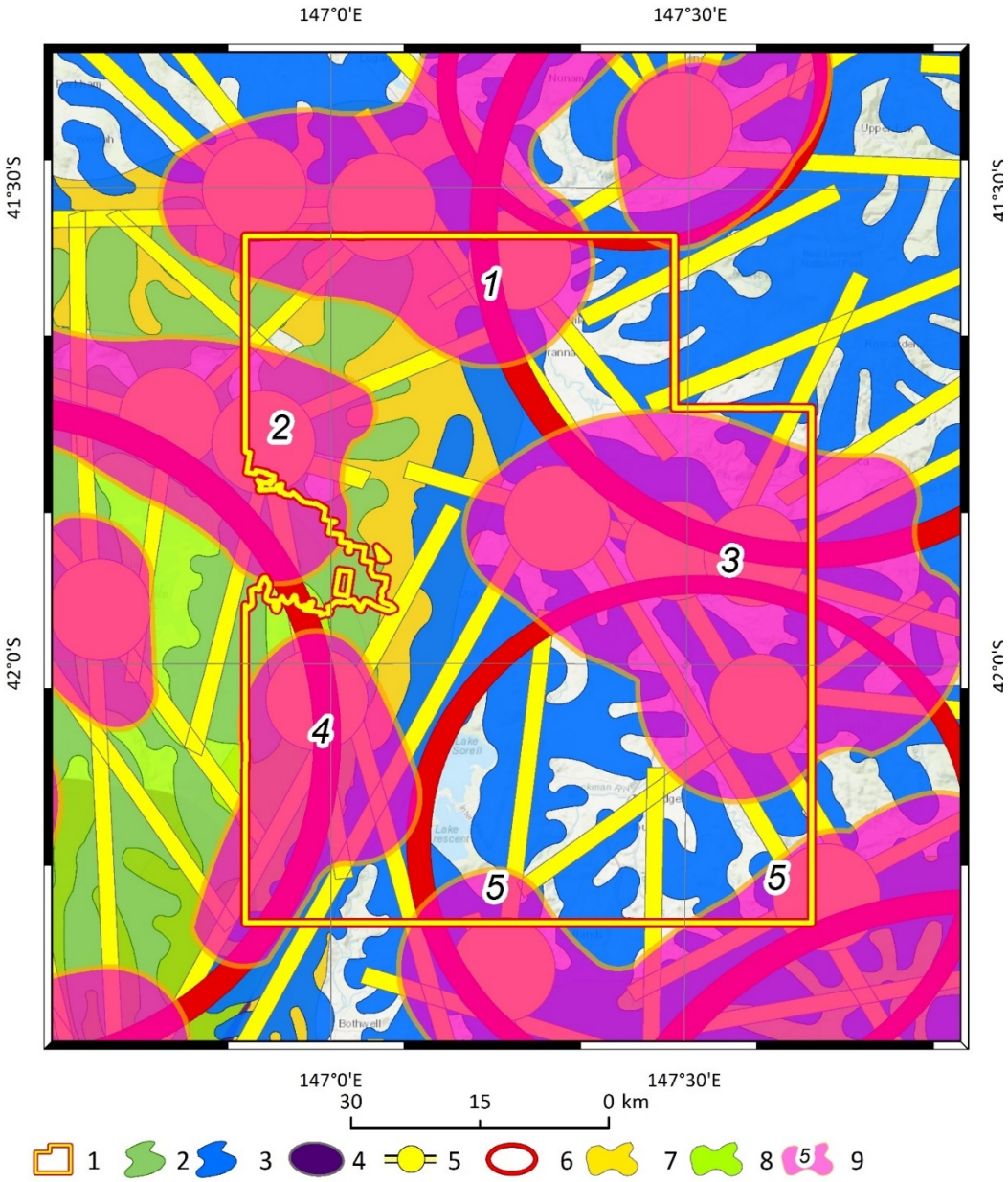


Figure 62: Areas of convergence of predictive criteria on the map of litho-dynamic flows. 1:500,000.
1 – location of EL30/2011; 2 - flows of Western litho-dynamic subsystem; 3 – flows of East litho-dynamic subsystem; 4 - depressions; 5 – linear structure of tension and nodes of their intersection; 6 – circular structures and their numbers; 7 –contact zone of Eastern and Western litho-dynamic subsystems; 8 – paleo-delta; 9 – prognostic areas.

Because the most perspective areas from the view point of relief plasticity are litho-dynamic flows-convexities, the most HC-prospective areas within the previously identified prognostic areas are identified as their parts associated with flows-convexities – **Figure 63**.

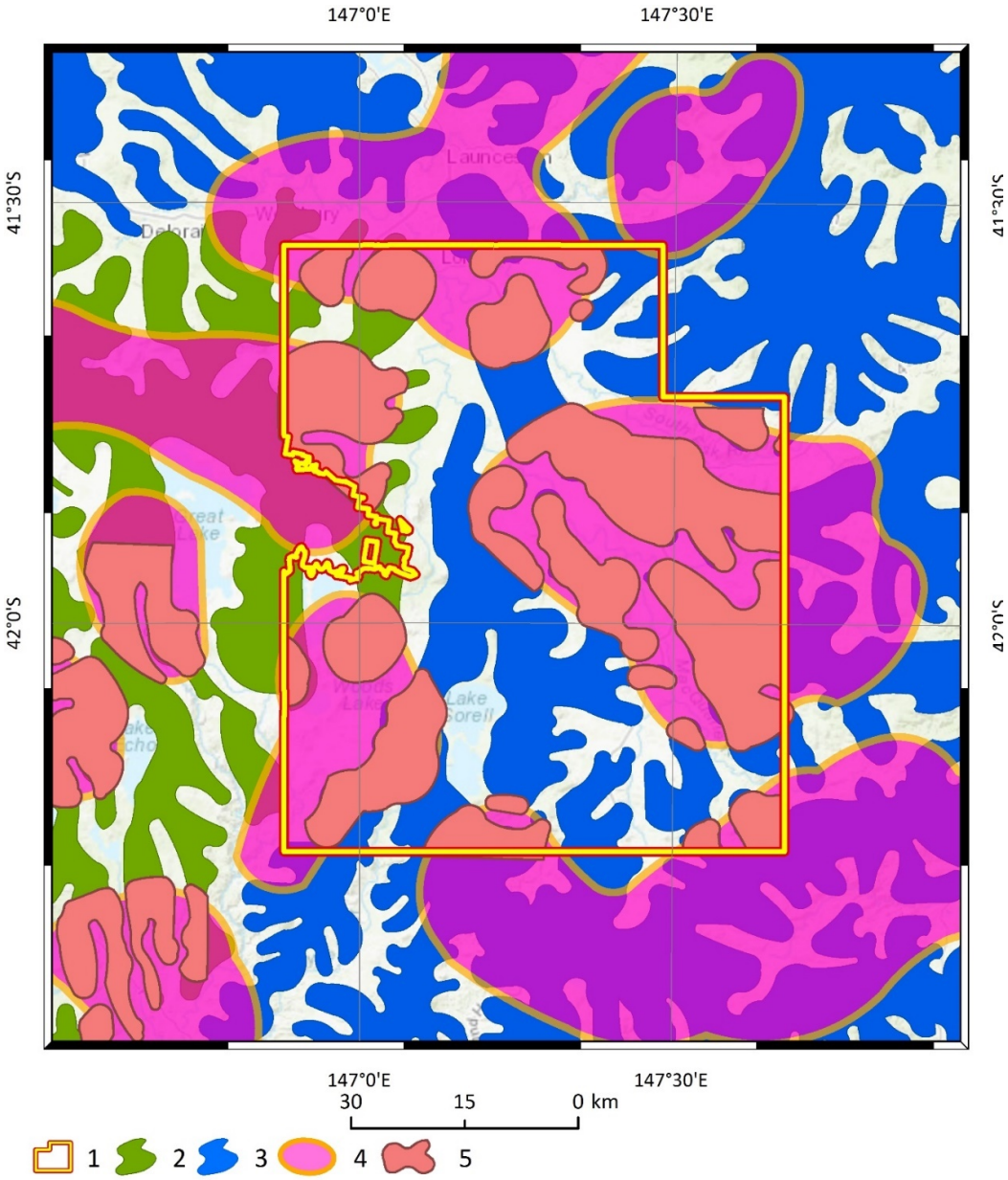


Figure 63: HC-prospective areas on previously identified prognostic areas of EL30/2011. 1:500,000.
1 – location of EL30/2011; 2 - flows of Western litho-dynamic subsystem; 3 – flows of East litho-dynamic subsystem; 4 – prognostic areas; 5 – prognostic areas on the flow increases.

In order to further clarify the above prediction at the scale of 1:500,000, PRA at 1:100 000 is being conducted.

2.5 STRUCTUREMETRIC ANALYSIS (SMA)

The maps of stress fields and plays are shown in **Figure 64** and **Figure 65**. It is based on the processing of multispectral satellite data using the SMA criteria for identification of the key elements of deformation of the sedimentary cover and the basement.

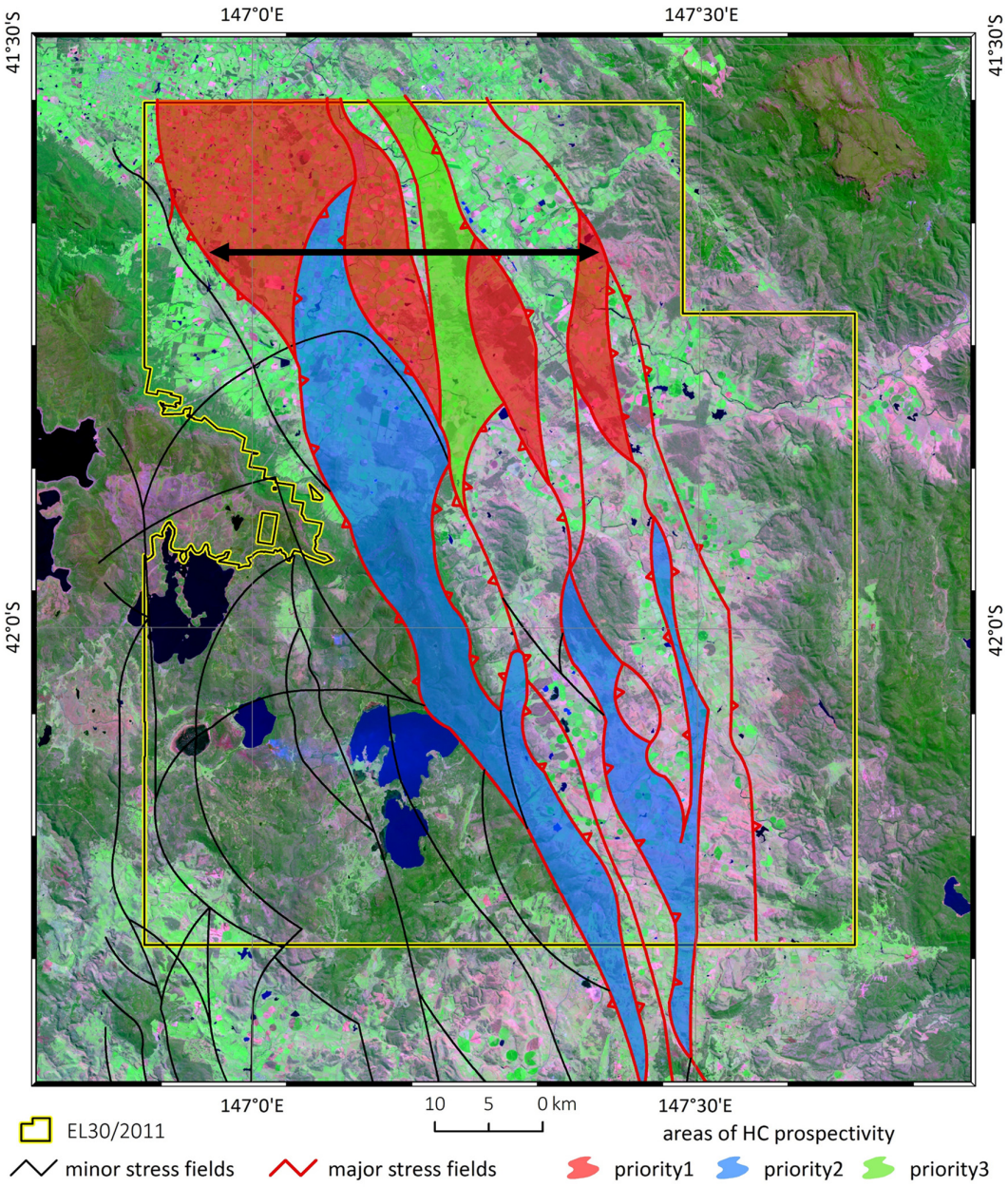


Figure 64: Superposition of Structuremetric analysis and geodynamic analysis. 1:100,000.
Colored area – SMA plays; Black and red line – stress fields; Black arrow – trend for further SMA evaluation at local scales.

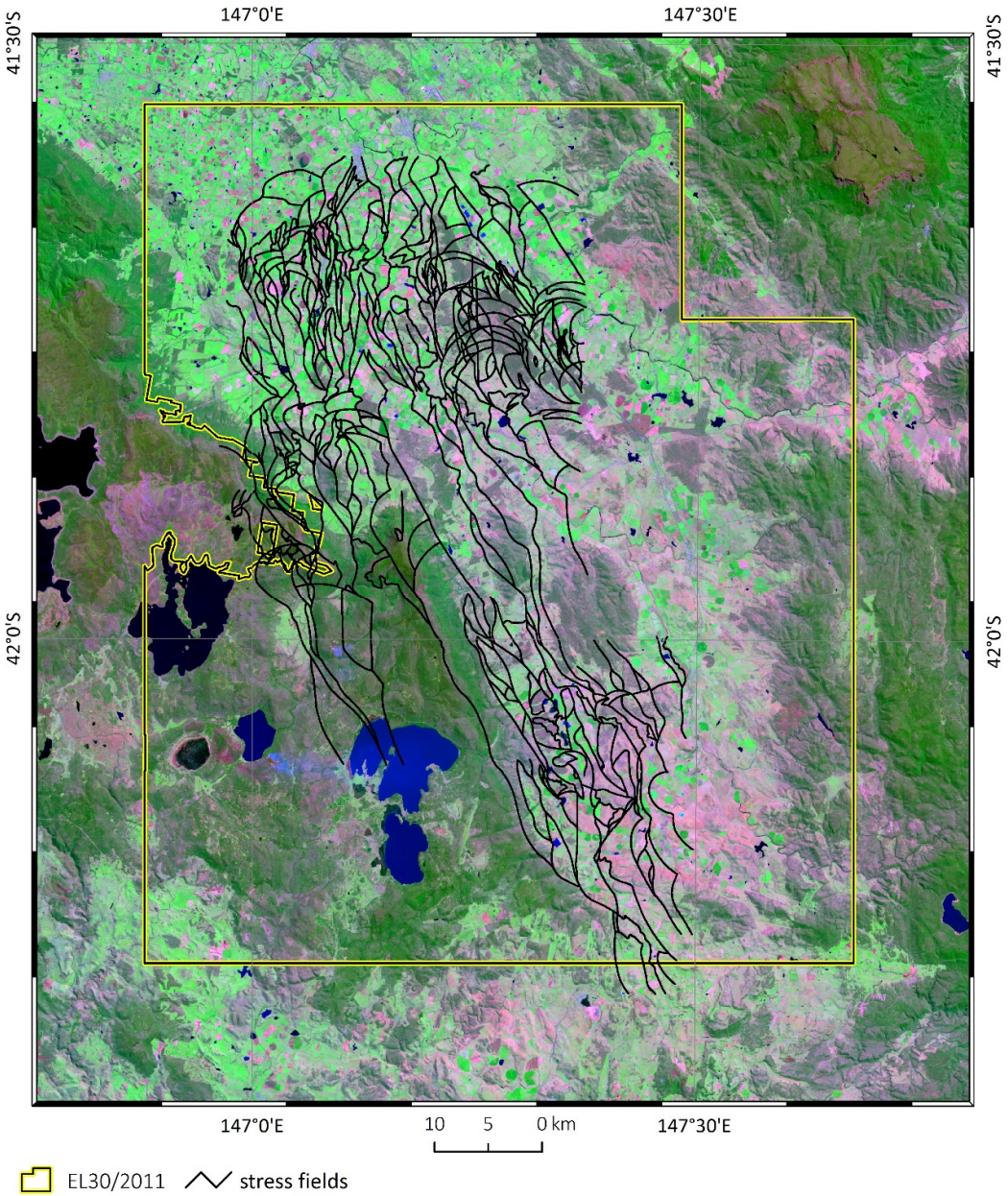


Figure 65: Local mapping of stress fields. 1:25,000.

The trend shown in **Figure 64** with the black arrows was SMA-processed at the scale of 1:25,000. The result is shown in **Figure 66**. It displays the potential HC leads colored in red.

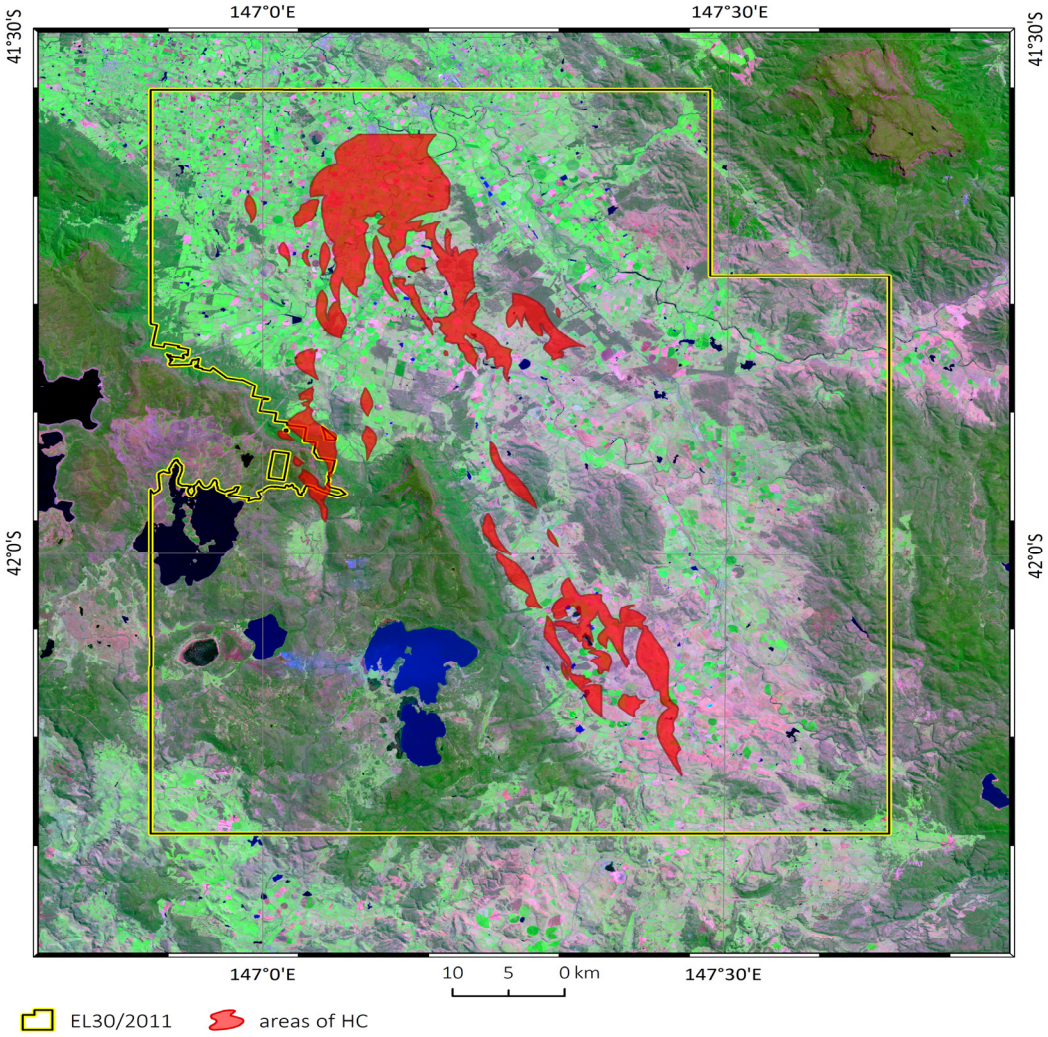


Figure 66: HC leads based on SMA analysis of local stress fields. 1:25,000.

Certain test areas of the trend shown in **Figure 64** with the black arrows were SMA-processed at the scale of 1:5,000. These areas are shown using purple rectangles in **Figure 67**. Sectors 5 through 10 are not positive for HCs at the local scale of 1:5,000, while sectors 1 through 4, 11, and 12 were positive for the presence of HC. The result is shown in **Figure 66**. It displays the potential HC leads colored in red.

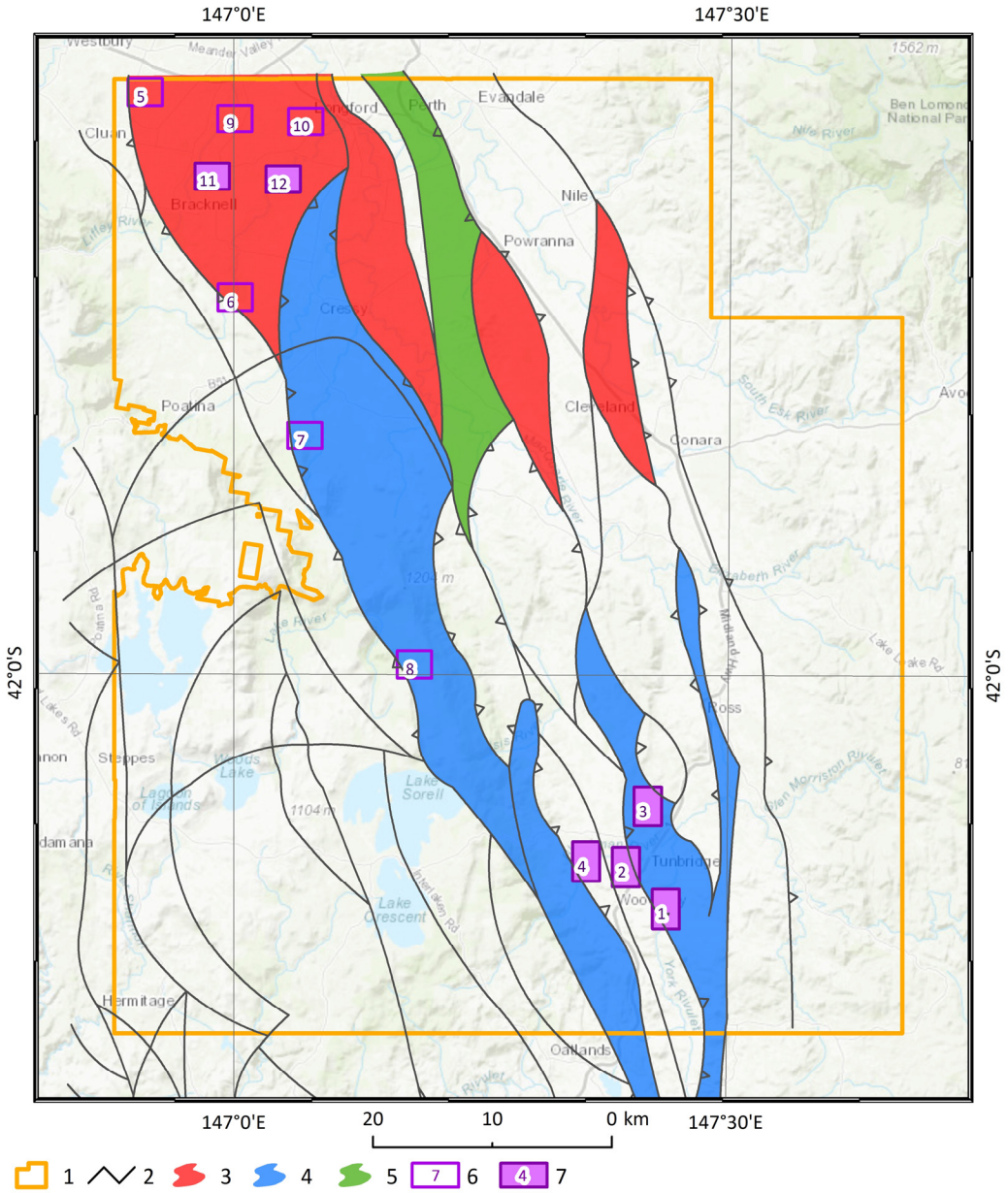


Figure 67: SMA QC areas at 1:5,000 within the HC trend delineated at 1:100,000.

1 – EL30/2011; 2 – Stress fields at 1:100,000; 3,4,5 – SMA plays of varying priority; 6 – SMA test area at 1:5,000 that was not positive for HC presence; 7 - SMA test area at 1:5,000 that was positive for HC presence.

The areas positive for HCs (according to SMA criteria) shown in **Figure 67** were superimposed with the SMA results obtained at the scale of 1:25,000 (**Figure 68**). Sectors 1 through 4 tested consistently positively for HCs at all three scales 1:5,000, 1:25,000 and 1:100,000, while sectors 11 and 12 do not integrate with SMA results at 1:25,000. This is being investigated. The sectors 5 through 10 are consistent for the absence of HC's at the scales of 1:5,000 and 1:25,000 – this result is consistent with the expectations of the process of high-grading of areas as the scale of investigation increases.

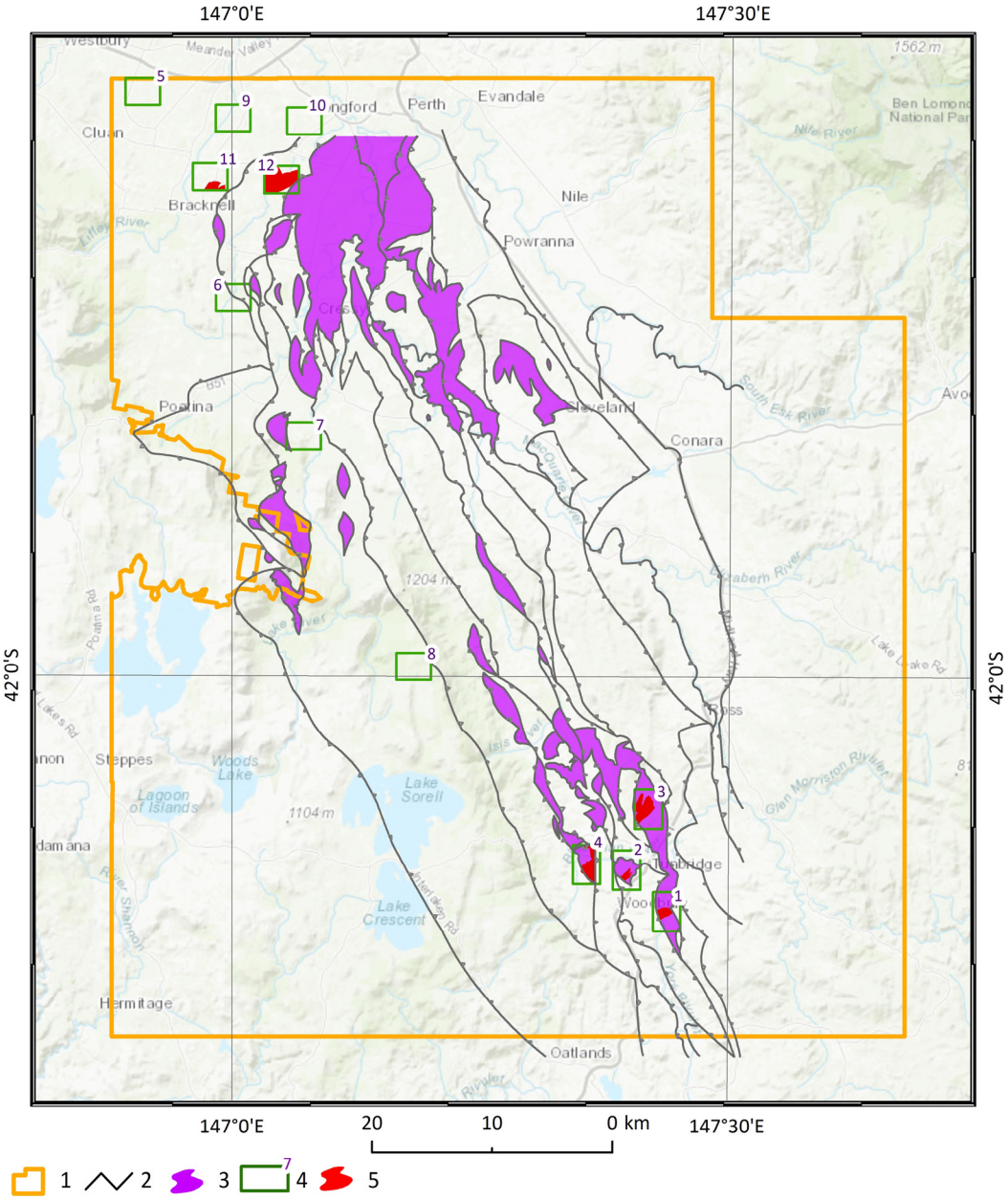


Figure 68: SMA QC areas at 1:5,000 within the HC leads delineated at 1:25,000.

1 – EL30/2011; 2 – stress fields;3 – SMA results at 1:25,000; 4 – SMA test area at 1:5,000; 5 - SMA test area at 1:5,000 positive for HC presence.

2.6 PROPRIETARY SPECTROMETRIC ANALYSIS (PSA)

Proprietary Spectrometric Analysis (PSA) uses a proprietary process of pattern recognition using the multi-spectral satellite data of varying resolutions. These patterns, when found, correspond to locations in the subsurface that are associated with the presence of HCs in the subsurface irrespective of their mode of accumulation.

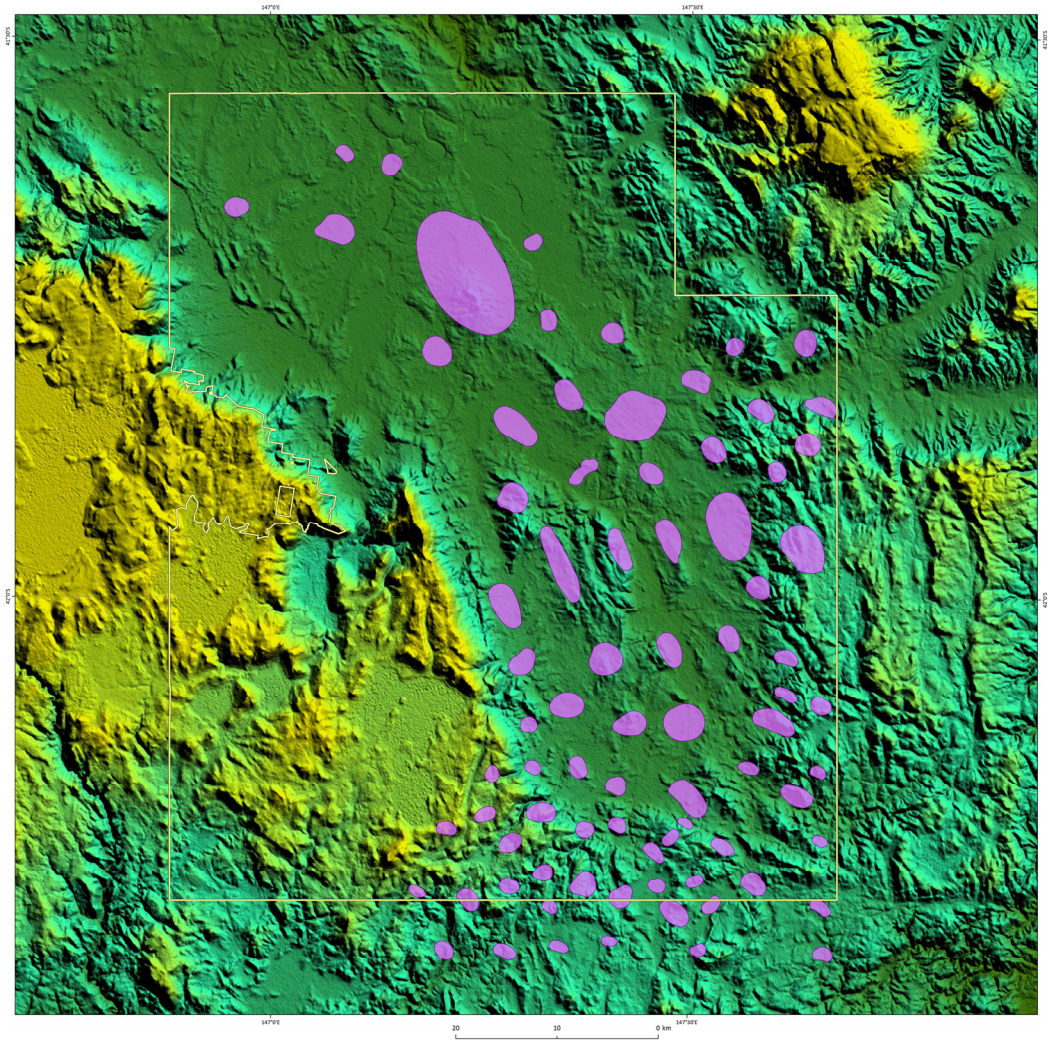


Figure 69: HC-bearing anomalies derived using PSA. 1:25,000.

The volumetric analysis performed based on the calculations of the volumes of prospective HC resources and conservative oil and gas saturation and recovery assumptions are shown in **Table 4**.

Table 4: Oil and gas prospective resources in place for EL30/2011.

OIL AND GAS PROSPECTIVE RESOURCES IN PLACE EL30/2011 LICENSE BLOCK		
Structure ##	Prospective Resources of the Structures	
	Oil	Natural Gas
	MMBO	BCF
1	4.96	0.80
2	6.90	1.11
3	7.09	0.99
4	20.14	0.05
5	167.45	116.39
6	4.07	2.25
7	13.44	7.94
8	5.34	0.01
9	7.44	4.19
10	4.47	2.54
11	9.85	5.60
12	24.27	13.94
13	10.89	6.19
14	39.41	22.62
15	9.11	5.23
16	8.89	5.10
17	8.53	4.89
18	6.98	3.46
19	7.42	4.10
20	9.18	5.07
21	5.59	3.21
22	9.54	5.42
23	13.44	7.80
24	26.11	14.84
25	10.99	6.31
26	15.11	8.59
27	42.28	21.24
28	31.30	17.80
29	22.24	12.65
30	8.49	4.87
31	12.17	6.92
32	16.44	9.25
33	12.68	7.21
34	8.83	5.02
35	5.35	3.04
36	3.52	2.00
37	13.46	7.65
38	11.68	6.64
39	22.53	12.93
40	14.67	8.34
41	4.17	2.39
42	5.14	2.92
43	3.90	2.24
44	3.51	2.00
45	5.86	3.33
46	5.25	3.02
47	16.69	9.49
48	3.43	1.97
49	3.05	1.75
50	8.36	4.75
51	3.46	1.98
52	4.58	2.60
53	5.92	3.37
54	7.89	4.48
55	4.02	2.28
56	3.90	2.24
57	5.02	2.85
58	3.87	2.20
59	2.59	1.47
60	5.16	1.85
61	2.43	1.38
62	2.88	1.65
63	6.84	3.89
64	4.04	2.32
65	4.58	2.60
66	2.95	1.68
67	8.91	5.11
68	6.26	3.56
69	3.08	1.73
70	8.72	5.01
71	2.98	1.69
72	3.75	2.79
73	7.37	4.18
74	3.95	2.26
75	4.64	2.63
76	4.14	2.37
77	3.16	1.79
78	2.14	1.23
79	2.46	1.39
80	4.07	2.33
EL30/2011 Total	**877.30**	**495.03**

The results for oil (in MMBO) shown in **Table 4** are mapped in **Figure 70**.

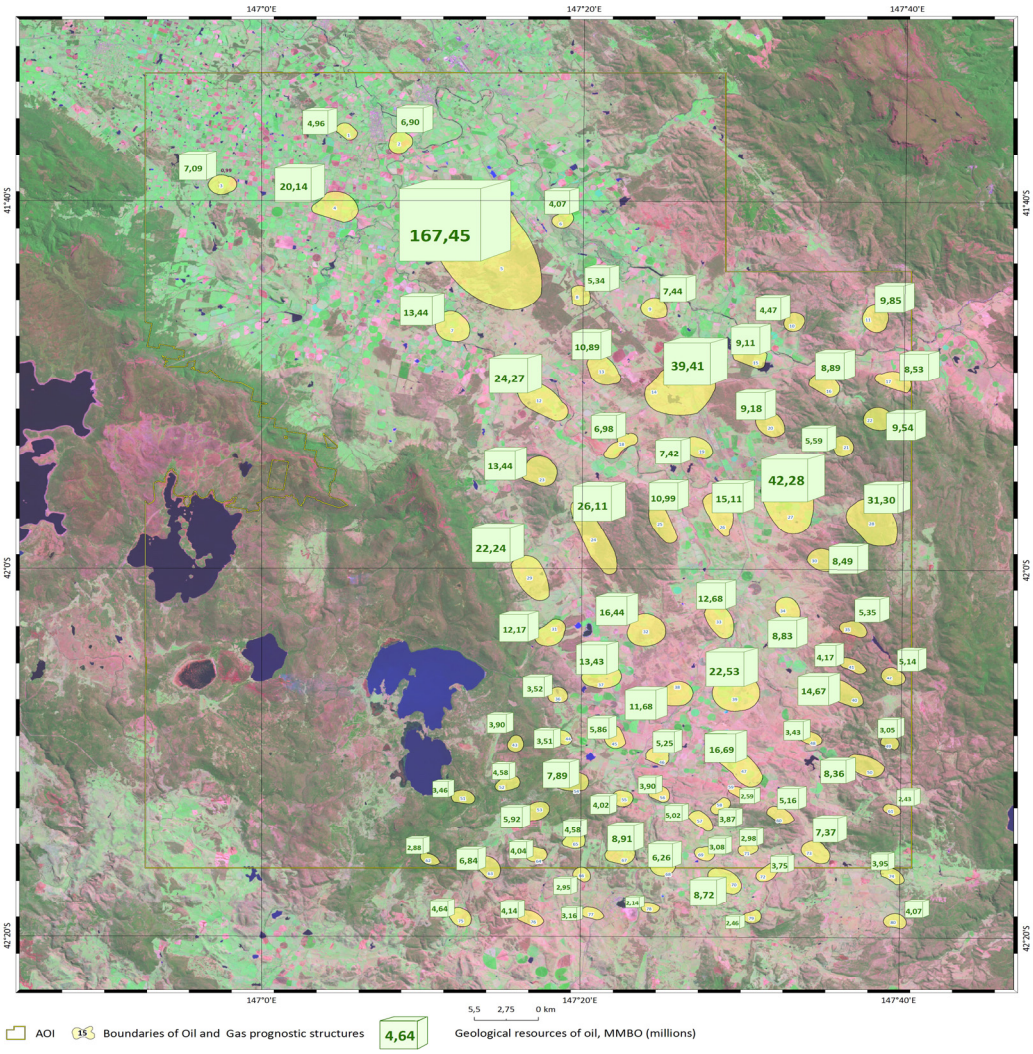


Figure 70: Prospective resources of oil (in MMBO) for each PSA anomaly.

The results for gas (in BCF) shown in **Table 4** are mapped in **Figure 71**.

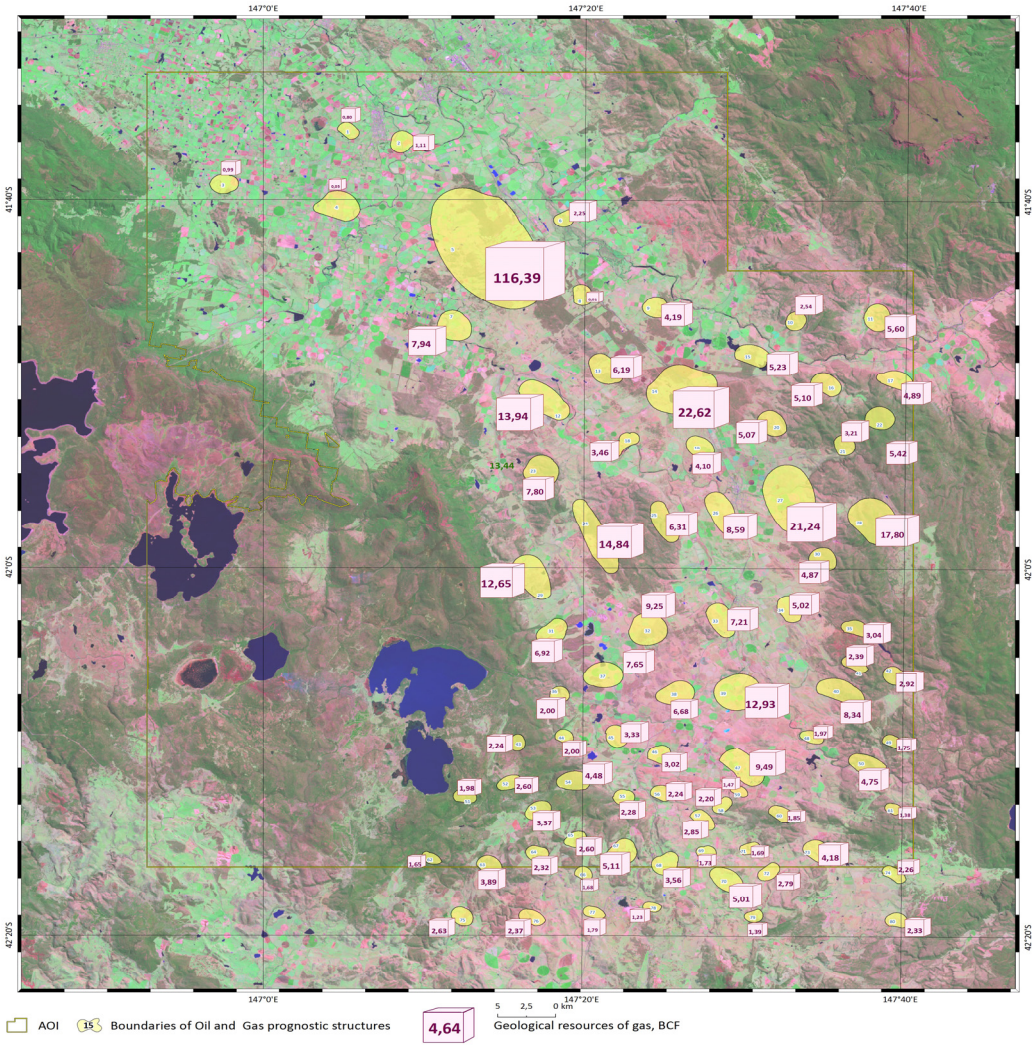


Figure 71 Prospective resources of gas (in BCF) for each PSA anomaly.

The results for oil and gas (in MMBO and gas) shown in **Table 4** are mapped in **Figure 72**.

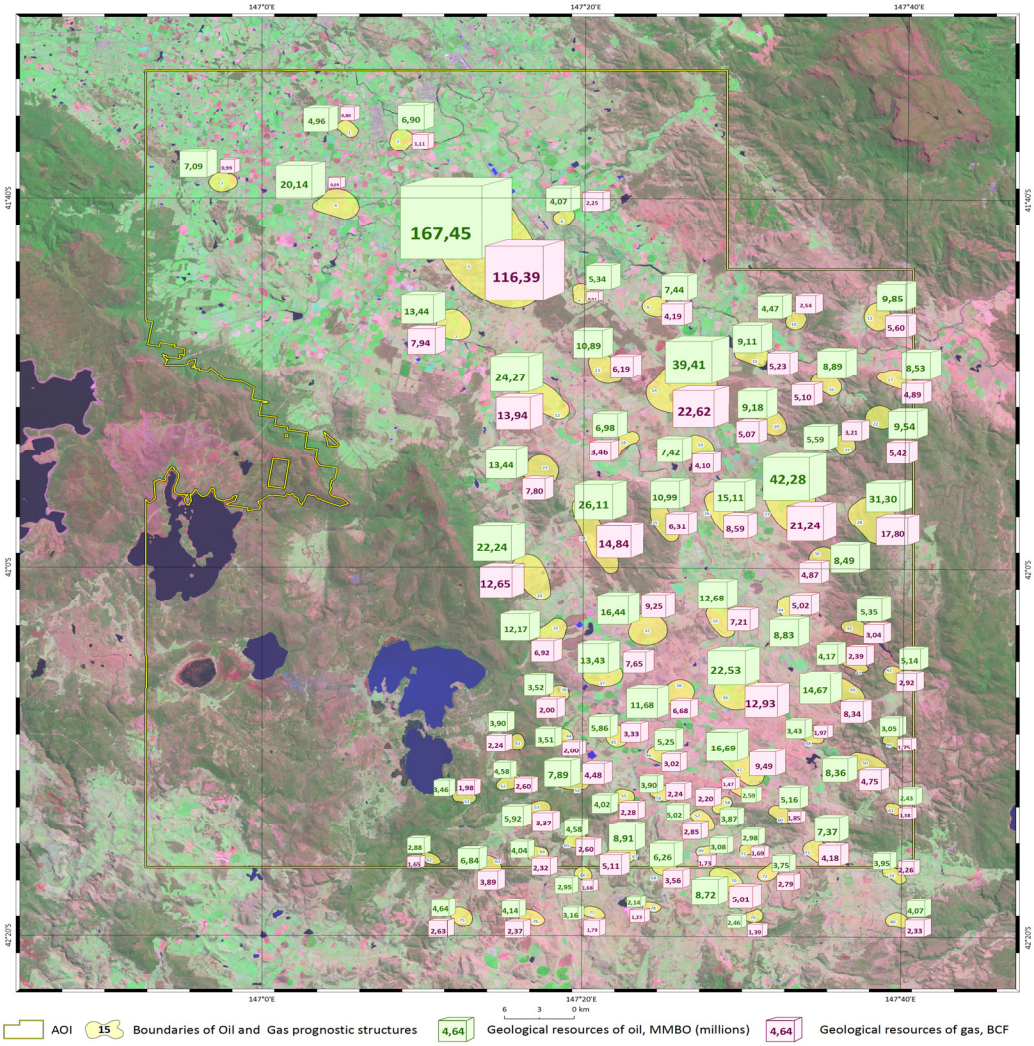


Figure 72: Prospective resources of oil and gas (in MMBO and BCF) for each PSA anomaly.

2.7 EXISTING 2D SEISMIC EVALUATION

POST-PROCESSING

The existing and previously processed seismic was post-processed for the purposes of noise reduction. The prost-processing process is as follows and is shown in :

The Structurally Oriented noise filters were applied along an orientation defined by the local structural vector at each point in the data: so the first step was to calculate the Dip and Azimuth volumes using Dip and Azimuth, and then to apply the noise reduction process using these volumes.

The SO Noise filters allowed to restrict the smoothing process to a 2D region around each point, defined by the Dip (defined as the orientation of maximum dip, the value found by

looking along the azimuth) and the Strike (defined by a horizontal line perpendicular to maximum dip) directions.

Mean filtering returned the average of the values within the neighborhood and was good at enhancing the continuity of reflectors.

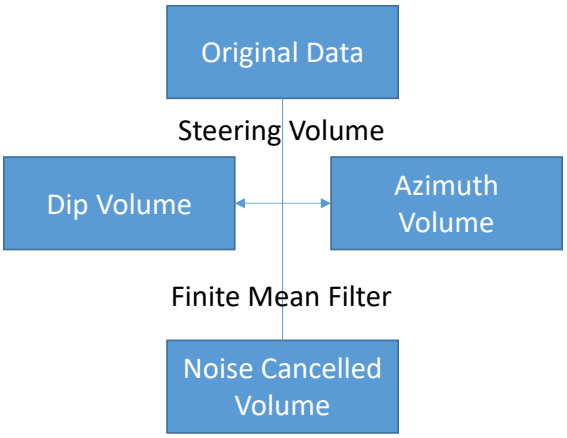


Figure 73: Noise cancellation work flow.

The result of the prost processing of one of the lines is demonstrated in . The entire post-processed set of 2D data is being submitted with this report.

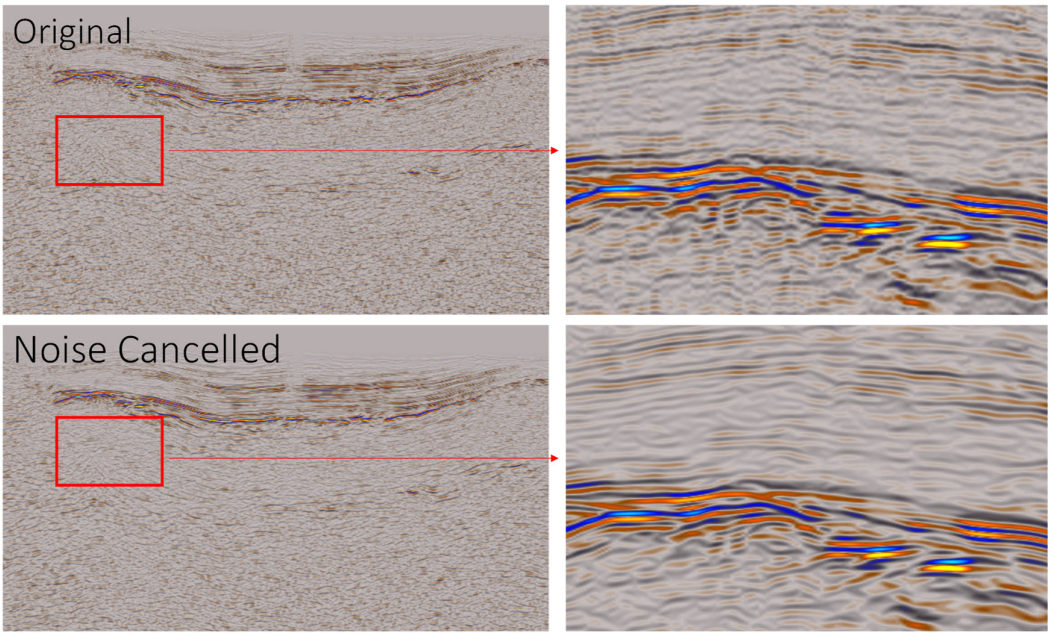


Figure 74: Original vs. noise-cancelled data.

INTERPRETATION OF THE AVAILABLE 2D POST-PROCESSED SEISMIC DATA

The postprocessed seismic data was evaluated in order to high-grade the previously delineated structures within EL30/2011. Their priority was determined as shown in **Table 5**.

Table 5: Priority assignment (column 'Id') for each previously delineated target.

Poly	Show	Label X	Label Y	Label Z	Label angle	Hole classification	Id	name
1	Yes	514304.	538912	12.00	0.00	Yes	10.00	01 Cressy Rise
2	Yes	527816.	538614	12.00	0.00	Yes	9.00	02 Nile River
3	Yes	511026.	538207	12.00	0.00	Yes	11.00	03 Macquarie River
4	Yes	497959.	538858	12.00	0.00	Yes	2.00	04 Bracknell Dome
5	Yes	528240.	536777	12.00	0.00	Yes	1.00	05 Stockwell
6	Yes	518736.	538469	12.00	0.00	Yes	6.00	06 Hummocky Hills
7	Yes	519841.	537880	12.00	0.00	Yes	7.00	07 Hummocky Hills Gondwana
8	Yes	477091.	538754	12.00	0.00	Yes	5.00	08 Quamby Fault Block
9	Yes	537014.	533420	12.00	0.00	Yes	4.00	09 Butlers Rise Gondwana
10	Yes	521070.	533695	12.00	0.00	Yes	8.00	10 Interlaken Gondwana
11	Yes	490363.	533959	12.00	0.00	Yes	12.00	11 Steppes
12	Yes	466626.	533874	12.00	0.00	Yes	3.00	12 Bellevue
13	Yes	468376.	528734	12.00	0.00	Yes	13.00	13 Thunderbolt

All of the interpretations are attached hereto by Appendix 3.

2.8 VISUALIZATION OF ALL PREVIOUS AND NEW PROSPECTS AND LEADS – WORK IN PROGRESS

Using the Visualization tool provided as a part of the STeP technology suite, all of the current seismic, and the future remote-sensing ones, are being visualized and assessed in connection with their oil and gas prospectivity. This tool helps integrate the traditional seismic datasets into the remote sensing process and results, and tie in horizons, lithology, etc. from the existing G&G data. Below are some of the results (work in progress) on the Bracknell Dome lead derived previously using 2D seismic.

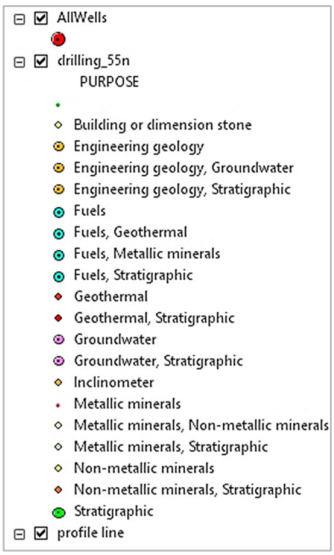


Figure 75: The base map of the Bracknell Dome area and positions of cross sections.

Two cross sections through the prospect (Section 1 and Section 2) were interpreted and integrated with the existing seismic lines in order to decipher geology and the lithological composition of these cross sections, as see in **Figure 76**, **Figure 77**, and **Figure 78**.

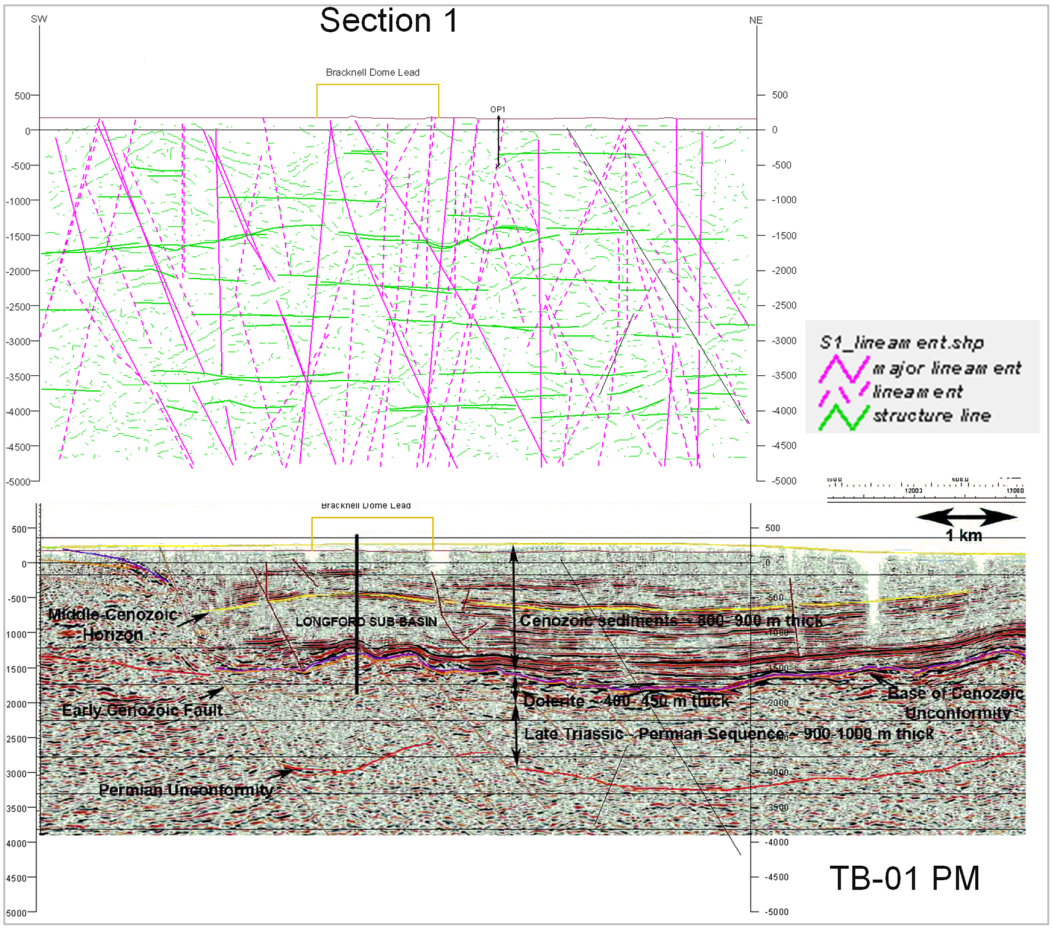


Figure 76: Cross Section 1 (using STeP) and seismic section TB-01 PM through the Bracknell Dome area.

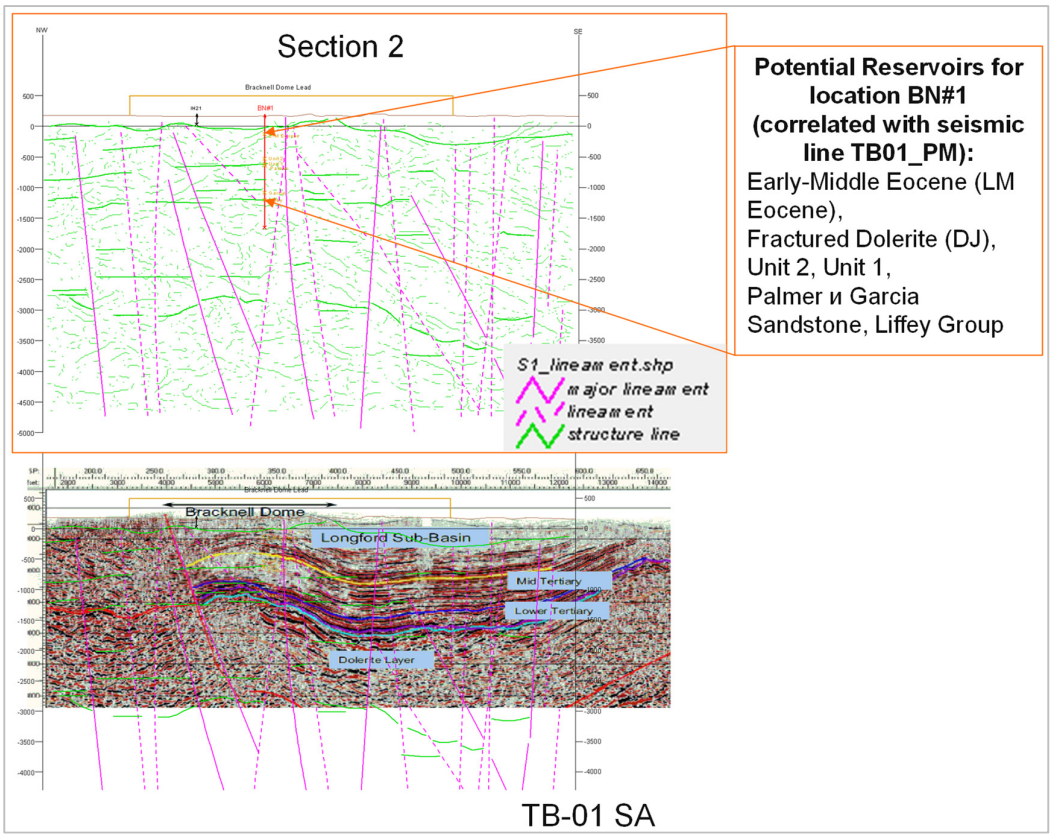


Figure 77: Cross Section 2 (using STeP), seismic section TB-01 PM through the Bracknell Dome area, and horizons picked on the STeP cross section as they correlate with the seismic section TB-01 SA.

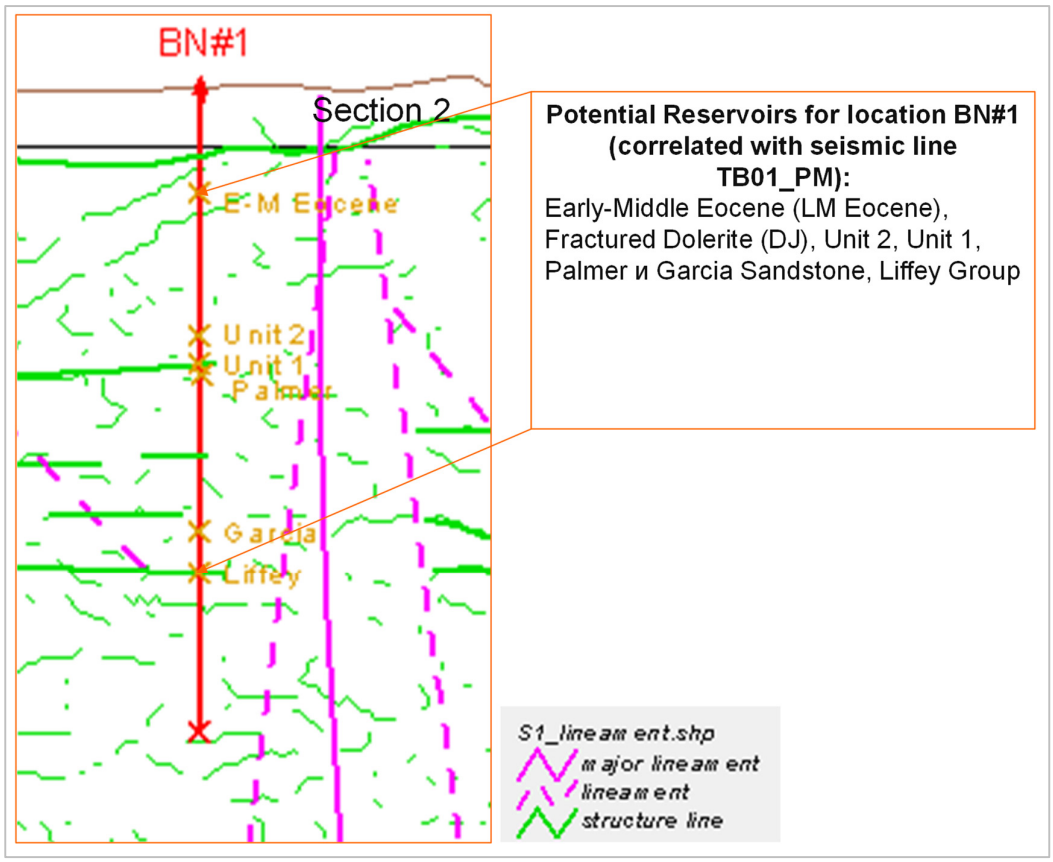


Figure 78: Zoomed in Cross Section 2 (using STeP) and horizons picked on the STeP cross section as they correlate with the seismic section TB-01 SA.

Visualization of the area and its subsurface was performed using the STeP Visualization Tool at the resolution equivalent to the scale of 1:100,000 as shown in **Figure 79**.

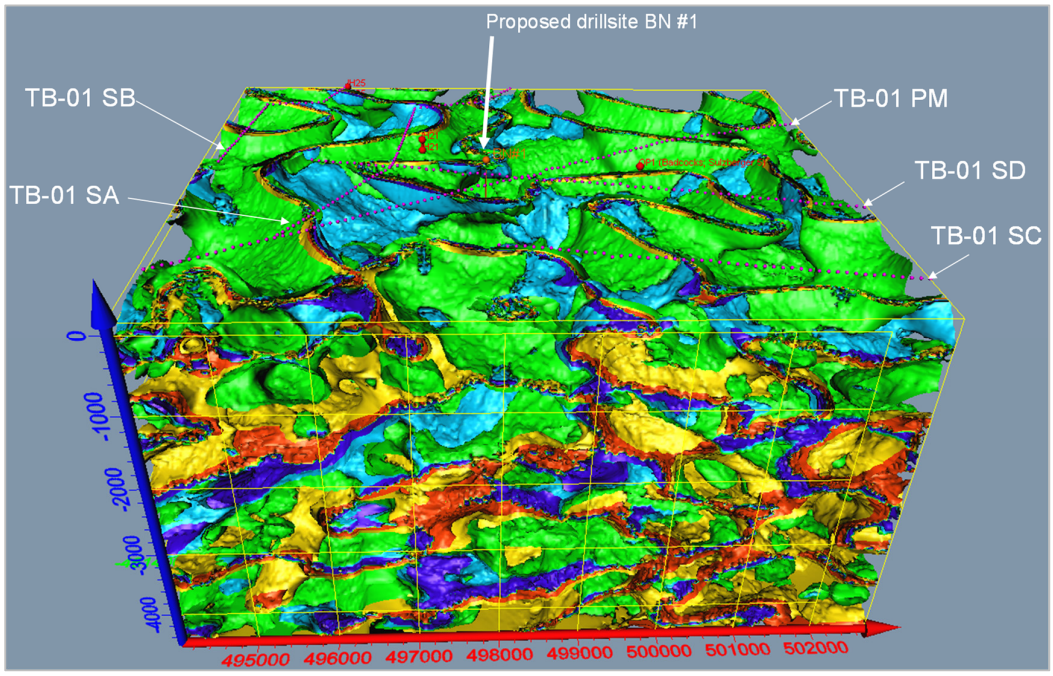


Figure 79: 3D visualization of the Bracknell Dome area. 1:100,000.

Visualization of the area and its subsurface was performed using the STeP Visualization Tool at the resolution equivalent to the scale of 1:50,000 as shown in **Figure 80**.

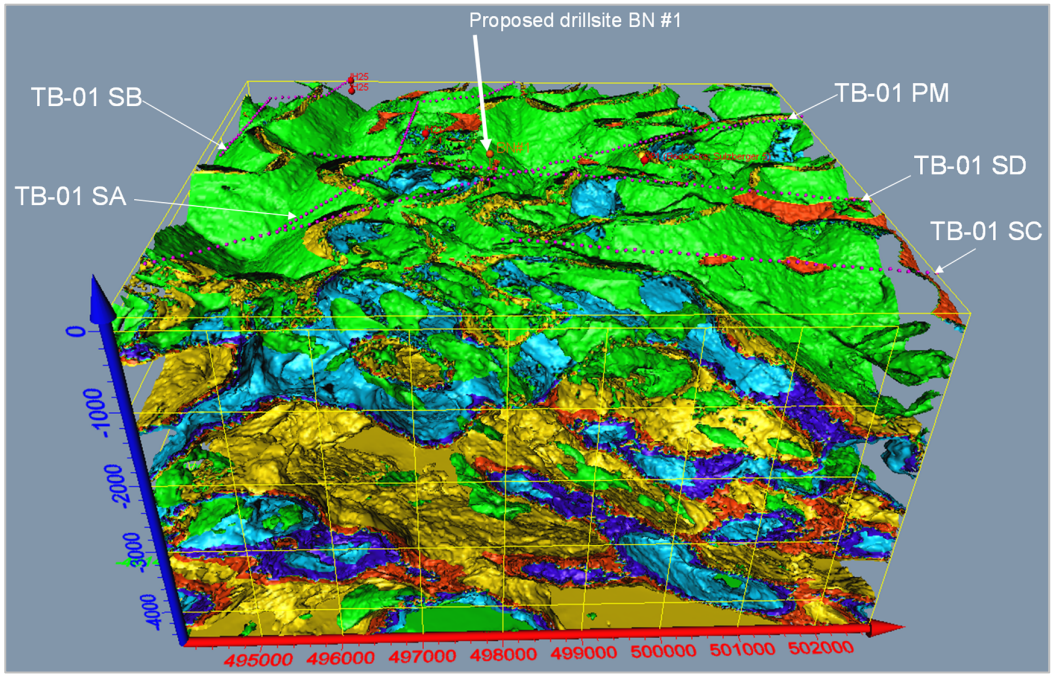


Figure 80: 3D visualization of the Bracknell Dome area. 1:50,000.

Visualization of the area and its subsurface was performed using the STeP Visualization Tool at the resolution equivalent to the scale of 1:25,000 as shown in **Figure 81**, **Figure 82**, **Figure 83**, **Figure 84**, and **Figure 85**. This work is ongoing.

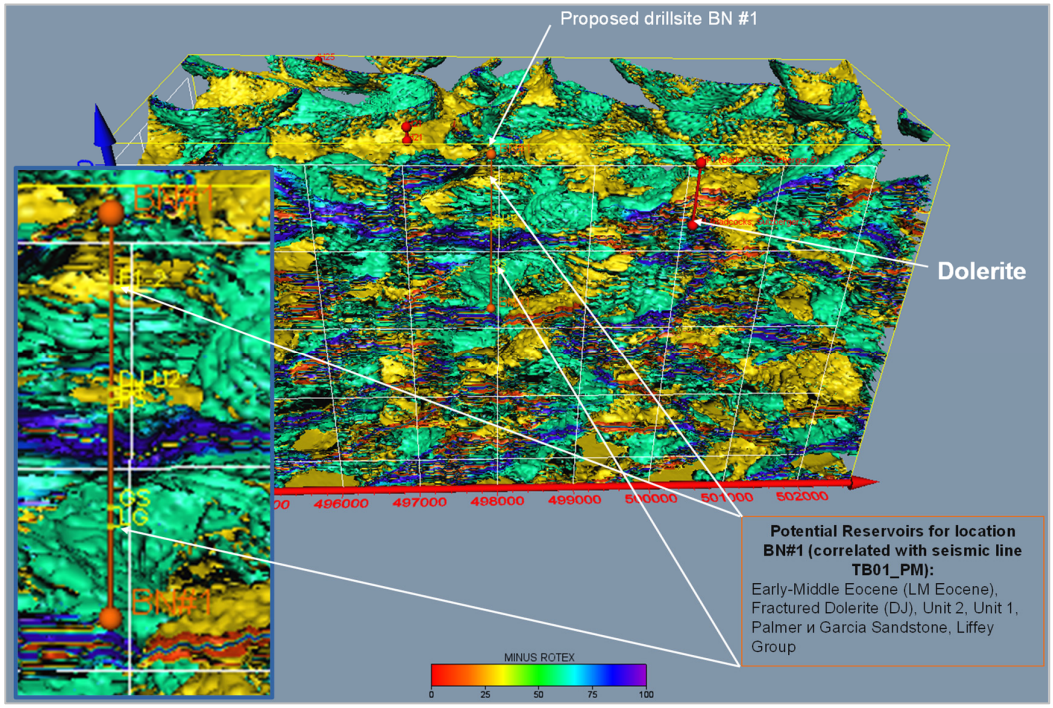


Figure 81: 3D visualization of the Bracknell Dome area and picked horizons. 1:25,000.

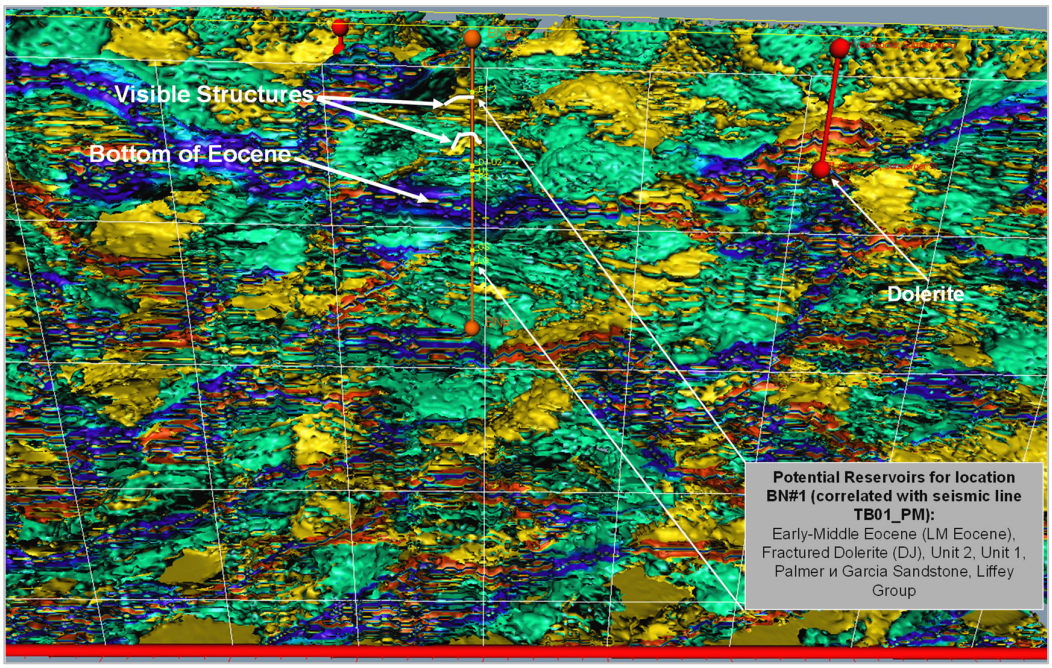


Figure 82: 3D visualization of the Bracknell Dome area and picked structure and horizons. 1:25,000.

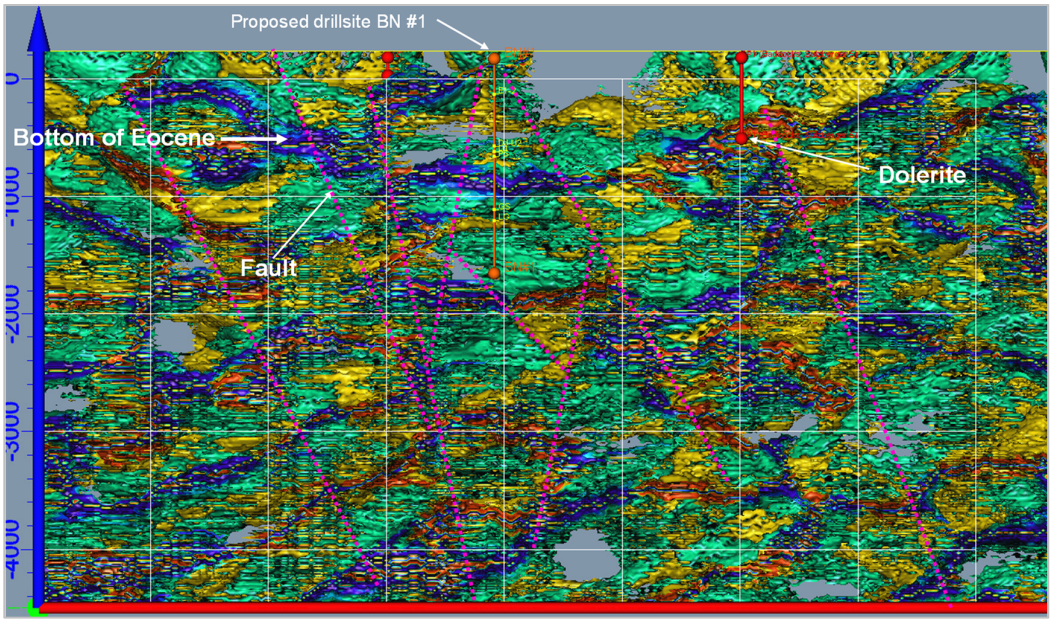


Figure 83: 3D visualization of the Bracknell Dome area and picked faults and horizons. 1:25,000.

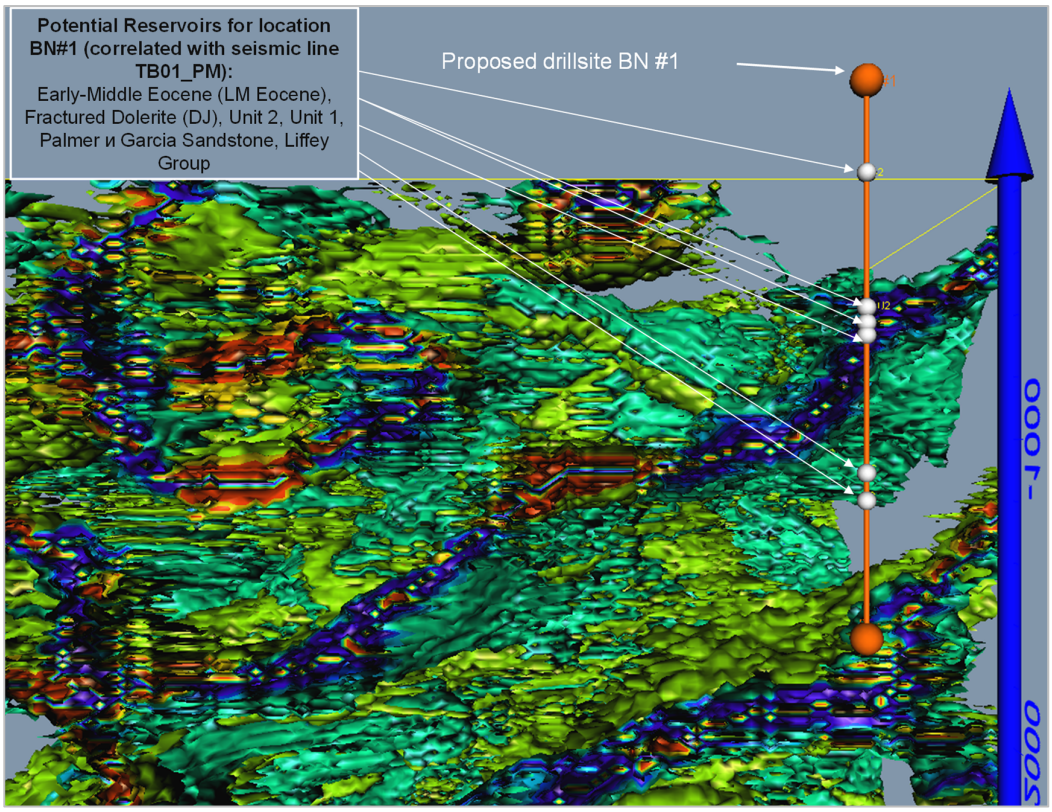


Figure 84: 3D visualization zoom into proposed drilling location at Bracknell Dome and picked structure. 1:25,000.

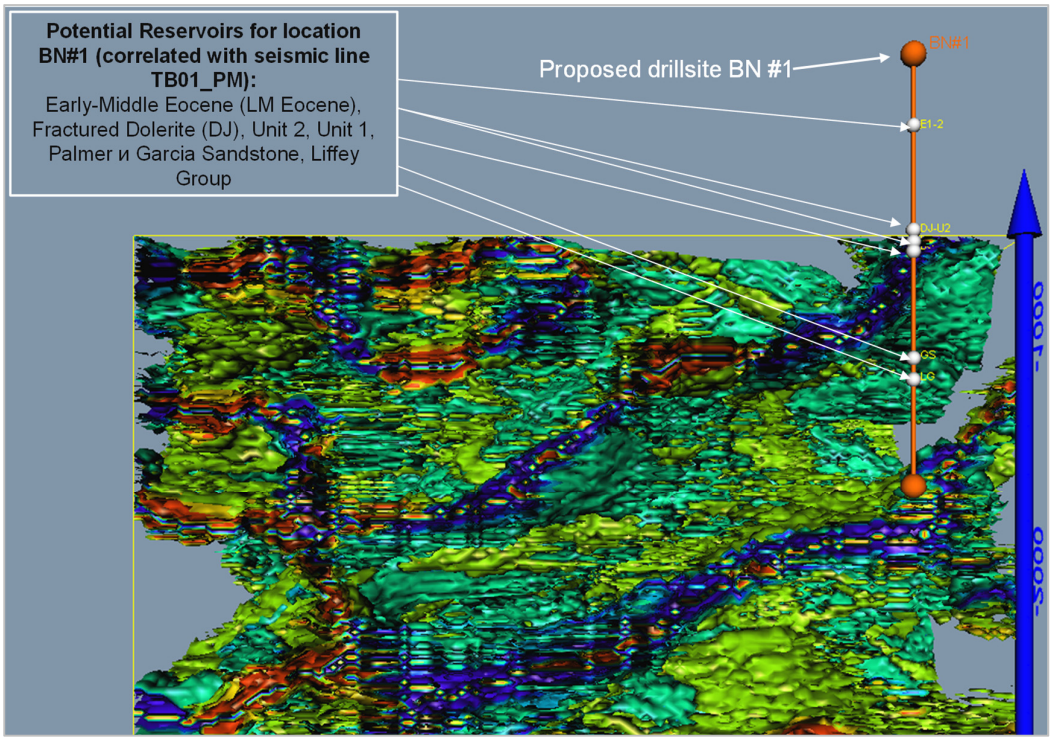


Figure 85: 3D visualization zoom into proposed drilling location at Bracknell Dome and picked structure. 1:25,000.

2.9 MORPHOMETRIC ANALYSIS (MMA)

Morphomeric analysis using the medium and local-scale resolutions is in progress. The following section is the continuation of the MMA section submitted for 2016.

RESIDUAL RELIEF MAPS

Residual relief consists of positive relief forms that lie above a given Base Level. Residual Relief maps show the volume of geomedium, which can be removed in the future via erosion and denudation given analogous geological, physical, and geographic conditions. This volume is calculated as an algebraic difference between the elevation of a hypsometric (current day) relief and the elevation of any Base Level. Hypsometric minus Base Level equals Residual Relief, the volume of geomedium that is deposited above the Base Level. The higher the order of a Base Level, the greater will be the values of the corresponding residual relief.

The quantity of Residual Relief maps is equal to the number of Base Level maps. Every Base Level corresponds to its residual relief. The higher the rank of the Base Level, the larger the mass quantities attributed to residual relief.

There are two types of residual relief - regional and local. Regional residual relief is a background type of relief that reflects the character and direction of the regional dip. Local residual relief reflects local tectonic activity, which can be interpreted to extract geologically meaningful data. Deducting regional residual relief (trend component) from the cumulative residual relief map renders informative Local Residual Relief maps.

The Cumulative Residual Relief maps are depicted in **Figure 86** - **Figure 89**.

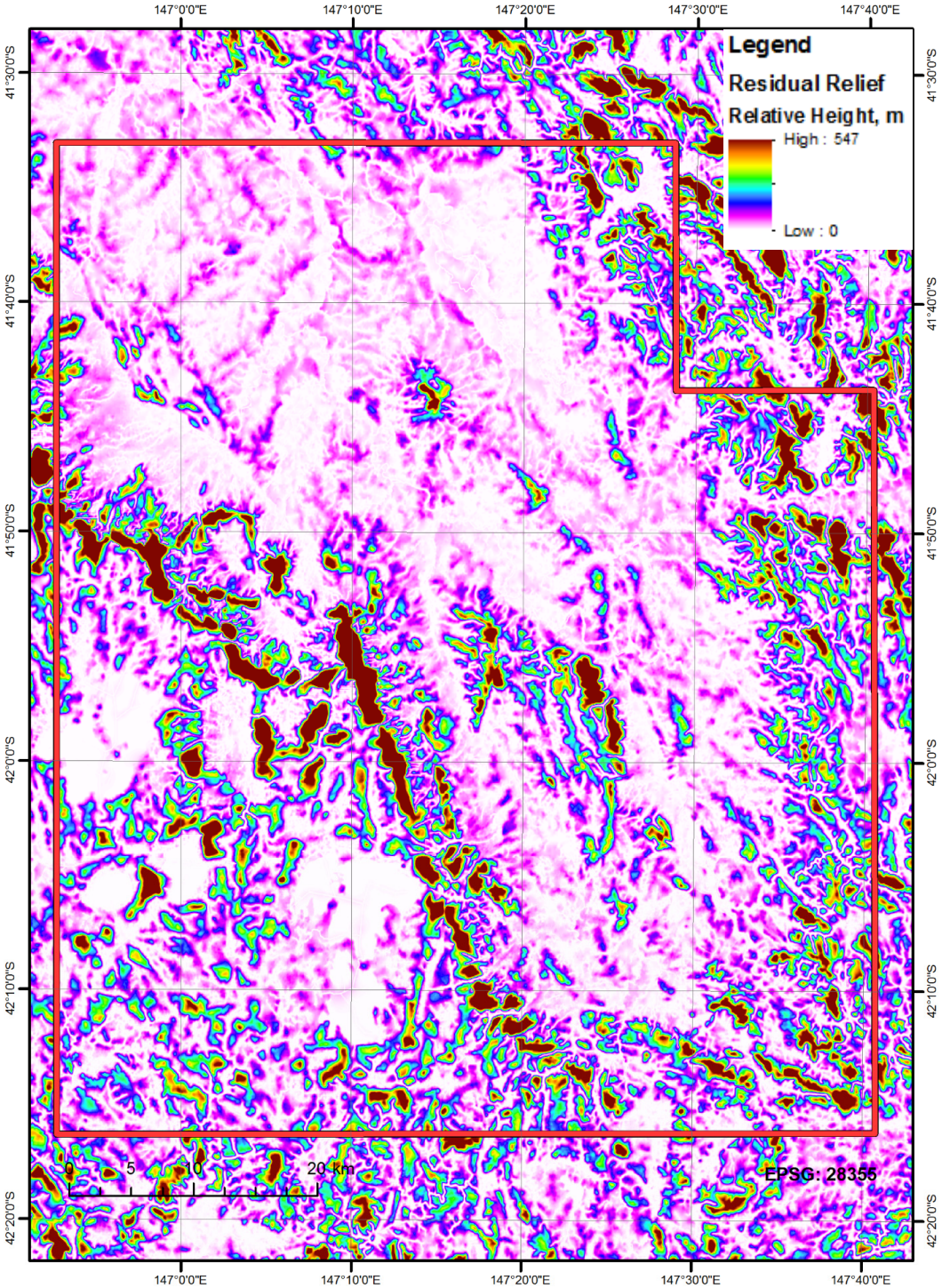


Figure 86: Cumulative Residual Relief map corresponding to Base Level 2.

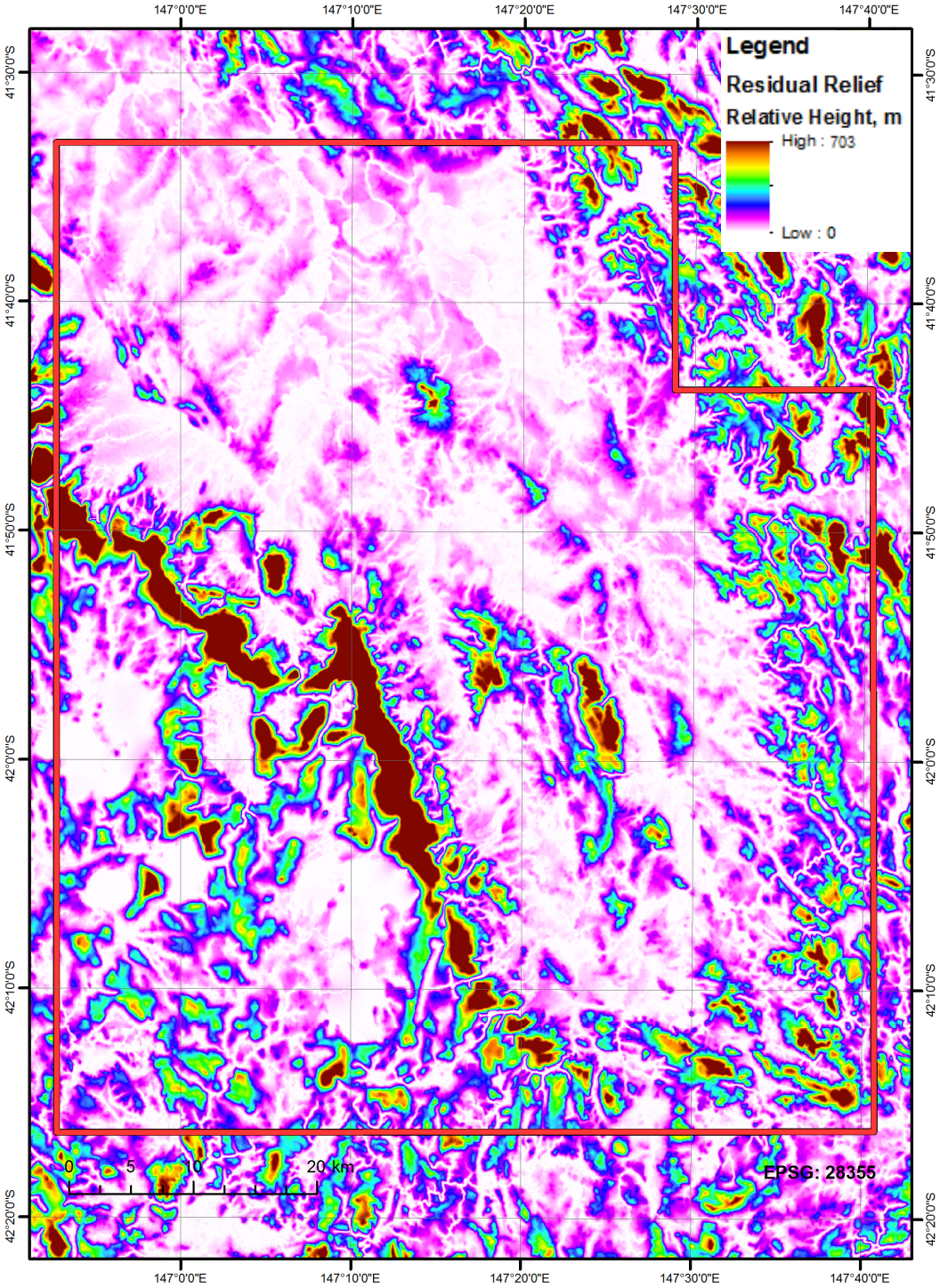


Figure 87: Cumulative Residual Relief map corresponding to Base Level 3.

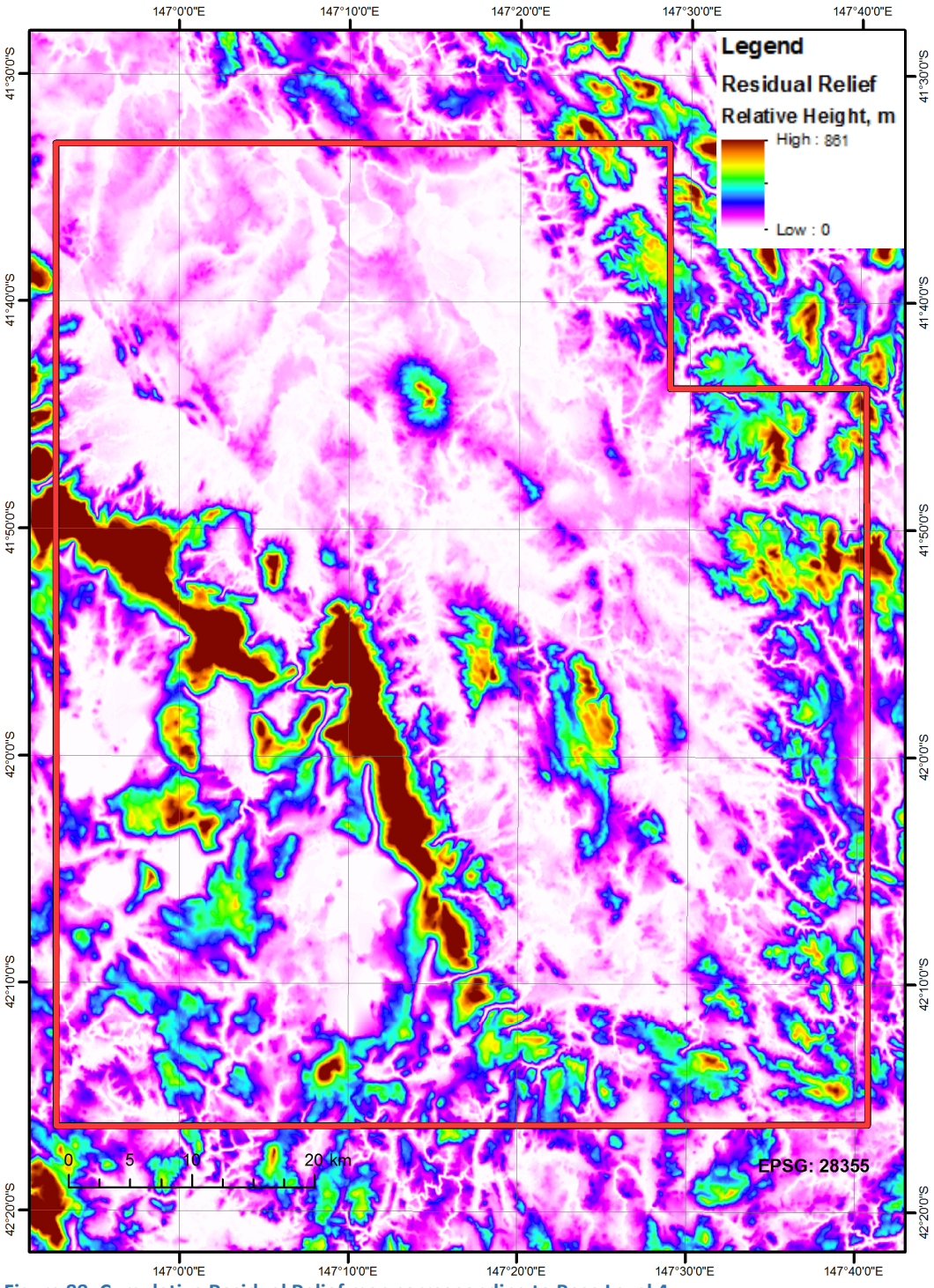


Figure 88: Cumulative Residual Relief map corresponding to Base Level 4.

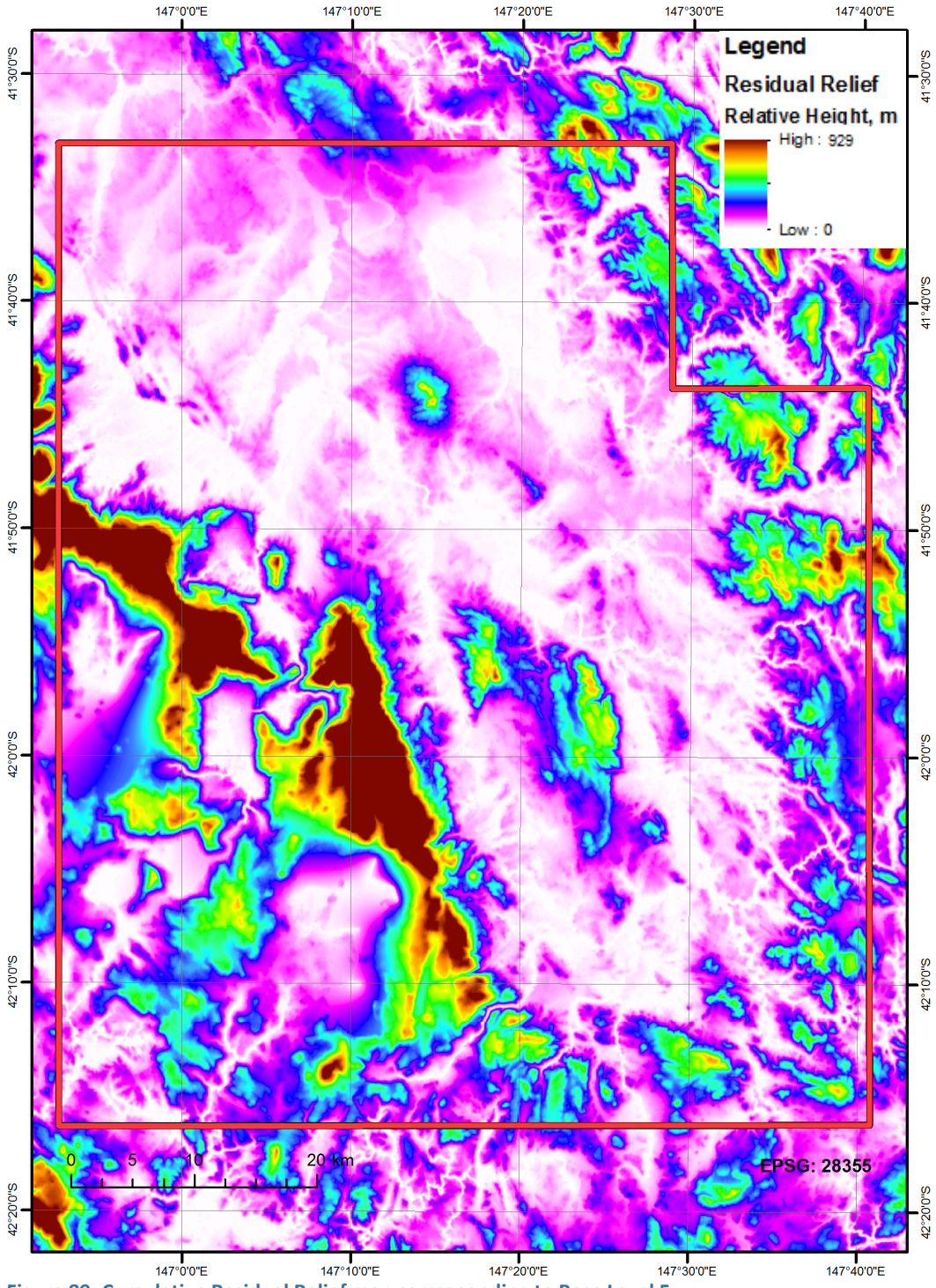


Figure 89: Cumulative Residual Relief map corresponding to Base Level 5.

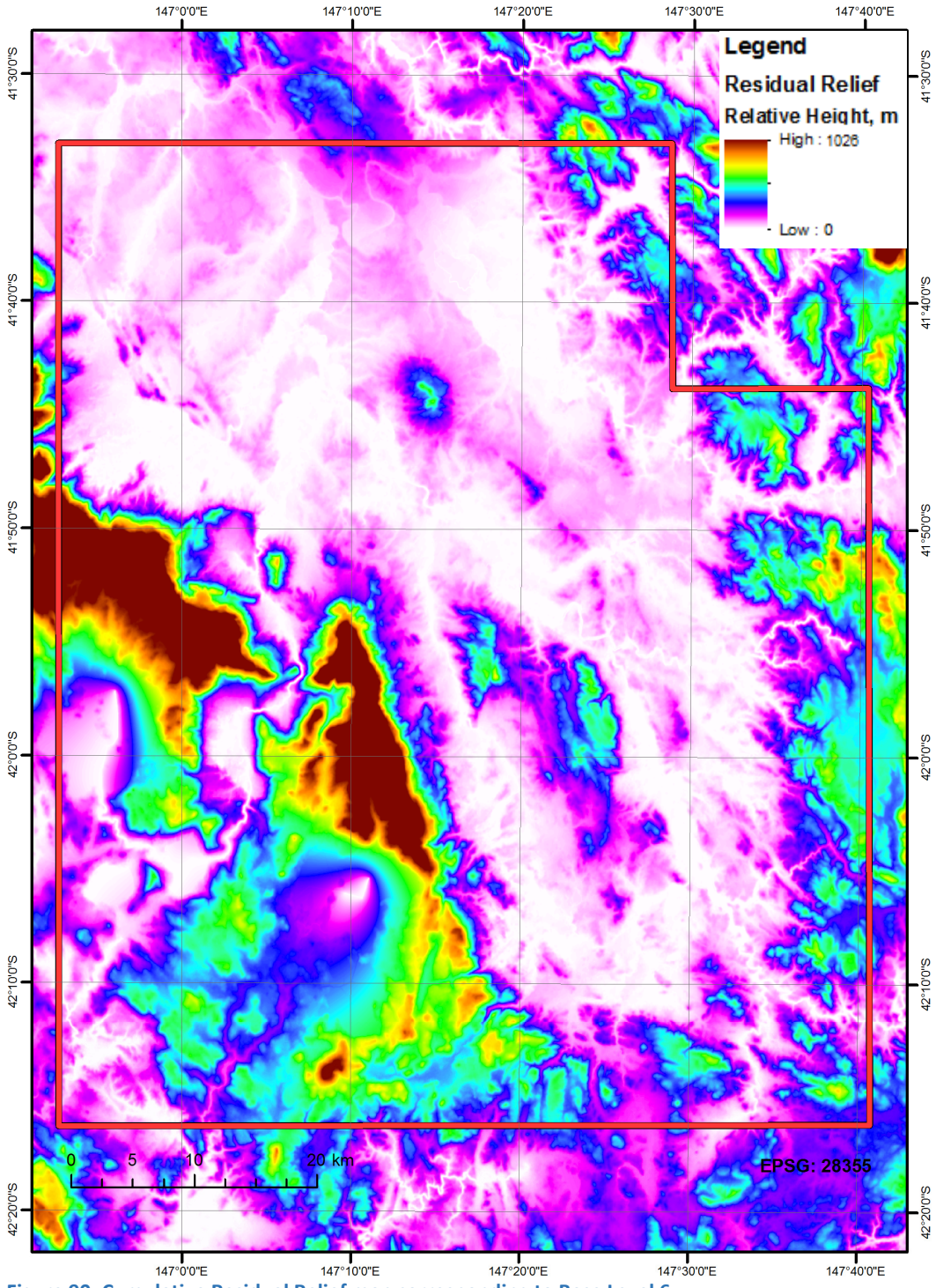


Figure 90: Cumulative Residual Relief map corresponding to Base Level 6.

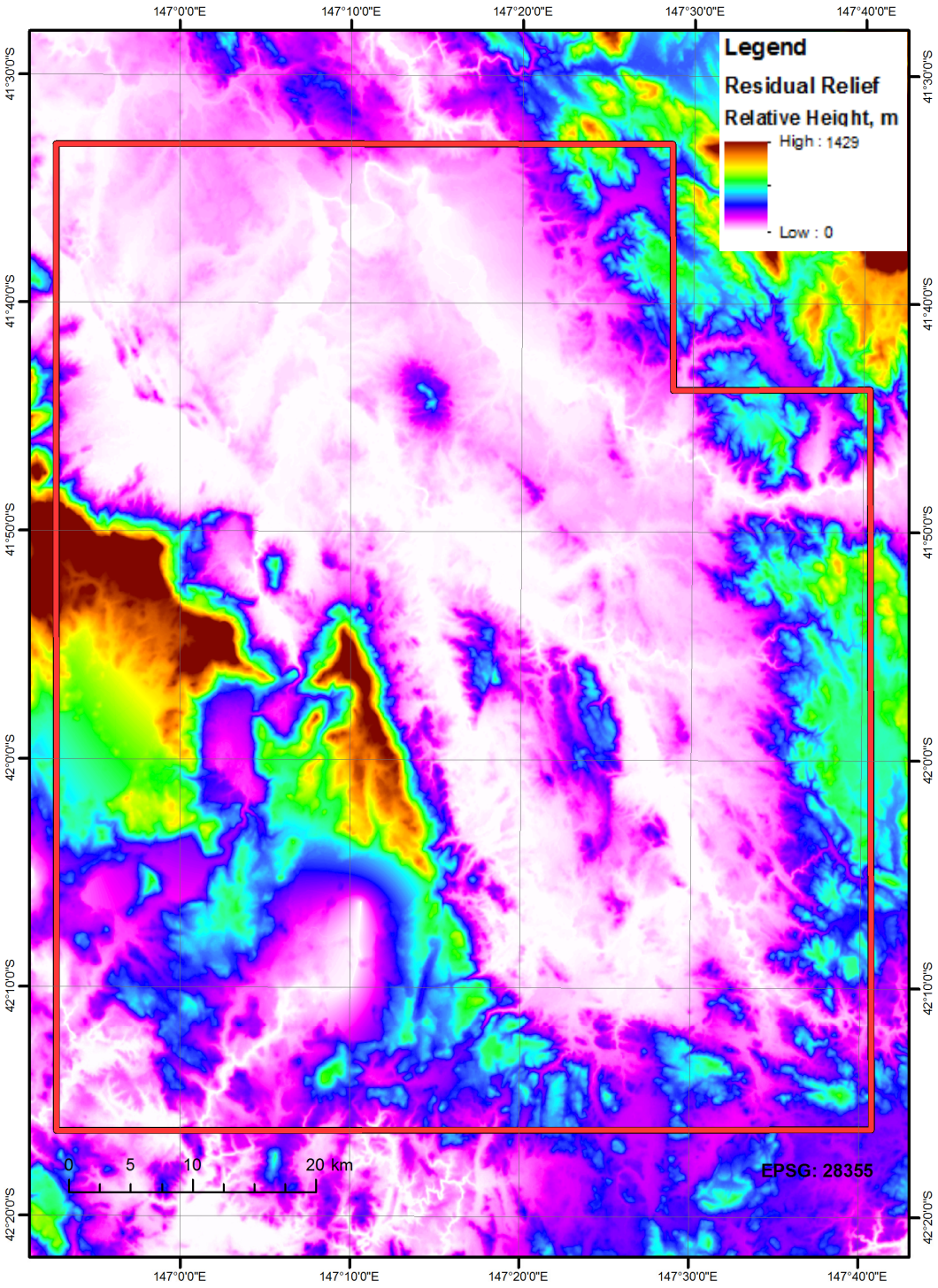


Figure 91: Cumulative Residual Relief map corresponding to Base Level 7.

The Regional (trend) components of the Residual Relief are displayed in

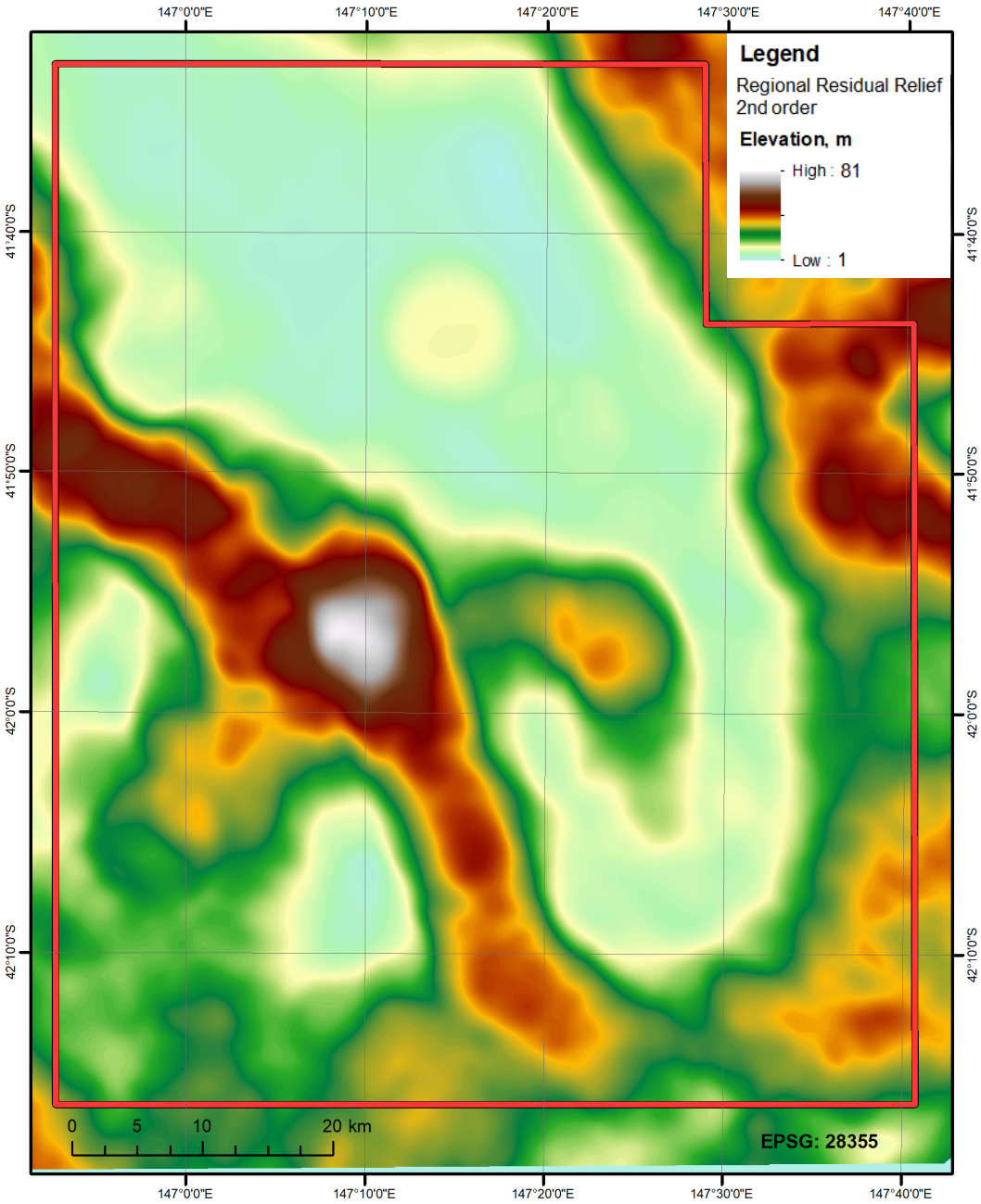


Figure 92: Regional (Trend) Residual Relief map corresponding to Base Level 2.

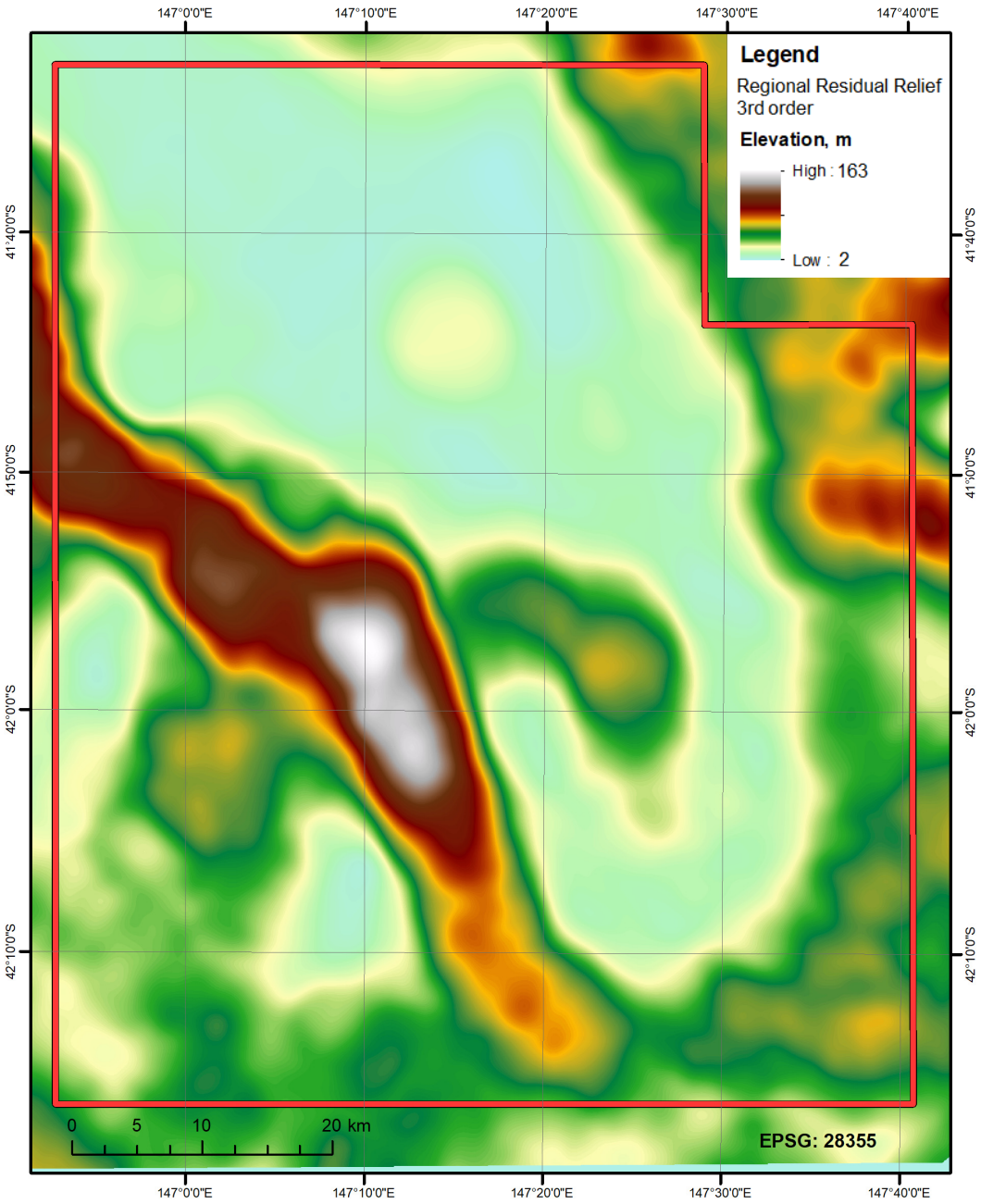


Figure 93: Regional (Trend) Residual Relief map corresponding to Base Level 3.

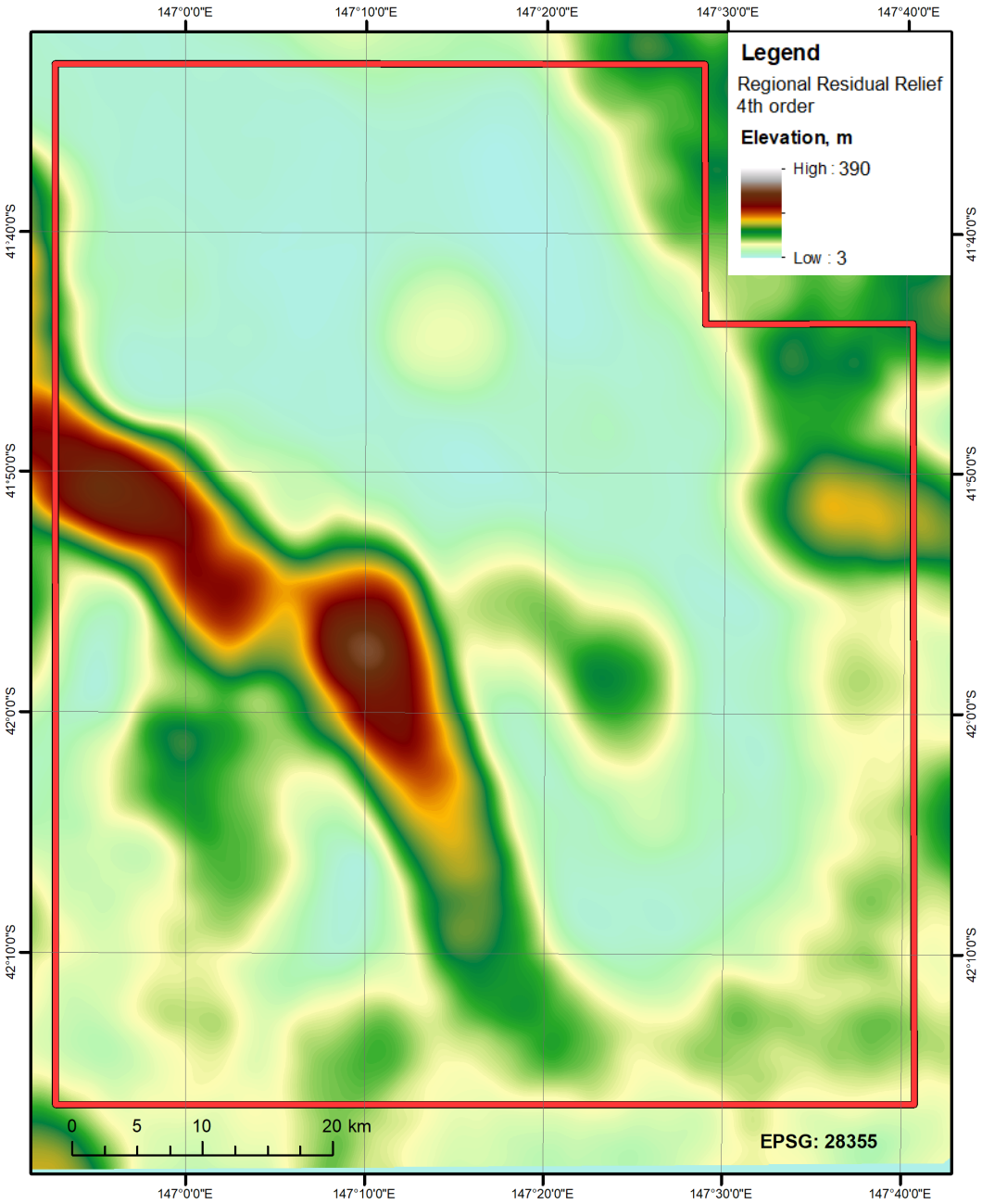


Figure 94: Regional (Trend) Residual Relief map corresponding to Base Level 4.

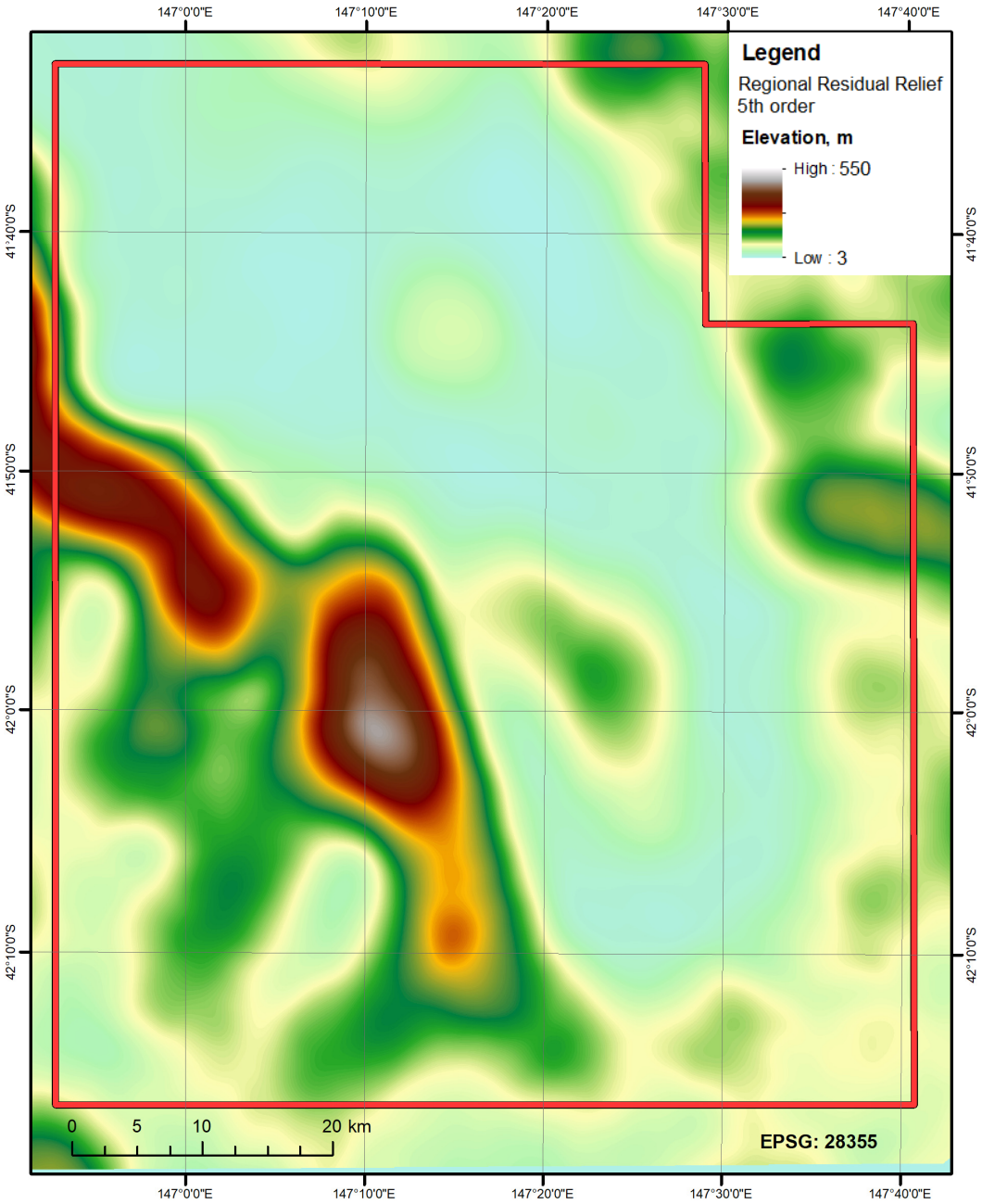


Figure 95: Regional (Trend) Residual Relief map corresponding to Base Level 5.

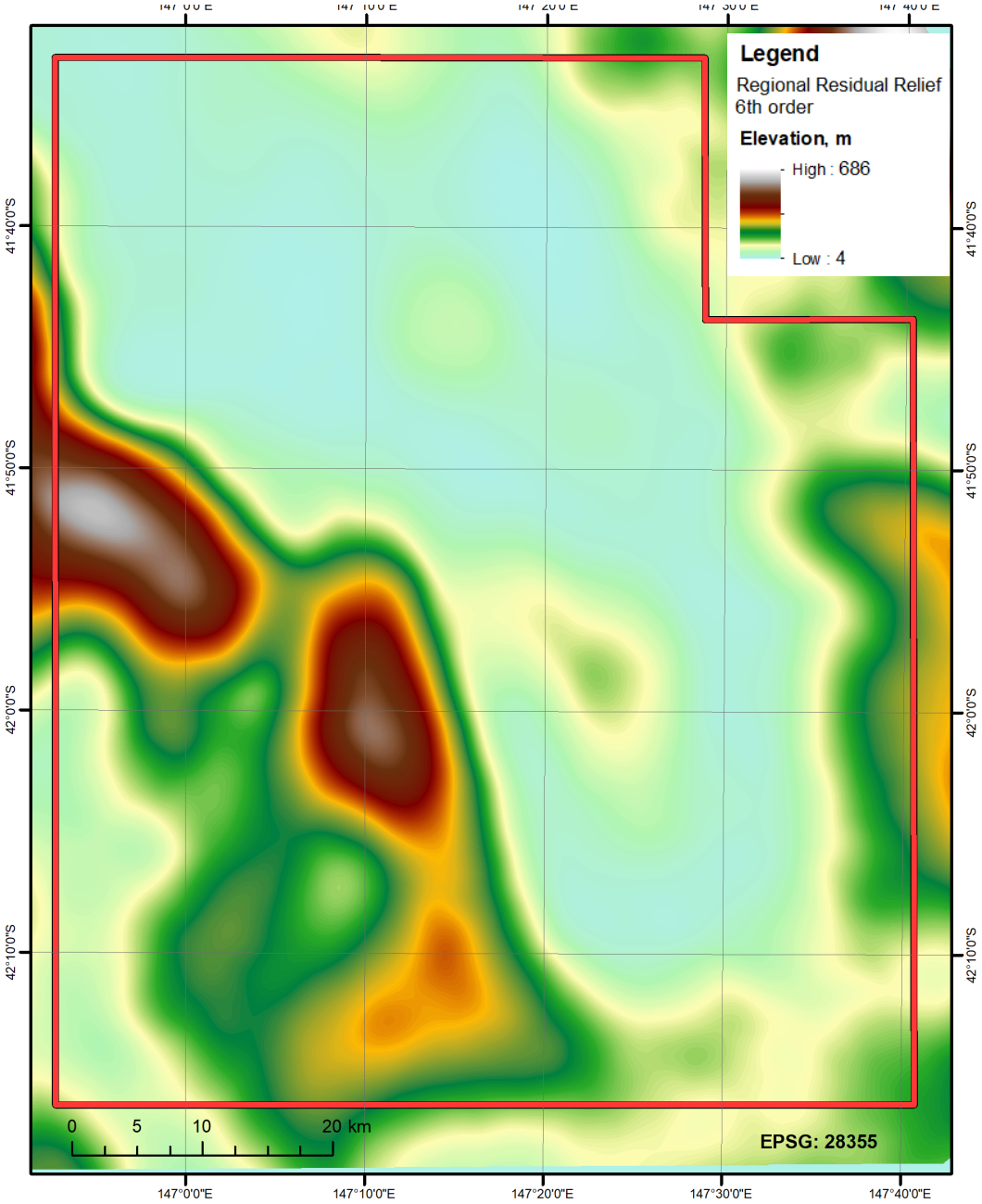


Figure 96: Regional (Trend) Residual Relief map corresponding to Base Level 6.

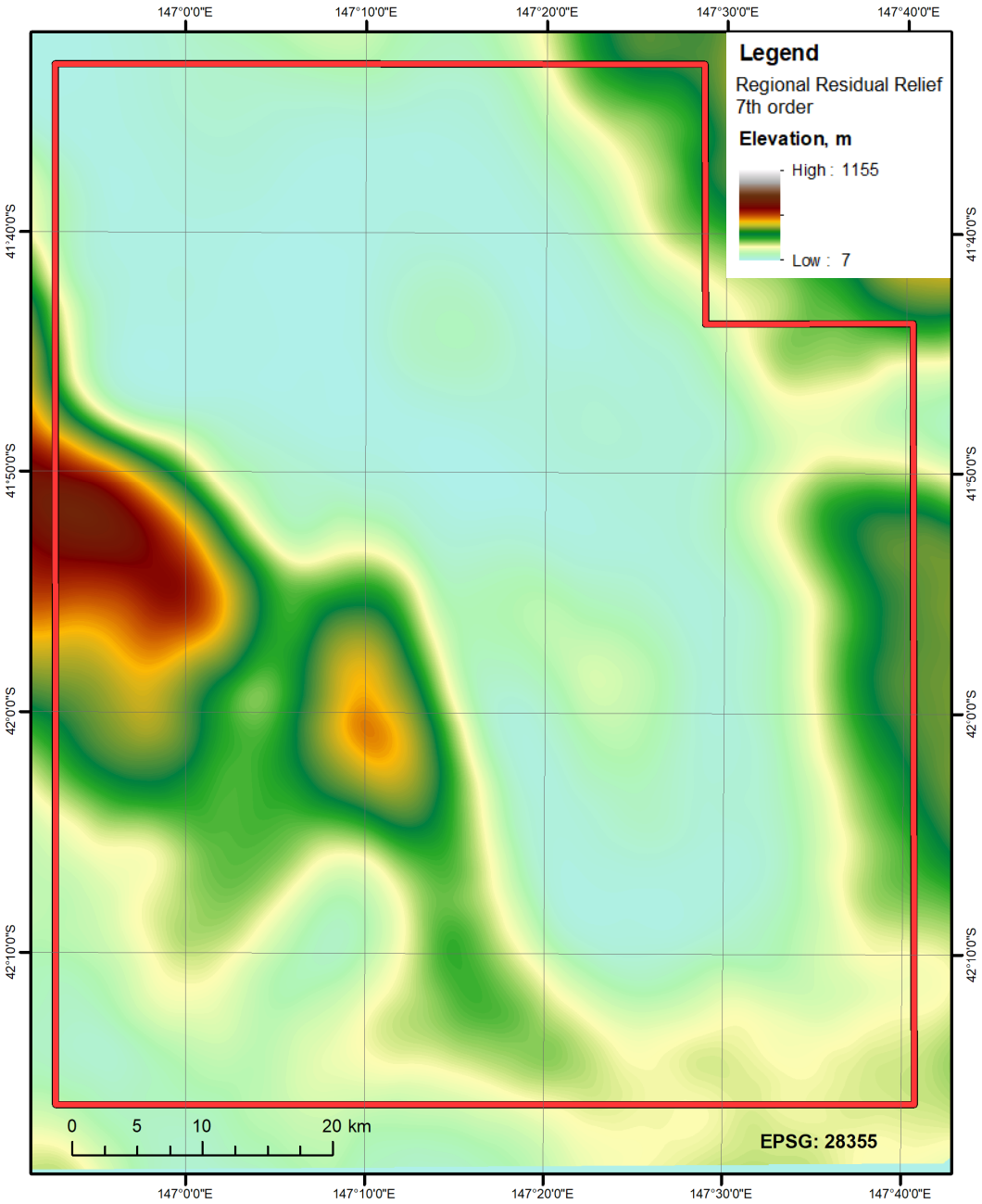
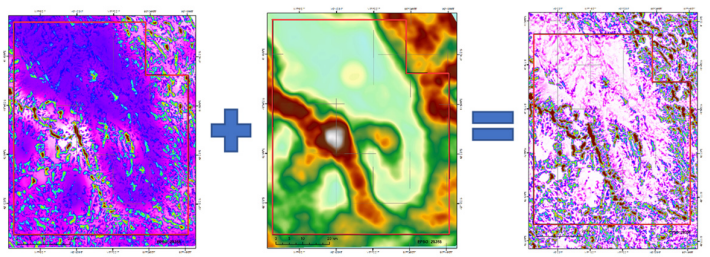


Figure 97: Regional (Trend) Residual Relief map corresponding to Base Level 7.

The Local Residual Relief has been extracted, as described above and is graphically shown below, and presented in **Figure 98** - **Figure 101**.



Local Residual Relief | Regional Residual Relief | Cumulative Residual Relief

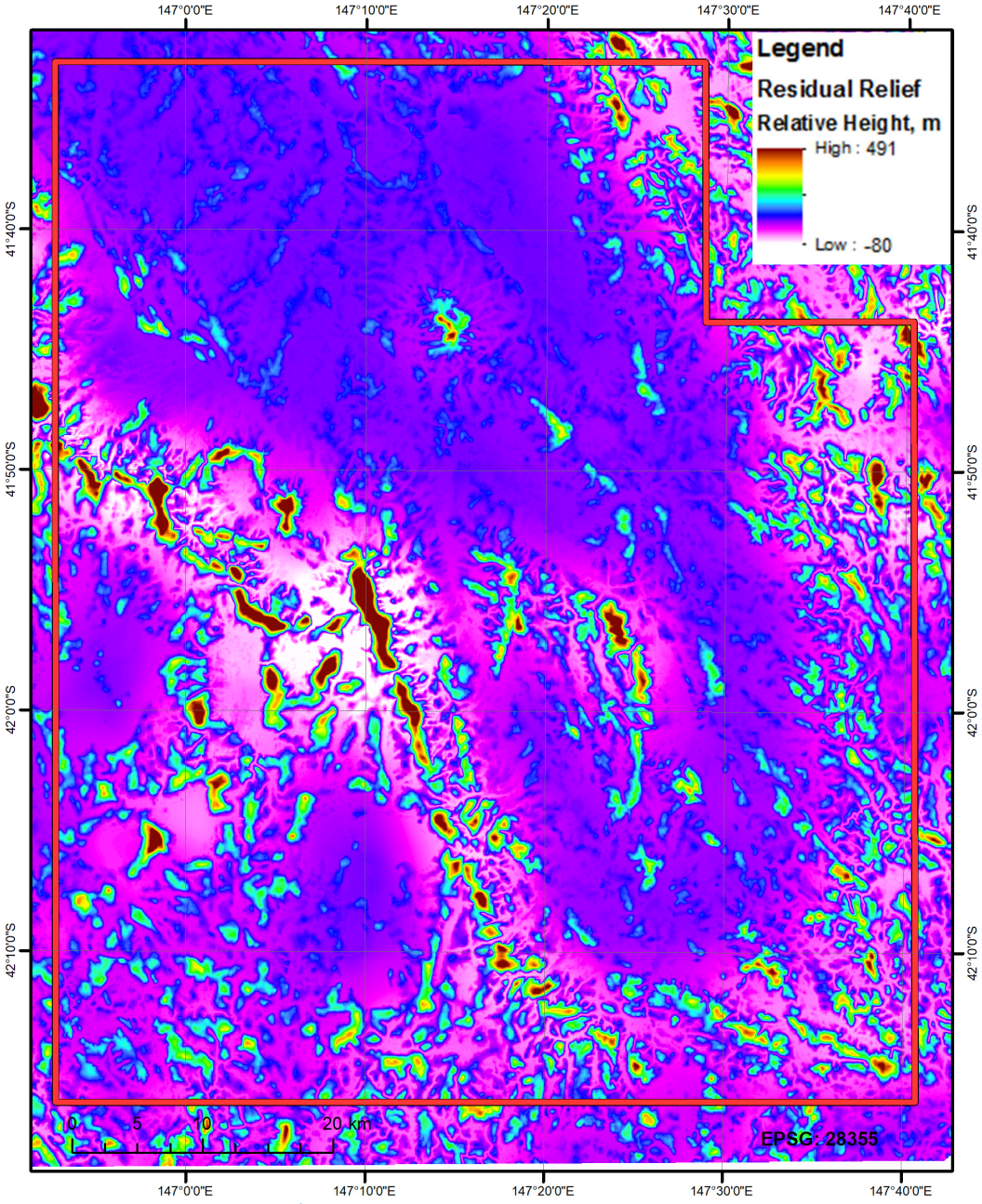


Figure 98: Local Residual Relief map corresponding to Base Level 2.

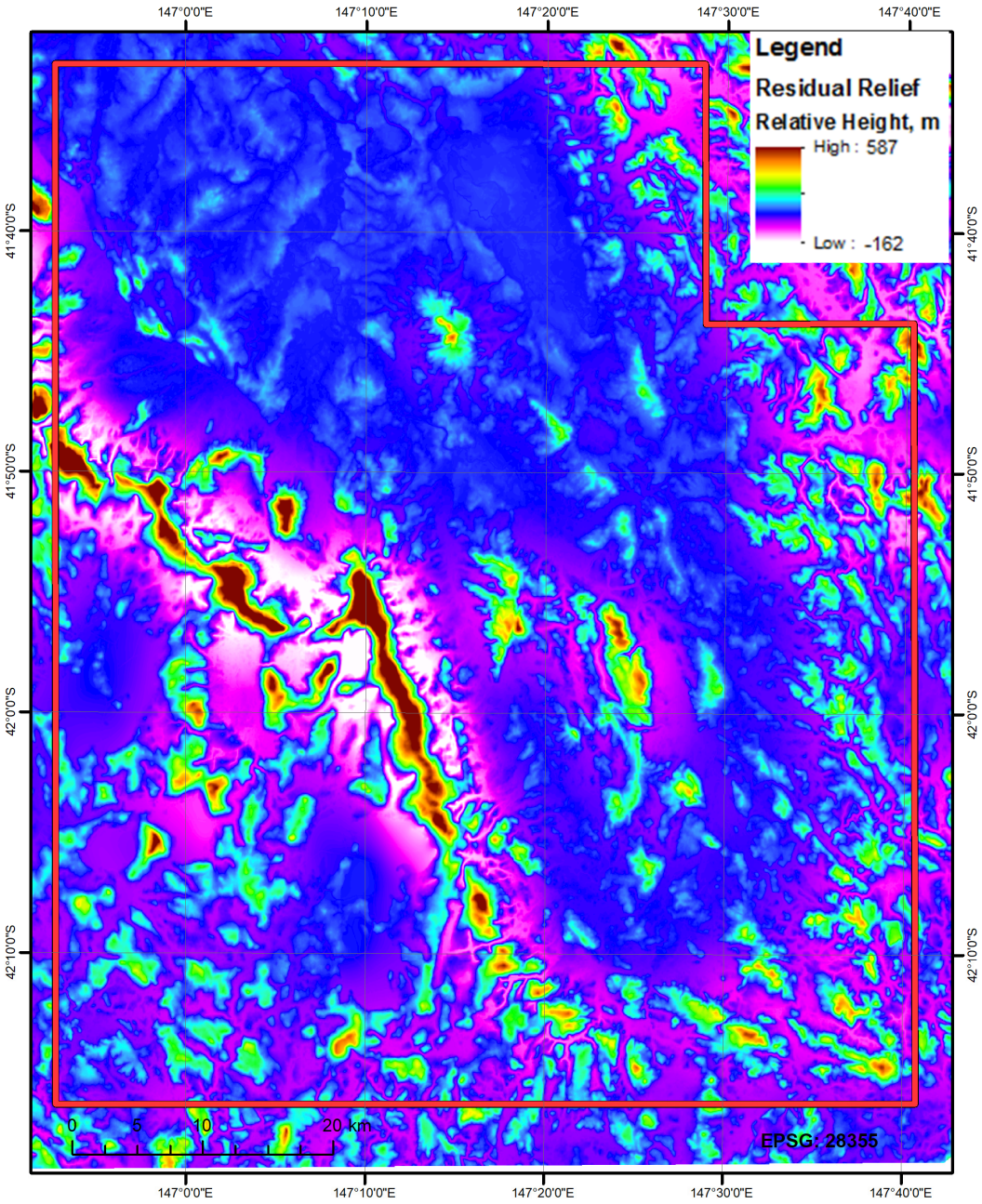


Figure 99: Local Residual Relief map corresponding to Base Level 3.

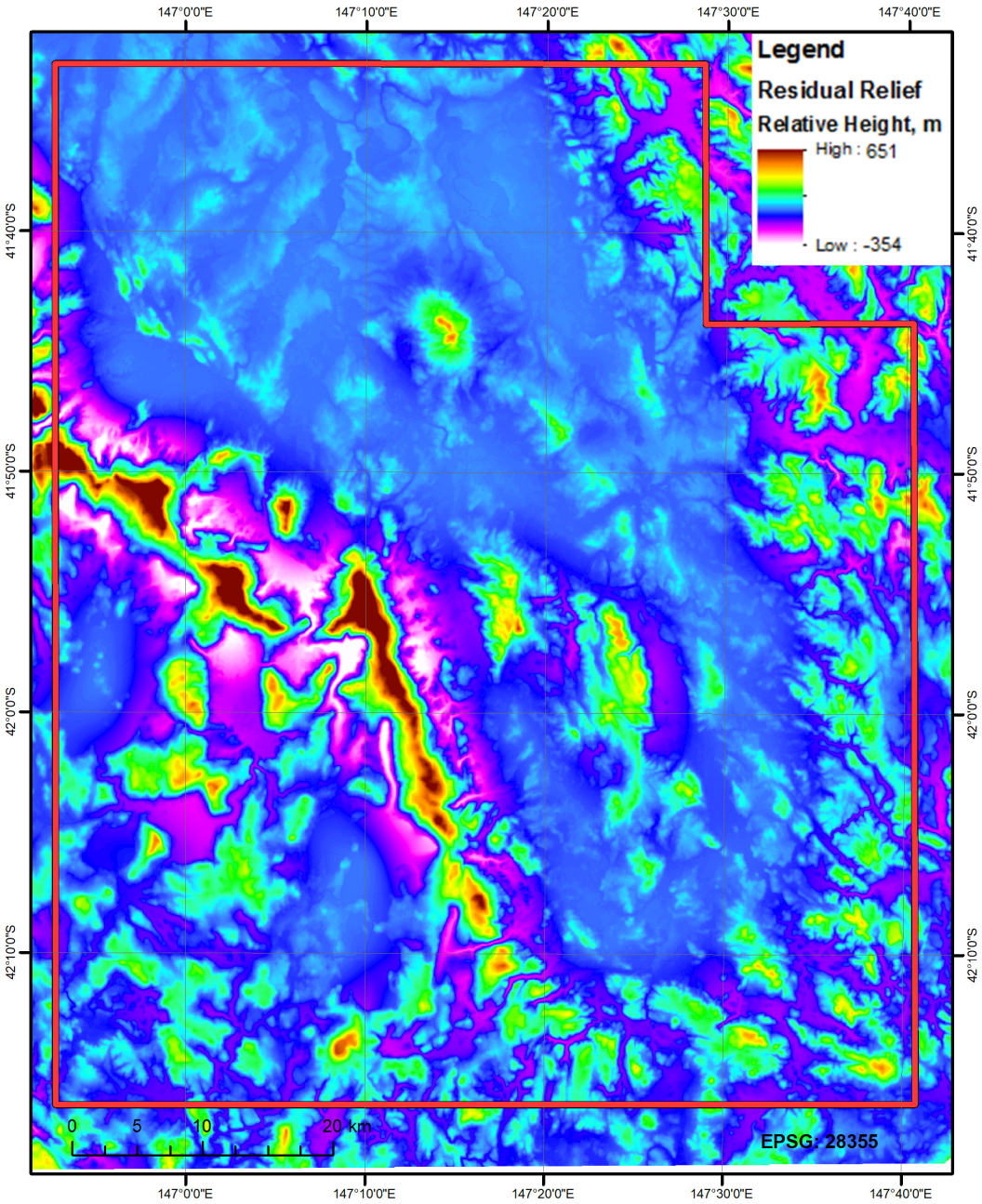


Figure 100: Local Residual Relief map corresponding to Base Level 4.

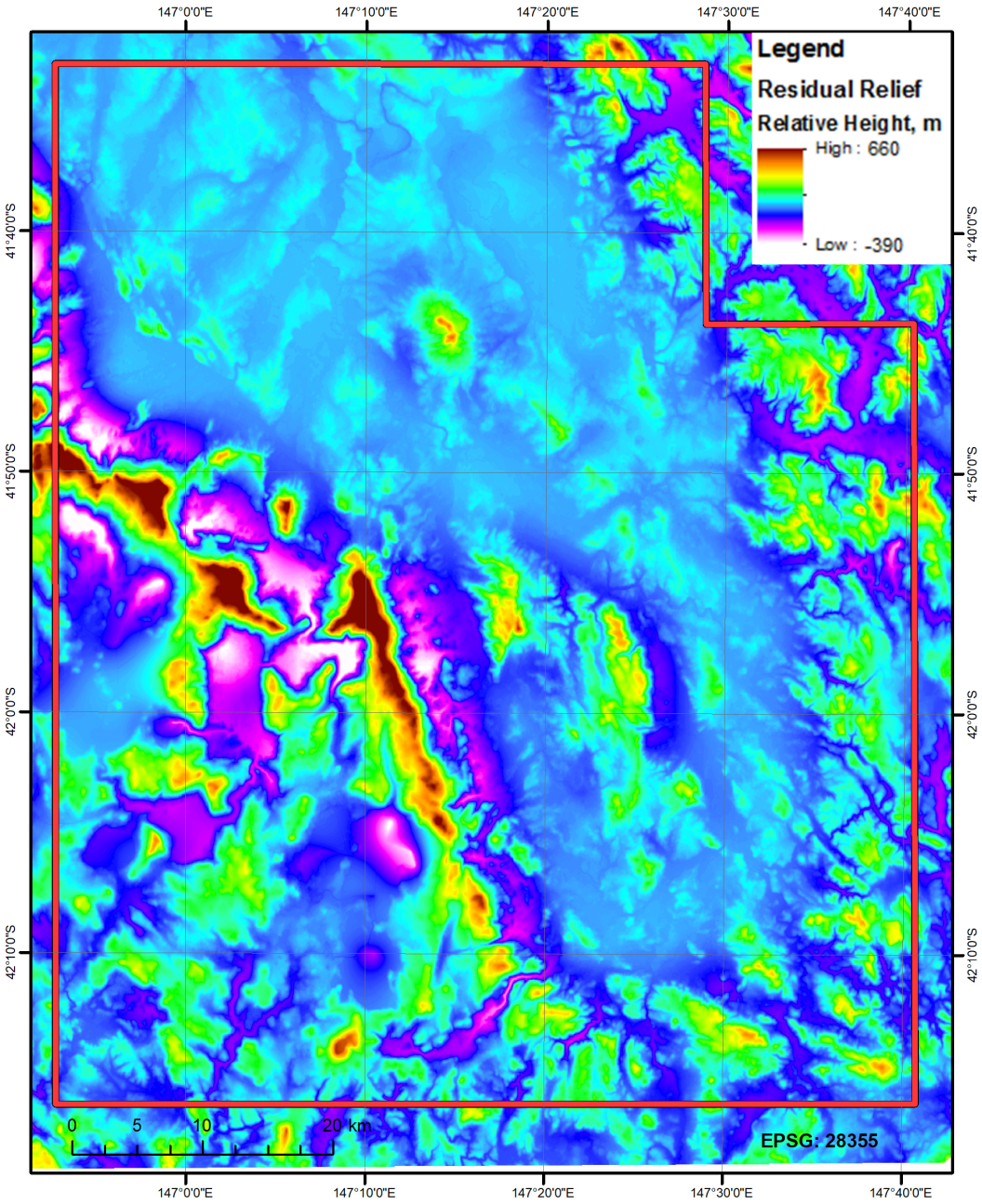


Figure 101: Local residual relief map corresponding to Base Level 5.

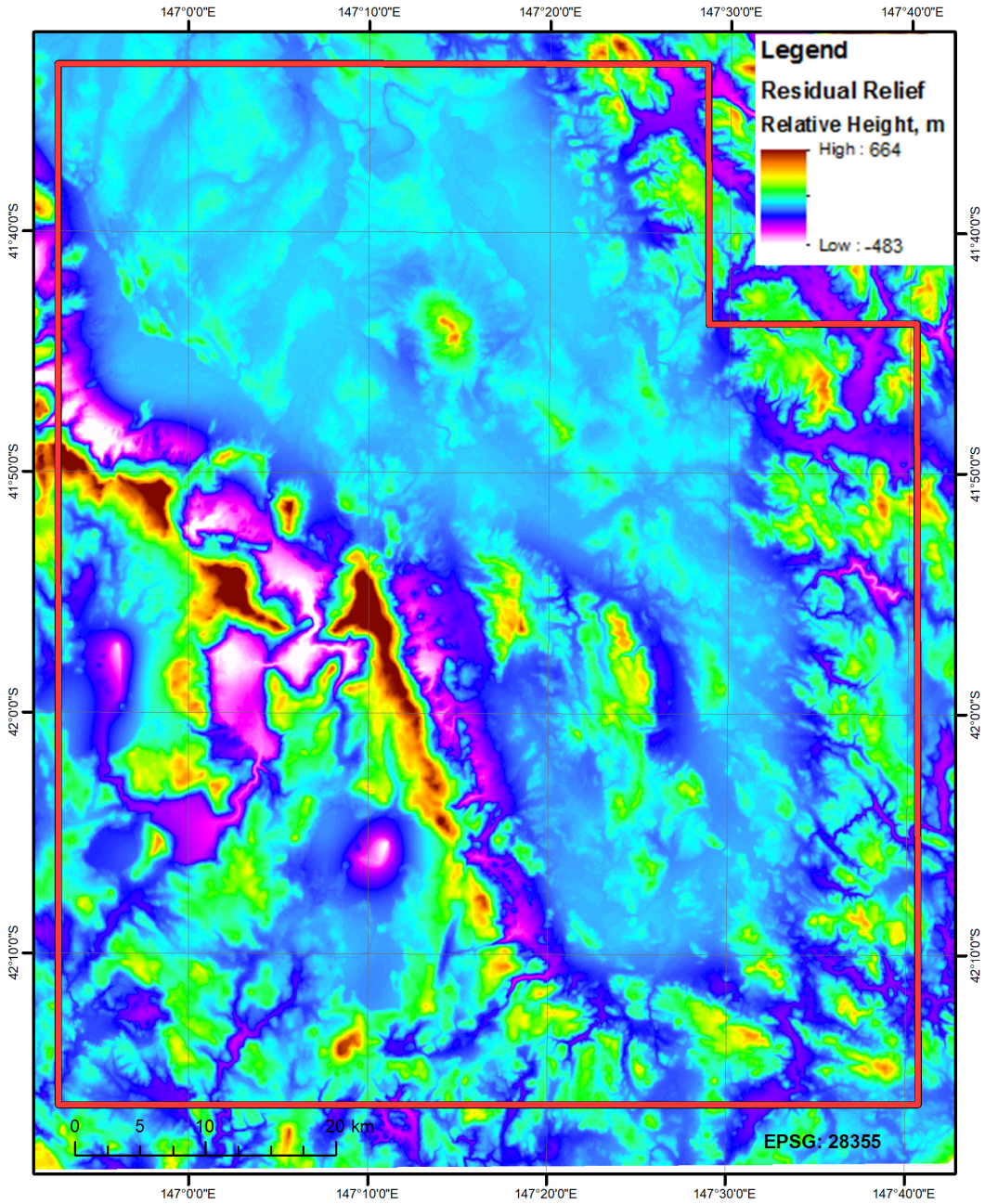


Figure 102: Local residual relief map corresponding to Base Level 6.

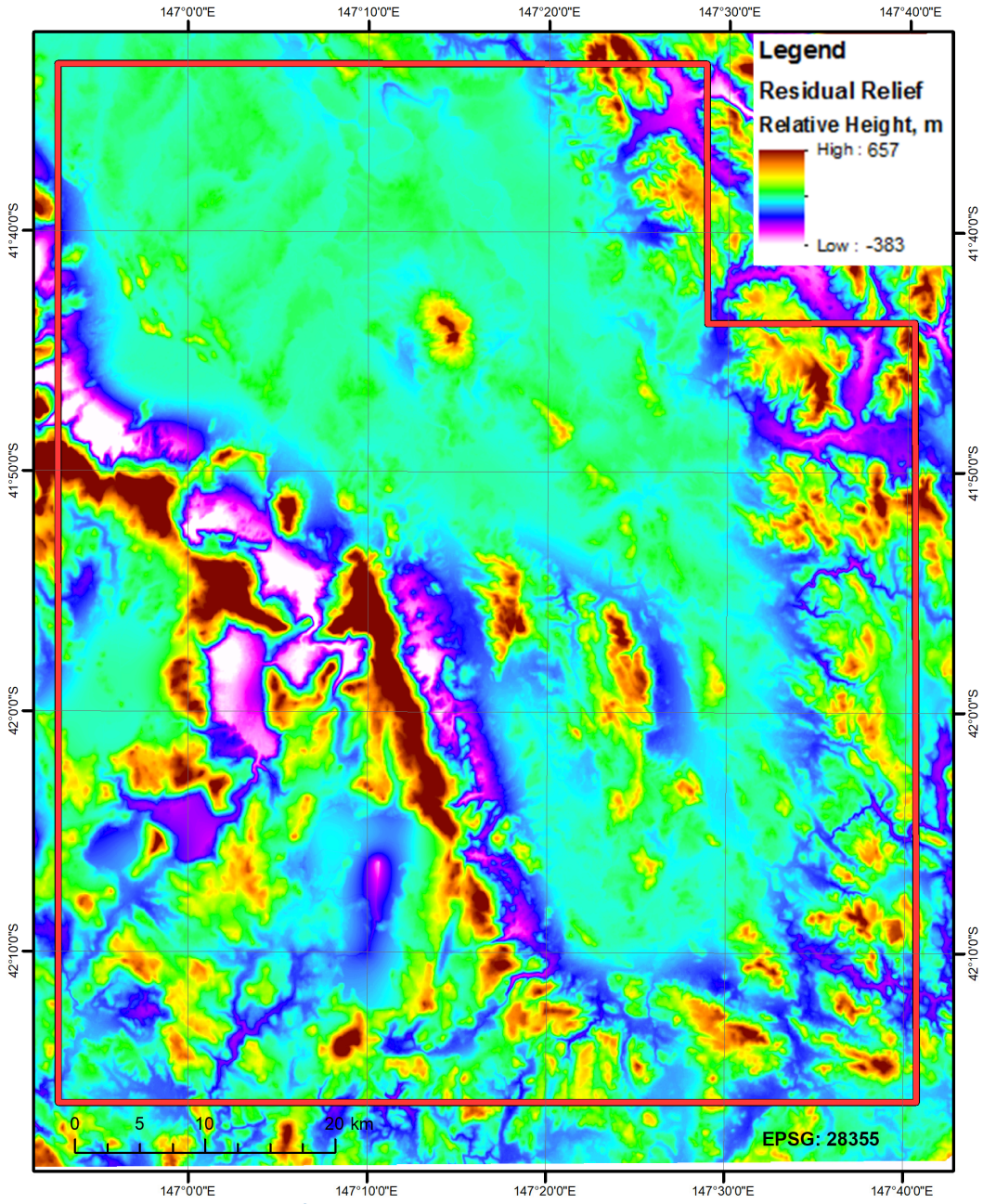


Figure 103: Local residual relief map corresponding to Base Level 7.

COMBINED ANALYSIS OF BASE LEVEL & RESIDUAL RELIEF MAPS

In order to confirm the existence of anticlines, a combined interpretation of residual relief and Base Level maps is required and provided in this report.

A combined interpretation of Base Level maps (isobase lines) and Residual Relief maps provides an opportunity to distinguish anticlinal structures. Potential anticlines can be distinguished on the aforementioned resulting maps based on the following two conditions: 1) thickening of isolines in a shape of a half-ellipse, horseshoe, loop, or «structural nose»; and 2) Local Residual Relief peaks coincide with the areas of thickening isobase lines and follow their "horseshoe-like" contours (described in item 1) as shown in Figure 106.

There are two major types of relief - direct and inverse. In direct relief, watersheds and anticlinal domes as well as river valleys and synclines coincide (**Figure 104**). Inverse relief works in reverse: river valleys are located above anticlinal domes, while watersheds correspond to synclines in the subsurface (**Figure 105**).

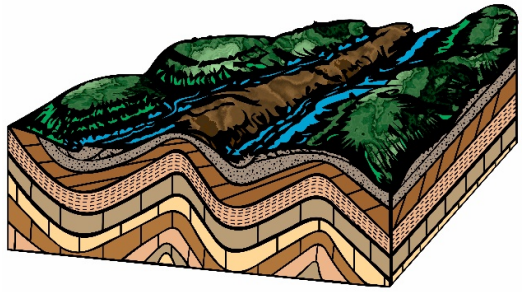


Figure 104: Example of direct relief

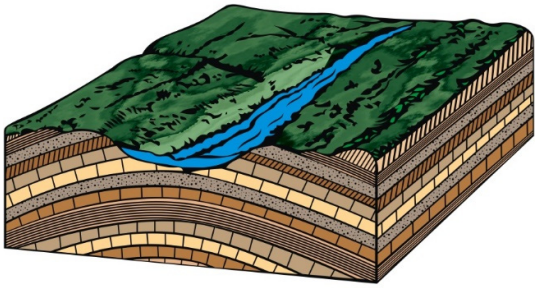


Figure 105: Example of inverse relief

In situations, where local anticlines that are reflected in a direct relief, the residual relief does the following: 1. it forms small enclosed structures; 2. its elevations at the periphery of such structures have small oval small almost closed contours with the internal side almost certainly contouring the anticlinal dome.

In situations, where local anticlines that are reflected in an inverse relief, the residual relief does the following: 1. above the anticlines, its elevations are almost equal to background values; 2. at the periphery of anticlines, it is characterized by high, distinct local elevations in an almost closed-loop concentric shape of a concave that is turned towards the anticlinal dome.

Local anticlinal folds can be detected by combining Base Level and Residual Relief maps as shown in **Figure 106**.

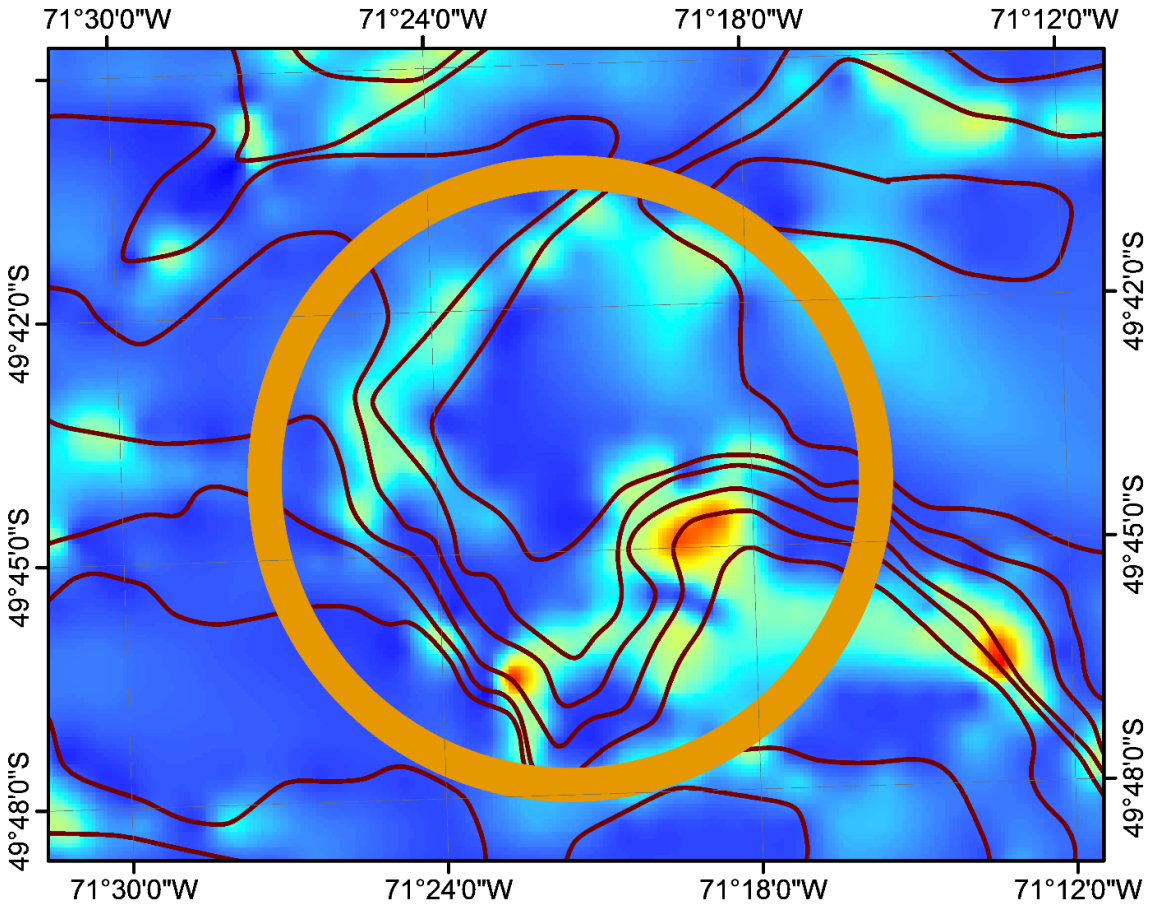


Figure 106: Example of revealing local tectonic structures.

Base Level and Local Residual Relief maps for Levels 2 through 7 have been combined to locate local anticlines as described above (**Figure 107** through **Figure 112**).

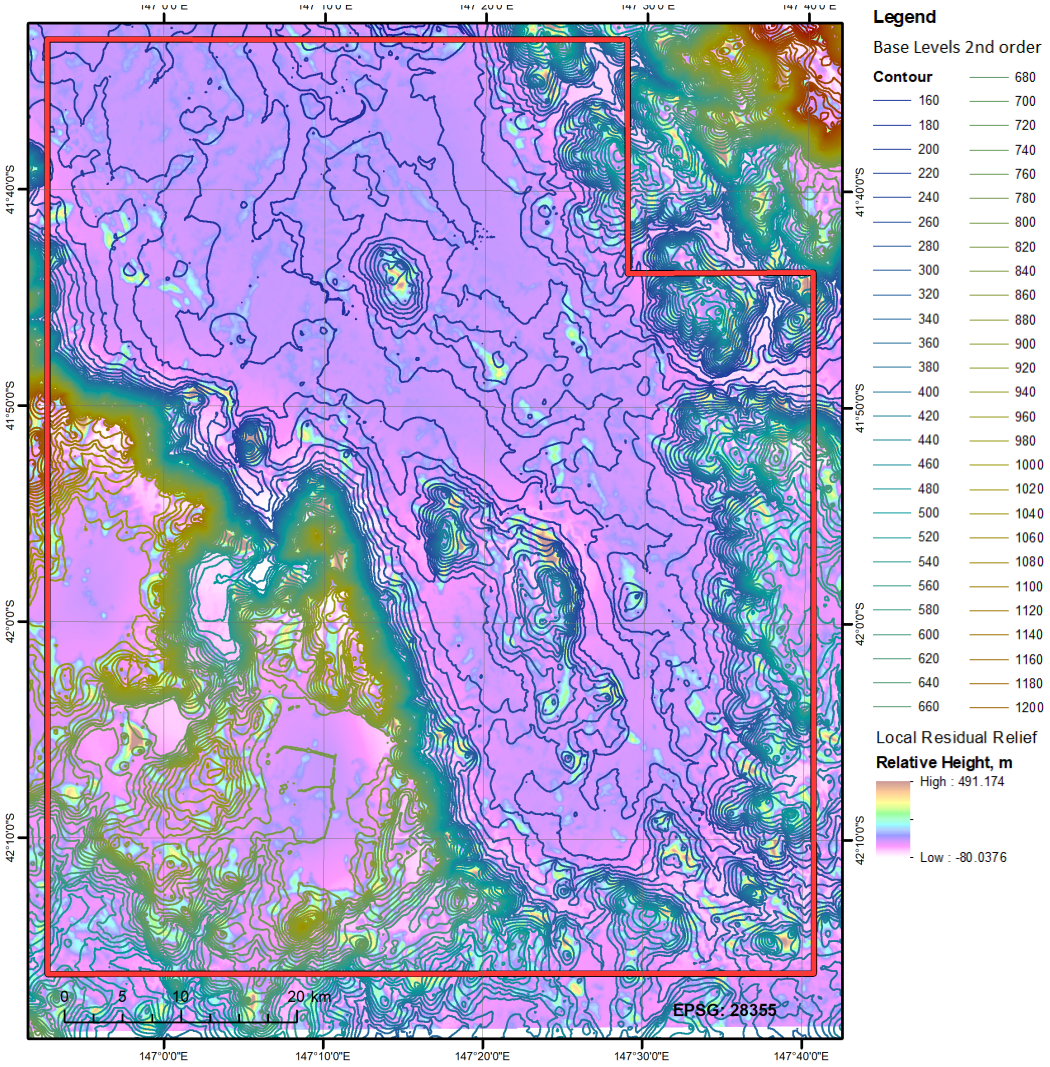


Figure 107: Local Residual Relief and Base Level maps 2nd order.

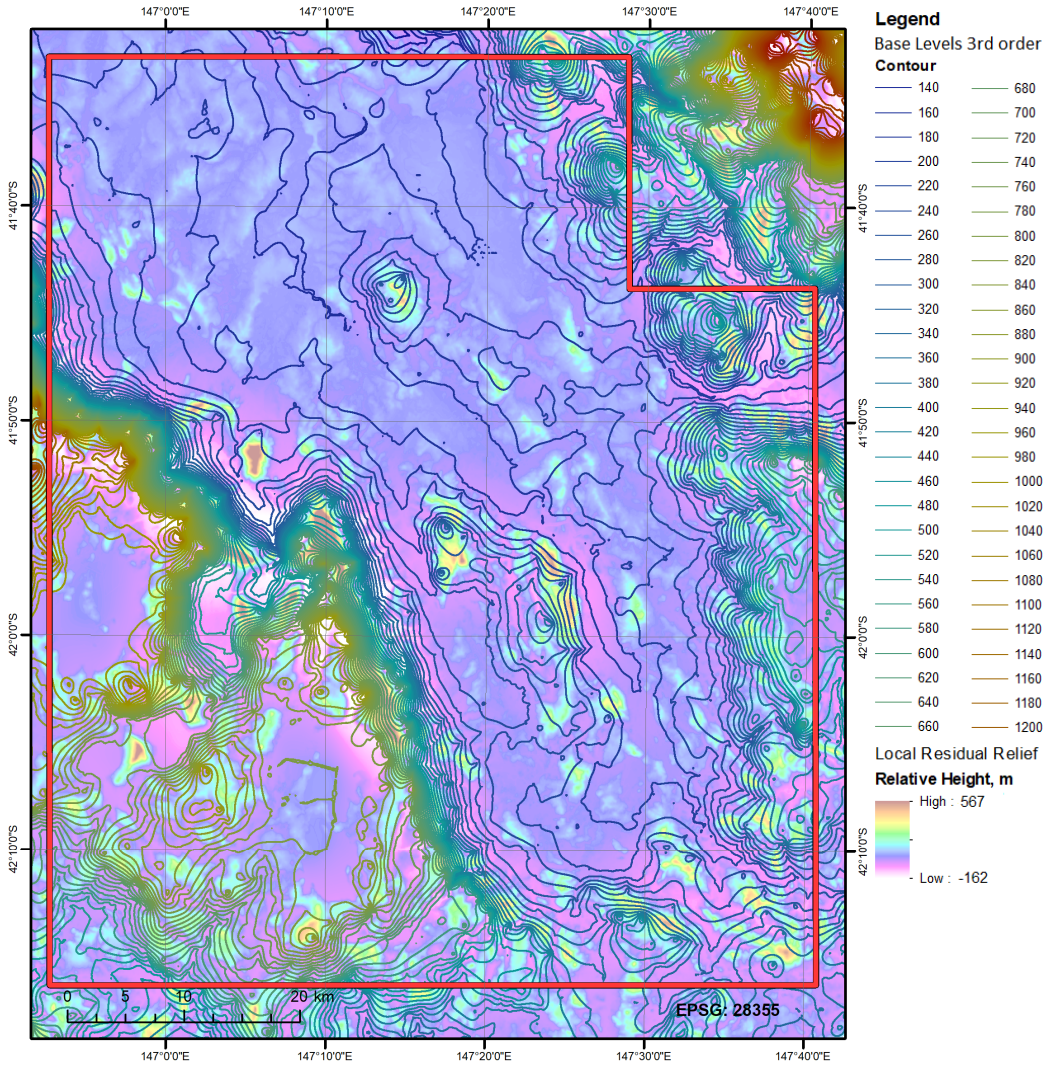


Figure 108: Local Residual Relief and Base Level maps 3rd order.

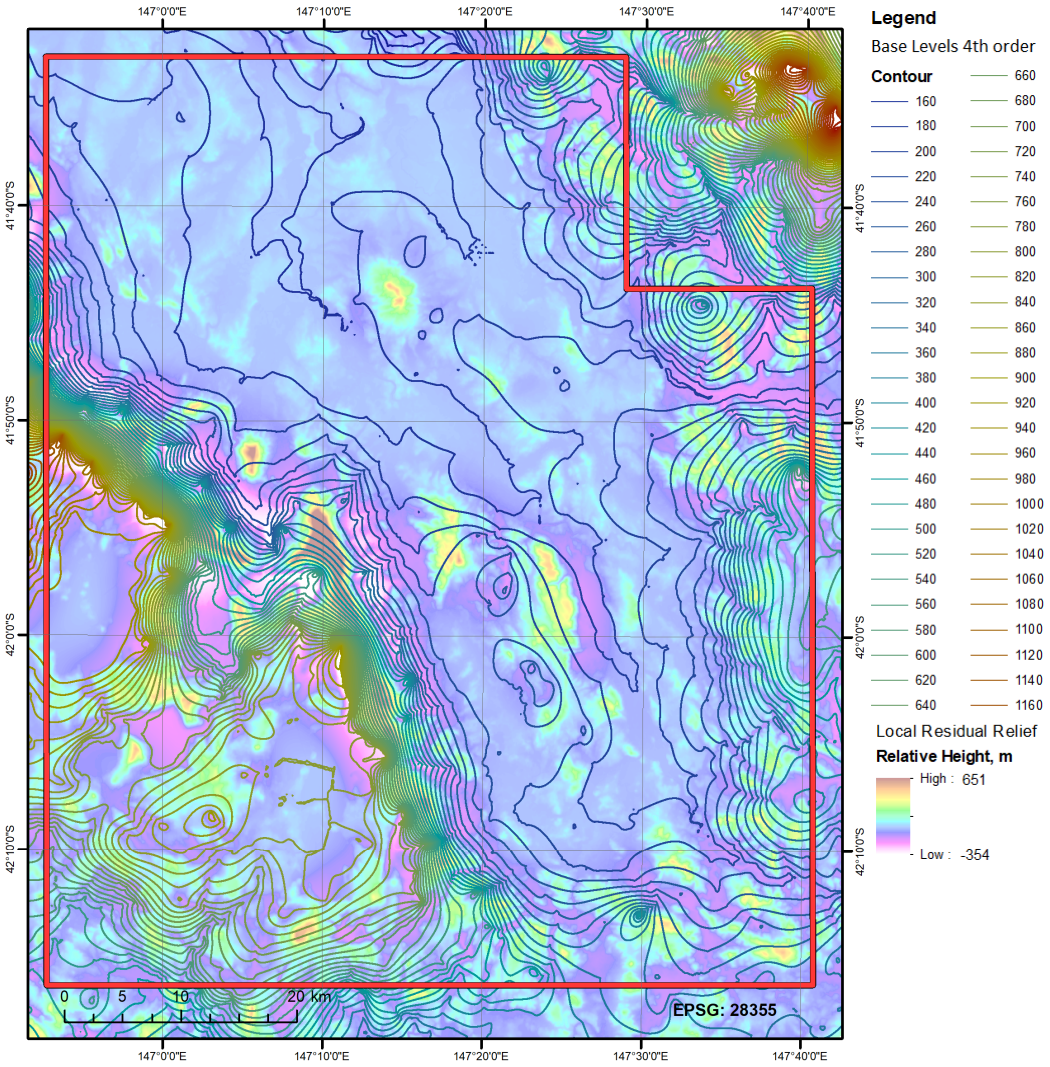


Figure 109: Local Residual Relief and Base Level maps 4th order.

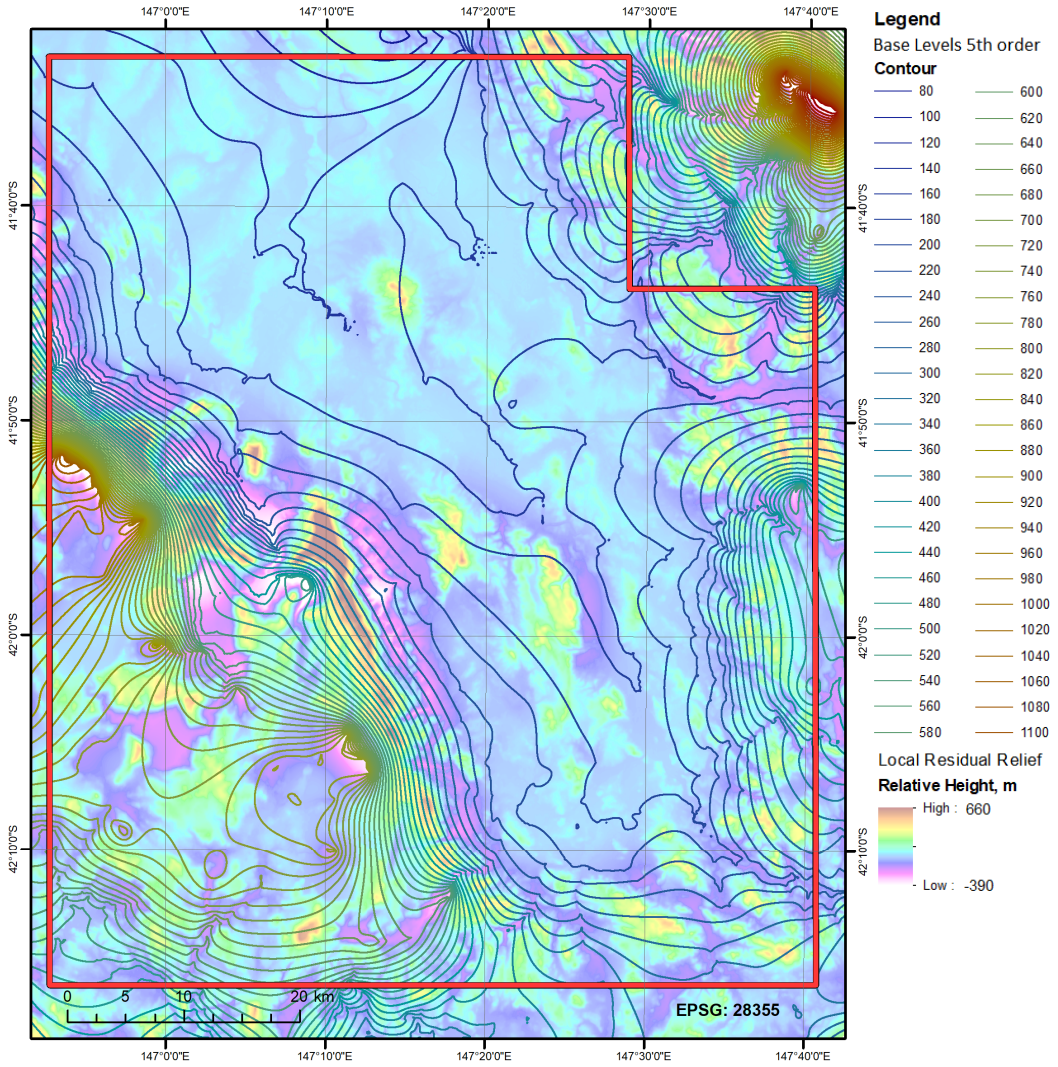


Figure 110: Local Residual Relief and Base Level maps 5th order.

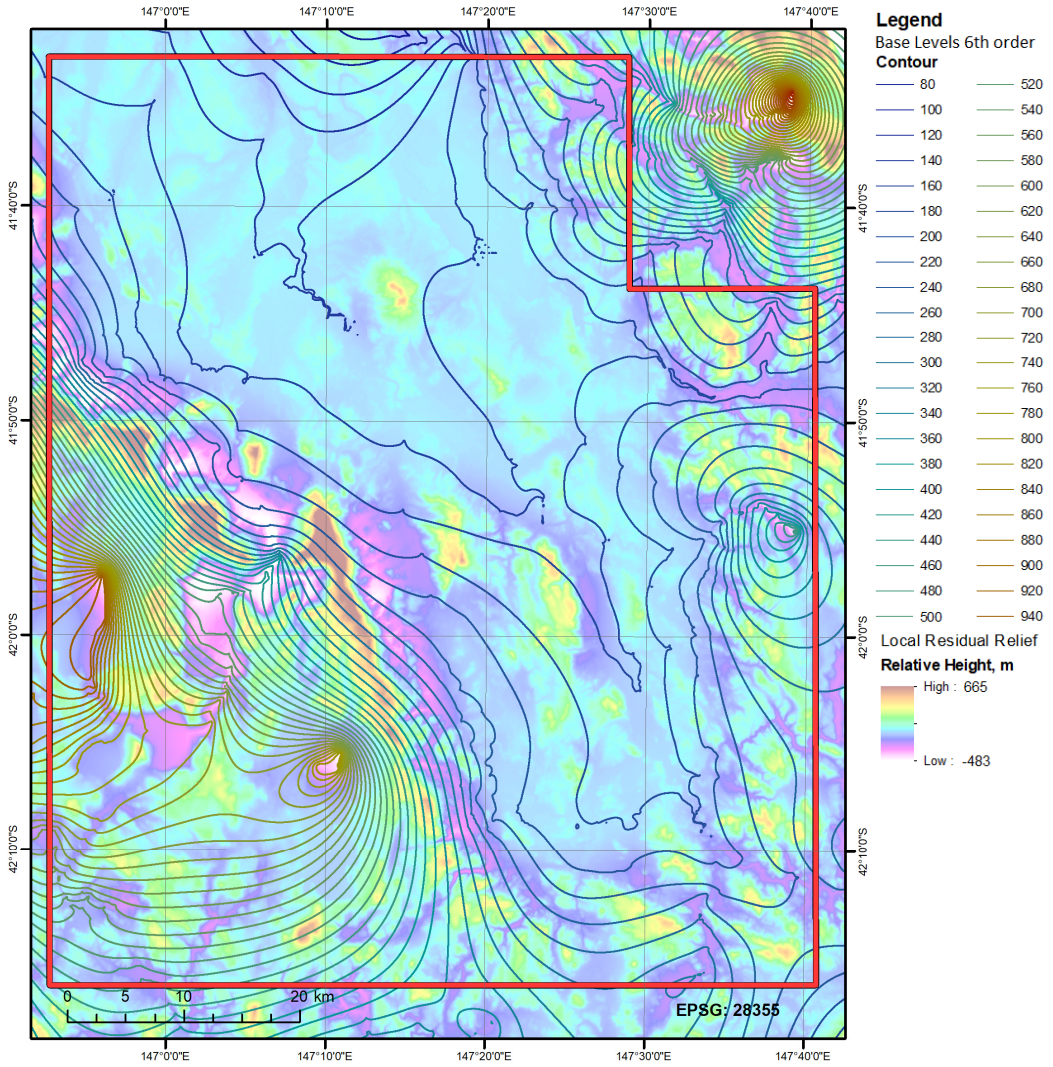


Figure 111: Local Residual Relief and Base Level maps 6th order.

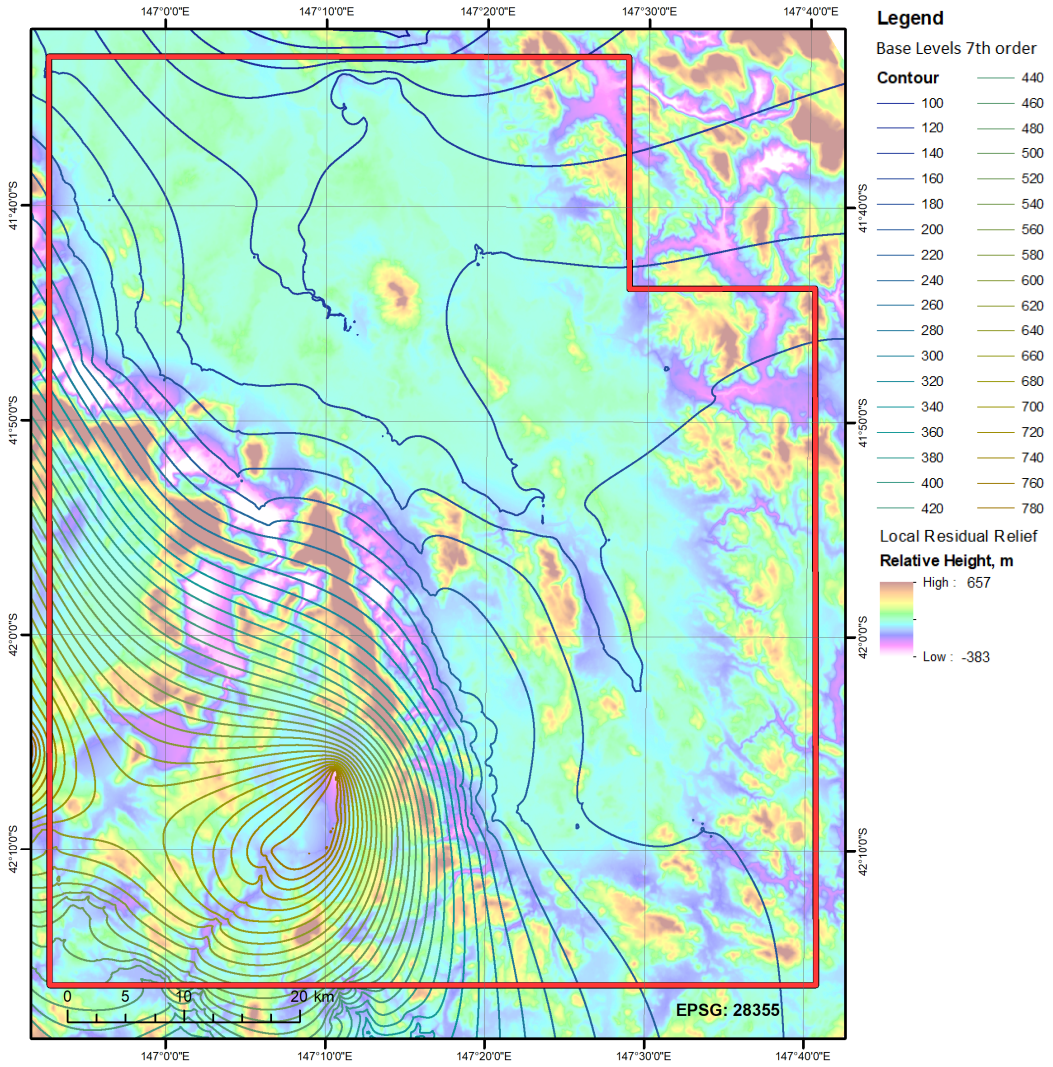


Figure 112: Local Residual Relief and Base Level maps 7th order.

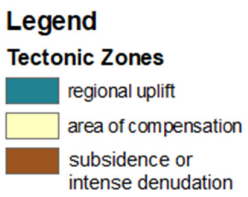
DIFFERENTIAL BASE LEVEL MAPS

Differential Base Level maps are created by an algebraic subtraction of elevations of a higher order Base Level map from a lower order one.

The highest difference between elevations of Base Levels is usually associated with local anticlines. Differential Base Level maps allow allocating zones of tectonic subsidence and uplift. Differential Base Level maps and the analysis of isobase lines' behavior allow distinguishing zones of recent (relative to levels) uplifts and subsidence areas, while the form of isobase lines helps identify anticlinal structures with local positive movements.

The higher the difference between Base Levels' elevations on a particular area, the more intense tectonic movements can be expected there. Positive differences correspond to positive tectonic movements (direct relief), and negative differences correspond to negative movements of local as well as regional structures. However, the latter case may result in the opposite outcome, where the negative gain of the relative height is caused by an intense local uplifting causing its upper shielding horizon to quickly dissect (significant mechanical stress and irreversible deformation affected by denudation and other forces of nature) leading to the lower, weaker horizons to erode. This is the mechanism of the mechanism of the formation of an inverse relief anticline. The third type the differential isobase surfaces is characterized by the values nearing zero and interpreted as paleo-valleys with the compensational relief (the rate of regional uplifting was compensated by that of erosion and exit of the sedimentary material).

From the HC-prospecting standpoint, the inverse and compensation types of relief (related to the negative and close to zero values of differential isobase surfaces) are of the most in**terest. The areas are colored brown and light-yellow in** Figure 113 through Figure 117.



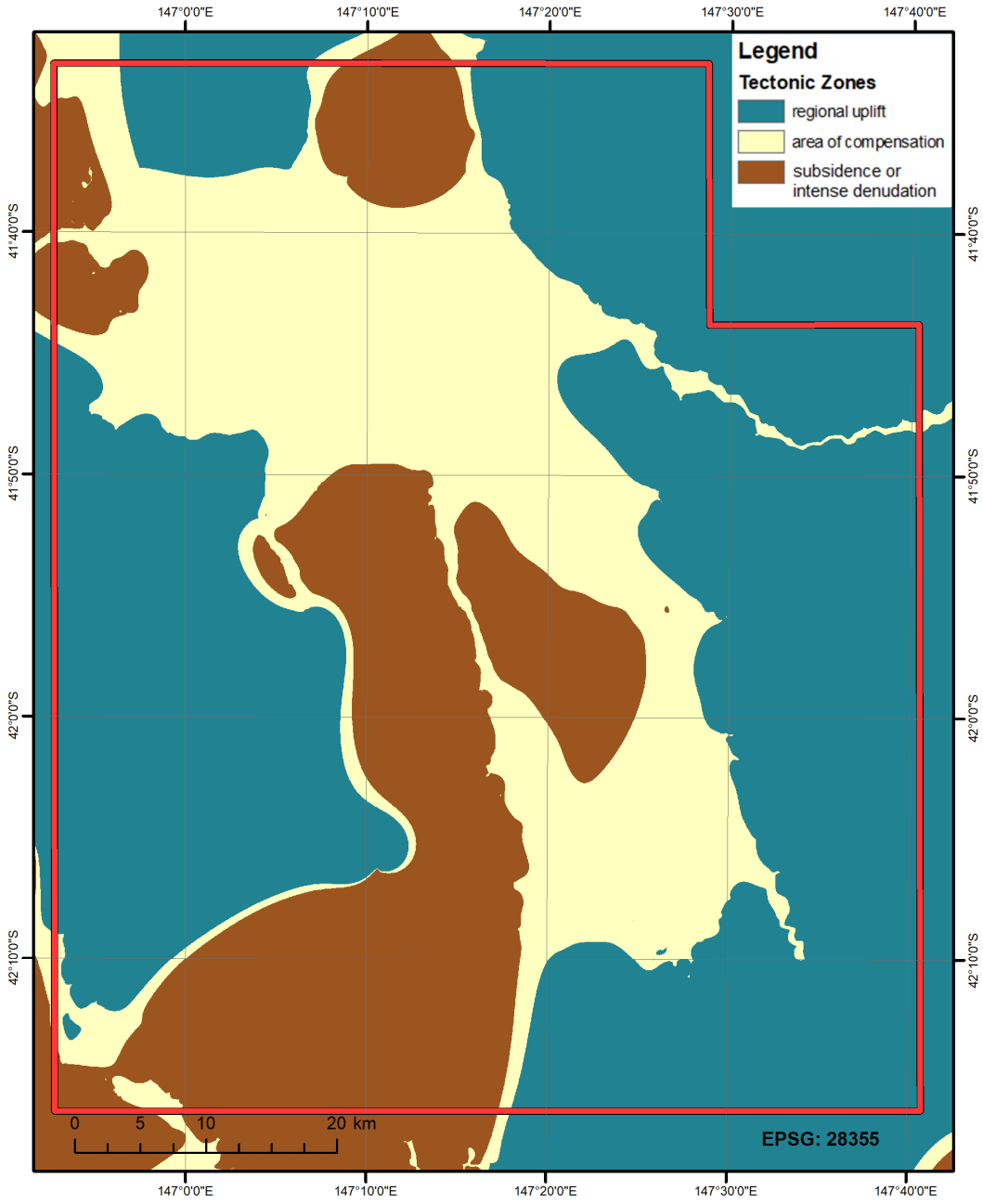


Figure 113: Difference of Base Levels 6 and 7.

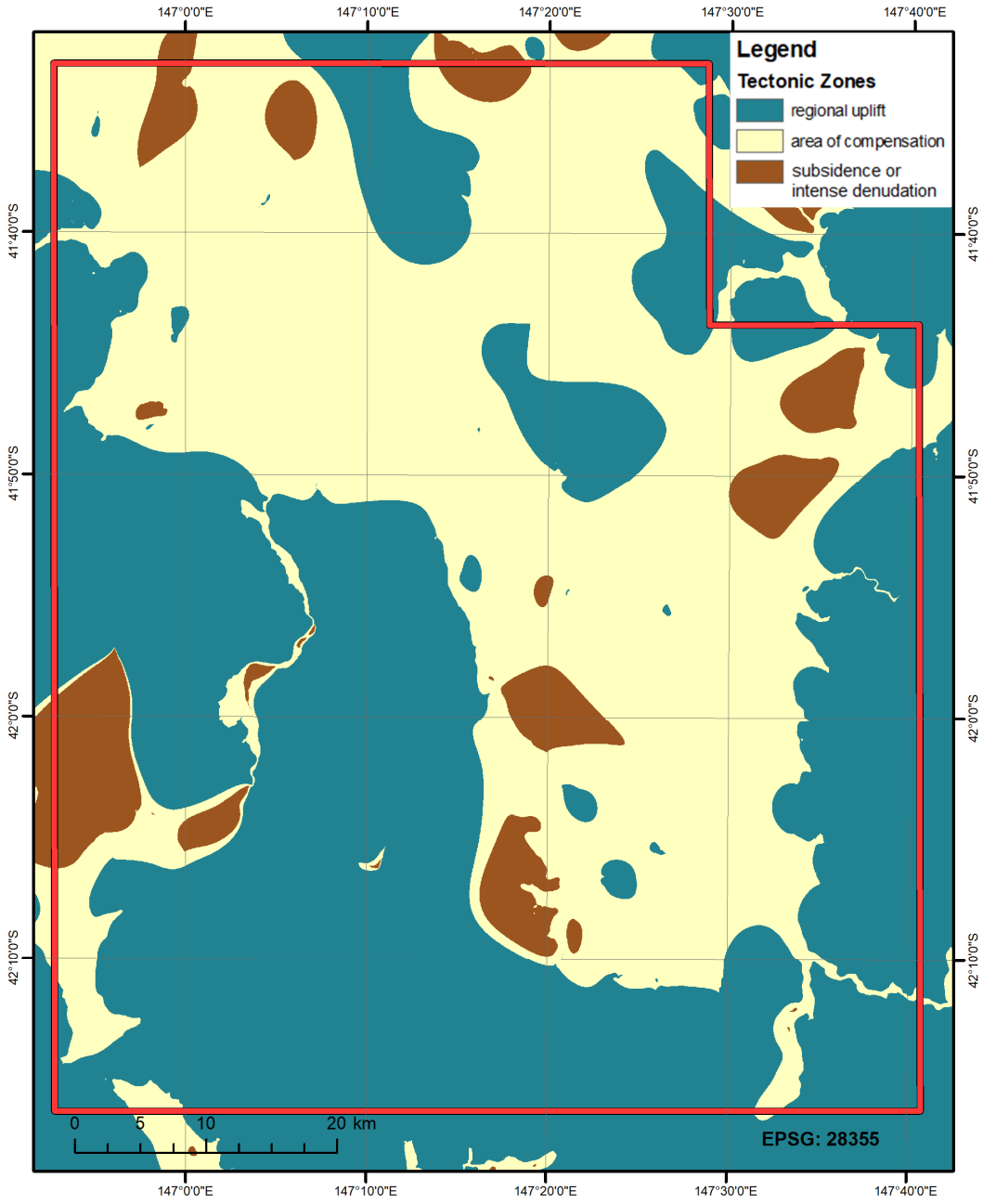


Figure 114: Difference of Base Levels 5 and 6.

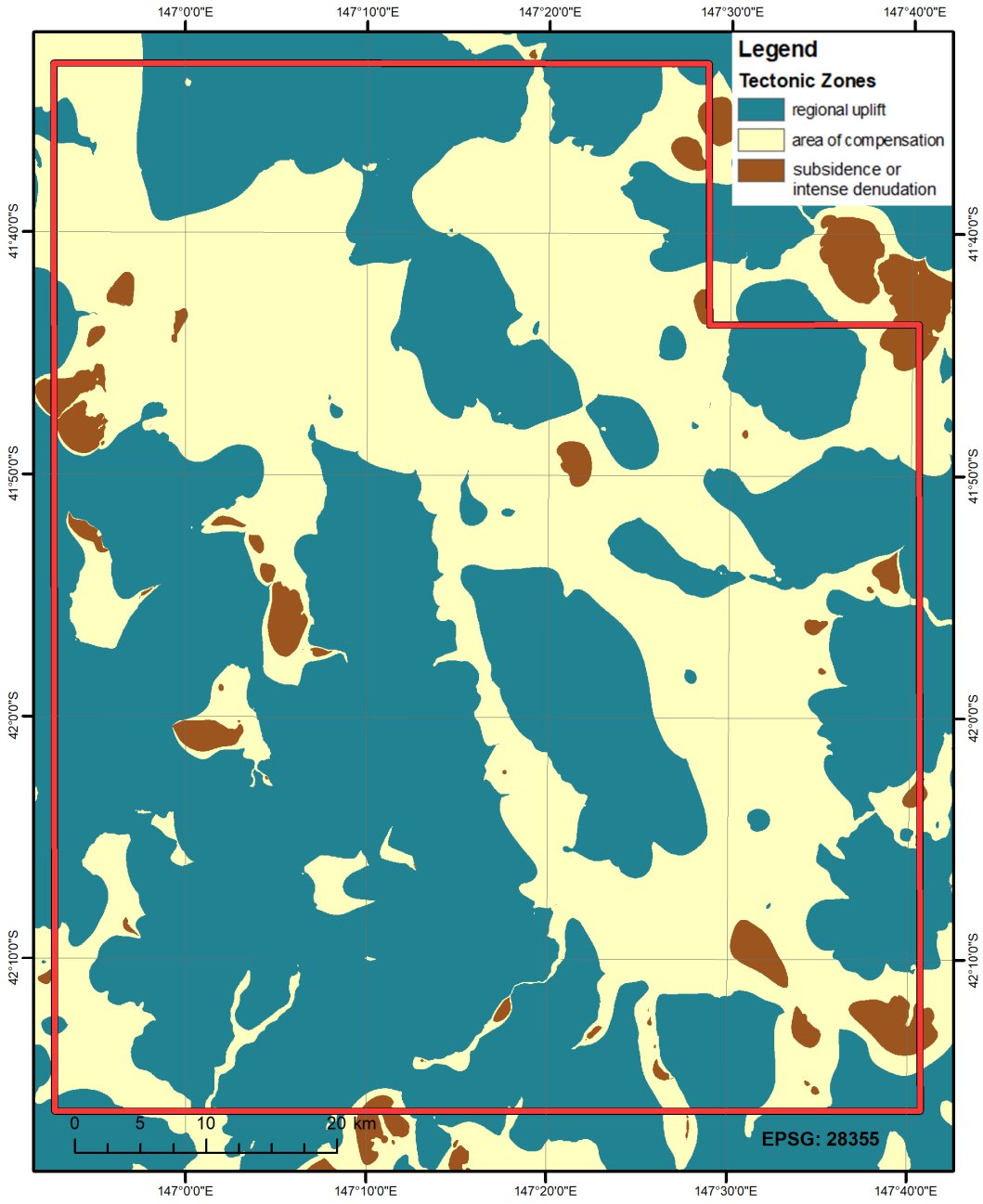


Figure 115: Difference of Base Levels 4 and 5.

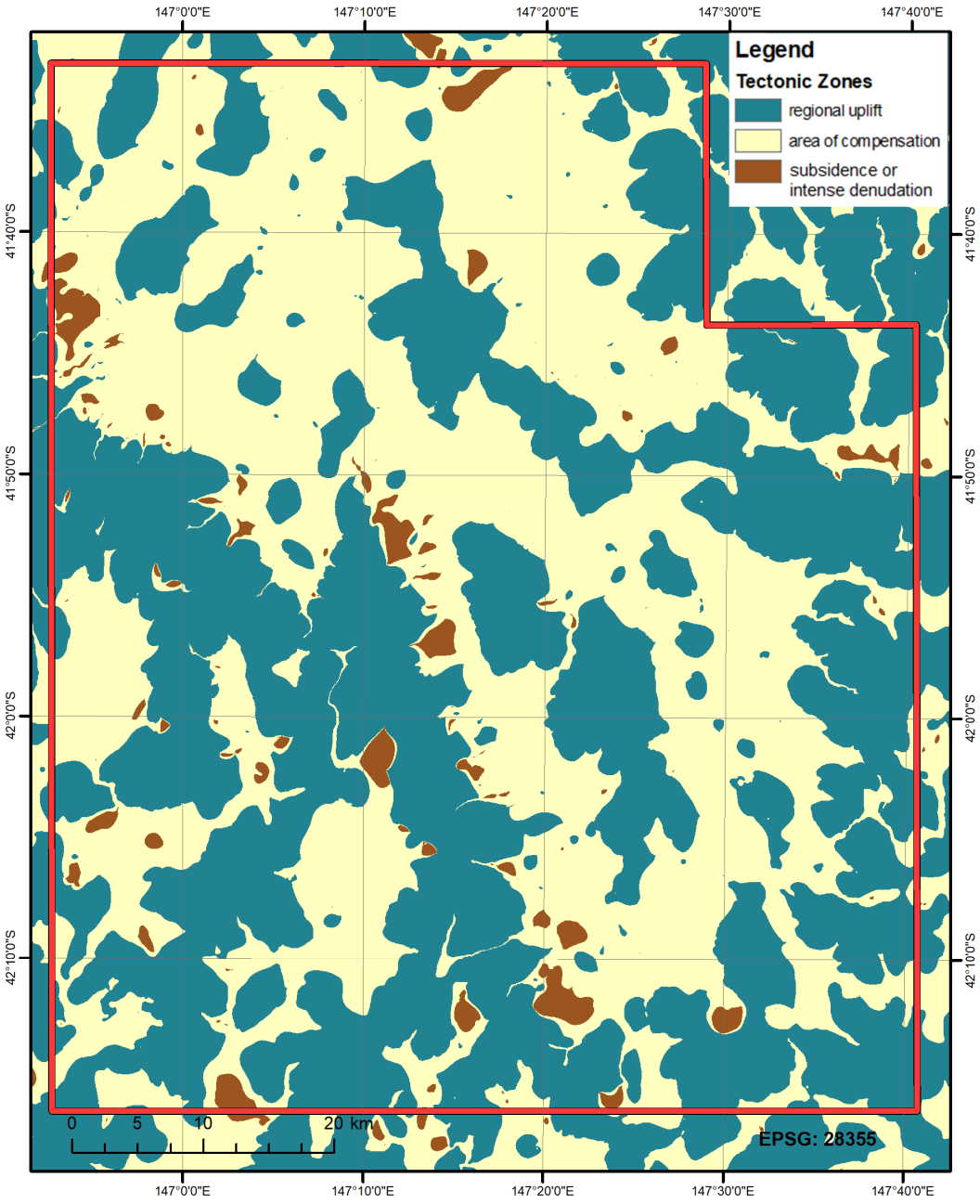


Figure 116: Difference of Base Levels 3 and 4.

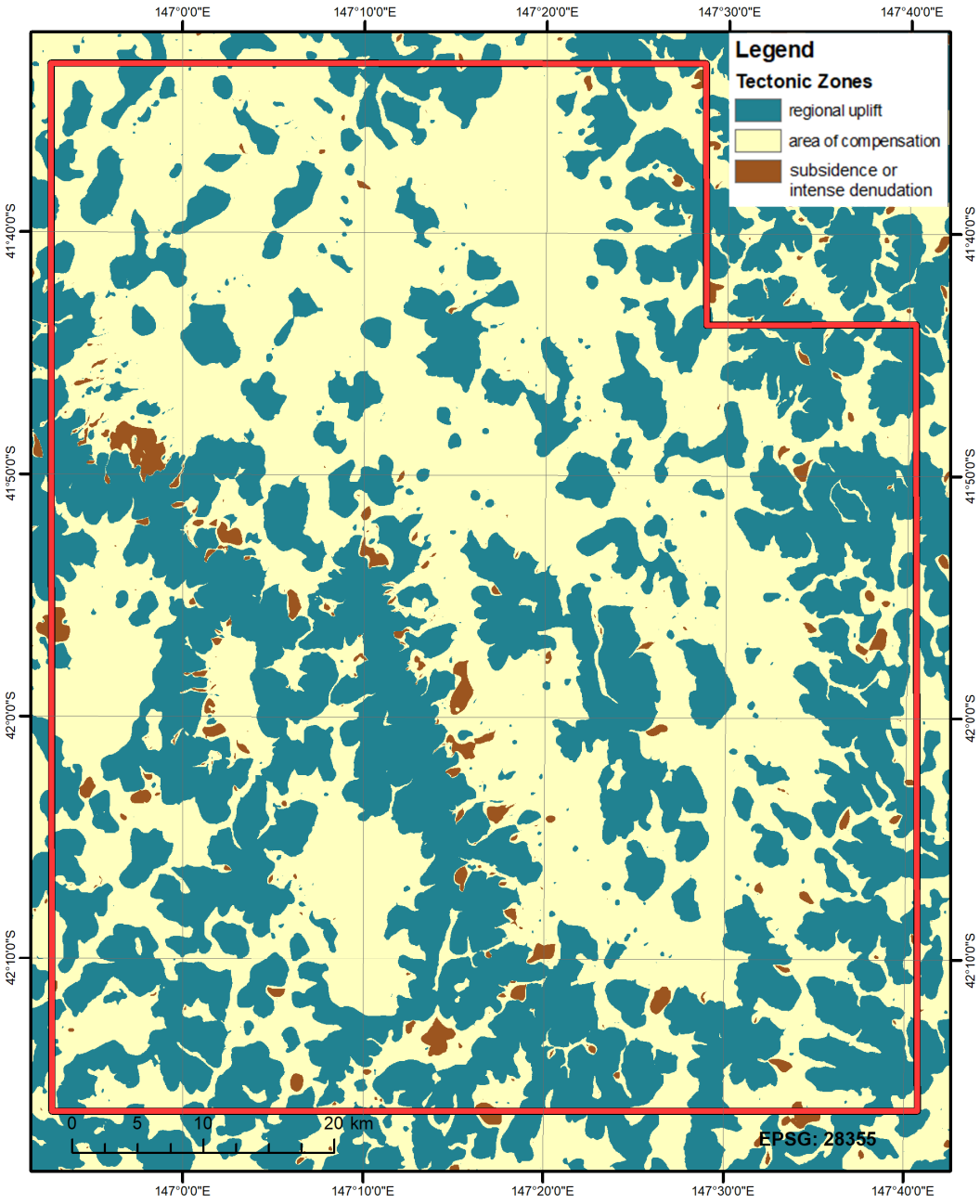


Figure 117: Difference of Base Levels 2 and 3.

Taking into account the areas of the negative values of the differential base surfaces (brown color) shown in **Figure 113** through **Figure 117**, their distribution is of note, evidencing for the existence of certain areas whose movements are different than the those of a regional nature both in terms of the rate and direction (**Figure 118** and **Figure 119**).



Figure 118: Difference between adjacent levels for Base Levels 2 through 7.

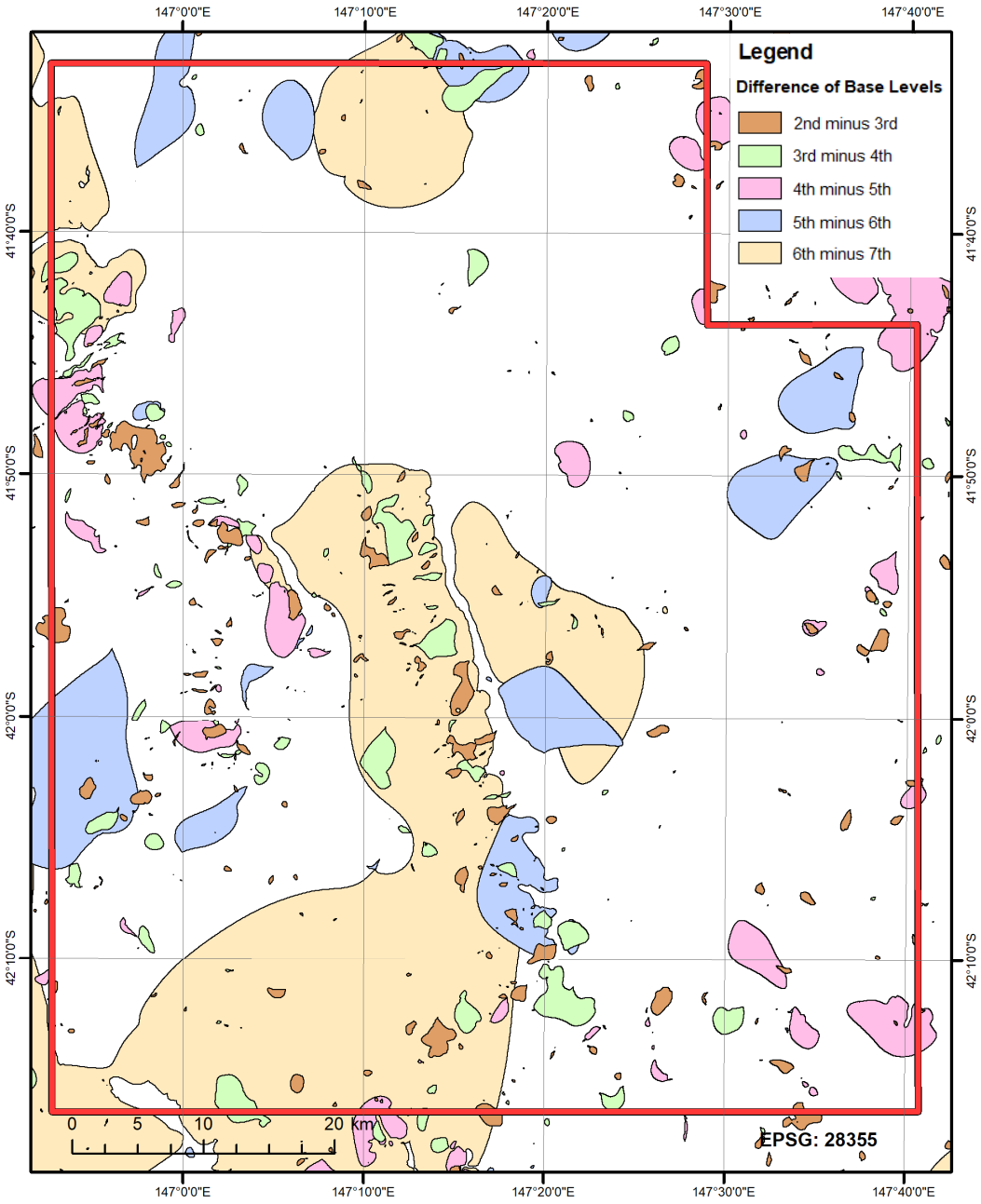


Figure 119: Potentially HC-prospective areas related to the intensive uplifting forming the inverse relief (relevant to the corresponding tectonic activation period).

Taking into account the areas of the near-zero values of the differential base surfaces (light-yellow color) shown in **Figure 113** through **Figure 117**, the paleo-valleys can be seen in **Figure 120** and **Figure 121**.

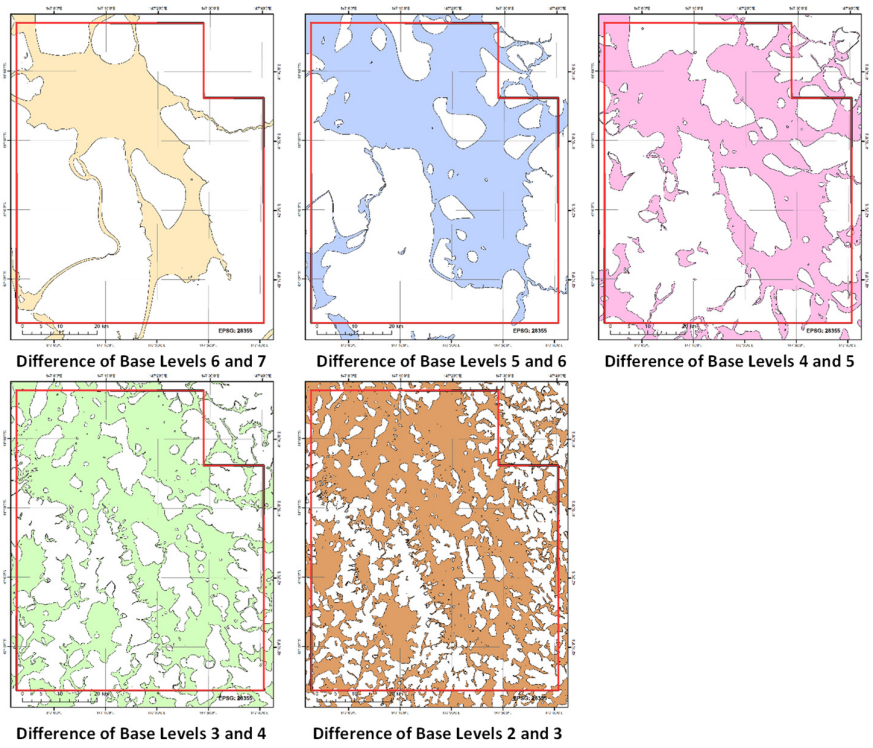


Figure 120: **Difference between adjacent levels for Base Levels 2 through 7.**

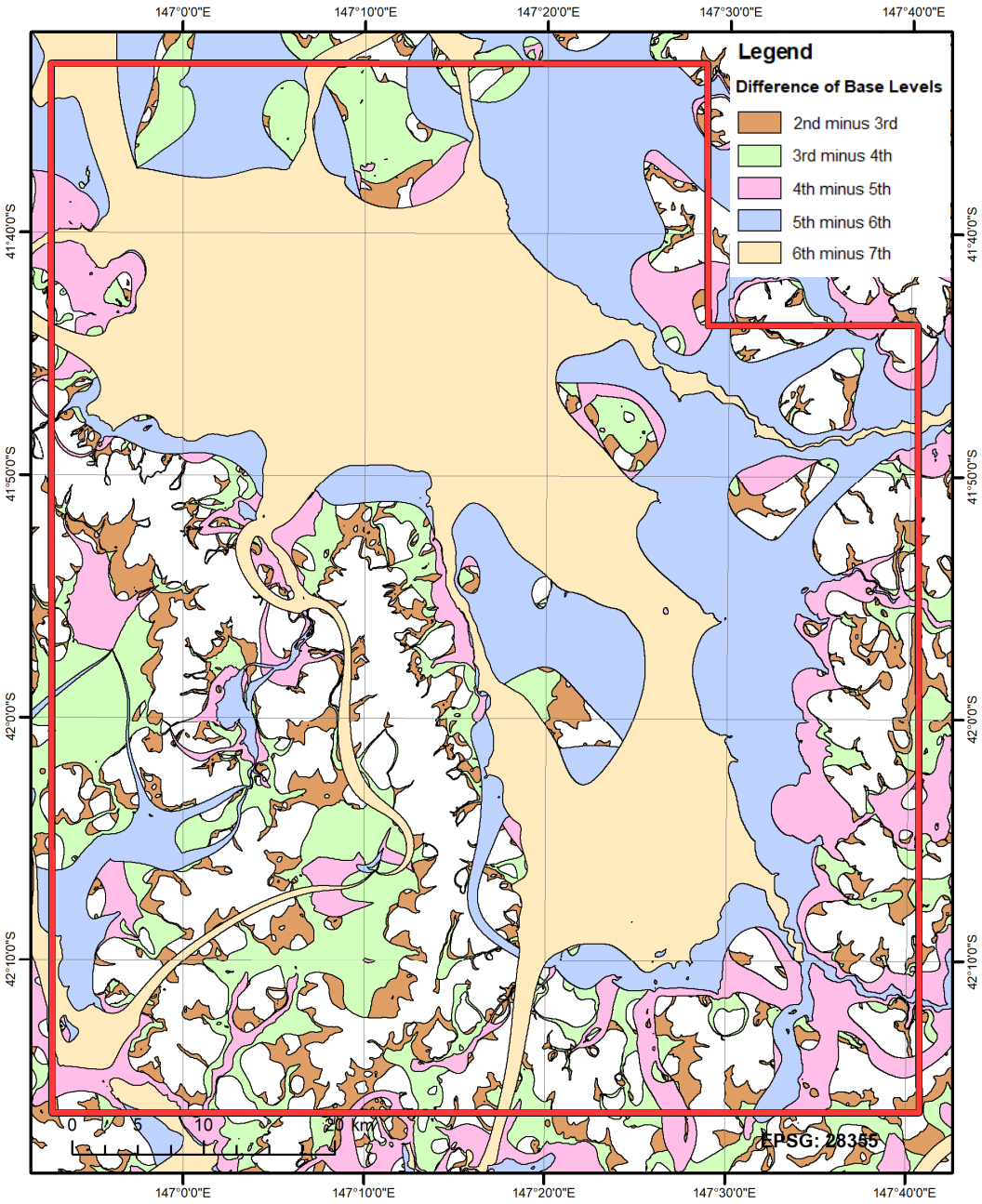


Figure 121: Potentially HC-prospective areas related to paleo-valleys.

2.10 RADAR DIFFERENTIAL INTERFEROMETRY

GENERAL INFORMATION

The development of satellite-based radars, new carriers launched into orbits with modern hardware and software, improved communication channels and parameters of sensory equipment open new opportunities for the effective implementation of monitoring studies of horizontal and vertical displacements of the Earth's surface. The methodology is called satellite radar interferometry.

Modern satellite radar systems with synthesized aperture (SAR - Synthetic Aperture Radar) scan the Earth's surface on both sides of the satellite's trajectory for the given bandwidths. The general registration scheme is shown in **Figure 122**.

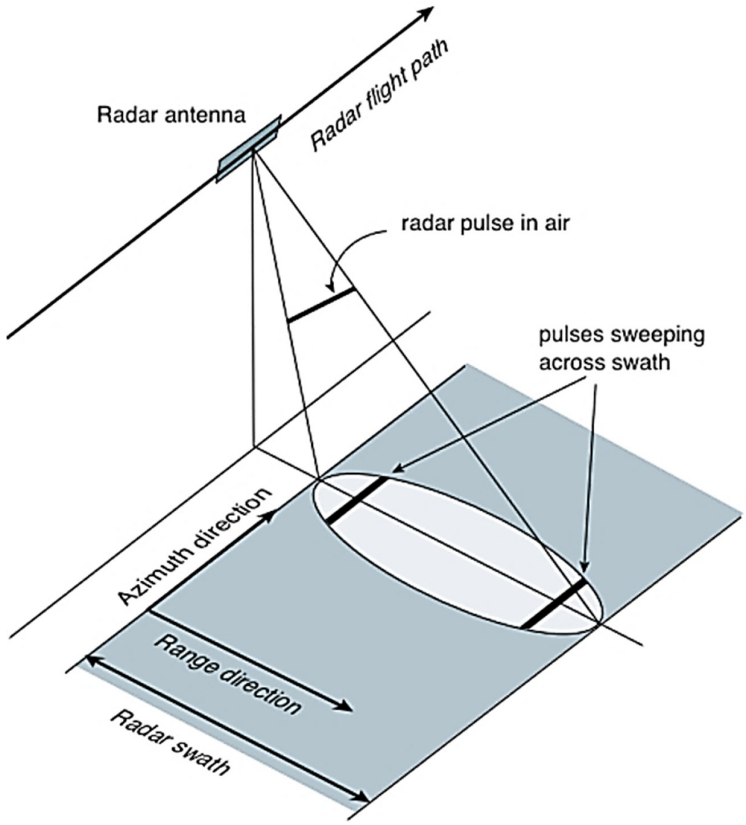


Figure 122: Schematic representation of the principle of scanning by a satellite radar system (Rosen, 2009 [1])

Radar systems with synthesized aperture work with a relatively small physical antenna. It emits a radar pulse at fixed time intervals propagating to the Earth's surface at a certain solid

[1] *Rosen, P. Principles and theory of radar interferometry. Tutorial for IGARSS, JPL, 2009. URL: https://www.grss-ieee.org/wp-content/uploads/2010/06/Radar_Interferometry_Part1.pdf*

angle away from the direction of motion of the platform. During the forward motion of the platform, the ground objects, scattering the energy emitted by the radar pulse, move within the projection of the radar beam relative to the radar antenna. Thus, objects are repeatedly irradiated from many positions of the radar. Accordingly, the antenna repeatedly receives the reflected signal from the same objects subsequently changing their position within the projection of the radar emitter to the Earth's surface. Because of this movement that is relative to the position of the antenna and the ground-based objects, the frequency and phase of the radar impulses change (the Doppler effect). Due to the motion of the platform, the Doppler differential frequency of the pulses reflected from an object increases from a certain minimum value at the time the object enters the projection of the radio beam to the maximum value for the intersection of the axis of symmetry of the projection (directed along the slant range direction), and then again drops to the minimum value, as the object leaves the projection of the radio beam. Each point inside the irradiation region is characterized by its inherent pattern of changing the Doppler frequencies. The values of frequency, amplitude, and phase characteristics of the radio signals reflected from the objects during the entire period of the objects' irradiation register onboard the satellite and are subsequently (together with the telemetry data) transmitted to the ground receiving stations.

Most modern civil-purpose satellite radar systems emit centimeter and decimeter wavelengths of electromagnetic waves. The most typical radar subranges (with the corresponding frequency bands and the wavelength spectrum) are given in **Table 6**.

Table 6. Sub-bands of modern satellite radars [2]

Sub-band	Ka	Ku	X	C	S	L	P
Frequency range, GHz	40-25	17.6-12	12-7.5	7.5-3.75	3.75-2	2-1	0.5-0.25
Wavelength range, cm	0.75-1.2	1.7-2.5	2.5-4	4-8	8-15	15-30	60-120

The most-used radars operate in the L sub-bands (Seasat, J-ERS-1, ALOS / PalSAR, ALOS-2), C (ERS-1/2, Radarsat-1/2, SRTM, ENVISAT / ASAR, Sentinel- 1a / 1b), X (SRTM, TerraSAR-X / TanDEM-X, COSMO-SkyMed-1/4).

Radar interferometry is a powerful method of remote sensing, which has proven itself as a productive and a high-precision technology for determining important characteristics of the geological environment (construction of digital terrain models, localization and quantification of vertical and plane displacements of the Earth's surface, monitoring the development of modern exogenous geological processes, etc.).

[2] *Alberto Moreira. A tutorial on synthetic aperture radar / Alberto Moreira, Pau Prats-Iraola, Marwan Younis, Gerhard Krieger, Irena Hajnsek, Konstantinos P Papathanassiou // IEEE Geoscience and remote sensing magazine. – 2013. – Vol.1, #1. – pp. 6-43. URL: http://elib.dlr.de/82313/1/SAR-Tutorial-March-2013.pdf*

The key idea is the comparison of two (or more) amplitude-phase images of the same terrain obtained at different times and at different spatial positions of the satellite. The presence of a phase component makes it possible to determine both the absolute elevation positions of points within the terrain and their relative displacements with a fairly high accuracy, commensurate with the wavelength. At the same time, the accuracy does not depend on the distance between the antenna and the surface. The geometry of satellite radar studies is shown in **Figure 123**.

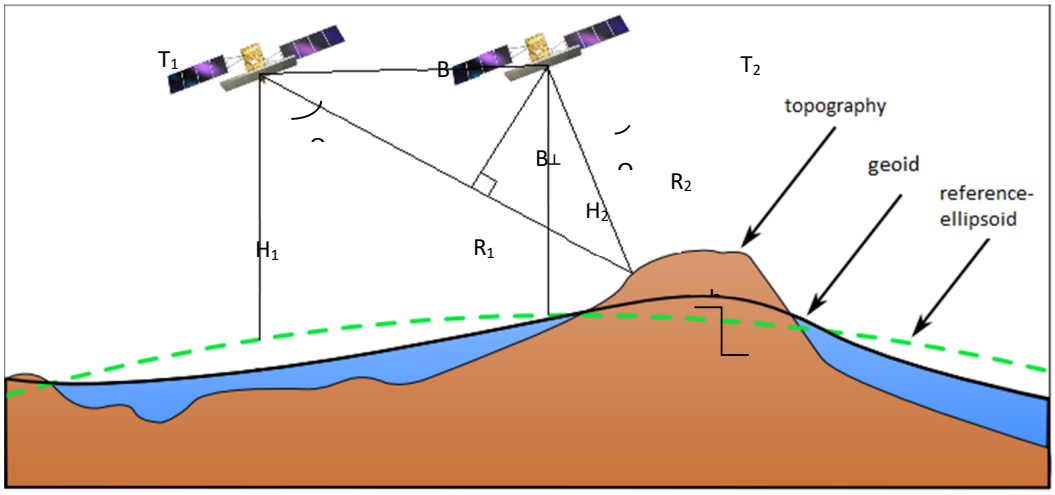


Figure 123: The geometric principle of obtaining radar interferometric pairs.

The phase of the radar wave is directly proportional to the path R, which the wave travels twice (from the source to the reflection point and in the opposite direction). Both images recorded at times T1 and T2 contain several different phase pictures, since the distances R1 and R2 are not the same. This phase difference (provided the known parameters the spatial orientation of the platforms and radar beams that are emitted/received by them - the heights of the orbits H1 and H2, the distances R1 and R2, the corresponding angles θ1 and θ2, and the baseline B and its transverse component $B_{\perp}$) provides the ability to determine the height 'h' of the reflection point above the surface of the reference ellipsoid. The described technology is known as InSAR (Interferometric Synthetic Aperture Radar) and is used to build digital elevation models.

The DInSAR (Differential Interferometric SAR) technology, however, allows determining the relative changes in the spatial arrangement of ground objects. If the terrestrial objects slightly change their spatial position within the time interval between two successive registrations (for example, due to uplifts, subsidence, landslides, landslides, etc. caused by natural and/or technogenic factors), an additional phase shift will appear that is independent of the baseline line. Generally, the interferometric phase (phase difference Δϕ) of DInSAR is based on the following constituents:

$$\Delta\varphi = \Delta\varphi_{topo} + \Delta\varphi_{disp} + \Delta\varphi_{atm} + \Delta\varphi_{noise}$$

$\Delta\phi_{topo}$ is the topographic phase advance; $\Delta\phi_{disp}$ - the phase difference caused by the change in coordinates of terrestrial objects during the time between scans; $\Delta\phi_{atm}$ - phase delay

associated with the effect of atmospheric conditions on the results of observations (in particular, the content of water vapor in the air); $\Delta\phi_{noise}$ is the component of the interference due to the phenomena of temporary decoding and loss of coherence of the radar images constituting the interferometric pair.

Comparing the technologies of InSAR and DInSAR, it is necessary to distinguish the special role of the concept of the baseline B (and its transverse component $B_{\perp}$): when solving the problem of obtaining a digital model of heights (InSAR), it is necessary to try to select radar images taken from satellite positions in which the transverse component of the baseline line is farily large; when solving the task of localizing and estimating the magnitude of the displacement of the Earth's surface (DInSAR), the highest accuracy can be achieved by reducing the transverse component of the baseline to zero (which is equivalent to eliminating the influence of the topographic phase).

However, even if the topographic phase is minimized, the results of determining the amount of ground displacement using only one pair of radar images may contain significant errors, since in this case it is impossible to estimate the effects the atmosphere and random interference. The interferometry technology of constant scatterers Ps (Persistent Scatterers) helped overcome these difficulties and obtaining truly high-precision and practically valuable results. It involves the use of a chain of radar images (at least 30) and SBaS (Small Baseline Subset) Determination of displacements from a series of radar images with a small baseline.

Differential radar interferometry in the variant of Ps achieves the maximum possible accuracy of estimation of displacements (in single millimeters vertically) automatically determining the presence of constant (stable) scatterers of the radar signal. For each of the points, the chronology of phase change in time is restored and then recalculated into displacements in millimeters. Additionally, special filtration is applied, eliminating the possible influence of the atmosphere on the interferometric phase.

Interferometry of small baselines SBaS, in contrast to the interferometry of permanent scatterers, is a less automated option requiring a greater operator's skillset. This technology operates at submillimeter precision due to cross-processing of a very large number of interferometric pairs. For example, using 15 input images renders the total number of pairs equal to 105. Of these, using the criterion of the minimum baseline, 30-40% of pairs are selected and processed using the specialized software.

AREA OF INTEREST AND SOURCE DATA

EL30/2011 (**Figure 124**) covers the basin of the MacQuarie River, has a linear size of approximately 66x80 km and is limited by the approximate longitude range 146°52'E - 147°41'E and the latitude range 41°33'S - 42°16'S. Geomorphologically, the study area can be conditionally divided into a hilly plain (extending in the direction of NW-SE, characterized by the average elevation marks of 200 m and occupying approximately 60% of the territory) and elevations, mountain ridges and massifs (elevations along the eastern border of the area are characterized by medium altitudes at 500 m, and the

mountain massif in the South-Western part of the area - with average altitudes of 900 m, the highest point of the terrain - Mount Millers Bluff is 1,210 m).

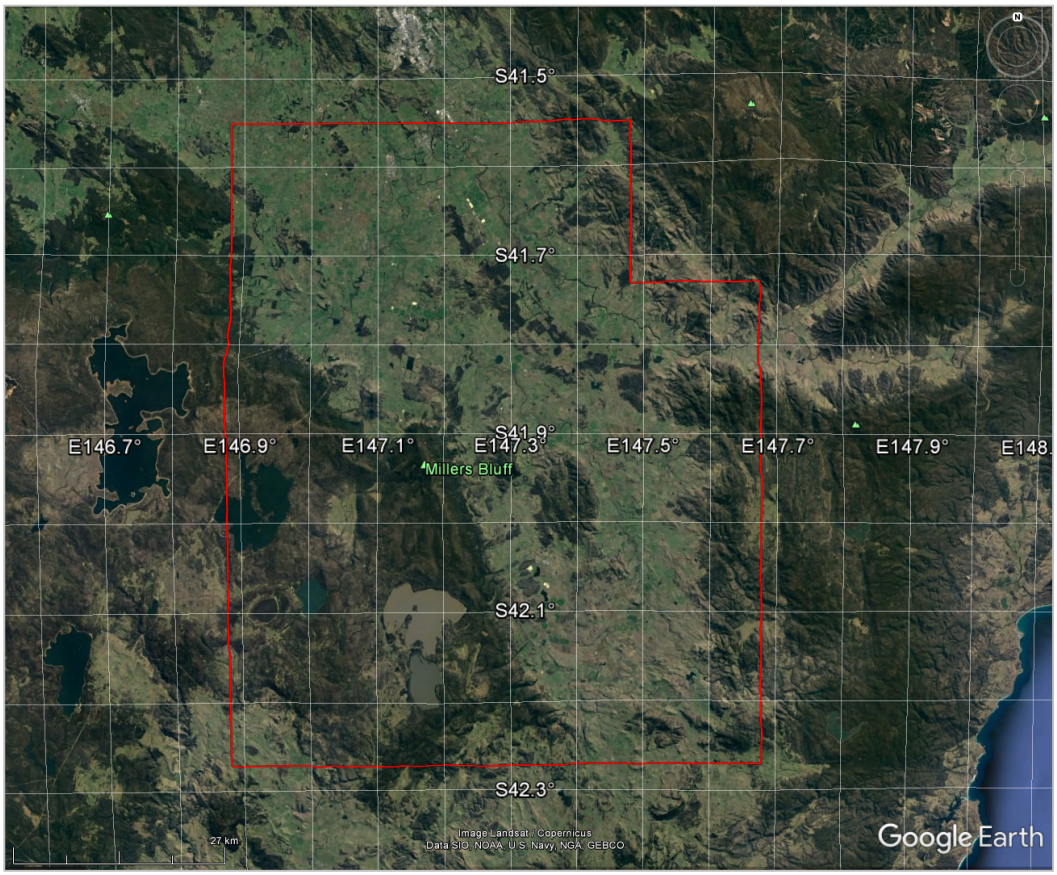


Figure 124: AOI EL30/2011

The results of satellite imagery Sentinel-1a, -1b radar obtained during the period 2016/12/03 - 2017/09/05 were used. Generally, all the available scenes were analyzed. For the interferometric processing, 7 scenes were selected (covering the period 2017/06/13 - 2017/09/05), to which 2 scenes were added from 2016 (2016/12/03 and 2016/12/15). The complete list of utilized scenes is shown in **Table 7**. The most complete radar coverage of the area is with the relative orbit parameter of 147.

The specialized software SARScape (v.5.2) was used and integrated into the remote sensing data processing system ENVI (v.5.3). The processing was carried out using SBaS small baseline interferometry technology.

Table 7. Characteristics of input data

1 *S1A_IW_SLC__1SDV_20161203T191735_20161203T191802_014219_016FBC_5A89.SAFE*

Annotation

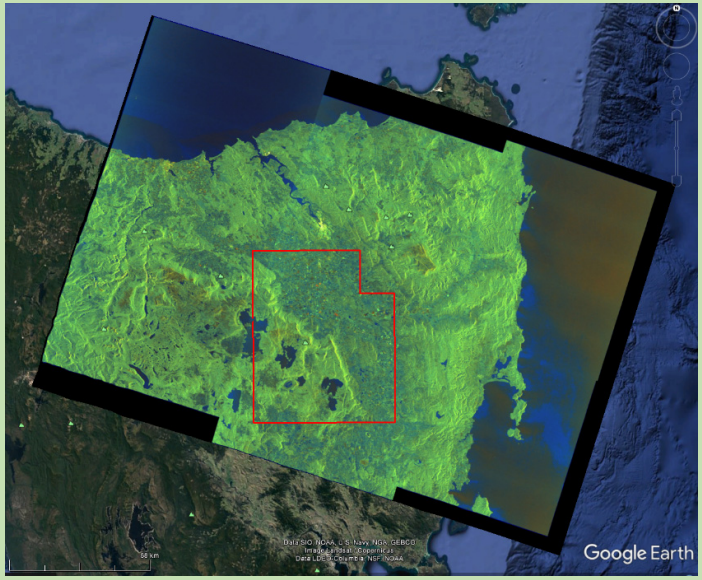
- s1a-iw1-slc-vh-20161203t191736-20161203t191801-014219-016fbc-001.xml
- s1a-iw2-slc-vh-20161203t191737-20161203t191802-014219-016fbc-002.xml
- s1a-iw3-slc-vh-20161203t191735-20161203t191800-014219-016fbc-003.xml
- s1a-iw1-slc-vv-20161203t191736-20161203t191801-014219-016fbc-004.xml
- s1a-iw2-slc-vv-20161203t191737-20161203t191802-014219-016fbc-005.xml
- s1a-iw3-slc-vv-20161203t191735-20161203t191800-014219-016fbc-006.xml

Annotation/calibration

- noise-s1a-iw1-slc-vh-20161203t191736-20161203t191801-014219-016fbc-001.xml
- noise-s1a-iw2-slc-vh-20161203t191737-20161203t191802-014219-016fbc-002.xml
- noise-s1a-iw3-slc-vh-20161203t191735-20161203t191800-014219-016fbc-003.xml
- noise-s1a-iw1-slc-vv-20161203t191736-20161203t191801-014219-016fbc-004.xml
- noise-s1a-iw2-slc-vv-20161203t191737-20161203t191802-014219-016fbc-005.xml
- noise-s1a-iw3-slc-vv-20161203t191735-20161203t191800-014219-016fbc-006.xml
- calibration-s1a-iw1-slc-vh-20161203t191736-20161203t191801-014219-016fbc-001.xml
- calibration-s1a-iw2-slc-vh-20161203t191737-20161203t191802-014219-016fbc-002.xml
- calibration-s1a-iw3-slc-vh-20161203t191735-20161203t191800-014219-016fbc-003.xml

Date: 2016-12-03T20:46:54

Class: SENTINEL-1 Interferometric Wide Swath Level 1 Product



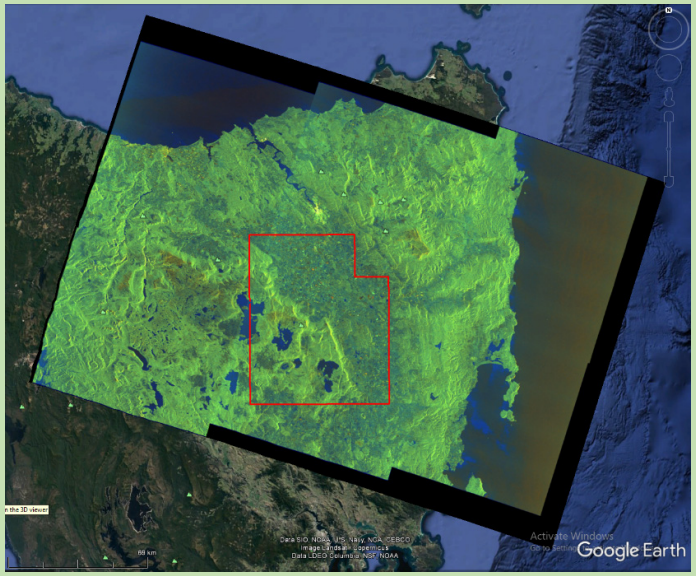
• calibration-s1a-iw1-slc-vv-20161203t191736-20161203t191801-014219-016fbc-004.xml • calibration-s1a-iw2-slc-vv-20161203t191737-20161203t191802-014219-016fbc-005.xml • calibration-s1a-iw3-slc-vv-20161203t191735-20161203t191800-014219-016fbc-006.xml **Measurement** • s1a-iw1-slc-vh-20161203t191736-20161203t191801-014219-016fbc-001.tiff • s1a-iw2-slc-vh-20161203t191737-20161203t191802-014219-016fbc-002.tiff • s1a-iw3-slc-vh-20161203t191735-20161203t191800-014219-016fbc-003.tiff • s1a-iw1-slc-vv-20161203t191736-20161203t191801-014219-016fbc-004.tiff • s1a-iw2-slc-vv-20161203t191737-20161203t191802-014219-016fbc-005.tiff • s1a-iw3-slc-vv-20161203t191735-20161203t191800-014219-016fbc-006.tiff	
2. *S1A_IW_SLC__1SDV_20161215T191736_20161215T191803_014394_01754A_E905.SAFE*	
Annotation • s1a-iw1-slc-vh-20161215t191736-20161215t191801-014394-01754a-001.xml • s1a-iw2-slc-vh-20161215t191737-20161215t191802-014394-01754a-002.xml • s1a-iw3-slc-vh-20161215t191738-20161215t191803-014394-01754a-003.xml • s1a-iw1-slc-vv-20161215t191736-20161215t191801-014394-01754a-004.xml • s1a-iw2-slc-vv-20161215t191737-20161215t191802-014394-01754a-005.xml • s1a-iw3-slc-vv-20161215t191738-20161215t191803-014394-01754a-006.xml •	**Date**: 2016-12-15T22:28:04 **Class**: SENTINEL-1 Interferometric Wide Swath Level 1 Product

Annotation/calibration

- noise-s1a-iw1-slc-vh-20161215t191736-20161215t191801-014394-01754a-001.xml
- noise-s1a-iw2-slc-vh-20161215t191737-20161215t191802-014394-01754a-002.xml
- noise-s1a-iw3-slc-vh-20161215t191738-20161215t191803-014394-01754a-003.xml
- noise-s1a-iw1-slc-vv-20161215t191736-20161215t191801-014394-01754a-004.xml
- noise-s1a-iw2-slc-vv-20161215t191737-20161215t191802-014394-01754a-005.xml
- noise-s1a-iw3-slc-vv-20161215t191738-20161215t191803-014394-01754a-006.xml
- calibration-s1a-iw1-slc-vh-20161215t191736-20161215t191801-014394-01754a-001.xml
- calibration-s1a-iw2-slc-vh-20161215t191737-20161215t191802-014394-01754a-002.xml
- calibration-s1a-iw3-slc-vh-20161215t191738-20161215t191803-014394-01754a-003.xml
- calibration-s1a-iw1-slc-vv-20161215t191736-20161215t191801-014394-01754a-004.xml
- calibration-s1a-iw2-slc-vv-20161215t191737-20161215t191802-014394-01754a-005.xml
- calibration-s1a-iw3-slc-vv-20161215t191738-20161215t191803-014394-01754a-006.xml

Measurement

- s1a-iw1-slc-vh-20161215t191736-20161215t191801-014394-01754a-001.tiff
- s1a-iw2-slc-vh-20161215t191737-20161215t191802-014394-01754a-002.tiff
- s1a-iw3-slc-vh-20161215t191738-20161215t191803-014394-01754a-003.tiff
- s1a-iw1-slc-vv-20161215t191736-20161215t191801-014394-01754a-004.tiff
- s1a-iw2-slc-vv-20161215t191737-20161215t191802-014394-01754a-005.tiff
- s1a-iw3-slc-vv-20161215t191738-20161215t191803-014394-01754a-006.tiff



3. *S1A_IW_SLC__1SDV_20170613T191737_20170613T191804_017019_01C588_BE3E.SAFE*

Annotation

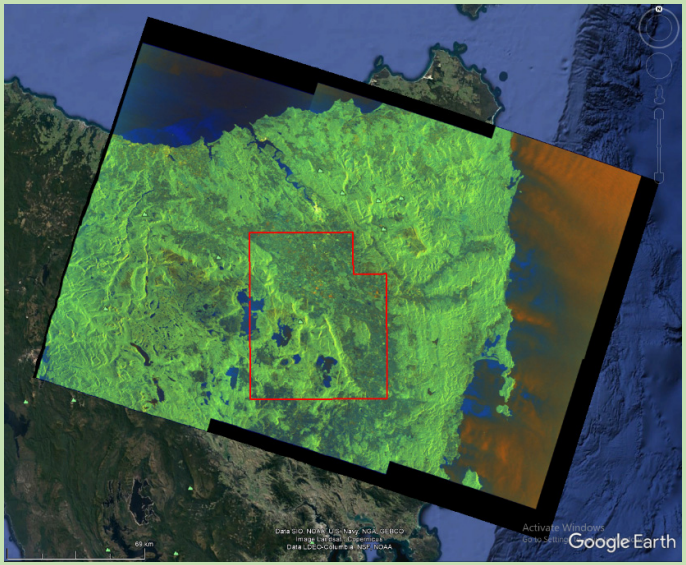
- s1a-iw1-slc-vh-20170613t191737-20170613t191802-017019-01c588-001.xml
- s1a-iw2-slc-vh-20170613t191738-20170613t191803-017019-01c588-002.xml
- s1a-iw3-slc-vh-20170613t191739-20170613t191804-017019-01c588-003.xml
- s1a-iw1-slc-vv-20170613t191737-20170613t191802-017019-01c588-004.xml
- s1a-iw2-slc-vv-20170613t191738-20170613t191803-017019-01c588-005.xml
- s1a-iw3-slc-vv-20170613t191739-20170613t191804-017019-01c588-006.xml

Annotation/calibration

- noise-s1a-iw1-slc-vh-20170613t191737-20170613t191802-017019-01c588-001.xml
- noise-s1a-iw2-slc-vh-20170613t191738-20170613t191803-017019-01c588-002.xml
- noise-s1a-iw3-slc-vh-20170613t191739-20170613t191804-017019-01c588-003.xml
- noise-s1a-iw1-slc-vv-20170613t191737-20170613t191802-017019-01c588-004.xml
- noise-s1a-iw2-slc-vv-20170613t191738-20170613t191803-017019-01c588-005.xml
- noise-s1a-iw3-slc-vv-20170613t191739-20170613t191804-017019-01c588-006.xml
- calibration-s1a-iw1-slc-vh-20170613t191737-20170613t191802-017019-01c588-001.xml
- calibration-s1a-iw2-slc-vh-20170613t191738-20170613t191803-017019-01c588-002.xml
- calibration-s1a-iw3-slc-vh-20170613t191739-20170613t191804-017019-01c588-003.xml
- calibration-s1a-iw1-slc-vv-20170613t191737-20170613t191802-017019-01c588-004.xml

Date: 2017-06-13T21:09:18

Class: SENTINEL-1 Interferometric Wide Swath Level 1 Product

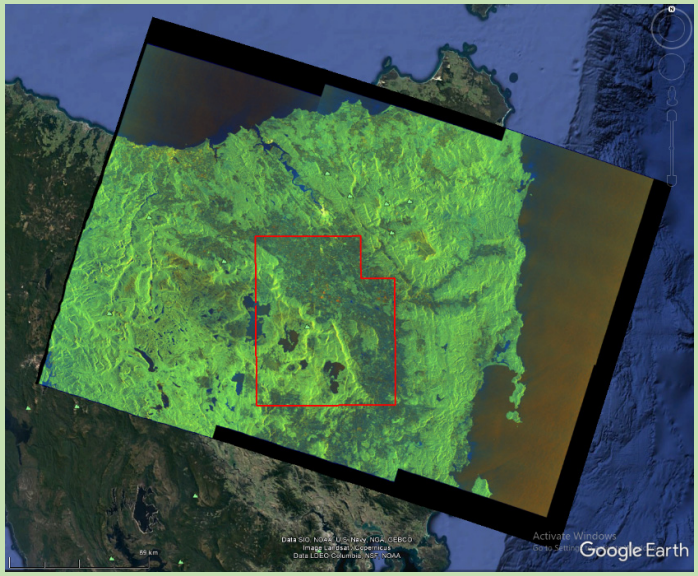


• calibration-s1a-iw2-slc-vv-20170613t191738-20170613t191803-017019-01c588-005.xml • calibration-s1a-iw3-slc-vv-20170613t191739-20170613t191804-017019-01c588-006.xml **Measurement** • s1a-iw1-slc-vh-20170613t191737-20170613t191802-017019-01c588-001.tiff • s1a-iw2-slc-vh-20170613t191738-20170613t191803-017019-01c588-002.tiff • s1a-iw3-slc-vh-20170613t191739-20170613t191804-017019-01c588-003.tiff • s1a-iw1-slc-vv-20170613t191737-20170613t191802-017019-01c588-004.tiff • s1a-iw2-slc-vv-20170613t191738-20170613t191803-017019-01c588-005.tiff • s1a-iw3-slc-vv-20170613t191739-20170613t191804-017019-01c588-006.tiff	
4. *S1A_IW_SLC__1SDV_20170625T191738_20170625T191805_017194_01CADD_5E4B.SAFE*	
Annotation • s1a-iw1-slc-vh-20170625t191738-20170625t191803-017194-01cadd-001.xml • s1a-iw2-slc-vh-20170625t191739-20170625t191804-017194-01cadd-002.xml • s1a-iw3-slc-vh-20170625t191740-20170625t191805-017194-01cadd-003.xml • s1a-iw1-slc-vv-20170625t191738-20170625t191803-017194-01cadd-004.xml • s1a-iw2-slc-vv-20170625t191739-20170625t191804-017194-01cadd-005.xml • s1a-iw3-slc-vv-20170625t191740-20170625t191805-017194-01cadd-006.xml **Annotation/calibration** • noise-s1a-iw1-slc-vh-20170625t191738-20170625t191803-017194-01cadd-001.xml	**Date**: 2017-06-25T21:05:02 **Class**: SENTINEL-1 Interferometric Wide Swath Level 1 Product

- noise-s1a-iw2-slc-vh-20170625t191739-20170625t191804-017194-01cadd-002.xml
- noise-s1a-iw3-slc-vh-20170625t191740-20170625t191805-017194-01cadd-003.xml
- noise-s1a-iw1-slc-vv-20170625t191738-20170625t191803-017194-01cadd-004.xml
- noise-s1a-iw2-slc-vv-20170625t191739-20170625t191804-017194-01cadd-005.xml
- noise-s1a-iw3-slc-vv-20170625t191740-20170625t191805-017194-01cadd-006.xml
- calibration-s1a-iw1-slc-vh-20170625t191738-20170625t191803-017194-01cadd-001.xml
- calibration-s1a-iw2-slc-vh-20170625t191739-20170625t191804-017194-01cadd-002.xml
- calibration-s1a-iw3-slc-vh-20170625t191740-20170625t191805-017194-01cadd-003.xml
- calibration-s1a-iw1-slc-vv-20170625t191738-20170625t191803-017194-01cadd-004.xml
- calibration-s1a-iw2-slc-vv-20170625t191739-20170625t191804-017194-01cadd-005.xml
- calibration-s1a-iw3-slc-vv-20170625t191740-20170625t191805-017194-01cadd-006.xml

Measurement

- s1a-iw1-slc-vh-20170625t191738-20170625t191803-017194-01cadd-001.tiff
- s1a-iw2-slc-vh-20170625t191739-20170625t191804-017194-01cadd-002.tiff
- s1a-iw3-slc-vh-20170625t191740-20170625t191805-017194-01cadd-003.tiff
- s1a-iw1-slc-vv-20170625t191738-20170625t191803-017194-01cadd-004.tiff
- s1a-iw2-slc-vv-20170625t191739-20170625t191804-017194-01cadd-005.tiff
- s1a-iw3-slc-vv-20170625t191740-20170625t191805-017194-01cadd-006.tiff



5. *S1A_IW_SLC__1SDV_20170707T191738_20170707T191806_017369_01D020_5AD9.SAFE*

Annotation

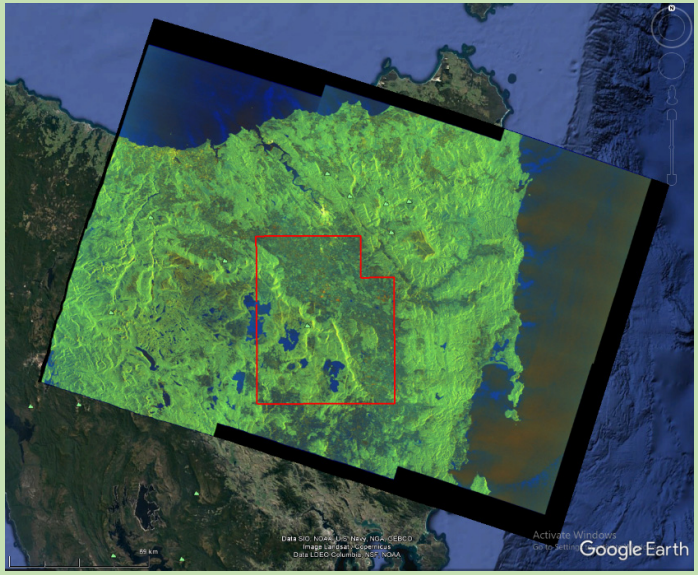
- s1a-iw1-slc-vh-20170707t191738-20170707t191804-017369-01d020-001.xml
- s1a-iw2-slc-vh-20170707t191739-20170707t191805-017369-01d020-002.xml
- s1a-iw3-slc-vh-20170707t191740-20170707t191806-017369-01d020-003.xml
- s1a-iw1-slc-vv-20170707t191738-20170707t191804-017369-01d020-004.xml
- s1a-iw2-slc-vv-20170707t191739-20170707t191805-017369-01d020-005.xml
- s1a-iw3-slc-vv-20170707t191740-20170707t191806-017369-01d020-006.xml

Annotation/calibration

- noise-s1a-iw1-slc-vh-20170707t191738-20170707t191804-017369-01d020-001.xml
- noise-s1a-iw2-slc-vh-20170707t191739-20170707t191805-017369-01d020-002.xml
- noise-s1a-iw3-slc-vh-20170707t191740-20170707t191806-017369-01d020-003.xml
- noise-s1a-iw1-slc-vv-20170707t191738-20170707t191804-017369-01d020-004.xml
- noise-s1a-iw2-slc-vv-20170707t191739-20170707t191805-017369-01d020-005.xml
- noise-s1a-iw3-slc-vv-20170707t191740-20170707t191806-017369-01d020-006.xml
- calibration-s1a-iw1-slc-vh-20170707t191738-20170707t191804-017369-01d020-001.xml
- calibration-s1a-iw2-slc-vh-20170707t191739-20170707t191805-017369-01d020-002.xml
- calibration-s1a-iw3-slc-vh-20170707t191740-20170707t191806-017369-01d020-003.xml
- calibration-s1a-iw1-slc-vv-20170707t191738-20170707t191804-017369-01d020-004.xml
- calibration-s1a-iw2-slc-vv-20170707t191739-20170707t191805-017369-01d020-005.xml

Date: 2017-07-11T13:16:49

Class: SENTINEL-1 Interferometric Wide Swath Level 1 Product

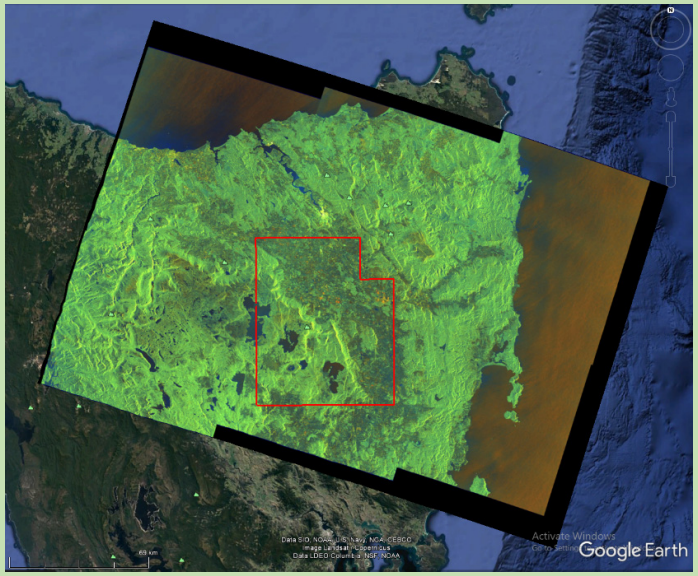


• calibration-s1a-iw3-slc-vv-20170707t191740-20170707t191806-017369-01d020-006.xml **Measurement** • s1a-iw1-slc-vh-20170707t191738-20170707t191804-017369-01d020-001.tiff • s1a-iw2-slc-vh-20170707t191739-20170707t191805-017369-01d020-002.tiff • s1a-iw3-slc-vh-20170707t191740-20170707t191806-017369-01d020-003.tiff • s1a-iw1-slc-vv-20170707t191738-20170707t191804-017369-01d020-004.tiff • s1a-iw2-slc-vv-20170707t191739-20170707t191805-017369-01d020-005.tiff • s1a-iw3-slc-vv-20170707t191740-20170707t191806-017369-01d020-006.tiff	
6. *S1A_IW_SLC__1SDV_20170719T191739_20170719T191806_017544_01D579_B61E.SAFE*	
Annotation • s1a-iw1-slc-vh-20170719t191739-20170719t191804-017544-01d579-001.xml • s1a-iw2-slc-vh-20170719t191740-20170719t191805-017544-01d579-002.xml • s1a-iw3-slc-vh-20170719t191741-20170719t191806-017544-01d579-003.xml • s1a-iw1-slc-vv-20170719t191739-20170719t191804-017544-01d579-004.xml • s1a-iw2-slc-vv-20170719t191740-20170719t191805-017544-01d579-005.xml • s1a-iw3-slc-vv-20170719t191741-20170719t191806-017544-01d579-006.xml **Annotation/calibration** • noise-s1a-iw1-slc-vh-20170719t191739-20170719t191804-017544-01d579-001.xml • noise-s1a-iw2-slc-vh-20170719t191740-20170719t191805-017544-01d579-002.xml	**Date**: 2017-07-19T21:04:00 **Class**: SENTINEL-1 Interferometric Wide Swath Level 1 Product

- noise-s1a-iw3-slc-vh-20170719t191741-20170719t191806-017544-01d579-003.xml
- noise-s1a-iw1-slc-vv-20170719t191739-20170719t191804-017544-01d579-004.xml
- noise-s1a-iw2-slc-vv-20170719t191740-20170719t191805-017544-01d579-005.xml
- noise-s1a-iw3-slc-vv-20170719t191741-20170719t191806-017544-01d579-006.xml
- calibration-s1a-iw1-slc-vh-20170719t191739-20170719t191804-017544-01d579-001.xml
- calibration-s1a-iw2-slc-vh-20170719t191740-20170719t191805-017544-01d579-002.xml
- calibration-s1a-iw3-slc-vh-20170719t191741-20170719t191806-017544-01d579-003.xml
- calibration-s1a-iw1-slc-vv-20170719t191739-20170719t191804-017544-01d579-004.xml
- calibration-s1a-iw2-slc-vv-20170719t191740-20170719t191805-017544-01d579-005.xml
- calibration-s1a-iw3-slc-vv-20170719t191741-20170719t191806-017544-01d579-006.xml

Measurement

- s1a-iw1-slc-vh-20170719t191739-20170719t191804-017544-01d579-001.tiff
- s1a-iw2-slc-vh-20170719t191740-20170719t191805-017544-01d579-002.tiff
- s1a-iw3-slc-vh-20170719t191741-20170719t191806-017544-01d579-003.tiff
- s1a-iw1-slc-vv-20170719t191739-20170719t191804-017544-01d579-004.tiff
- s1a-iw2-slc-vv-20170719t191740-20170719t191805-017544-01d579-005.tiff
- s1a-iw3-slc-vv-20170719t191741-20170719t191806-017544-01d579-006.tiff



7. *S1A_IW_SLC__1SDV_20170812T191741_20170812T191808_017894_01E023_B3B3.SAFE*

Annotation

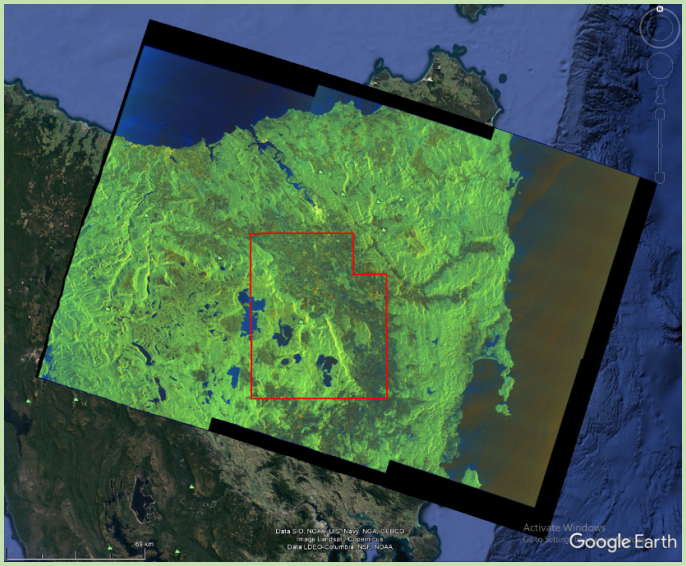
- s1a-iw1-slc-vh-20170812t191741-20170812t191806-017894-01e023-001.xml
- s1a-iw2-slc-vh-20170812t191742-20170812t191807-017894-01e023-002.xml
- s1a-iw3-slc-vh-20170812t191743-20170812t191808-017894-01e023-003.xml
- s1a-iw1-slc-vv-20170812t191741-20170812t191806-017894-01e023-004.xml
- s1a-iw2-slc-vv-20170812t191742-20170812t191807-017894-01e023-005.xml
- s1a-iw3-slc-vv-20170812t191743-20170812t191808-017894-01e023-006.xml

Annotation/calibration

- noise-s1a-iw1-slc-vh-20170812t191741-20170812t191806-017894-01e023-001.xml
- noise-s1a-iw2-slc-vh-20170812t191742-20170812t191807-017894-01e023-002.xml
- noise-s1a-iw3-slc-vh-20170812t191743-20170812t191808-017894-01e023-003.xml
- noise-s1a-iw1-slc-vv-20170812t191741-20170812t191806-017894-01e023-004.xml
- noise-s1a-iw2-slc-vv-20170812t191742-20170812t191807-017894-01e023-005.xml
- noise-s1a-iw3-slc-vv-20170812t191743-20170812t191808-017894-01e023-006.xml
- calibration-s1a-iw1-slc-vh-20170812t191741-20170812t191806-017894-01e023-001.xml
- calibration-s1a-iw2-slc-vh-20170812t191742-20170812t191807-017894-01e023-002.xml
- calibration-s1a-iw3-slc-vh-20170812t191743-20170812t191808-017894-01e023-003.xml

Date: 2017-08-12T21:03:01

Class: SENTINEL-1 Interferometric Wide Swath Level 1 Product



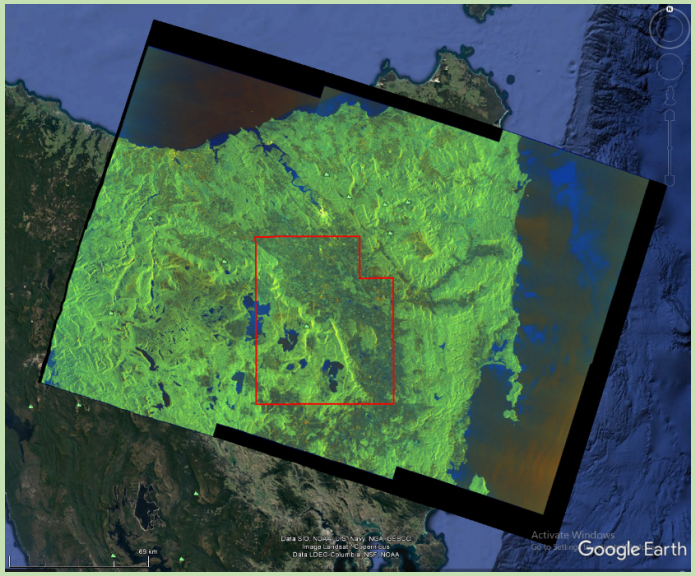
• calibration-s1a-iw1-slc-vv-20170812t191741-20170812t191806-017894-01e023-004.xml • calibration-s1a-iw2-slc-vv-20170812t191742-20170812t191807-017894-01e023-005.xml • calibration-s1a-iw3-slc-vv-20170812t191743-20170812t191808-017894-01e023-006.xml **Measurement** • s1a-iw1-slc-vh-20170812t191741-20170812t191806-017894-01e023-001.tiff • s1a-iw2-slc-vh-20170812t191742-20170812t191807-017894-01e023-002.tiff • s1a-iw3-slc-vh-20170812t191743-20170812t191808-017894-01e023-003.tiff • s1a-iw1-slc-vv-20170812t191741-20170812t191806-017894-01e023-004.tiff • s1a-iw2-slc-vv-20170812t191742-20170812t191807-017894-01e023-005.tiff • s1a-iw3-slc-vv-20170812t191743-20170812t191808-017894-01e023-006.tiff	
8. *S1A_IW_SLC__1SDV_20170824T191741_20170824T191808_018069_01E56E_48CF.SAFE*	
Annotation • s1a-iw1-slc-vh-20170824t191741-20170824t191806-018069-01e56e-001.xml • s1a-iw2-slc-vh-20170824t191742-20170824t191807-018069-01e56e-002.xml • s1a-iw3-slc-vh-20170824t191743-20170824t191808-018069-01e56e-003.xml • s1a-iw1-slc-vv-20170824t191741-20170824t191806-018069-01e56e-004.xml • s1a-iw2-slc-vv-20170824t191742-20170824t191807-018069-01e56e-005.xml • s1a-iw3-slc-vv-20170824t191743-20170824t191808-018069-01e56e-006.xml	**Date**: 2017-08-24T21:09:24 **Class**: SENTINEL-1 Interferometric Wide Swath Level 1 Product

Annotation/calibration

- noise-s1a-iw1-slc-vh-20170824t191741-20170824t191806-018069-01e56e-001.xml
- noise-s1a-iw2-slc-vh-20170824t191742-20170824t191807-018069-01e56e-002.xml
- noise-s1a-iw3-slc-vh-20170824t191743-20170824t191808-018069-01e56e-003.xml
- noise-s1a-iw1-slc-vv-20170824t191741-20170824t191806-018069-01e56e-004.xml
- noise-s1a-iw2-slc-vv-20170824t191742-20170824t191807-018069-01e56e-005.xml
- noise-s1a-iw3-slc-vv-20170824t191743-20170824t191808-018069-01e56e-006.xml
- calibration-s1a-iw1-slc-vh-20170824t191741-20170824t191806-018069-01e56e-001.xml
- calibration-s1a-iw2-slc-vh-20170824t191742-20170824t191807-018069-01e56e-002.xml
- calibration-s1a-iw3-slc-vh-20170824t191743-20170824t191808-018069-01e56e-003.xml
- calibration-s1a-iw1-slc-vv-20170824t191741-20170824t191806-018069-01e56e-004.xml
- calibration-s1a-iw2-slc-vv-20170824t191742-20170824t191807-018069-01e56e-005.xml
- calibration-s1a-iw3-slc-vv-20170824t191743-20170824t191808-018069-01e56e-006.xml

Measurement

- s1a-iw1-slc-vh-20170824t191741-20170824t191806-018069-01e56e-001.tiff
- s1a-iw2-slc-vh-20170824t191742-20170824t191807-018069-01e56e-002.tiff
- s1a-iw3-slc-vh-20170824t191743-20170824t191808-018069-01e56e-003.tiff
- s1a-iw1-slc-vv-20170824t191741-20170824t191806-018069-01e56e-004.tiff
- s1a-iw2-slc-vv-20170824t191742-20170824t191807-018069-01e56e-005.tiff



- s1a-iw3-slc-vv-20170824t191743-20170824t191808-018069-01e56e-006.tiff

9. *S1A_IW_SLC__1SDV_20170905T191742_20170905T191809_018244_01EAC1_942E.SAFE*

Annotation

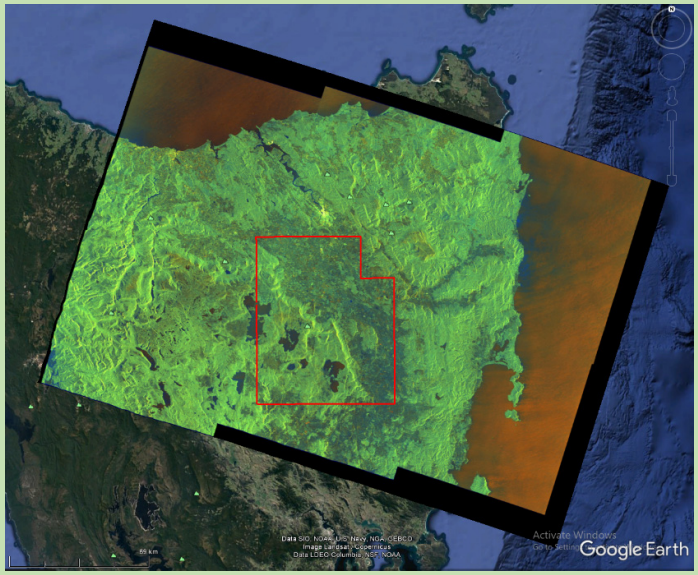
- s1a-iw1-slc-vh-20170905t191742-20170905t191807-018244-01eac1-001.xml
- s1a-iw2-slc-vh-20170905t191743-20170905t191808-018244-01eac1-002.xml
- s1a-iw3-slc-vh-20170905t191744-20170905t191809-018244-01eac1-003.xml
- s1a-iw1-slc-vv-20170905t191742-20170905t191807-018244-01eac1-004.xml
- s1a-iw2-slc-vv-20170905t191743-20170905t191808-018244-01eac1-005.xml
- s1a-iw3-slc-vv-20170905t191744-20170905t191809-018244-01eac1-006.xml

Annotation/calibration

- noise-s1a-iw1-slc-vh-20170905t191742-20170905t191807-018244-01eac1-001.xml
- noise-s1a-iw2-slc-vh-20170905t191743-20170905t191808-018244-01eac1-002.xml
- noise-s1a-iw3-slc-vh-20170905t191744-20170905t191809-018244-01eac1-003.xml
- noise-s1a-iw1-slc-vv-20170905t191742-20170905t191807-018244-01eac1-004.xml
- noise-s1a-iw2-slc-vv-20170905t191743-20170905t191808-018244-01eac1-005.xml
- noise-s1a-iw3-slc-vv-20170905t191744-20170905t191809-018244-01eac1-006.xml
- calibration-s1a-iw1-slc-vh-20170905t191742-20170905t191807-018244-01eac1-001.xml
- calibration-s1a-iw2-slc-vh-20170905t191743-20170905t191808-018244-01eac1-002.xml
- calibration-s1a-iw3-slc-vh-20170905t191744-20170905t191809-018244-01eac1-003.xml

Date: 2017-09-05T21:04:43

Class: SENTINEL-1 Interferometric Wide Swath Level 1 Product



- calibration-s1a-iw1-slc-vv-20170905t191742-20170905t191807-018244-01eac1-004.xml
- calibration-s1a-iw2-slc-vv-20170905t191743-20170905t191808-018244-01eac1-005.xml
- calibration-s1a-iw3-slc-vv-20170905t191744-20170905t191809-018244-01eac1-006.xml

Measurement

- s1a-iw1-slc-vh-20170905t191742-20170905t191807-018244-01eac1-001.tiff
- s1a-iw2-slc-vh-20170905t191743-20170905t191808-018244-01eac1-002.tiff
- s1a-iw3-slc-vh-20170905t191744-20170905t191809-018244-01eac1-003.tiff
- s1a-iw1-slc-vv-20170905t191742-20170905t191807-018244-01eac1-004.tiff
- s1a-iw2-slc-vv-20170905t191743-20170905t191808-018244-01eac1-005.tiff
- s1a-iw3-slc-vv-20170905t191744-20170905t191809-018244-01eac1-006.tiff

PROCESSING

IMPORT & MAKE CONNECTION GRAPH

The processing graph was calculated after the import of radar images. The main idea is to analyze the spatial and temporal base for all pairs of images with the subsequent selection of those pairs that can be used to determining the displacements of the Earth's surface.

Based on the analysis of the baseline between all possible pairs (**Figure 125**), the maximum value of the perpendicular component between the position of the satellite during survey was not greater than 150 m. Thus, all the considered images were suitable for interferometric processing using the DInSAR technology.

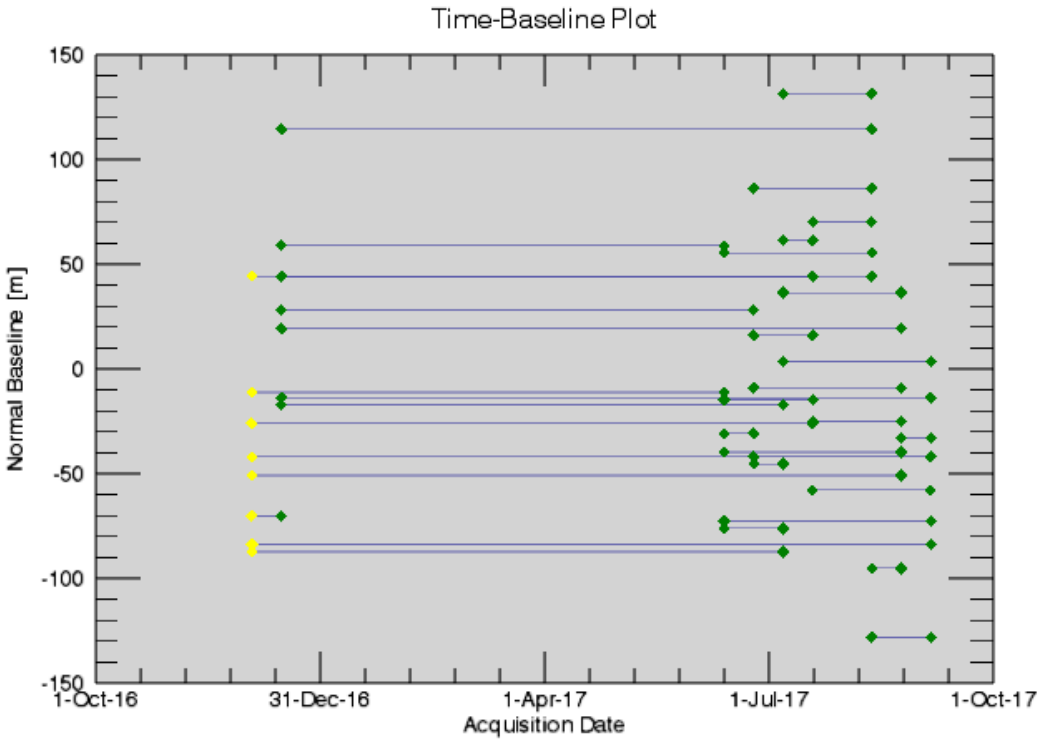


Figure 125: Time-Position plot, which provides the normal distance between the Super Master (y axis) and the input acquisition dates (x axis).
Yellow color - the first image (Super Master) acquired on 2016/12/03

The second criterion of the suitability of images for the interferometric processing is the analysis of the time base or the time interval between the dates of obtaining the images. Ideally, these gaps should be sufficiently small, i.e. to avoid the effect of temporal decorrelation of images for varying reasons such as changes in vegetation cover, precipitation, water level changes, hydro-system, etc., and other technogenic processes. The graph of mutual temporal bases with the corresponding values of the normal components of the baselines is shown in **Figure 126**.

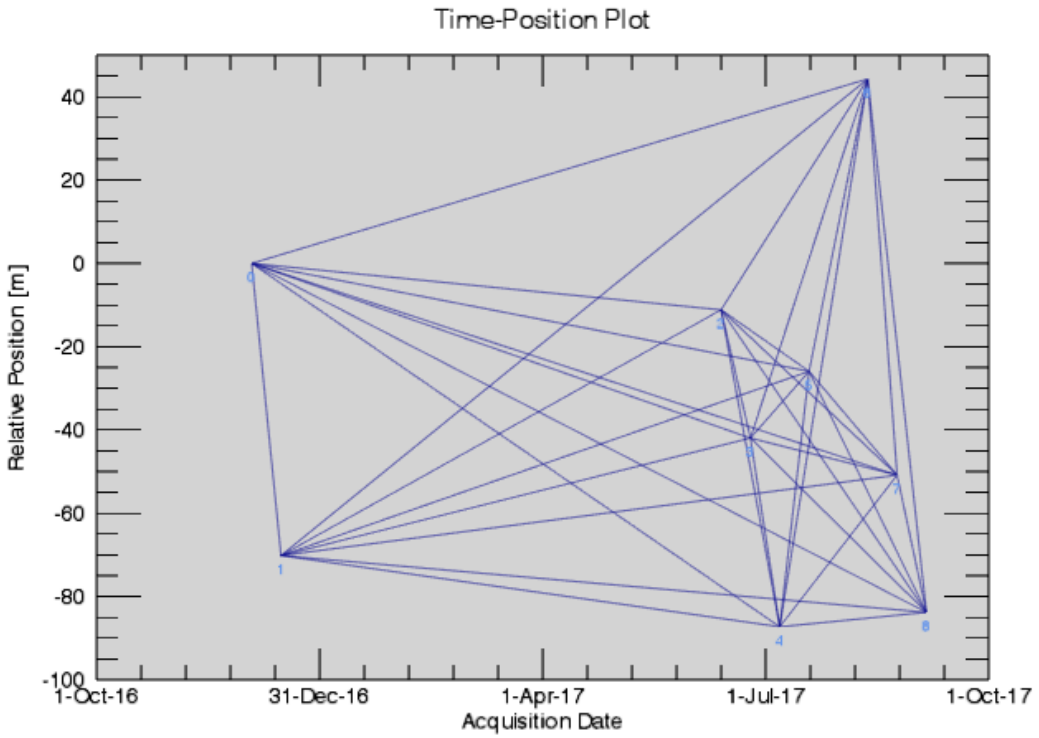


Figure 126: Time-Baseline plot - provides the normal baseline (y axis) and the input acquisition dates (x axis).

This functionality defines the SAR pair combination and connection network, which is used for the generation of the multiple differential interferograms.

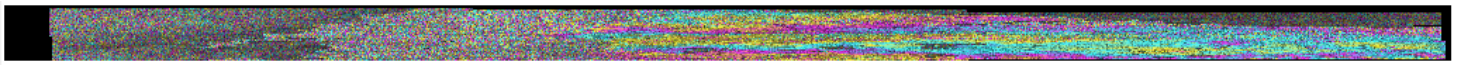
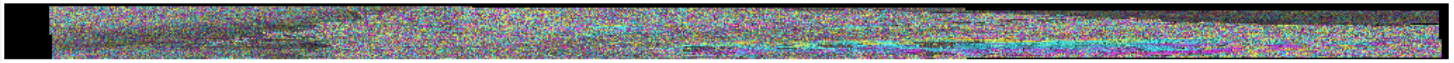
Thus, all 9 images were used, and the total number of interferometric pairs was 36. Other statistical characteristics include:

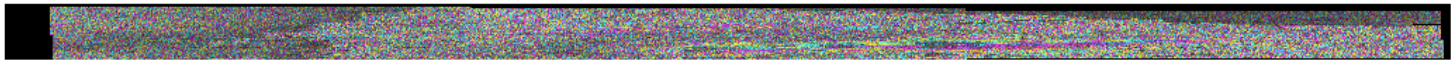
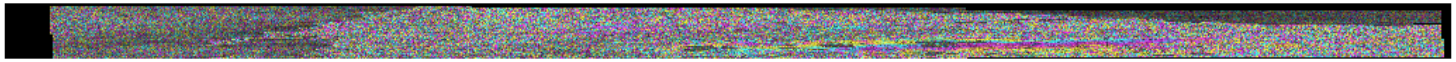
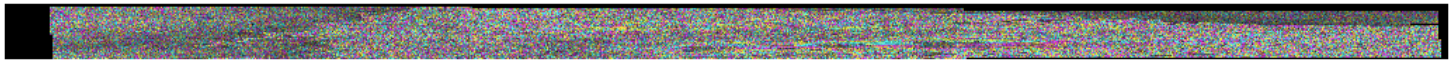
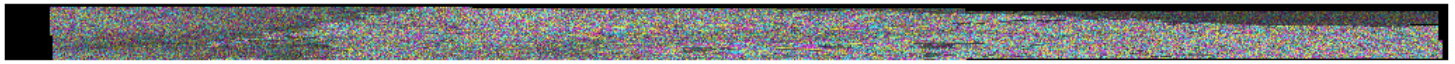
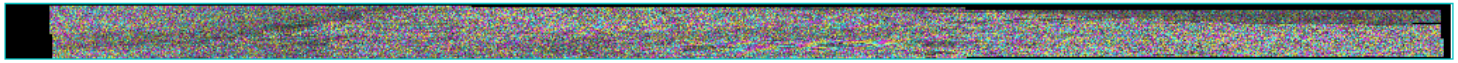
- Mean Absolute Normal Baseline found: 51.58155873
- Max Absolute Normal Baseline found: 131.0386963
- Min Absolute Normal Baseline found: 3.566750526
- Max Critical Baseline Percentage admitted: 45
- Min Critical Baseline Percentage admitted: 0

RADAR INTERFEROMETRY PROCESS

For each interferometric pair, a differential interferogram DInSAR was calculated, representing the interferometric phase difference $\Delta\phi$, which is (as shown above) the superposition of the following components: the topographic phase advance, the phase difference caused by the change in coordinates of the terrestrial objects during the time between the scans, the phase delays caused by the influence of atmospheric conditions on the results of observations (particularly the content of water vapor in the air), and the interference caused by the phenomena of temporary decoding and loss of coherence of radar images within the interferometric pair. The sets of initial differential interferograms are presented in **Table 8**.

Table 8: Source (not expanded) interferograms

The image of the differential interferogram	Pair
MASTER : 0 [sentinel1_147_20161203_191736644_IW_SIW1_D_VV_slc_list] ID : [0] SLAVE : [sentinel1_147_20161215_191736136_IW_SIW1_D_VV_slc_list] ID : [1] SLAVE : [sentinel1_147_20170613_191737736_IW_SIW1_D_VV_slc_list] ID : [2] SLAVE : [sentinel1_147_20170625_191738515_IW_SIW1_D_VV_slc_list] ID : [3] SLAVE : [sentinel1_147_20170707_191738988_IW_SIW1_D_VV_slc_list] ID : [4] SLAVE : [sentinel1_147_20170719_191739667_IW_SIW1_D_VV_slc_list] ID : [5] SLAVE : [sentinel1_147_20170812_191741148_IW_SIW1_D_VV_slc_list] ID : [6] SLAVE : [sentinel1_147_20170824_191741770_IW_SIW1_D_VV_slc_list] ID : [7] SLAVE : [sentinel1_147_20170905_191742162_IW_SIW1_D_VV_slc_list] ID : [8]	
	m0_s1
	m0_s2

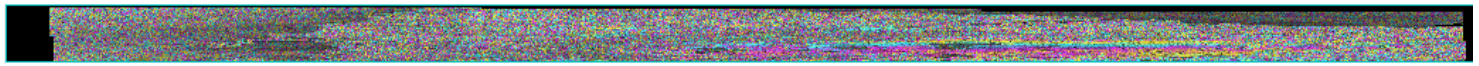
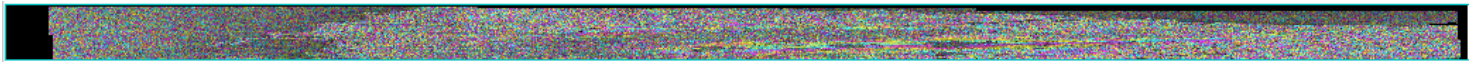
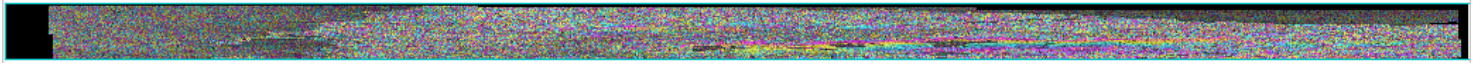
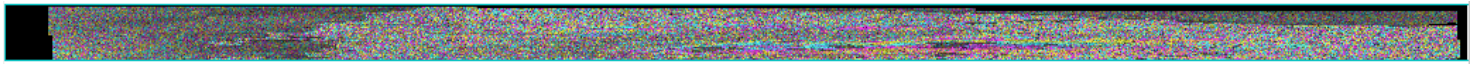
	m0_s3
	m0_s4
	m0_s5
	m0_s6
	m0_s7
	m0_s8

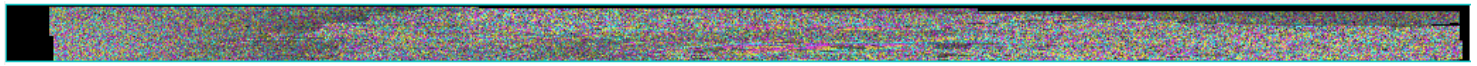
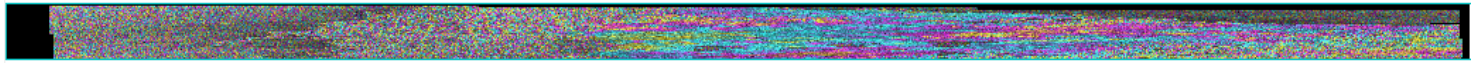
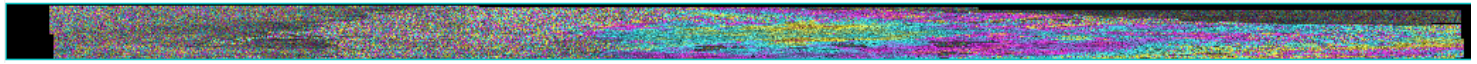
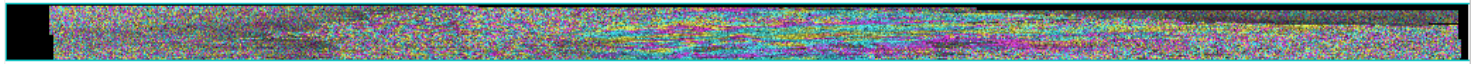
MASTER : 1 [sentinel1_147_20161215_191736136_IW_SIW1_D_VV_slc_list] ID : [1]

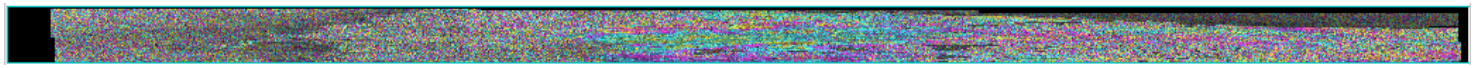
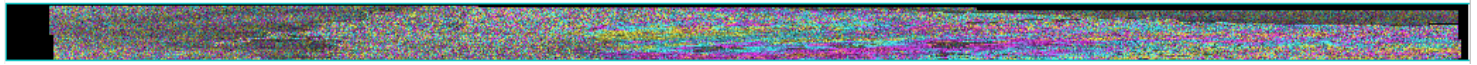
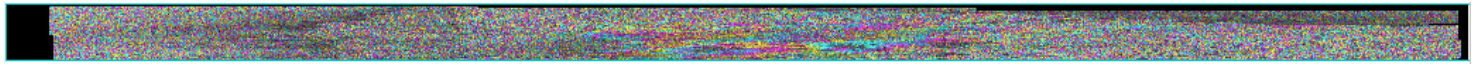
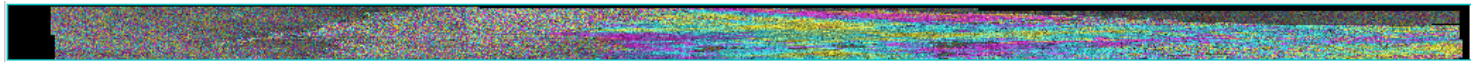
SLAVE : [sentinel1_147_20170613_191737736_IW_SIW1_D_VV_slc_list] ID : [2]

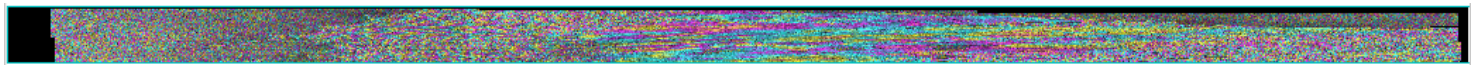
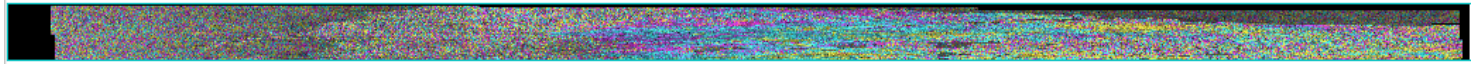
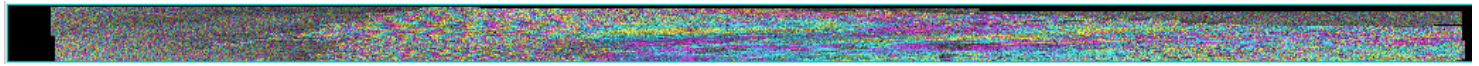
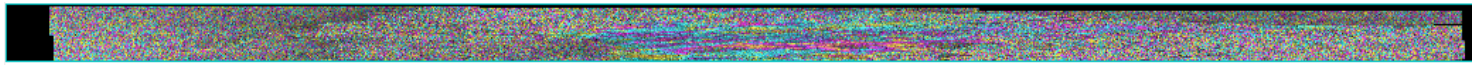
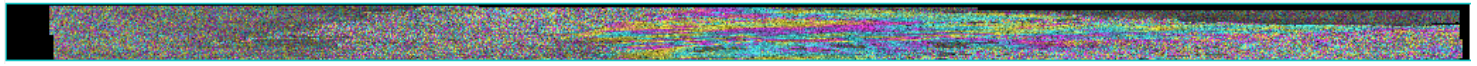
SLAVE : [sentinel1_147_20170625_191738515_IW_SIW1_D_VV_slc_list] ID : [3]

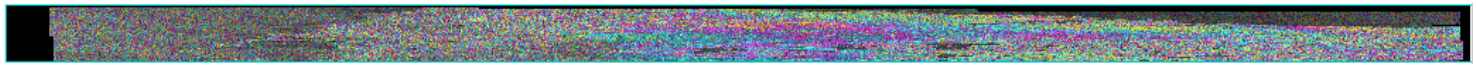
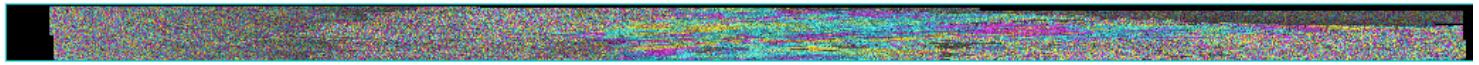
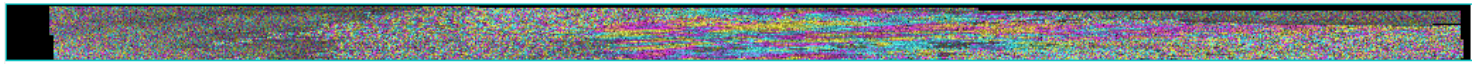
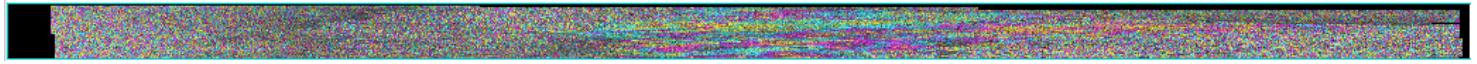
SLAVE : [sentinel1_147_20170707_191738988_IW_SIW1_D_VV_slc_list] ID : [4]

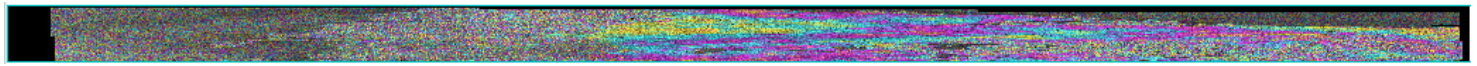
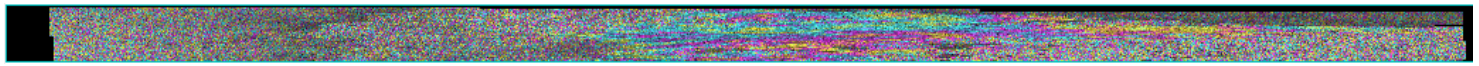
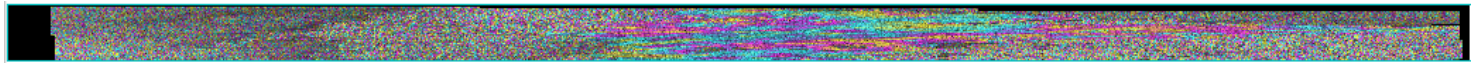
SLAVE : [sentinel1_147_20170719_191739667_IW_SIW1_D_VV_slc_list] ID : [5] SLAVE : [sentinel1_147_20170812_191741148_IW_SIW1_D_VV_slc_list] ID : [6] SLAVE : [sentinel1_147_20170824_191741770_IW_SIW1_D_VV_slc_list] ID : [7] SLAVE : [sentinel1_147_20170905_191742162_IW_SIW1_D_VV_slc_list] ID : [8]	
	m1_s2
	m1_s3
	m1_s4
	m1_s5
	m1_s6
	m1_s7

	m1_s8
MASTER : 2 [sentinel1_147_20170613_191737736_IW_SIW1_D_VV_slc_list] ID : [2] SLAVE : [sentinel1_147_20170625_191738515_IW_SIW1_D_VV_slc_list] ID : [3] SLAVE : [sentinel1_147_20170707_191738988_IW_SIW1_D_VV_slc_list] ID : [4] SLAVE : [sentinel1_147_20170719_191739667_IW_SIW1_D_VV_slc_list] ID : [5] SLAVE : [sentinel1_147_20170812_191741148_IW_SIW1_D_VV_slc_list] ID : [6] SLAVE : [sentinel1_147_20170824_191741770_IW_SIW1_D_VV_slc_list] ID : [7] SLAVE : [sentinel1_147_20170905_191742162_IW_SIW1_D_VV_slc_list] ID : [8]	
	m2_s3
	m2_s4
	m2_s5

	m2_s6
	m2_s7
	m2_s8
MASTER : 3 [sentinel1_147_20170625_191738515_IW_SIW1_D_VV_slc_list] ID : [3] SLAVE : [sentinel1_147_20170707_191738988_IW_SIW1_D_VV_slc_list] ID : [4] SLAVE : [sentinel1_147_20170719_191739667_IW_SIW1_D_VV_slc_list] ID : [5] SLAVE : [sentinel1_147_20170812_191741148_IW_SIW1_D_VV_slc_list] ID : [6] SLAVE : [sentinel1_147_20170824_191741770_IW_SIW1_D_VV_slc_list] ID : [7] SLAVE : [sentinel1_147_20170905_191742162_IW_SIW1_D_VV_slc_list] ID : [8]	
	m3_s4

	m3_s5
	m3_s6
	m3_s7
	m3_s8
MASTER : 4 [sentinel1_147_20170707_191738988_IW_SIW1_D_VV_slc_list] ID : [4] SLAVE : [sentinel1_147_20170719_191739667_IW_SIW1_D_VV_slc_list] ID : [5] SLAVE : [sentinel1_147_20170812_191741148_IW_SIW1_D_VV_slc_list] ID : [6] SLAVE : [sentinel1_147_20170824_191741770_IW_SIW1_D_VV_slc_list] ID : [7] SLAVE : [sentinel1_147_20170905_191742162_IW_SIW1_D_VV_slc_list] ID : [8]	
	m4_s5

	m4_s6
	m4_s7
	m4_s8
MASTER : 5 [sentinel1_147_20170719_191739667_IW_SIW1_D_VV_slc_list] ID : [5] SLAVE : [sentinel1_147_20170812_191741148_IW_SIW1_D_VV_slc_list] ID : [6] SLAVE : [sentinel1_147_20170824_191741770_IW_SIW1_D_VV_slc_list] ID : [7] SLAVE : [sentinel1_147_20170905_191742162_IW_SIW1_D_VV_slc_list] ID : [8]	
	m5_s6
	m5_s7
	m5_s8

MASTER : 6 [sentinel1_147_20170812_191741148_IW_SIW1_D_VV_slc_list] ID : [6] SLAVE : [sentinel1_147_20170824_191741770_IW_SIW1_D_VV_slc_list] ID : [7] SLAVE : [sentinel1_147_20170905_191742162_IW_SIW1_D_VV_slc_list] ID : [8]	
	m6_s7
	m6_s8
MASTER : 7 [sentinel1_147_20170824_191741770_IW_SIW1_D_VV_slc_list] ID : [7] SLAVE : [sentinel1_147_20170905_191742162_IW_SIW1_D_VV_slc_list] ID : [8]	
	m7_s8

INTERFEROGRAM REFINEMENT AND RE-FLATTENING

At this stage of the analysis, the orbital parameters are refined for a more accurate calculation and subsequent removal of the topographic component. A set of ground control points (GCP - geodetic control points) was created, uniquely linking the SAR geometry of interferometric images with the geographic coordinates of the reference DEM (DEM) and the altitude values that correspond to these coordinates. The process of creating GCP-points in the SBaS technology is fairly time-consuming, complex, and is performed interactively. Each coordinate position for such a point is determined based on the quality of the interferograms. The example of the accumulated GCP points within this project is shown in **Figure 127**. Poor quality of the interferograms did not allow localizing control points in the South-Eastern part of the area.



Figure 127: Geodetic Control Points.

INVERSION

The process of Inversion involves transitioning from the differential interferograms refined during the previous stage to the values of excesses and rates of displacement for the dates of the images. It is performed in two stages. Firstly, the interferograms are filtered, and smoothed; they are scanned and refined for phase values. The products are then optimized (particularly) by removing the atmospheric phase.

GEOCODING

The SBaS-technology resulting products are geocoded (according to the user-defined parameters) and can be re-projected to any other projection.

RESULTS

After the thorough analysis of all the interferograms, the pairs dating to 2016 were excluded from the analysis due to a significant loss of coherency and temporal decorrelation with the images dating to 2017.

The main result of the SBaS-technology interferometric work is a set of raster materials that characterize the magnitude, rate, and direction of displacements of the earth's surface for the period covered by the dates of acquisition of the radar images utilized herein. The base state of the Earth's surface (corresponding to zero offset) was adopted as 2017-06-13. All other displacement surfaces were calculated with respect to this date (**Figure 128** - **Figure 132**).

The interpretation of the shown surfaces is as follows: the cold colors correspond to the areas of the newest tectonic uplifts (dark blue corresponds to the largest uplifts), warm colors correspond to the latest tectonic subsidence (bright red corresponds to the subsidence with the highest amplitude). The delineation of the areas of local movements of the Earth's surface makes sense only if the areas of such anomalous movements could be localized to particular areas as compared to the rest of the surface. However, abnormal displacement values occurring within very small areas (pixel level) are often attributed to coastlines of water bodies, swamps, water bodies with seasonal fluctuations of water level, etc. and should be discarded for the purposes of this research.

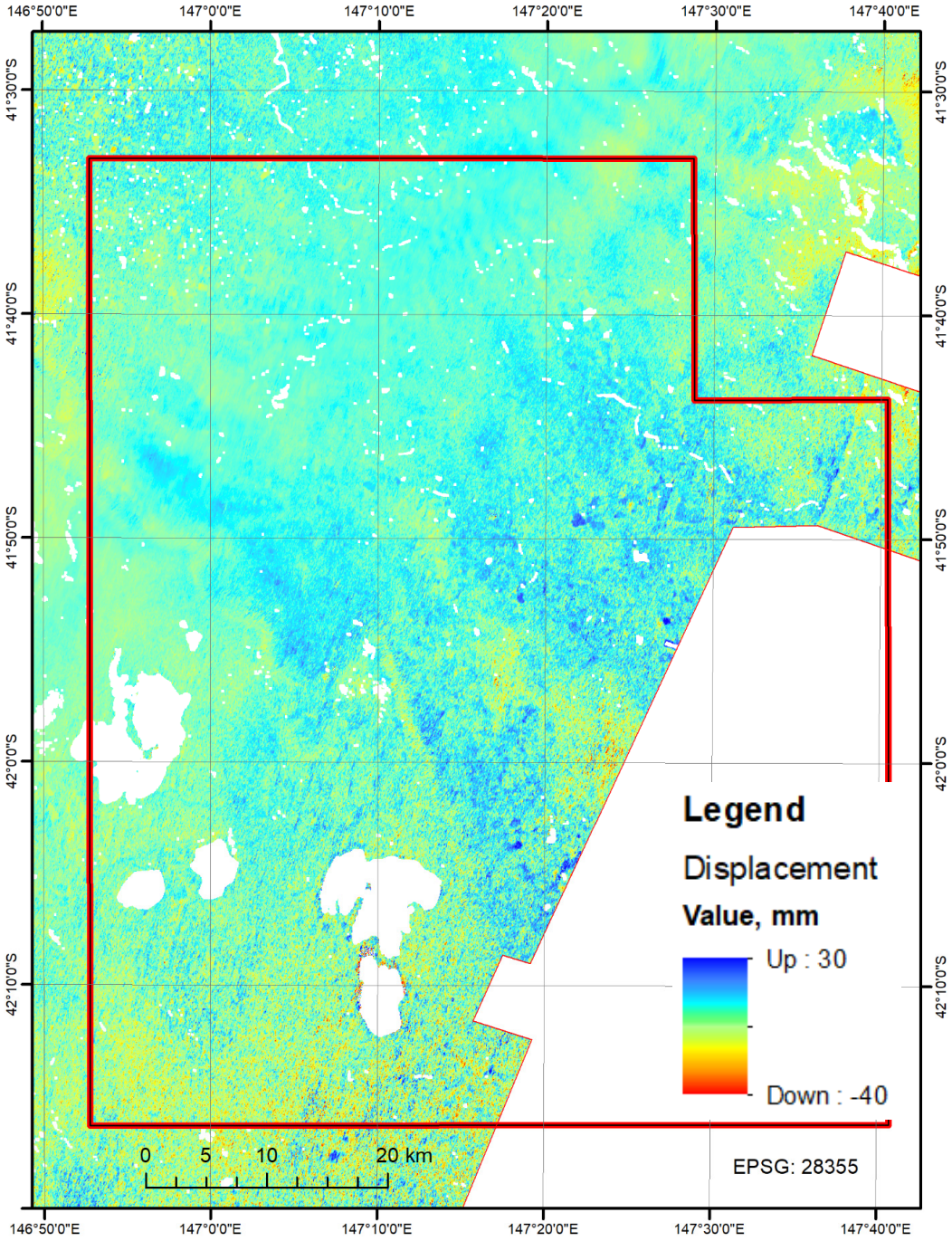


Figure 128: Displacement surface for the period 2017/06/25 – 2017/06/13.

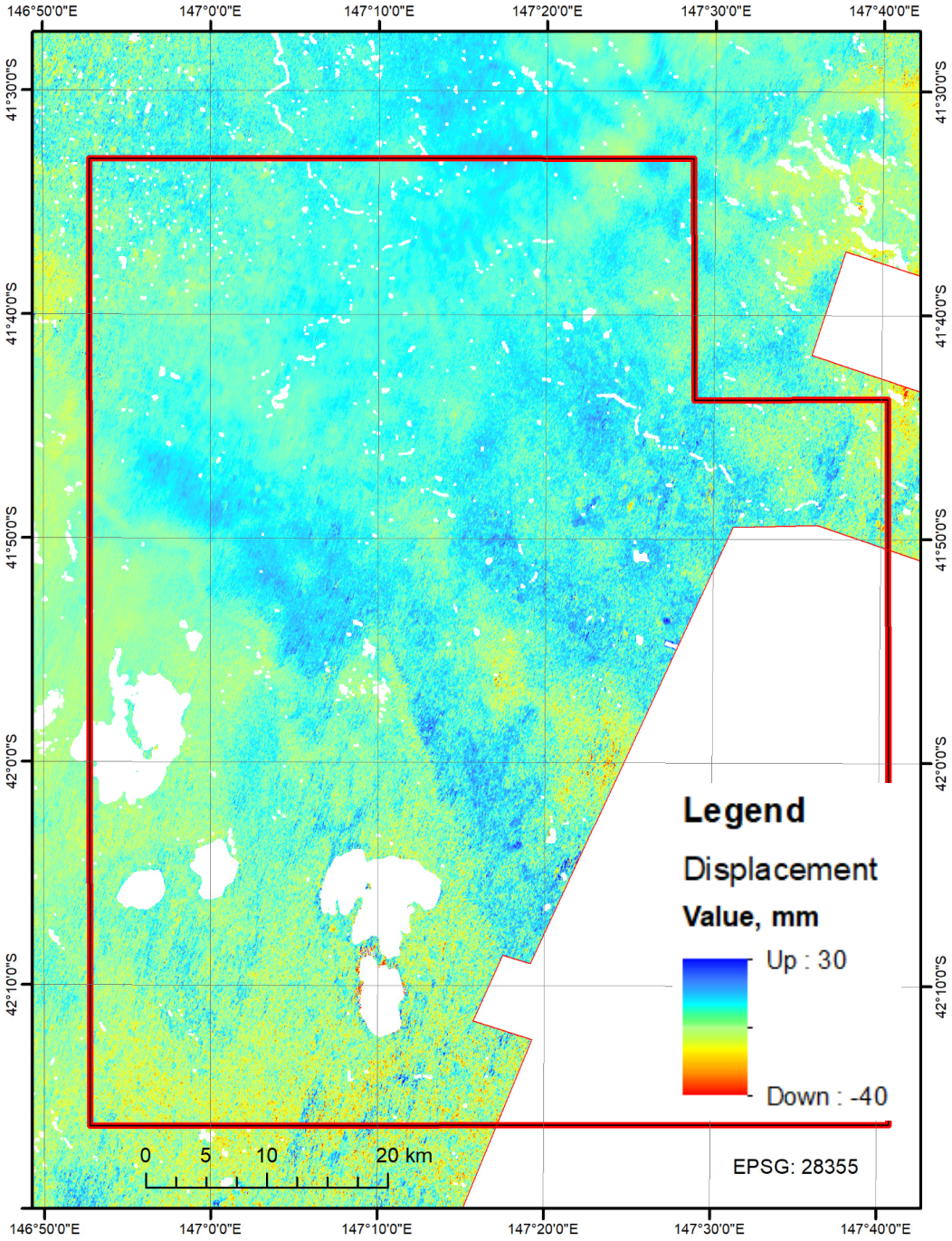


Figure 129: Displacement surface for the period 2017/07/07 – 2017/06/13.

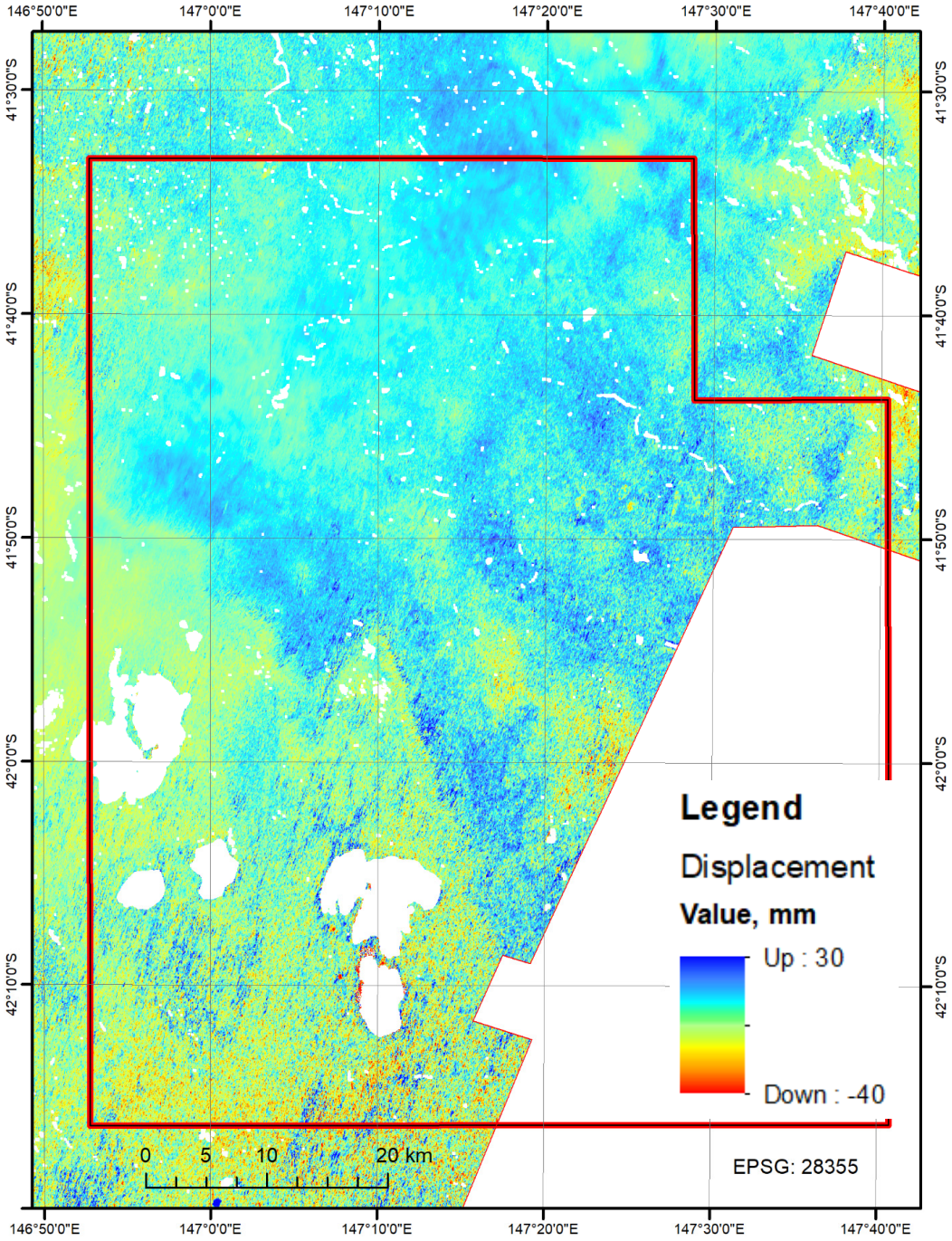


Figure 130: Displacement surface for the period 2017/07/19 – 2017/06/13.

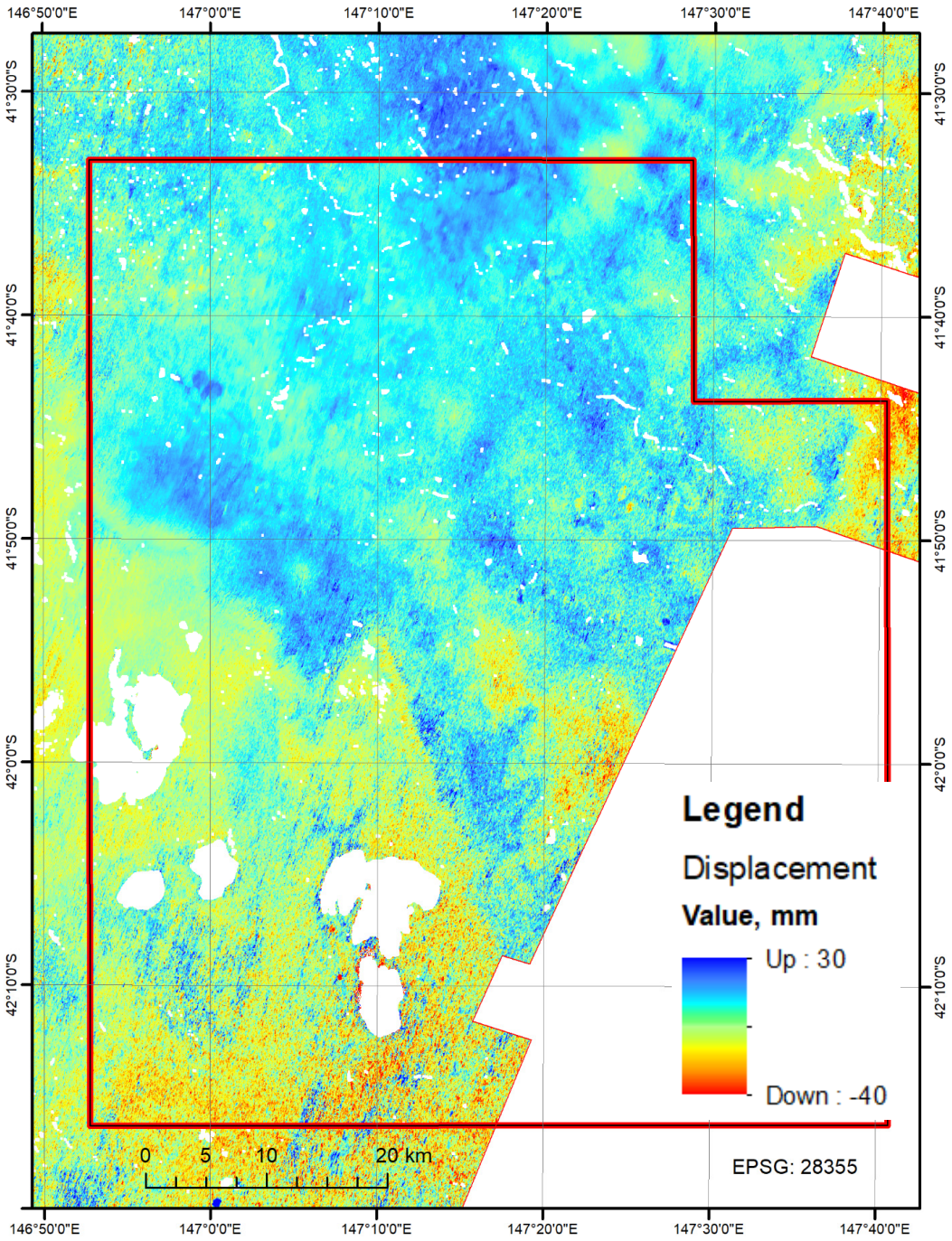


Figure 131: Displacement surface for the period 2017/08/12 – 2017/06/13.

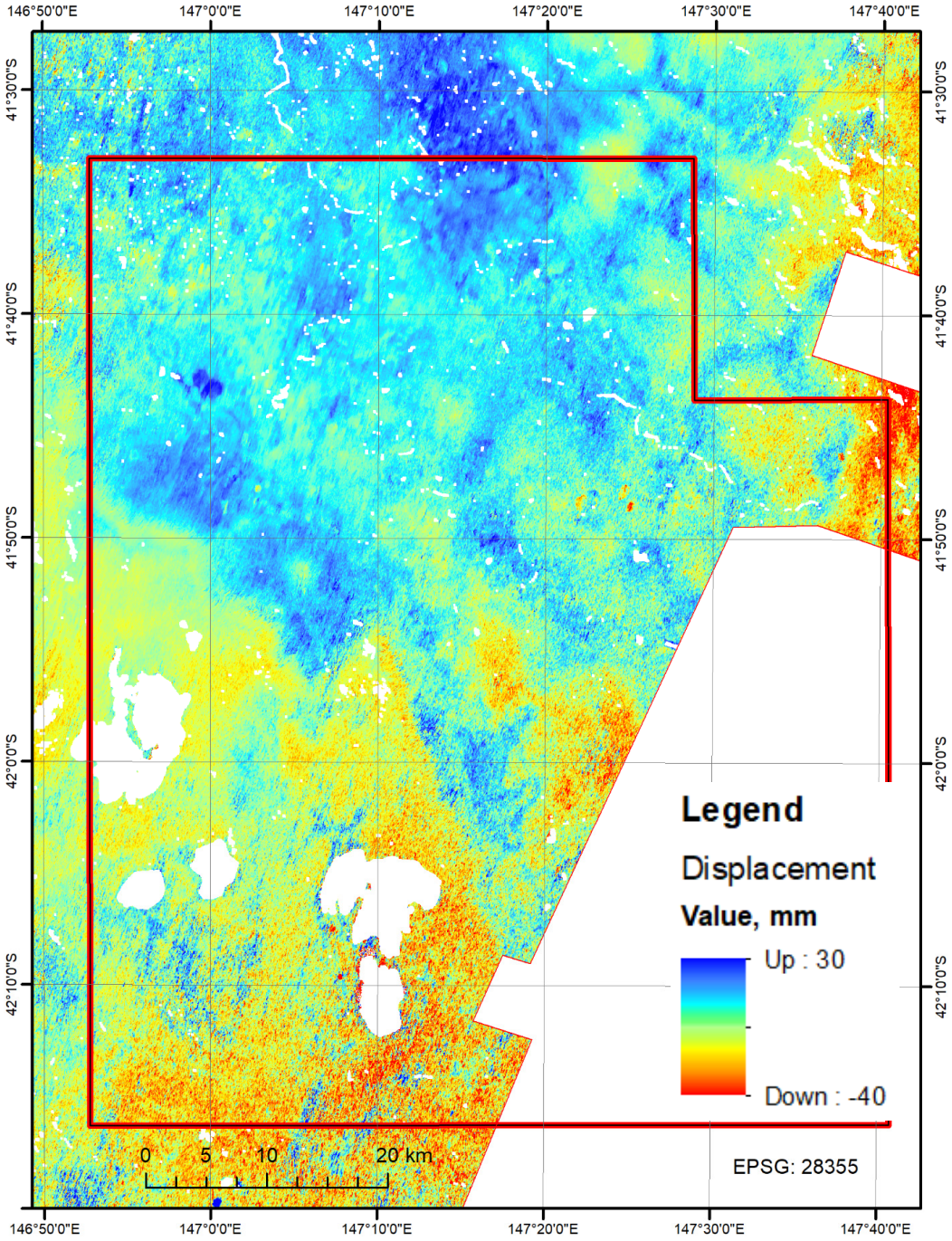


Figure 132: Displacement surface for the period 2017/09/05 – 2017/06/13.

Figure 133 displays the Time profiles of the development of the surface displacements measured in the specific locations along line A.

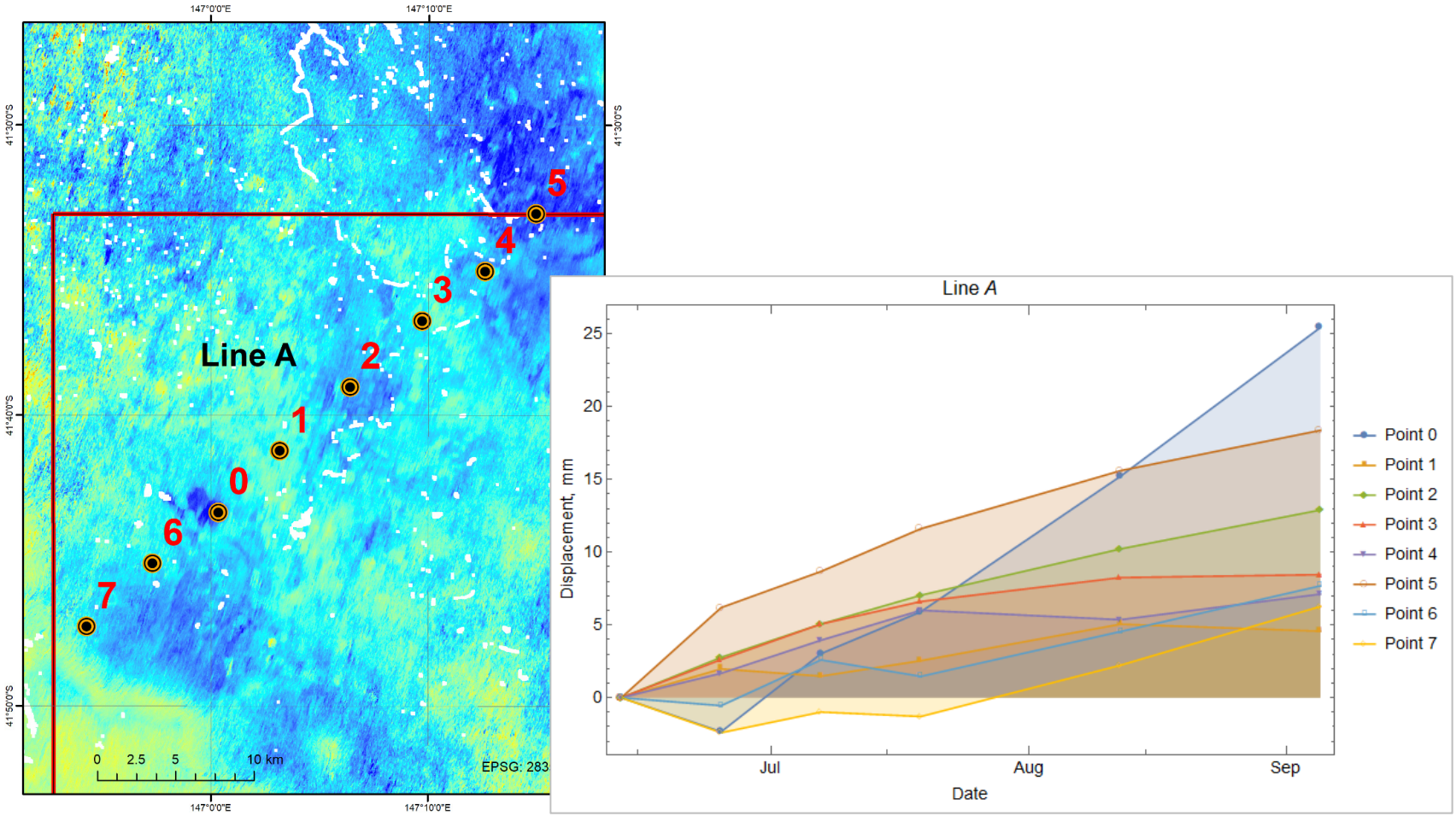


Figure 133: Time profiles of the surface displacements measured in specific location along line A.

CONCLUSIONS

The method of radar interferometry has a certain practical value when use for the purposes of localization and quantification of the amplitude of neotectonics movements. It has the following advantages:

- Regularity of acquisition of data;
- Low cost (per m2);
- Excellent coverage;
- Ability to receive values for a particular time and for every point within one scene;
- No access restrictions;
- Ability to conduct regular surveys.

The geological value of radar interferometry is substantial, as the method output the information on the newest neotectonic (including active denudational) processes. This information is of an independent merit, and it can be incorporate in other studies.

For the purposes of this study, the areas of a relatively stable uplifting are of the greatest interest. This process is likely to affect the entire cross section of the sedimentary cover and can lead to the formation of anticlinal HC traps. These areas are shown in **Figure 134**.

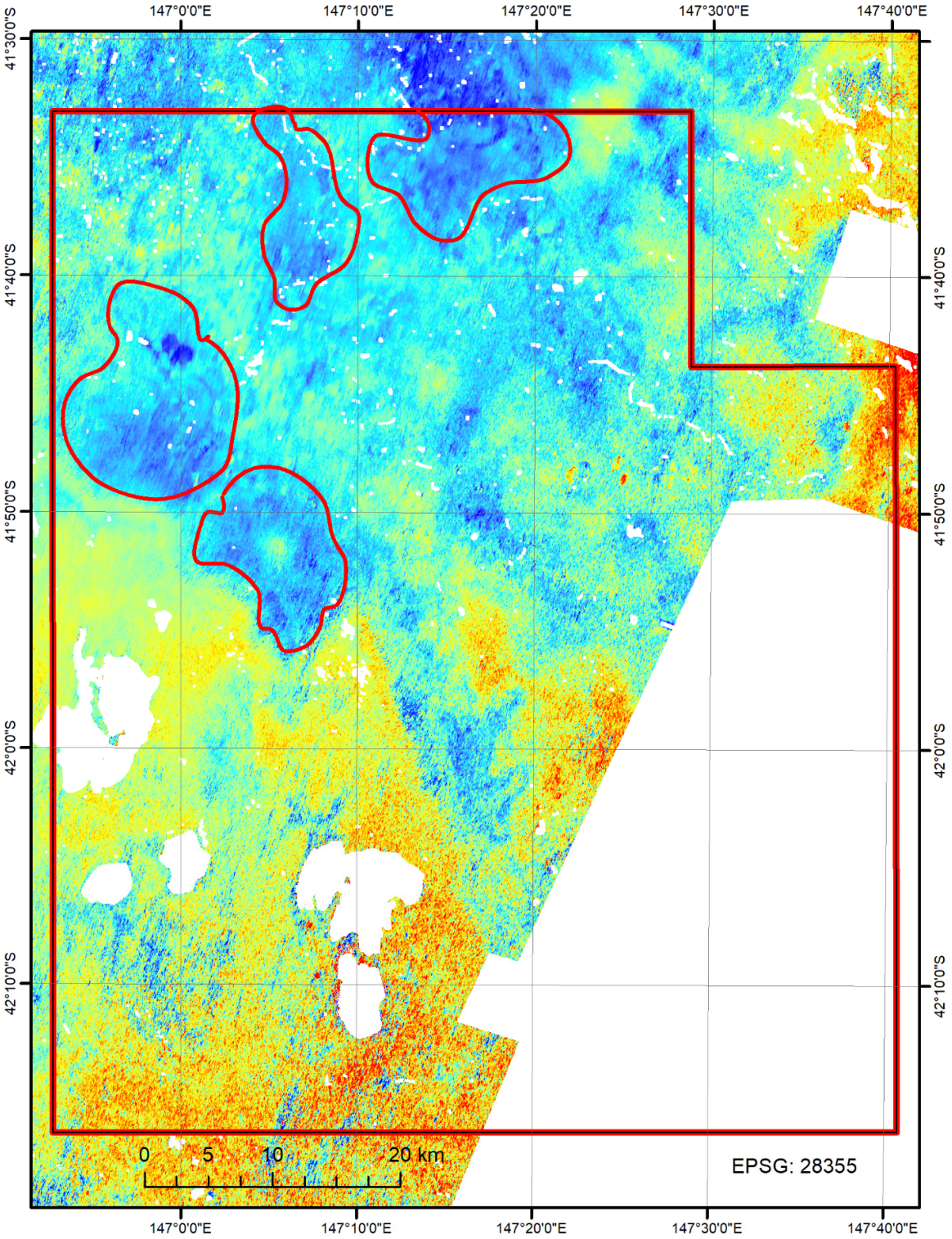
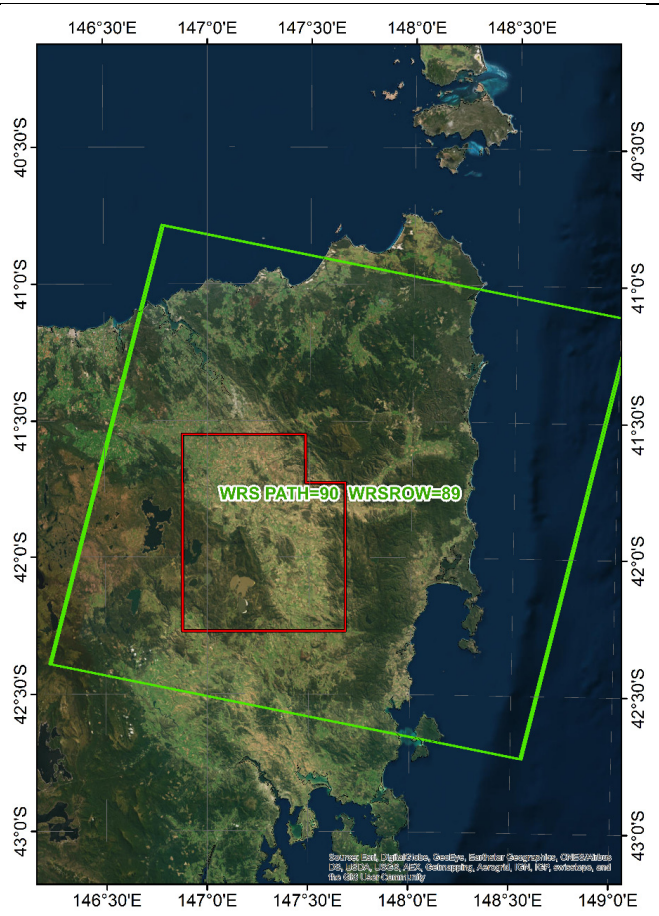


Figure 134: Contours (red) of potential anticlinal structural traps.

3. APPENDIXES

APPENDIX 1 – SOURCE SATELLITE DATA

MULTISPECTRAL DATA

DATA TYPE	PARAMETERS AND CHARACTERISTICS	OVERVIEW
Landsat-7 (ETM+)	**Sensor Technical Specifications** http://landsat.gsfc.nasa.gov/about/etm.html Sensor type: opto-mechanical Spatial Resolution: 30 m (60 m - thermal, 15-m pan) Spectral Range: 0.45 - 12.5 µm Number of Bands: 8 Temporal Resolution: 16 days Image Size: 183 km X 170 km Swath: 183 km Programmable: yes Status: with problems (after 2003)	

Band Number	Spectral range, µm	Spatial resolution
1	0.45-0.515	30 m
2	0.525-0.605	30 m
3	0.63-0.69	30 m
4	0.75-0.90	30 m
5	1.55-1.75	30 m
6 (H/L mode)	10.4-12.5	60 m
7	2.09-2.35	30 m
8	0.52-0.9	15 m

Most Landsat-7 ETM+ scenes are processed with the Standard Terrain Correction (Level 1T). Standard Terrain Correction provides systematic radiometric and geometric accuracy by incorporating ground control points while employing a Digital Elevation Model (DEM) for topographic accuracy.

Legend

EL-30 area

Tasmania boundary

ID and Acquisition date

LE70900892000097EDC00, 2000/04/06

LE70900892001099ASA00, 2001/04/09

ls7.png

Landsat-8 (OLI/TIRS)

Sensor Technical Specifications
http://landsat.gsfc.nasa.gov/?p=5081

OLI sensor	**TIRS sensor**
Sensor type: push broom	Sensor type: push broom
Spatial Resolution: 30 m (15-m pan)	Spatial Resolution: 100 m
Spectral Range: 0.43 – 1.39 µm	Spectral Range: 10.6 – 12.5 µm
Number of Bands: 9	Number of Bands: 2
Temporal Resolution: 16 days	Temporal Resolution: 16 days
Image Size: 185 km X 180 km	Image Size: 185 km X 180 km
Swath: 185 km	Swath: 185 km
Programmable: yes	Programmable: yes

Band Number	Spectral range, µm	Spatial resolution, m
1	0.433–0.453	30
2	0.450–0.515	30
3	0.525–0.600	30
4	0.630–0.680	30
5	0.845–0.885	30
6	1.560–1.660	60
7	2.100–2.300	30
8	0.500–0.680	15
9	1.360–1.390	30
10	10.6-11.2	100
11	11.5-12.5	100

Legend

EL-30 area

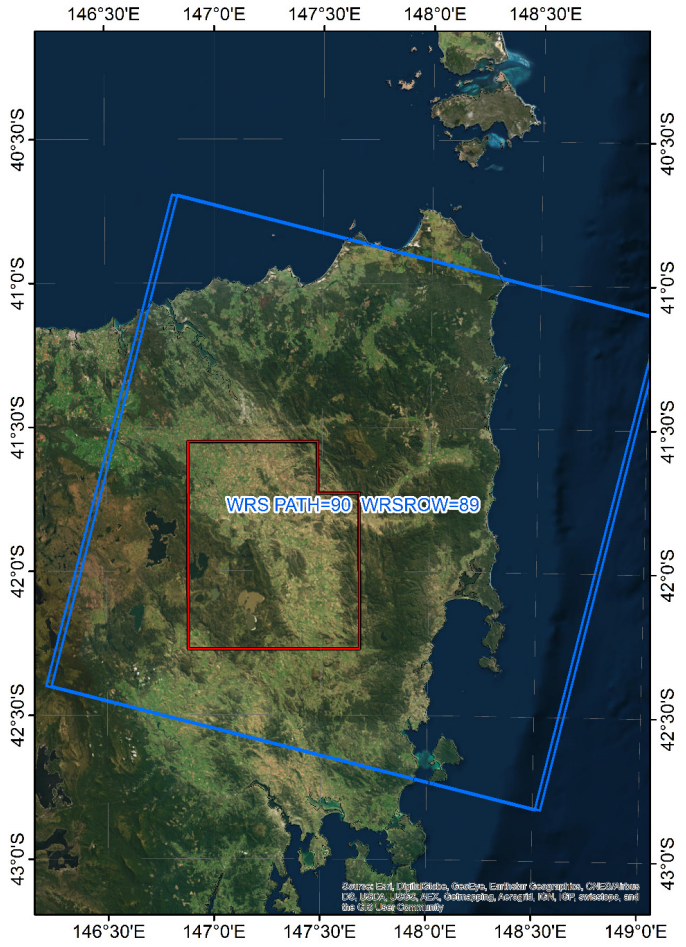
Tasmania boundary

ID and Acquisition date

LC80900892016357LGN02, 2016/12/22

LC80900892016133LGN00, 2016/05/12

LC80900892015290LGN00, 2015/10/17



ls8.png

Landsat-5 (TM)

Sensor Technical Specifications
http://landsat.gsfc.nasa.gov/?p=3217
Sensor type: opto-mechanical
Spatial Resolution: 30 m (120 m - thermal)
Spectral Range: 0.45 - 12.5 µm
Number of Bands: 7
Temporal Resolution: 16 days
Image Size: 185 km X 172 km
Swath: 185 km
Programmable: yes
Status: don't operates (after 2011)

Band Number	Spectral range, µm	Spatial resolution
1	0.45-0.52	30 m
2	0.52-0.60	30 m
3	0.63-0.69	30 m
4	0.76-0.90	30 m
5	1.55-1.75	30 m
6	10.4-12.5	120 m
7	2.08-2.35	30 m

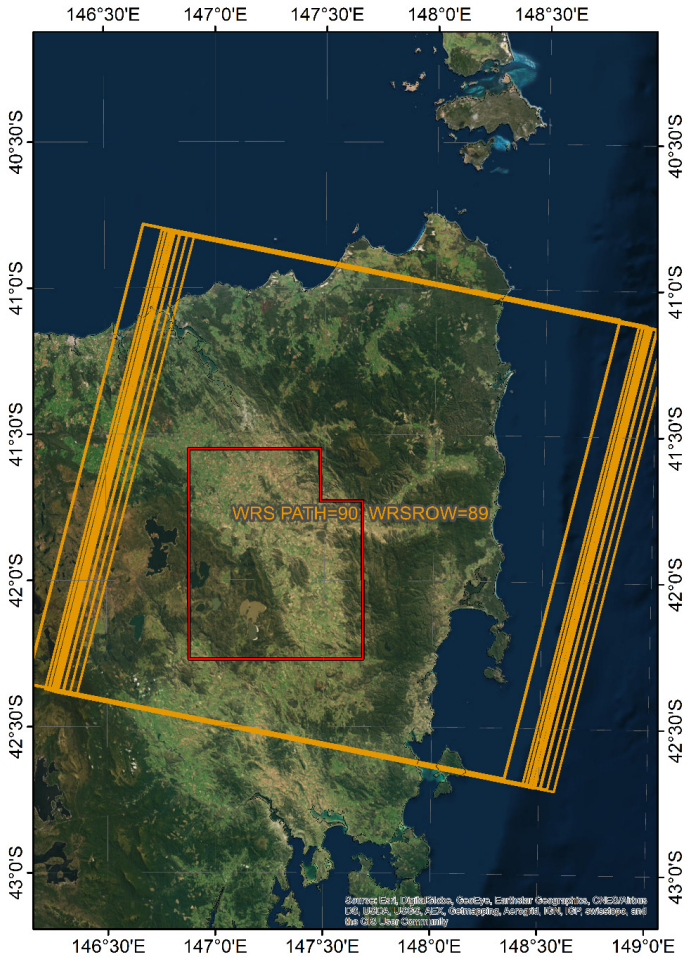
Most Landsat-5 TM scenes were processed with the Standard Terrain Correction (Level 1T). Standard Terrain Correction provides systematic radiometric and geometric accuracy by incorporating ground control points while employing a Digital Elevation Model (DEM) for topographic accuracy.

Legend

EL-30 area
Tasmania boundary

ID and Acquisition date

LT50900891988040ASA00, 1988/02/09
LT50900891988056ASA00, 1988/02/25
LT50900891989026ASA00, 1989/01/26
LT50900891990061ASA00, 1990/03/02
LT50900891991032ASA00, 1991/02/01
LT50900891996062ASA00, 1996/03/02
LT50900891996110ASA00, 1996/04/19
LT50900891998035ASA00, 1998/02/04
LT50900891998067ASA00, 1998/03/08
LT50900891999166ASA00, 1999/06/15
LT50900891999262ASA00, 1999/09/19
LT50900892004100ASA01, 2004/04/09
LT50900892004228ASA00, 2004/08/15
LT50900892004292ASA00, 2004/10/18
LT50900892004340ASA00, 2004/12/05
LT50900892005246ASA01, 2005/09/03
LT50900892010292ASA00, 2010/10/19



ls5.png

TERRA (ASTER)

Sensor Technical Specifications
http://asterweb.jpl.nasa.gov/

	VNIR subsystem	SWIR subsystem	TIR subsystem
Sensor type:	push broom		
Spatial Resolution:	15m	30m	90m
Spectral Range:	0.52 – 0.86 µm	1.6 – 2.43 µm	8.125 – 11.65 µm
Number of Bands:			
Temporal Resolution:	16 days		
Image Size:	60 km X 60 km		
Swath:	60 m		
Stereoscopic:	yes	no	no

Band Number	Spectral range, µm
1	0.52–0.60
2	0.63–0.69
3 (N)	0.78–0.86
4 (B)	0.78–0.86

Band Number	Spectral range, µm
5	1.6–1.7
6	2.145–2.185
7	2.185–2.225
8	2.235–2.285
9	2.295–2.365
10	2.360–2.430

Band Number	Spectral range, µm
11	8.125-8.475
12	8.475-8.825
13	8.925-9.275
14	10.25-10.95
15	10.95-11.65

TERRA (ASTER) Day mode

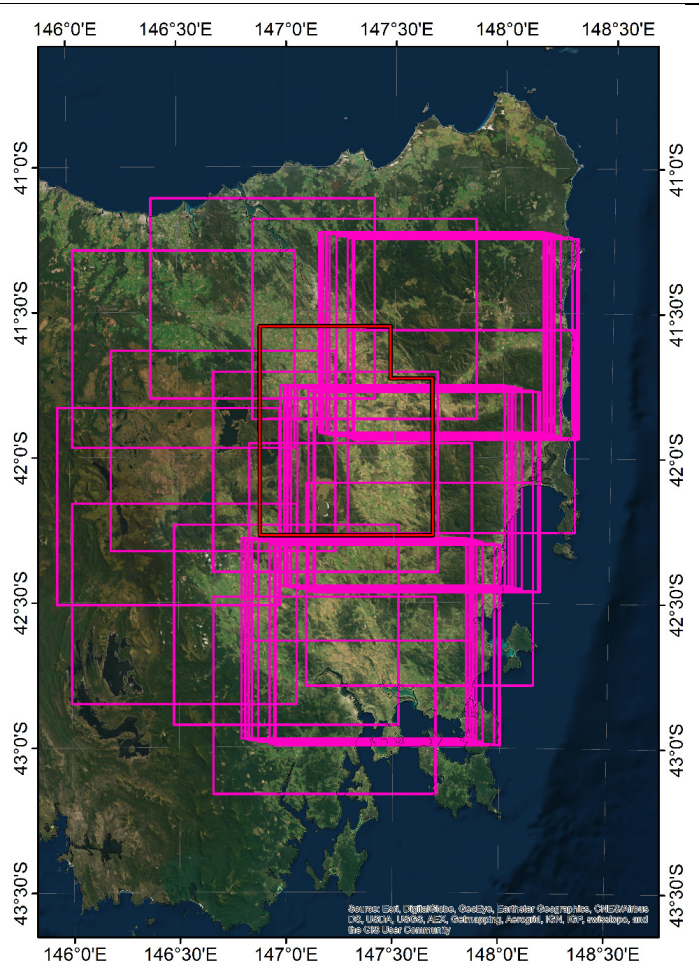
Legend

- EL-30 area
- Tasmania boundary

Terra Aster day imagery

ID and Acquisition date

- 2156189249, 2004/02/05
- 2157069093, 2004/08/17
- 2157069123, 2004/08/17
- 2157286239, 2004/09/25
- 2157548909, 2004/11/12
- 2157549177, 2004/11/12
- 2157686478, 2004/12/30
- 2157686496, 2004/12/30
- 2157686508, 2004/12/30
- 2160342206, 2006/10/01
- 2160342346, 2006/10/01
- 2160342383, 2006/10/01
- 2161256050, 2007/03/26
- 2161256244, 2007/03/26
- 2161256287, 2007/03/26
- 2162260729, 2007/10/20
- 2162260789, 2007/10/20
- 2162260799, 2007/10/20
- 2164225974, 2009/05/18
- 2164226008, 2009/05/18
- 2164226062, 2009/05/18
- 2165780577, 2010/06/22
- 2165780591, 2010/06/22
- 2165780639, 2010/06/22
- 2165830214, 2010/07/08
- 2165830264, 2010/07/08
- 2165830276, 2010/07/08
- 2166793753, 2011/03/12
- 2166863329, 2011/03/28
- 2166863663, 2011/03/28
- 2166896227, 2011/04/06
- 2166896229, 2011/04/06
- 2166896321, 2011/04/06
- 2167854349, 2012/02/04
- 2167854354, 2012/02/04
- 2167854434, 2012/02/04
- 2169934877, 2013/09/02
- 2169934948, 2013/09/02
- 2169934954, 2013/09/02
- 2171237392, 2014/07/19
- 2171237418, 2014/07/19
- 2171237514, 2014/07/19
- 2215135374, 2016/03/02
- 2215135408, 2016/03/02
- 2215135410, 2016/03/02



Aster_day.png

TERRA (ASTER) Night mode

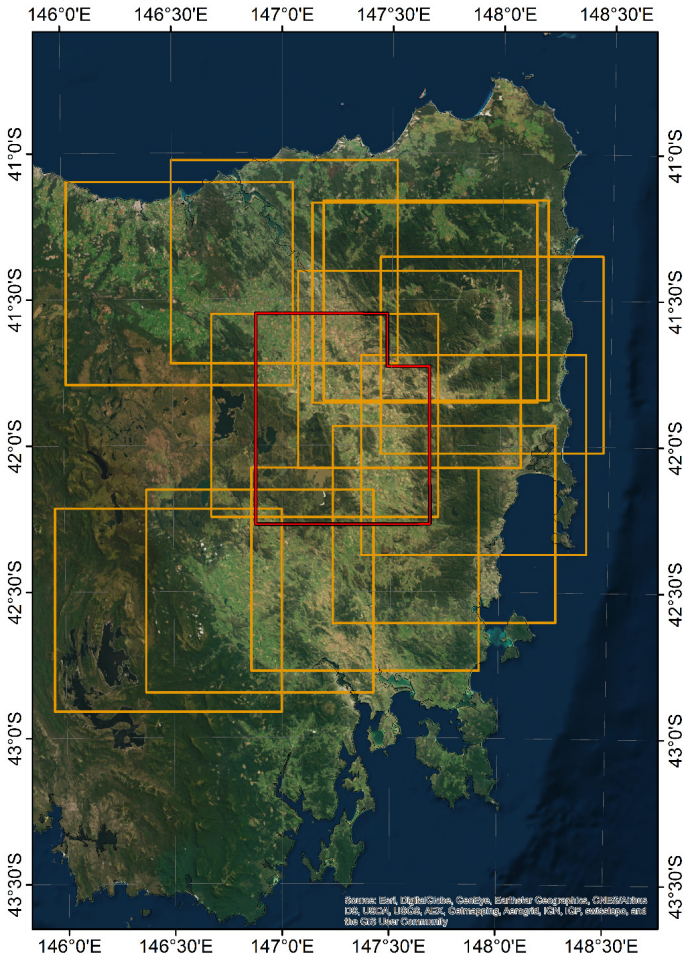
Legend

- EL-30 area
- Tasmania boundary

Terra Aster night imagery

ID and Acquisition date

- 2165610619, 2010/05/02
- 2165610782, 2010/05/02
- 2165610812, 2010/05/02
- 2165717840, 2010/06/03
- 2165717841, 2010/06/03
- 2166095256, 2010/09/07
- 2166127396, 2010/09/16
- 2166570362, 2011/01/15
- 2166570436, 2011/01/15
- 2166666836, 2011/02/07
- 2166666964, 2011/02/07
- 2166761493, 2011/03/04



Aster_night.png

SENTINEL 2

Sensor Technical Specifications

http://esamultimedia.esa.int/docs/S2-Data_Sheet.pdf

Spatial Resolution: 10m - 60m,

Spectral Range: 443 nm– 2190 nm

Number of Bands: 13

Temporal Resolution: 5 days

Swath: 190 km

Radiometric resolution 12bit

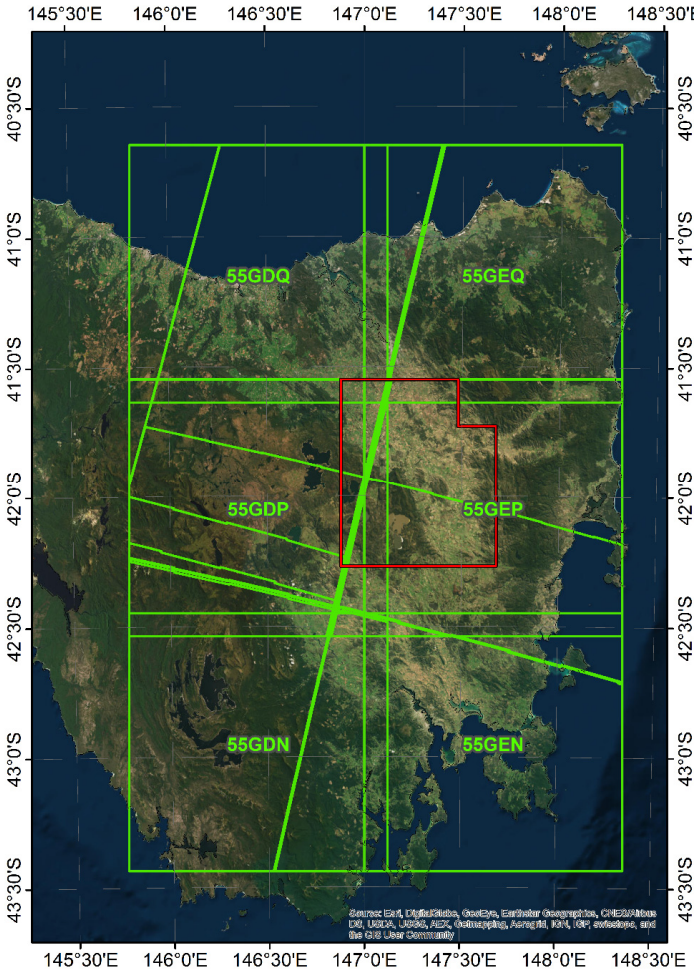
Band Number	Central wavelength (nm)	Bandwidth (nm)	Spatial resolution (m)
1	443.9	27	60
2	496.6	98	10
3	560.0	45	10
4	664.5	38	10
5	703.9	19	20
6	740.2	18	20
7	782.5	28	20
8	835.1	145	10
8a	864.8	33	20
9	945.0	26	60
10	1373.5	75	60
11	1613.7	143	20
12	2202.4	242	20

Legend

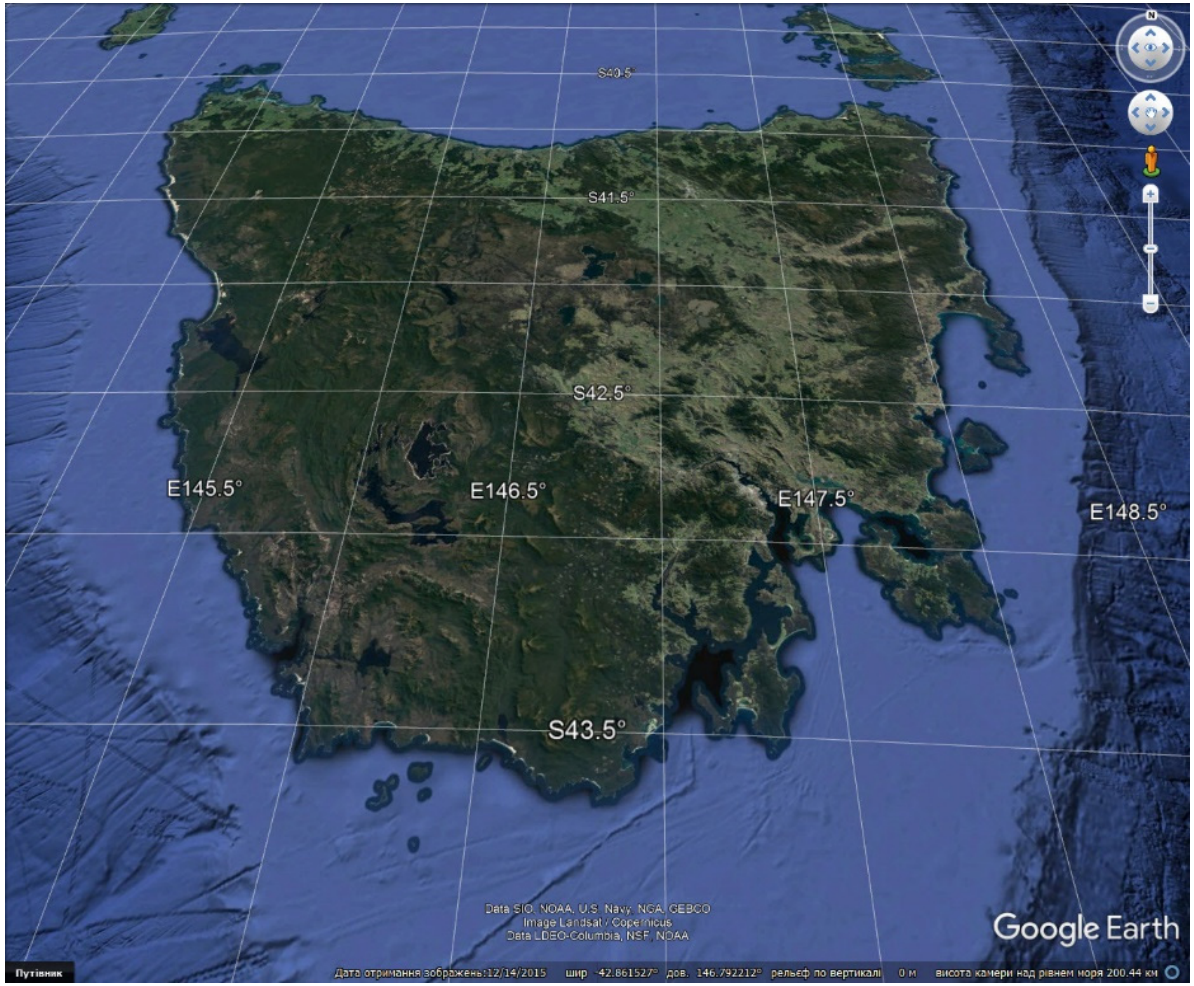
EL-30 area
Tasmania boundary

Tile name and date

55GDN, 2015-12-22*
55GDN, 2016-06-02*
55GDN, 2016-09-07*
55GDN, 2016-11-09*
55GDN, 2016-12-16*
55GDN, 2017-07-09*
55GDN, 2017-08-31*
55GDP, 2015-12-22*
55GDP, 2016-05-20*
55GDP, 2016-06-02*
55GDP, 2016-09-07*
55GDP, 2016-11-09*
55GDP, 2016-12-16*
55GDP, 2017-01-28*
55GDP, 2017-04-18*
55GDP, 2017-05-08*
55GDP, 2017-07-09*
55GDP, 2017-08-31*
55GDP, 2016-05-20*
55GDP, 2016-06-02*
55GDQ, 2016-11-09*
55GDQ, 2016-06-02*
55GDQ, 2017-01-28*
55GDQ, 2017-04-18*
55GDQ, 2017-05-08*
55GDQ, 2017-07-09*
55GDQ, 2017-08-31*
55GEN, 2015-12-22*
55GEN, 2016-12-16*
55GEN, 2017-07-09*
55GEP, 2016-05-20*
55GEP, 2016-06-02*
55GEP, 2016-11-09*
55GEP, 2016-12-16*
55GEP, 2017-01-28*
55GEP, 2017-04-18*
55GEP, 2017-05-08*
55GEP, 2017-08-31*
55GEQ, 2016-05-20*
55GEQ, 2016-06-02*
55GEQ, 2016-11-09*
55GEQ, 2017-04-18*
55GEQ, 2017-05-08*
55GEQ, 2017-08-31*



Sentinel-2.png

Google Earth On-line service	Google Earth is a virtual globe, map, and geographical information program. http://www.google.com/earth/index.html It maps the Earth by the superimposition of images obtained from middle resolution satellite imagery (Landsat-8, Sentinel-2, Spot-5), high resolution satellite imagery (World-View & GeoEye), aerial photography and Topographical Data (SRTM)	 *GoogleEarth_Image.jpg*

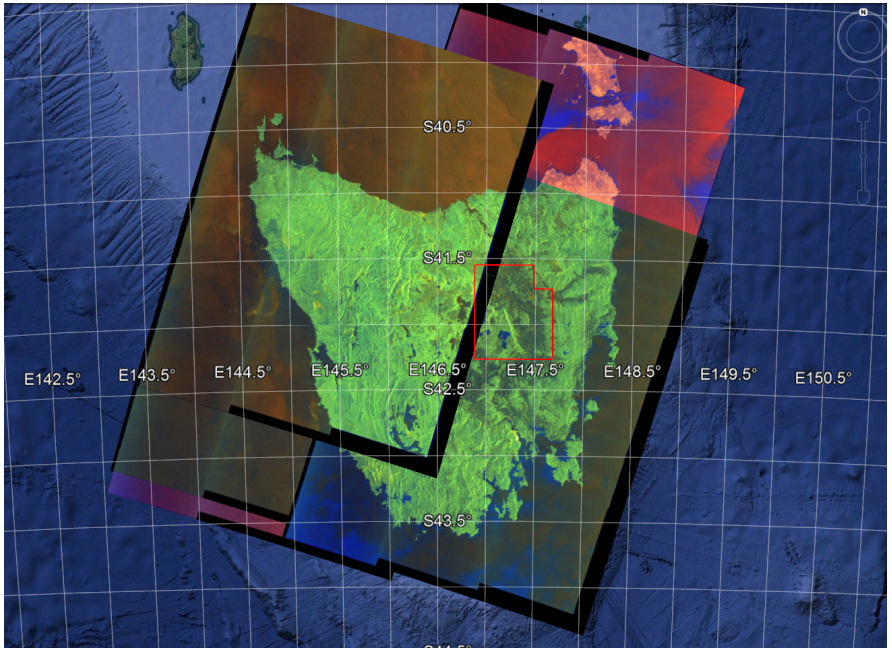
RADAR DATA

DATA TYPE	PARAMETERS AND CHARACTERISTICS
Sentinel 1	Sensor Technical Specifications http://esamultimedia.esa.int/docs/S1-Data_Sheet.pdf **Type:** C-Band SAR **Centre frequency:** 5.405 GHz **Polarization:** VV+VH ***OR*** HH+HV **Temporal Resolution:** 12 days **Swaths:** • Strip Map Mode with 80 km swath and 5x5 m (range x azimuth) spatial resolution • Interferometric Wide-Swath Mode with 250 km swath, 5x20 m (range x azimuth) spatial resolution and burst synchronisation for interferometry • Extra-Wide-Swath Mode with 400 km swath and 20x40 m (range x azimuth) spatial resolution • Wave Mode with 5x5 m (range x azimuth) spatial resolution leap-frog sampled images of 20x20 km at 100 km along the orbit, with alternating 23º and 36.5º incidence angles. **Products:** • Single Look Complex (SLC) products Products consist of focused SAR data and provided in slant-range geometry. It include a single look in each dimension using the full available signal bandwidth and complex samples (real and imaginary) preserving the phase information. • Ground Range Detected (GRD) products Products consist of focused SAR data that has been detected, multi-looked and projected. Pixel values represent detected magnitude. Phase information is lost.

Sentinel 1 GRD (Ground Range Detected)

List of GRDH Sentinel-1 imagery

S1A_IW_GRDH_1SDV_20150430T192530_20150430T192559_005717_00756D_D994
S1A_IW_GRDH_1SDV_20150430T192559_20150430T192622_005717_00756D_FB35
S1A_IW_GRDH_1SDV_20150507T191704_20150507T191733_005819_0077C1_ECB1
S1A_IW_GRDH_1SDV_20150507T191733_20150507T191758_005819_0077C1_5307
S1A_IW_GRDH_1SDV_20151015T192537_20151015T192606_008167_00B798_AF1B
S1A_IW_GRDH_1SDV_20151015T192606_20151015T192629_008167_00B798_776D
S1A_IW_GRDH_1SDV_20151022T191711_20151022T191740_008269_00BA6E_5646
S1A_IW_GRDH_1SDV_20151022T191740_20151022T191805_008269_00BA6E_9B48
S1A_IW_GRDH_1SDV_20160927T192536_20160927T192603_013242_015148_3A70
S1A_IW_GRDH_1SDV_20161021T192542_20161021T192607_013592_015C50_F308
S1A_IW_GRDH_1SDV_20161021T192607_20161021T192633_013592_015C50_6C94
S1A_IW_GRDH_1SDV_20161028T191737_20161028T191802_013694_015F70_92F7
S1A_IW_GRDH_1SDV_20161121T191737_20161121T191802_014044_016A4A_2353
S1A_IW_GRDH_1SDV_20161121T191802_20161121T191826_014044_016A4A_BE43
S1A_IW_GRDH_1SDV_20161126T192541_20161126T192606_014117_016C87_E422
S1A_IW_GRDH_1SDV_20161203T191737_20161203T191802_014219_016FBC_428D
S1A_IW_GRDH_1SDV_20161208T192530_20161208T192555_014292_017213_323E
S1A_IW_GRDH_1SDV_20161215T191737_20161215T191802_014394_01754A_E53A
S1A_IW_GRDH_1SDV_20161215T191802_20161215T191828_014394_01754A_81AE
S1A_IW_GRDH_1SDV_20170309T191734_20170309T191759_015619_019AF6_AD1C
S1A_IW_GRDH_1SDV_20170309T191759_20170309T191825_015619_019AF6_F5E7
S1A_IW_GRDH_1SDV_20170314T192527_20170314T192552_015692_019D2A_D887
S1A_IW_GRDH_1SDV_20170314T192552_20170314T192618_015692_019D2A_7F8B
S1A_IW_GRDH_1SDV_20170321T191734_20170321T191759_015794_01A02B_054E
S1A_IW_GRDH_1SDV_20170321T191759_20170321T191825_015794_01A02B_D0C6
S1A_IW_GRDH_1SDV_20170326T192528_20170326T192553_015867_01A259_9393
S1A_IW_GRDH_1SDV_20170326T192553_20170326T192619_015867_01A259_CB14
S1A_IW_GRDH_1SDV_20170402T191734_20170402T191759_015969_01A55A_0AF0
S1A_IW_GRDH_1SDV_20170402T191759_20170402T191825_015969_01A55A_67E8
S1A_IW_GRDH_1SDV_20170407T192528_20170407T192553_016042_01A791_221A
S1A_IW_GRDH_1SDV_20170407T192553_20170407T192619_016042_01A791_5D08
S1A_IW_GRDH_1SDV_20170414T191735_20170414T191800_016144_01AAB1_D1B6
S1A_IW_GRDH_1SDV_20170414T191800_20170414T191826_016144_01AAB1_6D7F
S1A_IW_GRDH_1SDV_20170419T192529_20170419T192554_016217_01ACF4_95D3
S1A_IW_GRDH_1SDV_20170419T192554_20170419T192620_016217_01ACF4_3DEF
S1A_IW_GRDH_1SDV_20170426T191735_20170426T191800_016319_01B008_9288
S1A_IW_GRDH_1SDV_20170426T191800_20170426T191826_016319_01B008_4C77
S1A_IW_GRDH_1SDV_20170501T192529_20170501T192554_016392_01B240_F726
S1A_IW_GRDH_1SDV_20170501T192554_20170501T192620_016392_01B240_7BDB
S1A_IW_GRDH_1SDV_20170508T191736_20170508T191801_016494_01B55B_080F
S1A_IW_GRDH_1SDV_20170508T191801_20170508T191827_016494_01B55B_A218
S1A_IW_GRDH_1SDV_20170513T192530_20170513T192555_016567_01B78E_C325
S1A_IW_GRDH_1SDV_20170513T192555_20170513T192621_016567_01B78E_A8C3
S1A_IW_GRDH_1SDV_20170520T191737_20170520T191802_016669_01BAB4_7DA5
S1A_IW_GRDH_1SDV_20170520T191802_20170520T191828_016669_01BAB4_B2FB
S1A_IW_GRDH_1SDV_20170525T192530_20170525T192555_016742_01BCEF_8C36
S1A_IW_GRDH_1SDV_20170525T192555_20170525T192621_016742_01BCEF_E8EA
S1A_IW_GRDH_1SDV_20170606T192531_20170606T192556_016917_01C268_A8AE
S1A_IW_GRDH_1SDV_20170606T192556_20170606T192622_016917_01C268_3F21
S1A_IW_GRDH_1SDV_20170613T191738_20170613T191803_017019_01C588_817E
S1A_IW_GRDH_1SDV_20170613T191803_20170613T191829_017019_01C588_509A



Sentinel1_GRDH.jpg

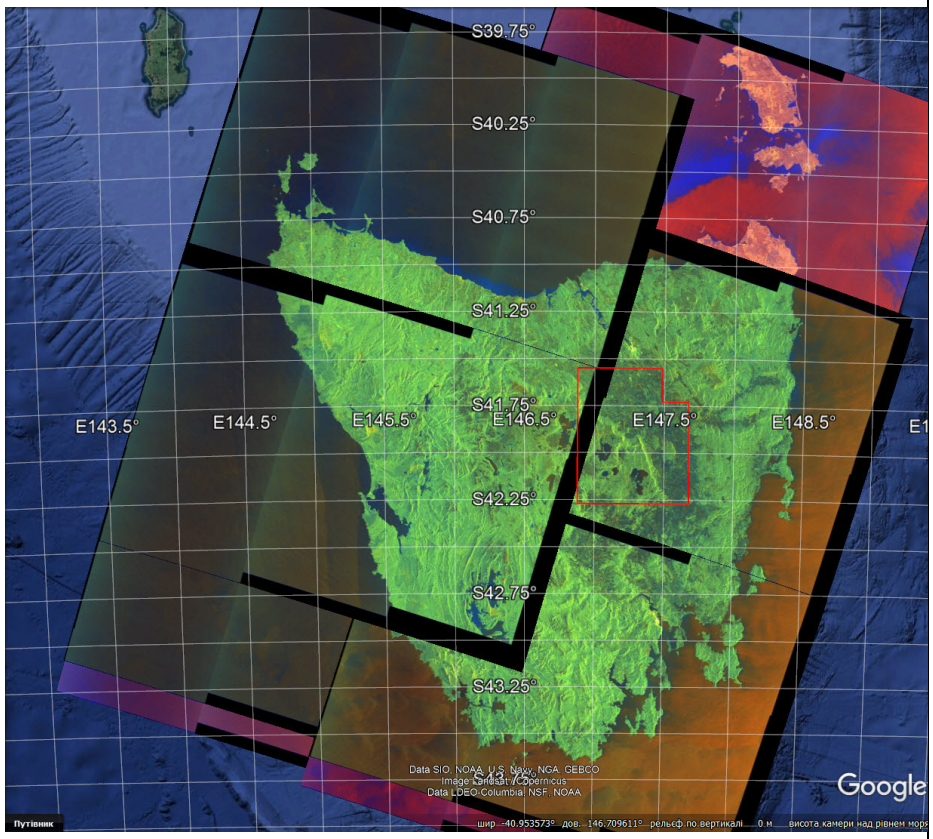
List of GRDH Sentinel-1 imagery p2

S1A_IW_GRDH_1SDV_20170618T192532_20170618T192557_017092_01C7C8_09EC
S1A_IW_GRDH_1SDV_20170618T192557_20170618T192623_017092_01C7C8_09CB
S1A_IW_GRDH_1SDV_20170625T191739_20170625T191804_017194_01CADD_8EFC
S1A_IW_GRDH_1SDV_20170625T191804_20170625T191830_017194_01CADD_EFF6
S1A_IW_GRDH_1SDV_20170630T192533_20170630T192558_017267_01CD10_6C3F
S1A_IW_GRDH_1SDV_20170630T192558_20170630T192624_017267_01CD10_919E
S1A_IW_GRDH_1SDV_20170707T191739_20170707T191804_017369_01D020_56BC
S1A_IW_GRDH_1SDV_20170707T191804_20170707T191830_017369_01D020_CD02
S1A_IW_GRDH_1SDV_20170712T192533_20170712T192558_017442_01D25D_17FC
S1A_IW_GRDH_1SDV_20170712T192558_20170712T192624_017442_01D25D_CA71
S1A_IW_GRDH_1SDV_20170719T191740_20170719T191805_017544_01D579_AF7D
S1A_IW_GRDH_1SDV_20170719T191805_20170719T191831_017544_01D579_440C
S1A_IW_GRDH_1SDV_20170724T192534_20170724T192559_017617_01D7B0_A163
S1A_IW_GRDH_1SDV_20170731T191741_20170731T191806_017719_01DAD4_656E
S1A_IW_GRDH_1SDV_20170731T191806_20170731T191832_017719_01DAD4_CB5D
S1A_IW_GRDH_1SDV_20170805T192535_20170805T192600_017792_01DD0A_D448
S1A_IW_GRDH_1SDV_20170805T192600_20170805T192626_017792_01DD0A_BB69

Sentinel 1 SLC (Single Look Complex)

List of SLC Sentinel-1 imagery

S1A_IW_SLC__1SDV_20151015T192537_20151015T192607_008167_00B798_2C07
S1A_IW_SLC__1SDV_20151015T192605_20151015T192629_008167_00B798_9DD0
S1A_IW_SLC__1SDV_20151022T191711_20151022T191741_008269_00BA6E_5CF3
S1A_IW_SLC__1SDV_20151022T191738_20151022T191805_008269_00BA6E_E183
S1A_IW_SLC__1SDV_20151022T191803_20151022T191825_008269_00BA6E_37D0
S1A_IW_SLC__1SDV_20160927T192535_20160927T192603_013242_015148_AC0C
S1A_IW_SLC__1SDV_20161021T192606_20161021T192633_013592_015C50_4861
S1A_IW_SLC__1SDV_20161203T191735_20161203T191802_014219_016FBC_5A89
S1A_IW_SLC__1SDV_20161203T191800_20161203T191825_014219_016FBC_1A77
S1A_IW_SLC__1SDV_20161208T192529_20161208T192556_014292_017213_9A8D
S1A_IW_SLC__1SDV_20161208T192554_20161208T192621_014292_017213_4567
S1A_IW_SLC__1SDV_20161215T191736_20161215T191803_014394_01754A_E905
S1A_IW_SLC__1SDV_20161215T191800_20161215T191828_014394_01754A_E391
S1A_IW_SLC__1SDV_20170525T192529_20170525T192556_016742_01BCEF_C8CC
S1A_IW_SLC__1SDV_20170525T192554_20170525T192621_016742_01BCEF_A2C5
S1A_IW_SLC__1SDV_20170606T192530_20170606T192557_016917_01C268_3501
S1A_IW_SLC__1SDV_20170606T192555_20170606T192622_016917_01C268_39FC
S1A_IW_SLC__1SDV_20170613T191737_20170613T191804_017019_01C588_BE3E
S1A_IW_SLC__1SDV_20170613T191802_20170613T191829_017019_01C588_C6C0
S1A_IW_SLC__1SDV_20170618T192531_20170618T192558_017092_01C7C8_7EF9
S1A_IW_SLC__1SDV_20170618T192556_20170618T192623_017092_01C7C8_8DF0
S1A_IW_SLC__1SDV_20170625T191738_20170625T191805_017194_01CADD_5E4B
S1A_IW_SLC__1SDV_20170625T191803_20170625T191830_017194_01CADD_BFDA
S1A_IW_SLC__1SDV_20170630T192532_20170630T192559_017267_01CD10_C589
S1A_IW_SLC__1SDV_20170630T192556_20170630T192624_017267_01CD10_D1CC
S1A_IW_SLC__1SDV_20170707T191738_20170707T191806_017369_01D020_5AD9
S1A_IW_SLC__1SDV_20170707T191803_20170707T191830_017369_01D020_5ED8
S1A_IW_SLC__1SDV_20170712T192532_20170712T192559_017442_01D25D_1C30
S1A_IW_SLC__1SDV_20170712T192557_20170712T192624_017442_01D25D_6638
S1A_IW_SLC__1SDV_20170719T191739_20170719T191806_017544_01D579_B61E
S1A_IW_SLC__1SDV_20170719T191804_20170719T191831_017544_01D579_7B96
S1A_IW_SLC__1SDV_20170724T192533_20170724T192600_017617_01D7B0_768F
S1A_IW_SLC__1SDV_20170724T192558_20170724T192625_017617_01D7B0_7460
S1A_IW_SLC__1SDV_20170731T191805_20170731T191832_017719_01DAD4_F38A
S1A_IW_SLC__1SDV_20170805T192534_20170805T192601_017792_01DD0A_6612
S1A_IW_SLC__1SDV_20170805T192559_20170805T192626_017792_01DD0A_4038
S1A_IW_SLC__1SDV_20170812T191741_20170812T191808_017894_01E023_B3B3
S1A_IW_SLC__1SDV_20170812T191805_20170812T191833_017894_01E023_977F
S1A_IW_SLC__1SDV_20170817T192534_20170817T192601_017967_01E256_8208
S1A_IW_SLC__1SDV_20170817T192559_20170817T192626_017967_01E256_C6EC
S1A_IW_SLC__1SDV_20170824T191741_20170824T191808_018069_01E56E_48CF
S1A_IW_SLC__1SDV_20170824T191806_20170824T191833_018069_01E56E_ACB6
S1A_IW_SLC__1SDV_20170905T191742_20170905T191809_018244_01EAC1_942E
S1A_IW_SLC__1SDV_20170905T191806_20170905T191834_018244_01EAC1_955D
S1A_IW_SLC__1SDV_20170910T192535_20170910T192602_018317_01ED0F_0E37
S1A_IW_SLC__1SDV_20170910T192600_20170910T192627_018317_01ED0F_C741



Sentinel1_SLC.jpg

Alos Palsar Level 1.1 Single-look complex (SLC)

Sensor Technical Specifications
http://www.pcigeomatics.com/geomatica-help/references/gdb_r/ALOS-1_PALSAR.html

Long name	PALSAR1
Short name	PS1
Sensor type	Synthetic Aperture Radar (SAR)
Platform	Advanced Land Observing Satellite-1 (ALOS-1)
Frequency	1.2 GHz
Band (wavelength)	L (22.9 centimeters)
Polarization	HH, HV, VH, VV (fully polarimetric)

This is the product of Single-look complex (SLC) equally spaced on slant range (equal to the spacing of sampling measurement) generated after rendering SAR processing to level 1.0 product.

Legend

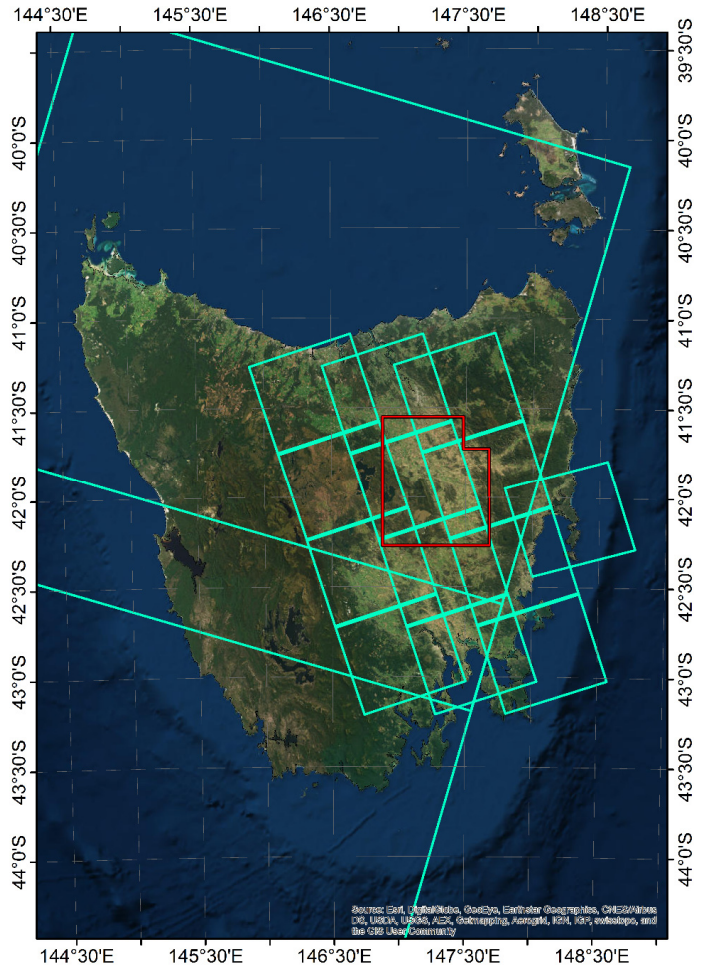
EL-30 area

Tasmania boundary

Alos Palsar Level1.1

ID and Acquisition date

ALPSRP074756310, 2007-06-20T13:37:24
ALPSRP074756320, 2007-06-20T13:37:32
ALPSRP074756330, 2007-06-20T13:37:41
ALPSRP074756340, 2007-06-20T13:37:49
ALPSRP076506310, 2007-07-02T13:33:06
ALPSRP076506320, 2007-07-02T13:33:14
ALPSRP076506330, 2007-07-02T13:33:22
ALPSRP076506340, 2007-07-02T13:33:31
ALPSRP078986310, 2007-07-19T13:35:13
ALPSRP078986320, 2007-07-19T13:35:21
ALPSRP078986330, 2007-07-19T13:35:29
ALPSRP078986340, 2007-07-19T13:35:37
ALPSRP080736330, 2007-07-31T13:31:10
ALPSRS143524450, 2008-10-03T23:56:08
ALPSRS143524500, 2008-10-03T23:56:49



Alos_palsar_L11.png

Alos Palsar Level 1.5

Sensor Technical Specifications
http://www.pcigeomatics.com/geomatica-help/references/gdb_r/ALOS-1_PALSAR.html

Long name	PALSAR1
Short name	PS1
Sensor type	Synthetic Aperture Radar (SAR)
Platform	Advanced Land Observing Satellite-1 (ALOS-1)
Frequency	1.2 GHz
Band (wavelength)	L (22.9 centimeters)
Polarization	HH, HV, VH, VV (fully polarimetric)

This is the product of Multi-look amplitude generated after rendering SAR processing to level 1.0 product, acquired in single polarization high resolution mode. The data are equally spaced on the ground.

Legend

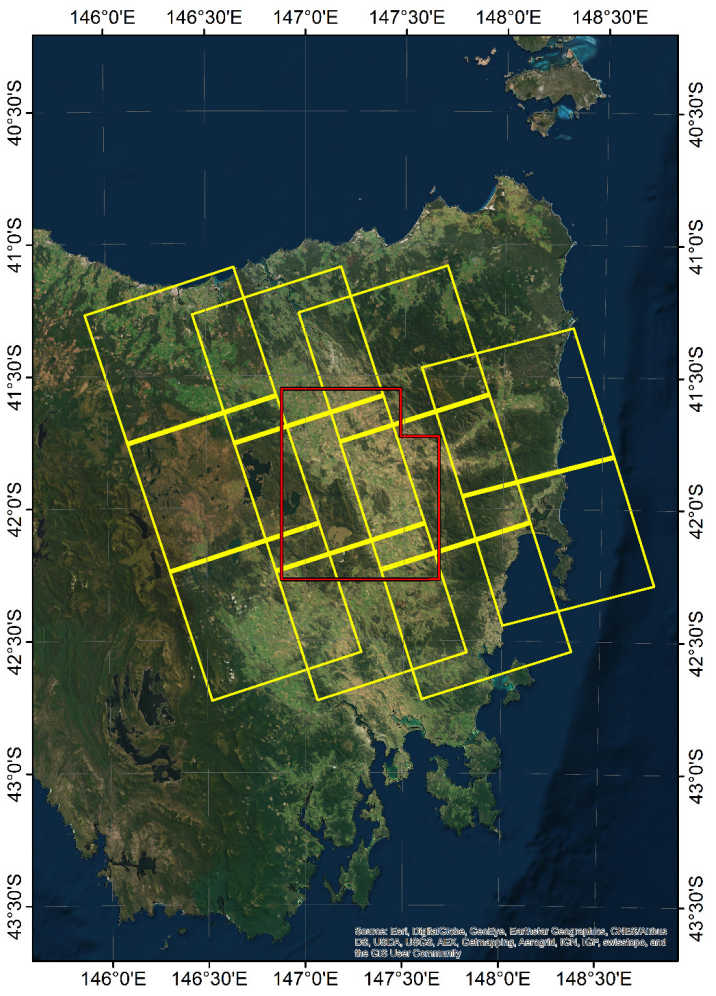
EL-30 area

Tasmania boundary

Alos Palsar Level1.5

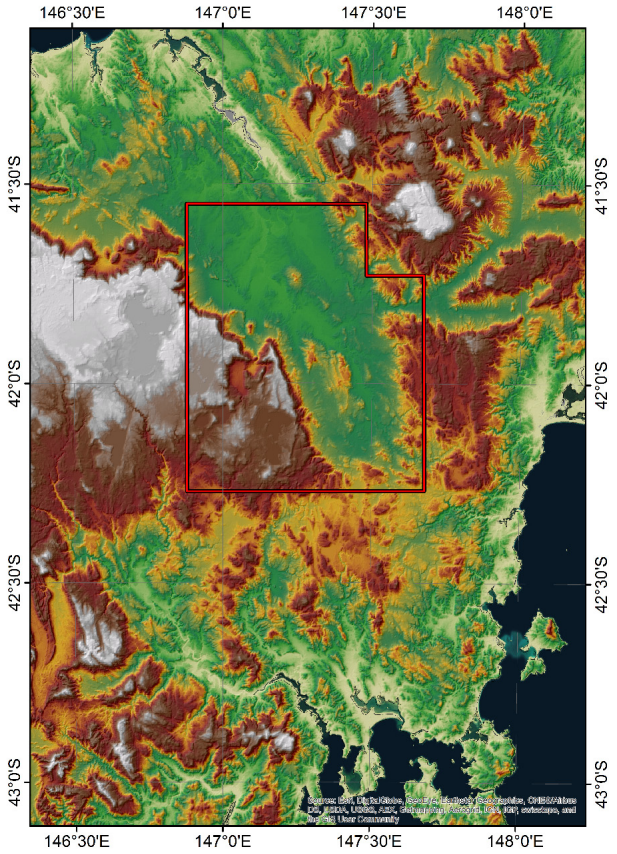
ID and Acquisition date

ALPSRP074756320, 2007-06-20T13:37:32
ALPSRP074756330, 2007-06-20T13:37:41
ALPSRP074756340, 2007-06-20T13:37:49
ALPSRP076506320, 2007-07-02T13:33:14
ALPSRP076506330, 2007-07-02T13:33:22
ALPSRP076506340, 2007-07-02T13:33:31
ALPSRP078986320, 2007-07-19T13:35:21
ALPSRP078986330, 2007-07-19T13:35:29
ALPSRP078986340, 2007-07-19T13:35:37
ALPSRP080736330, 2007-07-31T13:31:10
ALPSRP080736340, 2007-07-31T13:31:18



Alos_palsar_L15.png

TOPOGRAPHICAL DATA

DATA TYPE	PARAMETERS AND CHARACTERISTICS	
SRTM (Shuttle Radar Topography Mission)	Digital elevation model obtained by means of a specially modified radar system that flew on board Space Shuttle. http://srtm.csi.cgiar.org/	

SRTM Specification	
Resolution	3 arc-second (90 m)
Rows per tile	3,601
Bit Depth	16 bit
Versioning	The CGIAR-CSI version 4

SRTM.png

Australia National DEM based on SRTM

The 1 Second DSM and DEM are national elevation data products derived from the Shuttle Radar Topographic Mission (SRTM) data

SRTM Specification	
Resolution	1 arc-second (~30 m)
Bit Depth	16 bit
Versioning	June 2011, the Level-2

Legend

EL-30 area

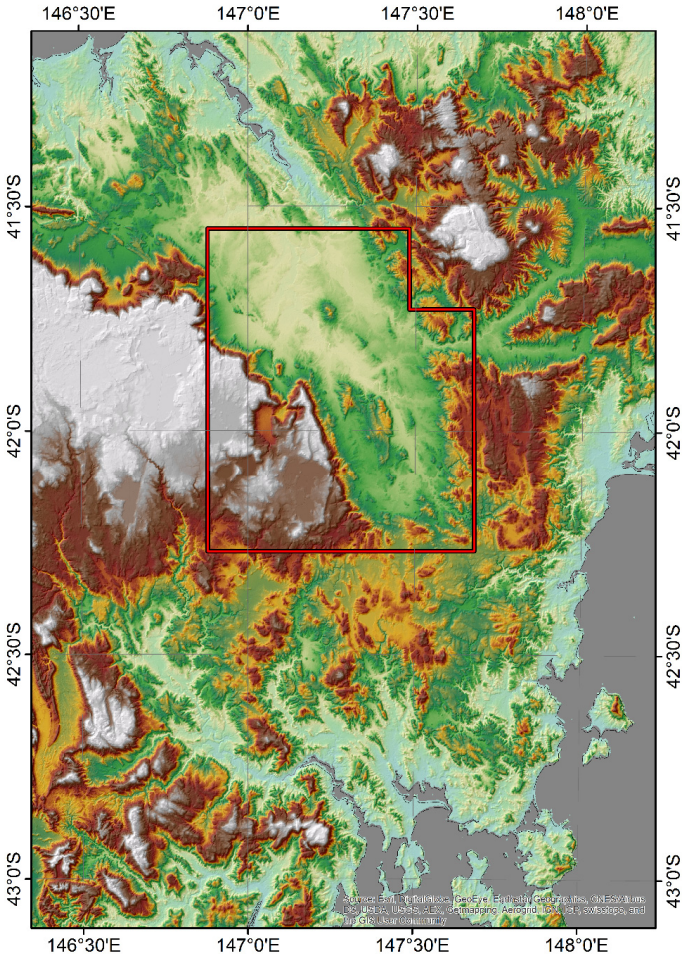
Tasmania boundary

Australia National DEM 25m

meters

High : 1602

Low : 0



Au_national.png

Aster GDEM v2 (Global Digital Elevation Model)

The ASTER Global Digital Elevation Model (ASTER GDEM) is a joint product developed and made available to the public by the Ministry of Economy, Trade, and Industry (METI) of Japan and the United States National Aeronautics and Space Administration (NASA). It is generated from data collected from the Advanced Spaceborne Thermal Emission and Reflection Radiometer (ASTER), a spaceborne earth observing optical instrument.

During October 2011 version 2 of Global Digital Elevation Model was publicly released. This is considered an improvement upon version 1. These improvements include increased horizontal and vertical accuracy, better horizontal resolution, reduced presence of artifacts, and more realistic values over water bodies.
https://asterweb.jpl.nasa.gov/gdem.asp

Aster GDTM Specifications	
Data Source	Aster
Resolution	1 arc-second (30 m)
Coverage	83 degrees north - 83 degrees south
Versioning	version 2 , 2011

Legend

EL-30 area

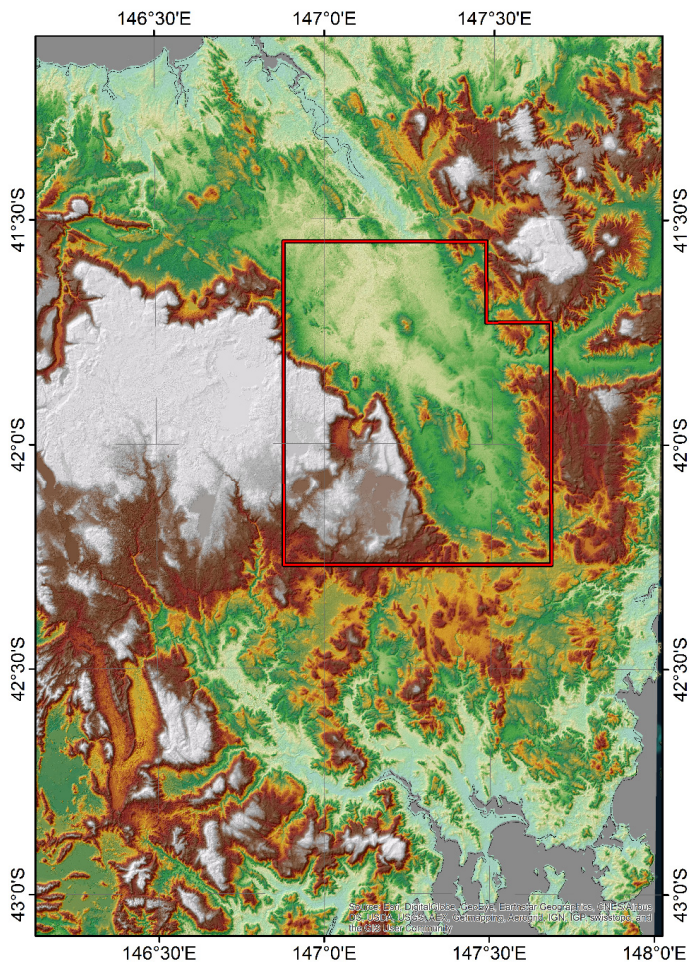
Tasmania boundary

Aster Gdem v2

meters

High : 1602

Low : 0



Aster_gdem.png

ASF radiometrically terrain corrected ALOS PALSAR

Technical Specifications
https://media.asf.alaska.edu/uploads/RTC/rtc_product_guide_v1.2.pdf

Alos DEM Specifications	
Resolution	12.5 m
Bit Depth	16 bit

Legend

EL-30 area

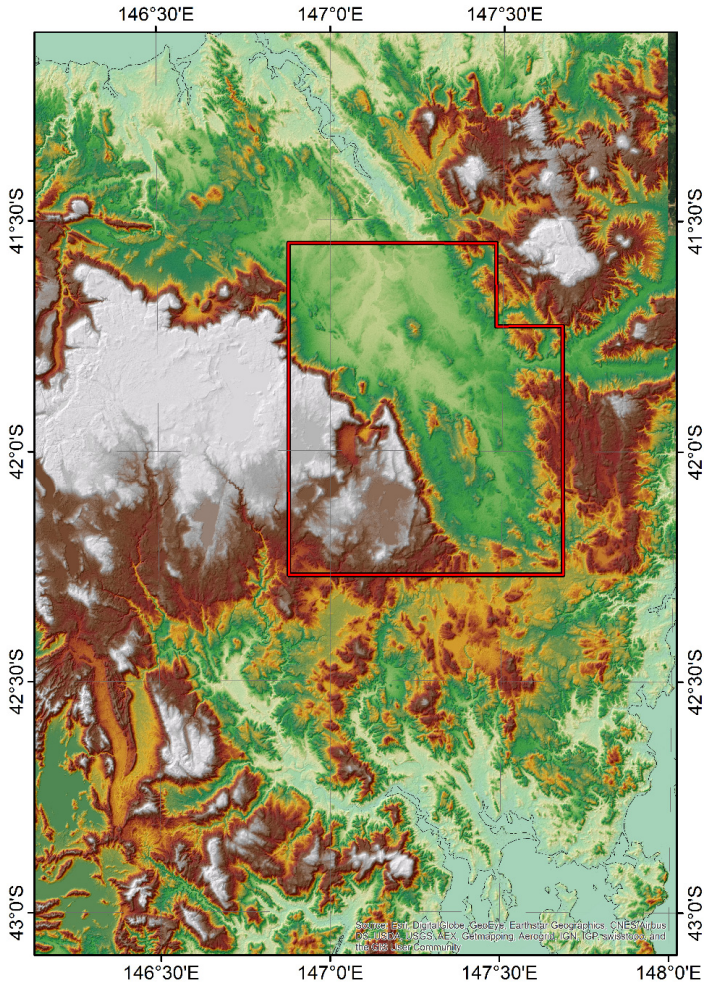
Tasmania boundary

Alos dem

meters

High : 1610

Low : 0



el_Alos_dem.png

APPENDIX 2 - EXISTING PROCESSED SEISMIC POST PROCESSING AND INTERPRETATION